Development of a thermal energy storage system with a wide temperature range using a natural mineral mixture as porous support of a phase change material

Carolina Cárdenas Ramírez

Doctoral thesis submitted for the degree of Doctor in Materials Engineering

Supervisors:
Professor Maryory A. Gómez Botero, PhD
Professor Franklin Jaramillo Isaza, PhD

Universidad de Antioquia
Facultad de Ingeniería
Doctorado en Ingeniería de Materiales
Medellín, Antioquia, Colombia
2021

“No sabe el porqué de este tornillo y construirá un puente”

Wislawa Szymborska

I. ABSTRACT

Among building elements, the envelope is a key component in providing shelter and in regulating the thermal energy of the indoor environment. In this regard, the incorporation of thermal energy storage elements, as phase change materials (PCM), is proposed as a solution to contribute to energy-efficient building performance. Material finishes that incorporate PCMs can minimize the heating and cooling loads through the building envelope due to their high energy storage capacity, achieving thermal comfort inside the building, and increasing thermal inertia. Regarding the type of PCM, fatty acids are an interesting choice because they come from renewable sources, are non-toxic, present no-subcooling and are abundant, which makes them financially competitive with paraffins and salts in the PCM market. Even though, it is recommended to encapsulate them for extend time applications as the solid to liquid phase change can lead to material losses and leakages.

Hence, in this work, three binary eutectic mixtures of fatty acids were chosen as potential thermal energy storage materials for being used in building elements. Capric-myristic acid (CA/MA), lauric-myristic acid (LA/MA), and palmitic-stearic acid (PA/SA) mixtures were selected due to their wide range of temperatures that could work for different uses within the construction sector as passive cooling, low temperature solar heating, and domestic water heating. Shape-stabilized PCMs (SS-PCMs) were produced with these eutectics to avoid leakage, using a Colombian natural porous clay as support. The eutectics and SS-PCMs produced were deeply characterized by the authors in terms of thermal properties, thermal stability, thermal reliability (up to 10000 cycles), thermal conductivity, chemical and physical properties, and percentage of leakage, among others.

Moreover, within the novelties of this work, the idea that controlling and analyzing the textural properties of the supports used for shape-stabilization of PCMs, from a top-down approach, can optimize the absorption capacity of the PCM and thus, the thermal properties of the general system, was studied. Hence, physical and chemical modifications of the clay support were performed to improve the absorption and thermal properties of the final SS-PCMs. Modifications included heat treatments, granulation, and sylanization of the clay supports. Heat treatments produce more pores into the support that improved leakage

retention of the PCM, and sylanization generates covalent bonds between the PCM and the clay.

Finally, two configurations for incorporating SS-PCMs in buildings were evaluated using an equipment designed to measure thermal variables in dynamic and steady-state of the materials. The setup aims to simulate indoor and outdoor conditions. First, the three powder SS-PCMs were evaluated in direct contact with the outdoor environment, to analyze their insulation capacities, heat storage, and performance under diurnal cycles. Second, an acrylic-based plaster was designed with the incorporation of two of the SS-PCMs which then was used as a finish of a fiber cement siding. In the last case, the SS-PCM-based acrylic plaster was evaluated as an indoor material, without direct contact with the outdoor environment. The research demonstrated the viability of these samples as potential candidates to be incorporated in building envelopes.

II. ACKNOWLEDGMENTS

Throughout the writing of this dissertation I have received a great deal of support and assistance.

First, I would like to express my deepest appreciation to my supervisors, Dr. Maryory Gómez and Dr. Franklin Jaramillo for their invaluable advice, support and guidance during my PhD study. You provided me with the tools that I needed to choose the right direction and successfully complete this journey.

I would also like to extend my deepest gratitude to Alexis Bonnett, CEO at Sumicol S.A.S. This adventure would not have been possible without you. Your visionary guidance pushed me to sharpen my thinking and brought my work to a higher level.

I am also enormously grateful to CIDEMAT research group at Universidad de Antioquia, which welcomed me these past years. The pertinent insights you provided me, and by far, the friends and colleagues I found there are invaluable.

My heartfelt appreciation goes to Andrés Cardona, John Fernando Correa, Jaime Ángel, Daniel Ribero, Pablo Barrera, Christian Diaz, Materiales & Pinturas group, and all the people from Organización Corona. Your unwavering support, advice and patience cannot be underestimated.

I would like to extend my sincere thanks to Dr. Luisa Cabeza, Dr. Ángel Fernández, and to the GREiA research group from Universitat de Lleida, moltes gràcies per tota la teva ajuda. Thanks for the opportunities I was given to further my research, for the warm welcoming, and for a wonderful collaboration.

I am eternally grateful to my mentors Prof. Ramiro Restrepo Restrepo, although no longer with us, continues to inspire by his inexhaustible intellectual energy and curiosity, and Prof. Claudia García García, for your friendship and support. You had profoundly shaped the way I approach questions, science and life.

I am pleased to acknowledge the financial assistance of Sumicol S.A.S and "Ministerio de Ciencia, Tecnología e Innovación – MINCIENCIAS" through the "Fondo Francisco José de Caldas" with the contract 036-2016/FP44842-324-2017 and "Convocatoria 758-Doctorado Nacional en Empresa 2016".

Last, but not least, I cannot begin to express my thanks to my family and friends who provided me with encouragement and unconditional love. You cheer me up every step of the road.

III. RESEARCH OUTPUT

From the results of this thesis the following articles were published:

1. **C. Cárdenas-Ramírez**, F. Jaramillo, M.A. Gómez, Systematic review of encapsulation and shape-stabilization of phase change materials, J. Energy Storage. 30 (2020) 101495. https://doi.org/10.1016/j.est.2020.101495.

2. **C. Cárdenas-Ramírez**, M.A. Gómez, F. Jaramillo, Characterization of a porous mineral as a promising support for shape- stabilized phase change materials, J. Energy Storage. 26 (2019) 101041. https://doi.org/10.1016/j.est.2019.101041.

3. **C. Cárdenas-Ramírez**, M.A. Gómez, F. Jaramillo, Comprehensive analysis of the thermal properties of capric-myristic, lauric-myristic and palmitic-stearic acids and their shape-stabilization in an inorganic support, J. Energy Storage. 34 (2021) 102015. https://doi.org/10.1016/j.est.2020.102015.

4. **C. Cárdenas-Ramírez**, F. Jaramillo, A.G. Fernández, L.F. Cabeza, M.A. Gómez, Influence of thermal treatments on the absorption and thermal properties of a clay mineral support used for shape-stabilization of fatty acids, J. Energy Storage. 36 (2021) 102427. https://doi.org/10.1016/j.est.2021.102427.

5. **C. Cárdenas-Ramírez**, M.A. Gómez, F. Jaramillo, A.G. Fernández, L.F. Cabeza, Thermal reliability of organic-organic phase change materials and their shape-stabilized composites, J. Energy Storage. 40 (2021) 102661. https://doi.org/https://doi.org/10.1016/j.est.2021.102661.

6. **C. Cárdenas-Ramírez**, M.A. Gómez, F. Jaramillo, A.G. Fernández, L.F. Cabeza, Experimental determination of thermal conductivity of fatty acid binary mixtures and their shape-stabilized composites, Renew. Energy. 175 (2021) 1167–1173. https://doi.org/10.1016/j.renene.2021.05.080.

Papers in progress:

1. **C. Cárdenas-Ramírez,** M.A. Gómez, F. Jaramillo, A.F Cardona, A.G. Fernández, L.F. Cabeza, Experimental steady-state and transient thermal performance of materials for thermal energy storage in building applications: from powder SS-PCMs to SS-PCM-based acrylic plaster.

As well, participation with oral presentations in the following international congresses:

1. Eurotherm Seminar Advances in Thermal Energy Storage, 15-17 May, 2019, Universitat de Lleida, Lleida, Spain.

2. CIES 2020: XVII Congresso Ibérico e XIII Ibero-americano de Energía Solar, 3-5 Novemeber, 2020, Campus do lumiar do laboratório nacional de energia e geología, Lisboa, Portugal.

TABLE OF CONTENTS

LIST OF FIGURES

LIST OF TABLES

LIST OF ACRONYMS & ABBREVIATIONS

Symbol	Quantity	Units
C	Heat capacity	J/°C
C_p or c	Specific heat capacity	kJ/kg·°C
$\overline{C_p}$ or $C_{p,avg}$	Average specific heat capacity	kJ/kg·°C
Dv10	10^{th} percentile of the cumulative volume distribution	µm
Dv50	Median particle size by volume	µm
Dv90	90^{th} percentile of the cumulative volume distribution	µm
f	Decrement factor or thermal stability coefficient (TSC)	-
ΔH_m	Latent heat of fusion/melting or enthalpy of fusion	kJ/kg
ΔH_s	Latent heat of solidification or enthalpy of solidification	kJ/kg
M	Mass	kg
Q	Heat flow density	W/m^2
q_{acc}	Heat accumulated	J
Q	Energy	J
T	Temperature	°C
T	Time	h
$T_{m,\ onset}$	Onset melting temperature	°C
$T_{m,\ peak}$	Melting peak temperature	°C
$T_{s,\ onset}$	Onset solidification temperature	°C
$T_{s,\ peak}$	Solidification peak temperature	°C
U-value	Thermal transmittance in steady-state	W/m^2·°C
∇T	Temperature gradient	K/m
ΔT	Temperature change	°C
Φ	Thermal lag or time lag	h
Λ	Thermal conductivity	W/m·K
λ_{avg_Liquid}	Average thermal conductivity of the liquid phase	W/m·K
λ_{avg_Solid}	Average thermal conductivity of the solid phase	W/m·K

Abbreviations

APTES	3-Aminopropyltriethoxysilane
CA/MA	Capric-myristic eutectic mixture
CG6, CG9, CG11	Coarse granulated clay support calcined at 600 °C, 900 °C, and 1100 °C
CS-OPCM	Core-shell organic phase change material
CS-PCM	Core-shell phase change material
DMSO	Dimethylsulphoxide
DSC	Differential scanning calorimetry
FT-IR	Fourier transform infrared spectroscopy
HR-TEM	High resolution-TEM image
LA/MA	Lauric-myristic eutectic mixture
LHTES	Latent heat thermal energy storage
MDSC	Modulated differential scanning calorimetry
PA/SA	Palmitic-stearic eutectic mixture
PCM	Phase change material
PCM/P	Shape-stabilized CA/MA in the RP support

PCM/M2	Shape-stabilized CA/MA in the modified support with HCl+APTES
PCM/M4	Shape-stabilized CA/MA in the modified support with DMSO+APTES
RP or P	Clay support without modification. Raw support
P4, P6, P9, P11	Clay support calcined at 400 °C, 600 °C, 900 °C, and 1100 °C
G6, G9, G11	Fine granulated clay support calcined at 600 °C, 900 °C, and 1100 °C
SAED	Selected area electron diffraction
SEM	Scanning electron microscopy
SS-CA/MA	Shape-stabilized CA/MA
SS-LA/MA	Shape-stabilized LA/MA
SS-PA/SA	Shape-stabilized PA/SA
SS-OPCM	Shape-stabilized organic phase change material
SS-PCM	Shape-stabilized phase change material
TEM	Transmission electron microscopy
TES	Thermal energy storage
TGA	Thermo-gravimetric analysis
XRD	X-ray diffraction
XRF	X-ray fluorescence

IV. INTRODUCTION

The global needs of an increasingly populated world, where 9 billion people are expected by 2050 **[1]**, imply great challenges in terms of natural resources, food, energy, infrastructure, communications, and housing. Some of the consequences of this population growth include a 70% increase in CO_2 emissions, the need for 50% more energy than the one we consume today, as well as an increase in global average temperature between 3 °C and 6 °C **[1]**, these events will have a strong environmental impact and will directly affect the quality of life of people. Within the energy area, it is well recognized that one of the causes of the increase of CO_2 emissions is the consumption of fossil fuels. This energy model generates a serious environmental impact in addition to be a limited resource coming from non-renewable sources. All over the world, sectors responsible for much of the energy consumption are industrial, transportation, and construction. Specifically, in construction, it is known from the European Union, that buildings represent 40% of energy consumption **[2]**. Thus, it is necessary to dig deeper into different areas such as economics, science, politics, architecture, and engineering, to try to decrease the carbon-foot and the energy-associated costs. Even more considering that the construction industry has a great impact on society as it affects the quality of life of people, promotes the generation of jobs, and influences the world's economic dynamics as contributes a 6% of the GDP (gross domestic product) **[2]**. Thus, it is necessary to advance in the different stages of the value chain **[3]** such as technology, materials and tools, processes and operations, business models, sector strategy, organizational culture, the collaboration between industries, marketing, policies, and regulations, among others.

The 2030 agenda for sustainable development, adopted by the United Nations Member States in 2015 **[4]**, provides 17 Sustainable Development Goals (SDGs) which are "an urgent call for action by all countries – developed and developing – in a global partnership" for improve health and education, reduce inequality, tackling climate change, and in general, to make the world a better place. Between these seventeen SDGs there are five that highlight the importance of sustainable energy:

SDG 7: to ensure access to affordable, reliable, sustainable and clean energy.
SDG 9: to build resilient infrastructure, promote inclusive and sustainable industrialization.

SDG 11: to make sustainable cities and communities.

SDG 12: to ensure responsible consumption and production.

SDG 13: to take urgent action to combat climate change.

Particularly, in Latin America and the Caribbean there are projected changes in the energy systems due to climate change. For instance, thermal electricity plants may become less efficient and hydroelectric power generation will be affected. In Perú it is estimated a 10% decrease in power output when glacier runoff, whereas in Salvador there will be a threatening of the economic return from the existing hydroelectric infrastructure, and so on as widely exposed by Reyer et al **[5]**. In fact, without going any further, at the present time there are a lot of energy inefficiencies that should be remediated. An example of good practices in the region towards energy sustainability is Brazil that had promoted the diversification of power supply, being its electricity sector recognized by the major use of hydroelectric power (95% of the country's electricity is supplied by hydroelectric plants during the rainy season), with increasing the participation of wind and solar energy **[6]**. Colombia, as well as Brazil, with highly available hydric resources presents an electric system reliable and competitive, nevertheless, as mention before, climatic phenomena as El Niño has affected the hydroelectric power generation during some periods for example in 2016 **[7]**.

Another aspect, that must be considered and increase the complexity of the problem is the geographical differences within a country and the social realities. For instance, according to the Köppen-Geiger classification Colombia is divided in nine types of climates **[8,9]**, as shown in **Table 1**. Thus, each region demands different strategies to overcome climate changes, to achieve sustainable energy/materials and to decrease the high costs related with energy consumption.

Table 1. Köppen-Geiger classification for climates in Colombia.

Köppen-Geiger Classification	Description	Number of cities	Examples
Af	Tropical rainforest climate	735	Buenaventura, Barrancabermeja, Apartadó
Aw	Tropical savanna climate	598	Cali, Barranquilla, Cartagena
Am	Tropical monsoon climate	543	Medellín, Bello, Itagüí, Envigado, Tuluá
Cfb	Oceanic climate	315	Bogota, Manizales, Popayán, Sogamoso
Csb	Warm-summer Mediterranean climate	64	Facatativá, Charta, Cachira, Villa de Leyva, Sáchica

Köppen-Geiger Classification	Description	Number of cities	Examples
BSh	Hot semi-arid climates	22	Cúcuta, Riohacha, Maicao
Cwb	Subtropical highland oceanic climate	12	Mamarongo, San Miguel, Nabusimake (San Sebastian de Rábago)
ET	Tundra climate	7	Vetas, Presidente, Resguardo, San Juan de Sumapaz
BWh	Hot desert climates	3	Taroa, Junain, Cabo de la Vela

It is considered that 80% of the Colombian cities are of warm climate, where the temperatures are greater than 24°C **[10]**. Thus the use of air conditioning has gone from being a luxury to becoming an indicator of quality of life **[11,12]**. The greatest uses of air conditioners are in residential buildings in warm cities and all over the country, even in cold weather cities, in the industries, offices, hospitals, banks and shopping centers. This, in turn, represents a high energy consumption. In 2006 the consumption associated with air conditioning was approximately 36 MWh/month for Bogotá (cold weather), 306 MWh/month for Medellín (temperate weather) and 775 MWh/month for Barranquilla (warm weather) **[13]**. Thus, it exists a big potential to lower energy consumption and optimize materials performance, even in tropical countries that present no seasons.

Regarding social reality in Latin America, some regions are not connected to the electric system. This is the case of Colombia, where some of the population away from urban areas do not have a reliable energy supply. According to some authors **[14]**, there are already technological solutions in the market to this problem, with autonomous systems based on photovoltaic panels that should deliver at least 10 kWh/day (calculated as the energy needed for an urban house with 3 or 4 inhabitants), but political actions are still need it for a wide implementation. Strategies as resilient cities, launched in Medellín **[15]**, Cali, Buenos Aires, Panamá, Quito, Río de Janeiro, Montevideo, México City and other 100 cities around the world by the Rockefeller Foundation in 2013 **[16,17]** tried to help understand the complexity of the cities and identified a series of drivers for urban resilience. According to Rockefeller Foundation, resilience is understood as "the capacity of individuals, communities, institutions, businesses, and systems within a city to survive, adapt, and grow, no matter what kinds of chronic stresses and acute shocks they experience". Being one of the objectives of the urban resilience the improvement of infrastructure and environment. These kind of

approaches to the social context of each city is very significant in order to build a better society in terms of sustainability.

In Colombia, some efforts have been done in terms of policies. In 2014 the government proposed a new law to encourage renewable energy development in the country **[18]**. The purpose of this law (Law 1715) is to promote the development and use of non-conventional sources of energy, especially those of a renewable nature through its integration into the electricity market, its participation in non-interconnected areas and other uses as a necessary means for sustainable economic development, reduction of greenhouse gas emissions and security of energy supply. Some incentives **[19]** outlined by the law include lower taxes for people who declare assets of renewable energy, materials bought for renewable energy projects will not have to pay the national value added tax of 16%, materials and labor that will have to be imported for renewable energy projects will not have to pay tariffs and access to a public and private fund to finance projects. As well, the resolution 549 of 2015 **[20]** provided a sustainable construction guide for saving water and energy in buildings. These policies try to improve the quality of life of Colombian inhabitants through environmental and social responsibility and should be the drivers for sustainable development. From the technological perspective this corresponds to a scientific challenge in the fields of sustainable energies, eco-efficient buildings and sustainable housing **[21]**, where it should exist a balance between user needs and the environment, and where resources are not adversely affected compromising the future of next generations.

Renewable energy technologies comprehend diverse applications such food and drug packaging **[22,23]**, solar heated biogas fermentation **[24]**, net-zero energy buildings **[25]**, domestic hot water systems **[26]**, thermal comfort in buildings **[27]**, construction and building materials **[28–30]** or energy efficiency simulations **[31,32]**. Remarkably, most of them involve the so-called phase change materials (PCMs) and thermal energy storage (TES) systems, due to its high energy storage (**Fig. 1**). Both organic and inorganic PCMs **[33]** can contribute to reduce energy costs, environmental damages and create innovative applications that cannot be reach with conventional technologies. These materials have been investigated for approximately one decade **[33]** as an opportunity for sustainable housing development as they help to minimize energy consumption within construction.

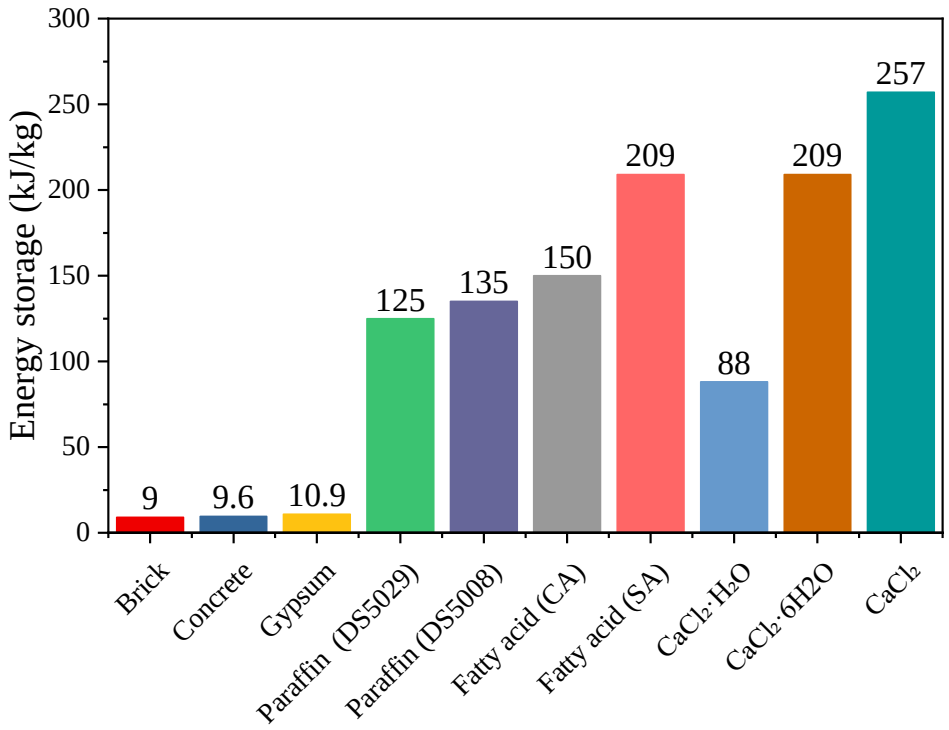

Fig. 1. Comparison of the heat storage capacity of some PCMs and typical construction materials.

PCMs base their properties on the absorption, storage and release of latent heat when undergoing a phase transformation, which can be from liquid to solid, from solid to solid, from liquid to gas, among others, and in addition this transformation must be reversible **[34]**. Research in this area includes topics ranging from choosing a suitable PCM **[28]**, study the methodologies to encapsulate PCM or to obtain a shape stabilized PCM **[35,36]**, evaluate the incorporation of PCMs into traditional building materials **[37,38]** until the application of proper techniques to characterize the PCMs and to measure the energy efficiency of the system **[39]**. TES is key to overcoming our dependency on fossil fuel burning and it plays a key role at both utility end and building end of energy supply chain **[40]**.

Particularly, the most used PCMs for low thermal applications, that are considered within a work temperature below 100°C **[41]**, such building and construction applications, are the ones from liquid to solid phase transformation, thus is necessary to contain them when they are in the liquid state to avoid material losses or leakage for its final application. Specially, eutectic mixtures of fatty acids **[42,43]** are notably interesting as their phase change temperature can be adjusted according to the desire application, are derived from sustainable sources, are non-toxic and with comparative low prices. The different technologies reported

in the literature for encapsulation or impregnation in porous materials still offer opportunities for improvement in terms of filtration, processing methods, scaling and selection of materials that serve as capsules or as porous supports. On the other hand, the same PCMs present certain peculiarities that require a deep study for their complete understanding as the change of density that exists when changing phase, the stability of the properties and, in some cases, the low thermal conductivities, phase segregation, subcooling and reversibility.

In this way, the purpose of this thesis is to design and develop a latent heat thermal energy storage system based on eutectic mixtures of fatty acids, using a Colombian porous clay as a support for producing shape-stabilized phase change materials (SS-PCMs). The result is intended to present a cost-effective production process and some SS-PCMS with a wide phase temperature range, low leakage, and good thermal properties, that can be useful for construction applications.

This thesis is written as a series of six chapters, as shown in **Fig. 2**. The first chapter is a literature review of encapsulation and shape-stabilization of phase change materials (Chapter I). The second chapter is a comprehensive analysis and characterization of the fatty acids used in this work as PCMs (Chapter II). The third topic is on the characterization of a Colombian mineral used as a support for shape-stabilization of the PCMs (Chapter III). Chapter IV corresponds to the production of SS-PCMs through the vacuum impregnation method. Chapter V is a study of chemical and physical modifications of the support to improve the TES system, and finally, Chapter VI comprehend steady state and transient thermal performance of some of the SS-PCMs obtained. Each chapter has its own introduction, methods, materials, results, discussion, and partial conclusions.

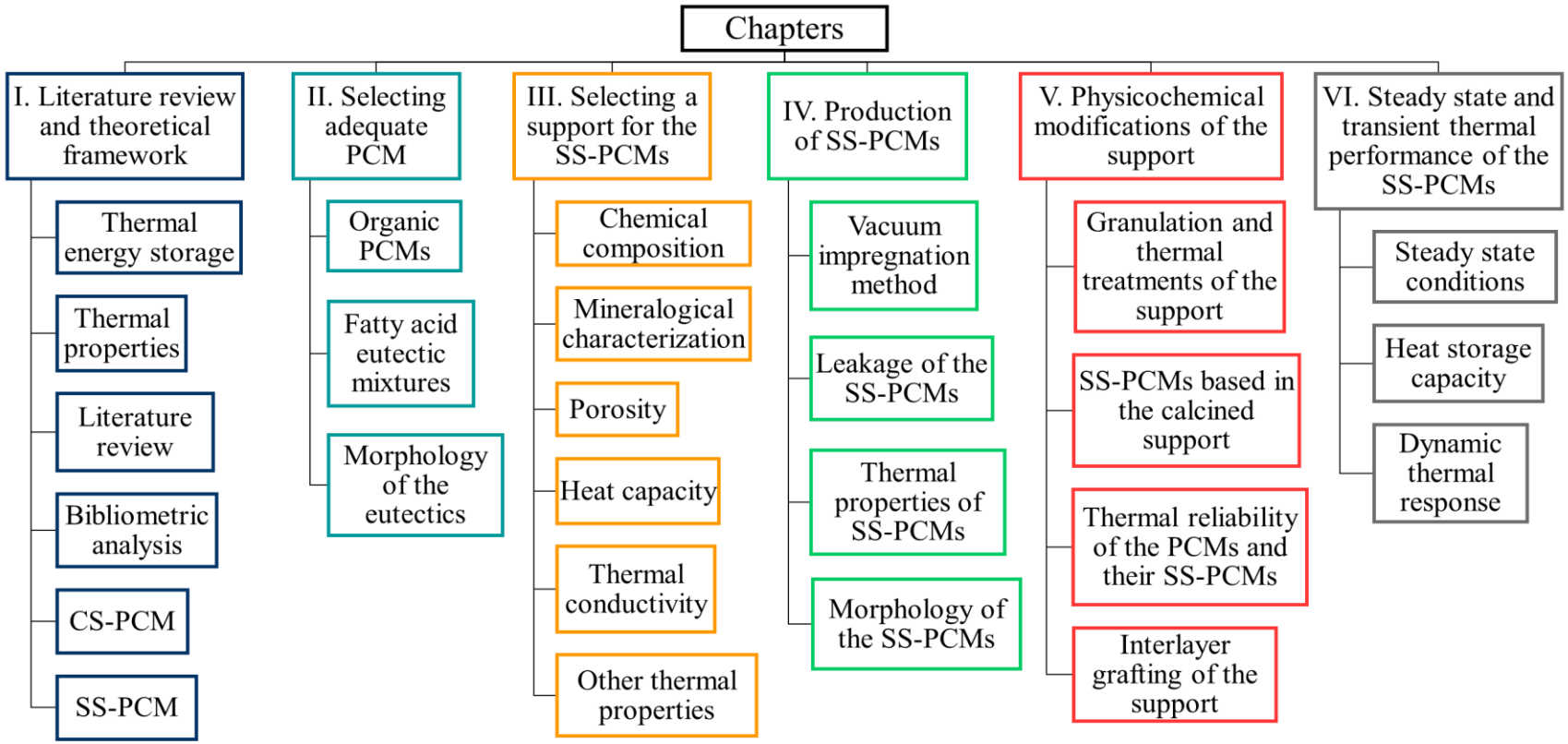

Fig. 2. Thesis structure.

V. OBJECTIVES

General Objective

To develop a latent heat thermal energy storage system (LHTES) of wide temperature range (Tm Onset ~19°C to 53°C), by improving the thermal and absorption properties of a Colombian natural mineral mixture as a porous support of an organic phase change material.

Specific Objectives

- To select organic phase change materials considering their thermal and thermodynamic properties of a combination of fatty acids for low temperature applications in a wide temperature range.
- To study the effect of the mineralogical phases of the support on the thermal properties (phase change temperature, thermal conductivity, enthalpy, specific heat) and absorption capacity of the system.
- To evaluate the vacuum-assisted impregnation method and intercalation for shape-stabilization of the eutectic phase change material to develop the energy storage system.
- To improve the physical-chemical properties of the support through superficial and thermal treatments for obtain an enhanced thermal energy storage system.

CHAPTER I.

Literature review and theoretical framework

In this section, the objectives are to present the basic theoretical framework associated with phase change materials (PCMs) and thermal energy storage (TES), to analyze the number of publications during the last 40 years and its distribution all over the world, to show the main authors and leading countries that have been publishing in the subject and their collaboration networks, to highlight the principals materials and methods that have been reported, and finally, to present a review that compare the most used methods and materials for containment of organic phase change materials.

1.1. Thermal energy storage

One of the major trends in materials science is the development of multifunctional materials with high performance that present one or more properties. These are the so-called intelligent or smart materials, which generates a response to an external stimulus such as stress, light, pressure, moisture, temperature, pH or electric/magnetic fields, among others **[44–46]**. Within these are the thermal energy storage (TES) materials that can absorb heat and then, due a change in temperature, release it again **[47]**. The heat storage by these TES materials can be divided in sensible, thermochemical or latent heat, as shown in **Fig. 3**. Thermal energy storage can be used in several sectors as food packaging, fermentation processes, food preservation, cold chain transportation logistic, power generation, construction and building materials, domestic heat water, space heating and thermal comfort **[23,26,41,48–53]**. In general, the aim of using TES materials is the reduction of energy consumption and operational costs **[54]**, integrate renewable energy into electricity production **[52]**, diminish pollutions of the environment **[54]**, and to temporarily store thermal energy at high or low temperatures **[48,55–57]** for numerous uses.

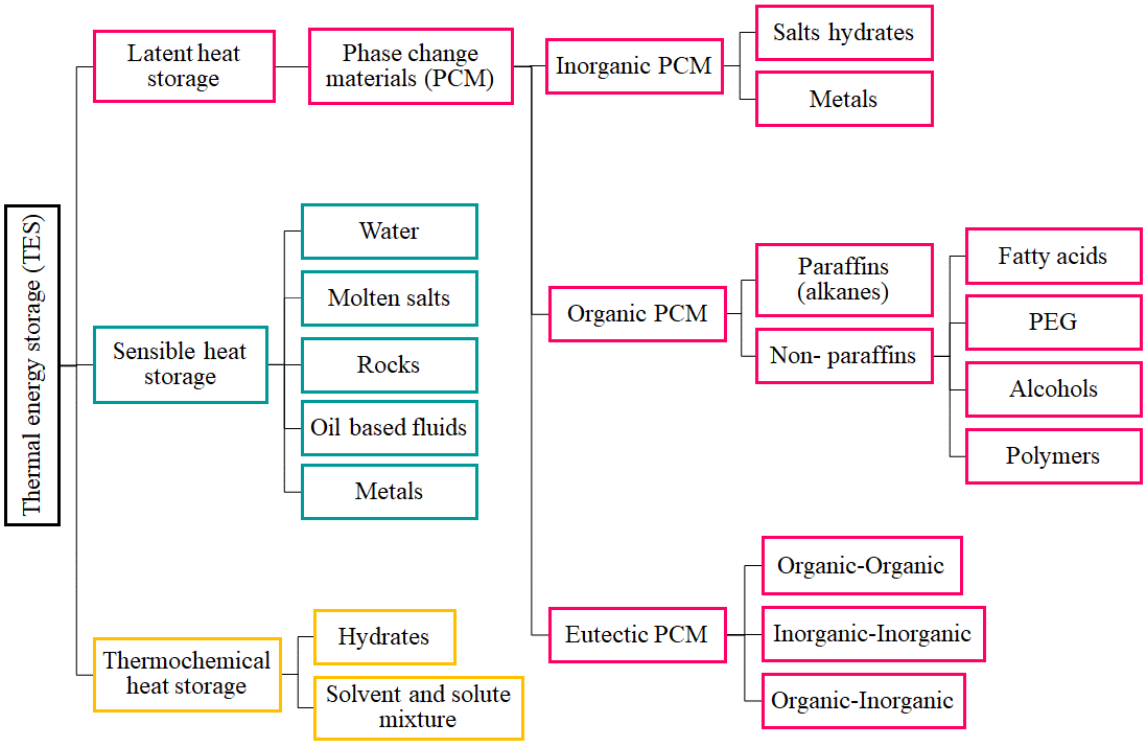

Fig. 3. Classification of thermal energy storage (TES) according to the type of thermal energy stored.

1.1.1. Sensible heat

Sensible heat thermal energy storage (SHTES) is by far the most common way of energy storage **[34]**. When sensible heat is stored an increasing in the temperature of the material occurs **[52]**. The amount of stored energy depends on density, specific heat and mass of the material, and can be calculated by **Eq. (1)**.

$$Q = \int_{T_i}^{T_f} mC_p dT = m\overline{C_p}(\Delta T) \qquad \textbf{(1)}$$

Where Q is the amount of heat, [J]; m the mass of the material [kg]; C_p the specific heat capacity of the material [J/kg·°C]; and ΔT is the temperature change [°C].

Some liquid materials that can be used to store sensible heat are water, oil-based fluids, molten salts, rocks and metals. It should be considered that materials such as water can be corrosive to other materials, so its storage is not easy and could present a significant loss of heat over time. The typical application of these sensible heat storage systems is in small power plants that have solar collectors to produce hot water. This represents a disadvantage

as large mass and volume of the material are required to store significant thermal energy, in addition, storage tanks for the material are usually mandatory.

1.1.2. Thermochemical heat storage

Thermochemical heat storage **[52]** corresponds to the use of the exothermic and endothermic reactions that may result in a material. The enthalpy of these systems are called heat of reaction and is the difference between the enthalpy of the substance at the end of the reaction and the enthalpy of the substance at the start of the reaction **[34]**. Sorption processes are also considered in this category, where a gas or vapor (sorbate) is fixed or captured by a solid or liquid material (sorbent). As stated by Mayinger et al. **[34]**, any chemical reaction can be used for TES systems if the heat produced by the reaction can be stored and then released when the reverse action takes place.

The disadvantages of these systems correspond to costs, behavior over time, toxicity and safety, corrosion and in general the technical complexity of these reactions in real applications. The advantages of the materials that store thermochemical heat are the high density of heat storage and low heat loss, among others.

1.1.3. Latent heat storage

Latent heat storage materials **[52]** or phase change materials, PCMs, change it phase during the energy storage process. In general, latent heat storage is greater than the sensible heat storage, and therefore less mass and volume of the material is required to obtain a good energy efficiency, in addition, the phase change happens at a constant temperature, thus avoiding inconveniences of corrosion by temperature and other handling problems. PCMs transitions can be from solid to liquid, from solid to solid or from liquid to vapor. The amount of latent heat, Q, stored by PCMs is given by **Eq. (2)**, where m is the mass of the material and Δh is the phase change enthalpy.

$$Q = m \cdot \Delta h \qquad \textbf{(2)}$$

Some of the disadvantages of these materials are the change of density and volume that exists when changing the phase, the stability of the properties over time and, in some cases, phase

segregation, subcooling and low thermal conductivities. PCMs can be organic, inorganic or eutectic as shown in **Fig. 3**. Some advantages and disadvantages are shown in **Table 2**.

Table 2. Advantages and disadvantages of organic, inorganic and eutectic phase change materials.

	Advantages	Disadvantages
Organic PCMs	• High energy storage capacity. • No subcooling. • Good chemical stability over time without segregation. • Fatty acids and alcohols come from renewable sources.	• Low thermal conductivity. • Flammability. • Possible instability at high temperatures. • PEG and paraffins come from non-renewable source.
Inorganic PCMs	• Almost double thermal storage capacity with respect to organic PCMs. • High thermal conductivity.	• The salts can present incongruent fusion and precipitation. • Possible dehydration of the salts.
Eutectic PCMs	• They merge and solidify congruently, avoiding segregation. • Adjustable phase change temperature by mixing different materials.	• Same disadvantages as the pure organic or inorganic phase change materials.

In general, as noted above, all thermal energy storage materials have certain advantages and disadvantages between them. Particularly, this work's attention is in organic latent heat storage phase change materials (OPCM), with solid to liquid transitions, as are more chemically stable than thermochemical storage materials, with higher heat capacity than sensible heat storage materials, present a relative ease of use, are commercially available and small volumes are required. For instance, the versatility of latent heat storage materials can be noticed in construction applications as the PCM not only can be used in the surrounding envelopes **[30,58]**, but also in the roofing **[59,60]**, flooring **[61]**, domestic hot water tanks **[62]** and energy equipment **[63,64]**. As well, in food industry can be used for refrigerated cabins **[23]**, food packaging **[22]** or even in fermentation systems **[24]**. Nevertheless, for most applications, solid to liquid phase change materials need containment by means of encapsulation or shape-stabilization since in liquid phase it can leakage or presents material losses. Encapsulated PCMs are called core-shell PCMs (CS-PCM) and those PCMs that are

supported in porous matrices, shape-stabilized PCMs (SS-PCM). These containment approaches will be discussed in detailed in subsequent sections.

It is worthy to note that the total energy of a TES system, if mechanical energy (kinetic, potential) and other internal energy are negligible, is composed by sensible and latent energy. Thus, the total amount of energy stored, Q, by a SS-PCM or CS-PCM is given by **Eq. (3)**.

$$Q = \int_{T_i}^{T_m} mC_p dT + \mathrm{m} \cdot \Delta\mathrm{h} + \int_{T_m}^{T_f} mC_p dT \qquad \textbf{(3)}$$

Where the first and third terms are related with the sensible heat stored and the second term with the latent heat stored. Hence, a better approach to compute the amount of energy stored by a PCM contained in a support or encapsulated is by using **Eq. (3)**, and not only the latent heat energy (**Eq. (2)**).

1.2. Thermal properties

For the development of TES systems based in phase change materials there are several thermophysical properties that are important. Some of them are temperature-dependent as the specific heat capacity and thermal conductivity. Other properties include the latent heat of fusion/solidification and the phase change temperature. Some of them will be described below.

1.2.1. Phase change temperatures

Melting and solidification of PCMs, with phase change from solid to liquid, are the main phenomena that governs the latent heat energy storage. Melting, sometimes called fusion, is characterized by a small volume change (<10%) **[34]**, and, while it happens, the material keeps its temperature constant. This temperature is called melting temperature, T_m. In the same way, during the solidification process where the PCM goes from liquid to solid, the phase change temperature is called solidification temperature, T_s. Each phase change is followed by an energy storage that, in thermodynamic parameters, correspond to the increase of the internal energy of the system, called enthalpy. For melting/solidification process the enthalpy is also called latent heat of fusion/solidification, heat of fusion/solidification or just phase change enthalpy.

Melting of some PCMs, like the hydrated salts, can be incongruent **[34,54]**, that means that phase change from solid to liquid occurs with a phase separation that can reduce the energy storage efficiency of the substance. Incongruent melting is an irreversible process. As well, subcooling, sometimes referred as supercooling, occurs when PCMs are cooled and solidify at a temperature below their melting point **[54]**, this phenomenon is typical of some molten salts. By the other hand, organic PCMs like fatty acids or paraffins, present congruent melting and no phase separation, nor subcooling, appears during the phase change temperatures.

1.2.2. Specific heat capacity

Heat capacity, C, is an extensive property that is defined as the ratio of the energy change and the resulting temperature change involved (**Eq. (4)**) **[65]**. Indicate the material ability to absorb heat from the surroundings and represent the energy necessary, dQ, to produce a unit change in temperature, dT, for one mole of a substance. Usually, heat capacity is specified in joules per °C, [J/°C]. From **Eq. (4)** can be observed that C is a function of the temperature.

$$C = \frac{dQ}{dT} \qquad \textbf{(4)}$$

The mechanisms of energy absorption, that affect heat capacity, in many materials are associated with increasing the vibrational energy of the atoms (mostly in nonconductors materials) or increasing in the free-electron kinetic energies (for metals).

When heat capacity is presented per unit mass it is called specific heat, that often is denoted by a lowercase c, or as C_p when the external pressure of the specimen remains constant. The units of specific heat are J/g·°C or kJ/kg·°C. Thus, specific heat capacity is an intensive property. In construction industry, the specific heat of a building, is often referred as thermal mass.

1.2.3. Thermal conductivity

Thermal conductivity is an essential property in order to understand the rate of charging/discharging of the system. The desirable thermal conductivity is in general the highest it can be achieved to ensure an optimum TES system. Thermal conductivity calculus for a pure material is based on the conduction rate equation (Fourier's law) **[66]**, **Eq. (5)**.

This equation expresses the heat flow density (W/m^2), $\boldsymbol{q}$, that is proportional to thermal conductivity (W/m·K), λ, and to the temperature gradient (K/m), ∇T. Basically, it tells how energy is transferred in form of heat flow through a surface.

$$\boldsymbol{q} = -\lambda \nabla T = -\lambda \left(\boldsymbol{i} \frac{\partial T}{\partial x} + \boldsymbol{j} \frac{\partial T}{\partial y} + \boldsymbol{k} \frac{\partial T}{\partial z} \right) \quad \textbf{(5)}$$

This expression can be simplified for the heat transfer rate in the x-direction, q_x, through a plane wall of area A, that is proportional to the temperature gradient, $\frac{dT}{dx}$, in this direction **[66]**, as shown in **Eq. (6)**.

$$q_x = -\lambda A \frac{dT}{dx} \quad \textbf{(6)}$$

From a physics point of view, at a microscopic level, thermal energy transport is due to the migration of free electrons (mainly for metals) and lattice vibrational waves (mainly for semiconductors and nonconductors). These lattice vibrational waves are termed phonons from a particle-like behavior **[66]**. Phonons are the analogous to the quantum of electromagnetic radiation, photons **[65]**. Hence, some authors have studied the phonon scattering mechanism in PCMs to increase thermal transmission **[67]**, as well, many attempts of enhancing thermal conductivity of PCMs can be found in literature, particularly for organic and nonconductors PCMs, as fatty acids, paraffins or polyethylene glycol, as they present low thermal conductivity compared with inorganic PCMs **[68]**. Thermal conductivity enhancement techniques for TES systems based on PCMs can be summarized in the addition of nanoparticles of carbon fiber, carbon nanotubes (CNT), graphene, magnesium and silver; metallic foams of titanium dioxide, nickel, copper or graphite foam; expanded graphite; and encapsulation of PCMs with silica or calcium carbonate **[67–70]**. By far, carbon-based additives are the most reported in literature.

Along with the enhancement mechanisms used to increase the thermal conductivity of the PCMs, the measurements techniques are as well important and needed to be understood to obtain accurate values. Thermal conductivity measurement depends on several variables such as state of the matter, structure, chemical composition, density, temperature, pressure, and humidity. Thus, the acquisition of appropriate thermal conductivity data should consider

those variables and conditions. In general, sources of error as convection and radiation should be avoided; as well, the contact resistance should be reduced as the effects of air between the sensor and the sample can change the data.

Thermal conductivity measurements are divided in steady-state or transient methods, as shown in **Fig. 4**. Steady-state methods **[71,72]** required the sample to have a constant temperature in each point of the sample during the measurement. These methods can be divided into comparative and absolute methods according to the technique used to measure the heat flux. In comparative methods, a reference sample with a known thermal conductivity is used to determine indirectly the thermal conductivity of the sample to be measured. In absolute methods, the heat flux is calculated from electrical power. Typical steady-state methods are radial heat flow, guarded hot plate, axial rod, and comparative method.

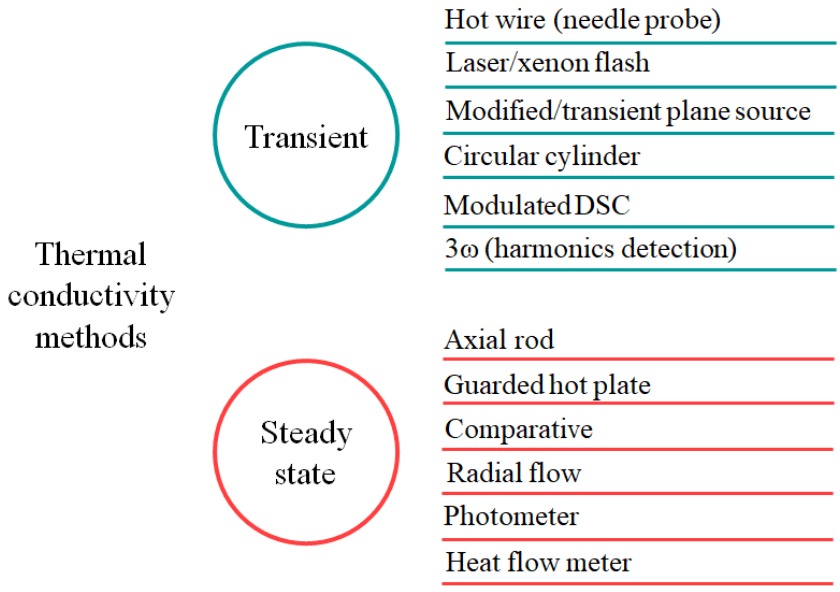

Fig. 4. Thermal conductivity test methods.

Transient state methods **[71,72]**, on the other hand, do not require the sample to reach a steady-state during the measurement and are based in the emission of a heat pulse. Hot wire, transient plane source, modulated differential scanning calorimetry (DSC) **[73]**, and laser flash analysis are some of the reported transient techniques. It is worthy to note that in steady-state and transient methods, the sample must reach thermal equilibrium with its surroundings before the measurement. This implies that steady-state methods require more time for stabilization compared with transient methods, and therefore implied longer test times. For this, and other reasons, thermal conductivity techniques are moving towards transient methods **[74]**.

Despite the numerous methods for measuring thermal conductivity, there are still no specific standards for thermal energy storage materials **[72]** and measurements should be selected according to each TES material conditions (sample homogeneity, size, type, form, phase). Even more, when having granular or porous materials, the effective thermal conductivity varies with the porosity or void fraction, the size distribution and packing arrangement **[66]**.

Moreover, in the literature can be found some experimental studies about the thermal conductivity of phase change materials, as presented in **Table 3**. Among the reported PCMs are pure fatty acids, fatty acid eutectic mixtures, and fatty acid methyl esters.

Table 3. Thermal conductivity of some PCMs found in the literature.

Phase change material	Thermal conductivity (W/m·K)	Temperature (°C)	Reference
capric acid	0.152~0.157	30.61	**[75]**
myristic acid	0.161~0.163	55.56	**[75]**
stearic acid	0.21	Ambient	**[76]**
palmitic acid	0.214	Ambient	**[77]**
polyethylene glycol	0.22	Ambient	**[78]**
methyl myristate	0.148 ~ 0.126	Liquid	**[79]**
methyl laurate	0.148 ~ 0.121	Liquid	**[79]**
methyl caprate	0.149 ~ 0.119	Liquid	**[79]**
lauric-palmitic-stearic acid	0.21	Ambient	**[80]**
capric-myristic acid	0.152	Liquid	**[75]**

Particularly, has been little discussion on the thermal conductivity of fatty acid eutectic mixtures as it can be barely found in the literature. Zhang et al. **[80]** performed measurements of lauric-palmitic-stearic acid eutectic (0.21 W/m·K); and, recently, Jebasingh et al. **[75]** evaluated capric-myristic acid eutectic in the liquid phase, (0.152 W/m·K). As can be seen, most of literature only reports thermal conductivity of pure PCMs and not eutectic mixtures, besides, it is usually evaluated at one temperature and the temperature dependence is not studied. In summary, our knowledge of thermal conductivity of phase change materials is largely based on very limited data that comprises just some typology of PCMs.

1.3. Systematic review

Different mechanisms and types of materials have been reported in the literature to contain PCMs. For instance, Jamekhorshid et al. **[81]** presented a review of microencapsulation methods of phase change materials, Millian et al. **[82]** presented as well a review on

encapsulation techniques for inorganic phase change materials and the influence on their thermophysical properties, Huang et al. **[27]** discussed the use of porous supports for shape-stabilization of PCMs, and so on. However, what is missing in the literature is a systematic review that compares both methods (encapsulation and shape-stabilization), to understand better the advantages and disadvantages of each one and that can serve as a guide for decision making. Moreover, a bibliometric analysis of the literature will show what are the past of current trends in research on the topic. Very few studies were dedicated to analyzing the publications from a systematic approach like Yatangababa et al. **[83]** that performed an analysis of the trends of encapsulation of phase change materials from 1990 to 2015 and Calderón et al. **[84]** who performed a bibliometric analysis about thermal energy storage in general. Thus, a systematic review focus in shape-stabilization (SS-PCM) and encapsulation (CS-PCM) of organic phase change materials was performed for the last 40 years and will be presented in the following sections.

1.3.1. Methodology used for the literature review

For the systematic literature review, Scopus® database was used as is well recognize as a complete abstract and citation database of peer-reviewed literature covering a wide range of subjects and sources. A bibliometric analysis study was performed in addition to literature maps, as a mechanistic approach to understand the global trends in encapsulation and shape-stabilization of organic shape materials like fatty acids, paraffins or polyethylene glycol. Then, a review was done to discuss these technologies, the materials associated with each and general advantages and disadvantages among them.

This research was conducted with the information acquire on October 28th, 2019. The information was collected between the years 1976 and 2019. The advanced search was limited to shape-stabilization (SS-PCM) and nano/microencapsulation, or core-shell, (CS-PCM) of organic PCMs. Macroencapsulation techniques as tubular or cylindrical capsules were excluded. The queries (QS) used for the analysis are presented in **Table 4** and **Table 5** for CS-PCM and SS-PCM, respectively. The search was performed using the fields title, abstract and keyword and three search strings were listed for each topic. The number of results for each query can be seen in **Fig. 5**.

Table 4. Query strings (QS) used for CS-PCM.

QS1:	("encapsulat*" OR "core-shell" OR "CS-PCM*") AND ("phase change material*" OR "PCM*")
QS1-A:	(QS1) AND NOT ("porous" OR "pipe-encapsul*" OR "shape stab*" OR "SS-PCM*" OR "form stab*" OR "high temperature*" OR "tubular macro encapsulat*" OR "encapsulat* w/3 aluminium tube*" OR "cylindrical w/4 capsule*")
QS1-B:	(QS1-A) AND ("organic phase change material*" OR "paraffin*" OR "non-paraffin*" OR "fatty acid*" OR "poly ethylene glycol" OR "PEG")

Table 5. Query strings (QS) used for SS-PCM.

QS2:	("shape stab*" OR "SS-PCM*" OR "form stab*" OR "porous network" OR "porous framework") AND ("phase change material*" OR "PCM*")
QS2-A:	(QS2) AND NOT ("encapsulat*" OR "core-shell" OR "CS-PCM*" OR "pipe-encapsul*" OR "high temperature*" OR "tubular macro encapsulat*" OR "encapsulat* w/3 aluminium tube*" OR "cylindrical w/4 capsule*")
QS2-B:	(QS2-A) AND ("organic phase change material*" OR "paraffin*" OR "non-paraffin*" OR "fatty acid*" OR "poly ethylene glycol" OR "PEG")

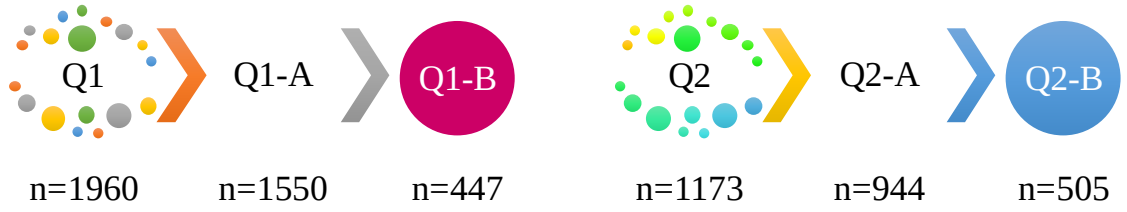

Fig. 5. Diagram with the number of publications (n) find for each query string (Q).

1.3.2. Bibliometric analysis and literature maps

The results of the bibliometric analysis are presented in this section. The number of publications found for the strings Q1-A (CS-PCM), Q1-B (CS-OPCM), Q2-A (SS-PCM) and Q2-B (SS-OPCM) are plotted in **Fig. 6**. First investigations of methods to contain phase change materials were made in the late 70s and early 80s, the core-shell/encapsulation (CS-PCM) method was the main one explored by researchers and only twenty years later shape-stabilization (SS-PCM) became a topic of interest. The breakthrough happens around 2000 when the number of publications increased for both methods, being the CS-PCM bigger than SS-PCM.

Even though, when the queries of CS-PCM and SS-PCM were crossed with organic PCMs the number of documents decrease for both, being similar among them. Is noteworthy that shape-stabilized of organic PCMs were studied only since 1998, while core-shell of organic PCMs had been studied since 1985. In addition, only 28.83% of the publications of CS-PCM correspond to organic PCMs, while for SS-PCM the percentage is 53.49%. Based in this publications trend, it can be noticed that the encapsulation and shape-stabilization of phase change materials is growing up from the last 10 years and is not yet a mature technology, besides that shape-stabilization is the most used technique to contain organic PCMs.

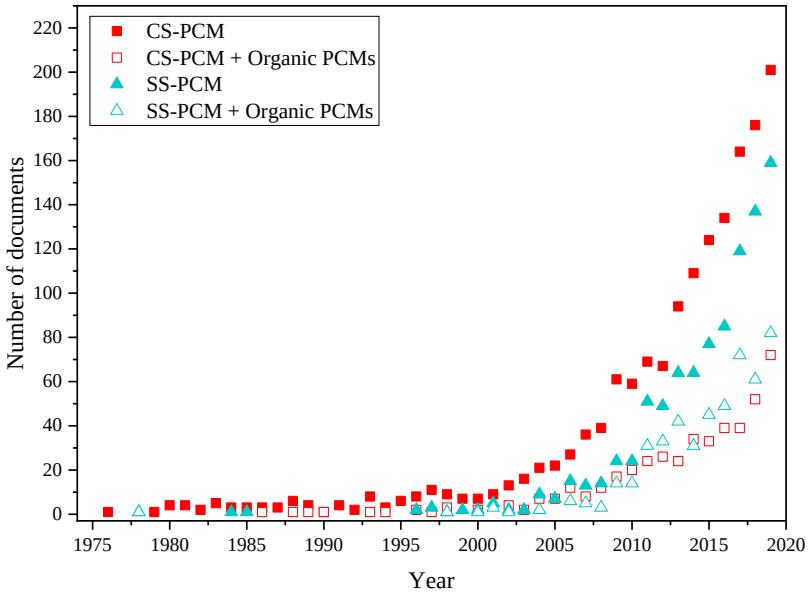

Fig. 6. Number of publications per year for CS-PCM and SS-PCM.

Furthermore, when analyzing the distribution of these documents over the world it can be seen from the maps in **Fig. 7** that the continents with the major number of publications during the last 40 years were Asia, Europe and North America, while Oceania, South America and Africa produced less number of publications. Particularly, China, by far, is the leading country in CS-PCM and SS-PCM investigations with 28.5% and 62.04%, respectively, followed by USA (13.56%) and India (6.37%) for CS-PCM and USA (5.09%) and Turkey (4.44%) for SS-PCM, as it can be seen more clearly in **Fig. 8**. The same countries are the leaders for research in the containment of organic PCMs.

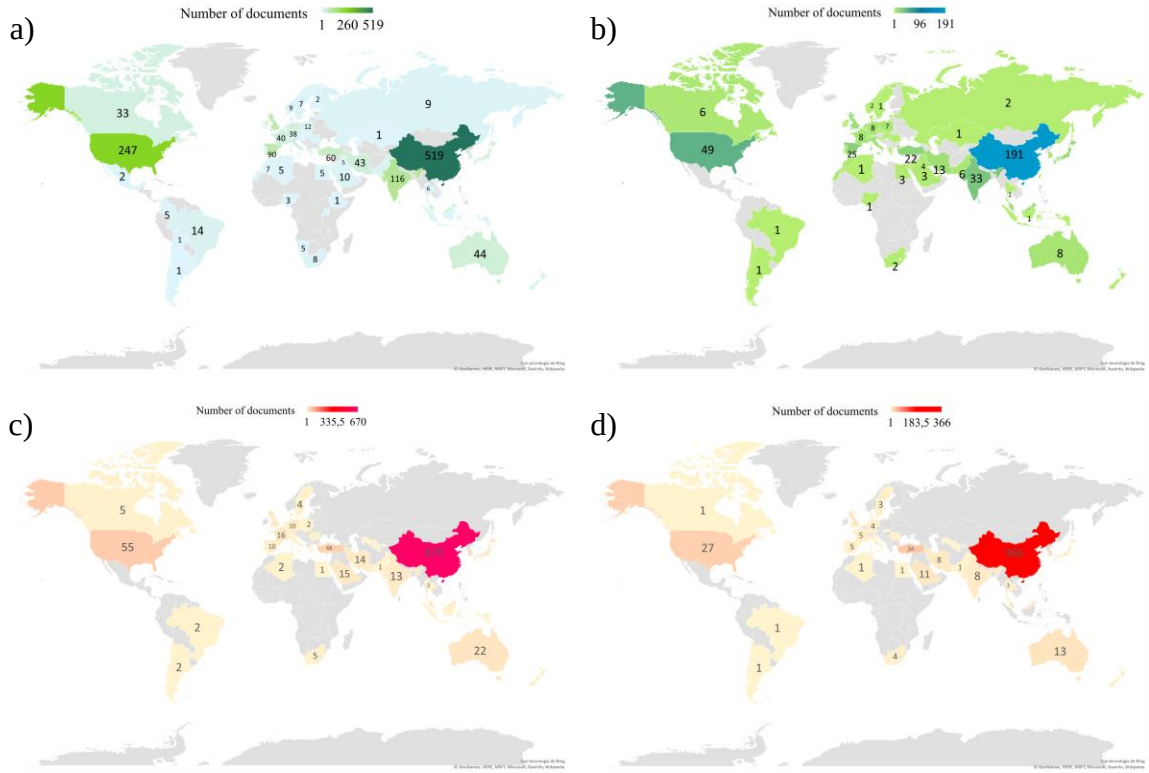

Fig. 7. Distribution of publications in the world for a) CS-PCM, b) CS-OPCM c) SS-PCM and d) SS-OPCM.

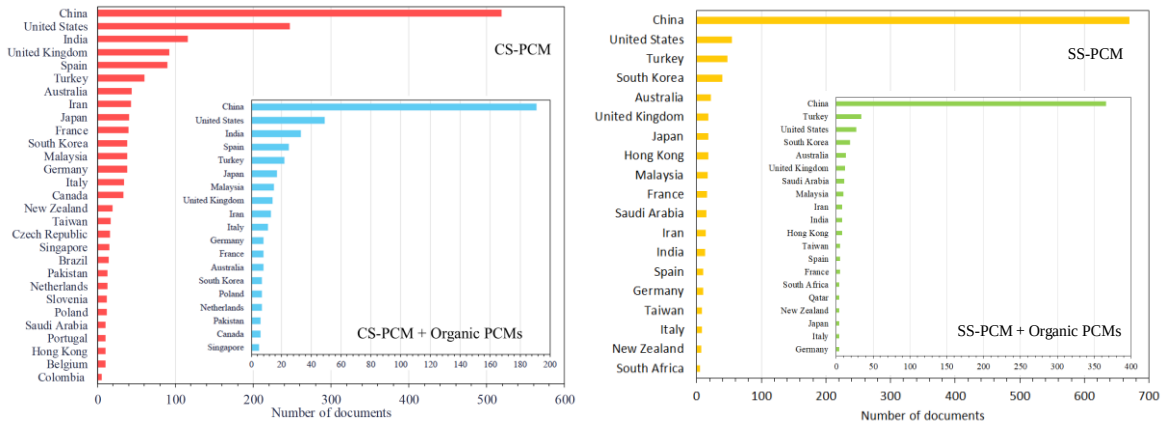

Fig. 8. Main countries that have published in CS-PCM (left) and SS-PCM (right). The insets correspond to CS-OPCM and SS-OPCM, respectively.

Another important factor to be considered in this kind of bibliometric analysis is the type of publication. **Fig. 9** shows the types of documents for each query, as expected, the main type of publication were the articles, followed by conference papers and reviews. Is interesting to note that a smaller amount of investigations in SS-PCM (**Fig. 9. c)**) were presented in conferences compared to CS-PCM (**Fig. 9. a)**). This could indicate an opportunity for more research in shape-stabilization of

PCMs. Although, the percentages of articles and conference papers were similar for CS-OPCM (**Fig. 9**. **b)**) and SS-OPCM (**Fig. 9. d)**).

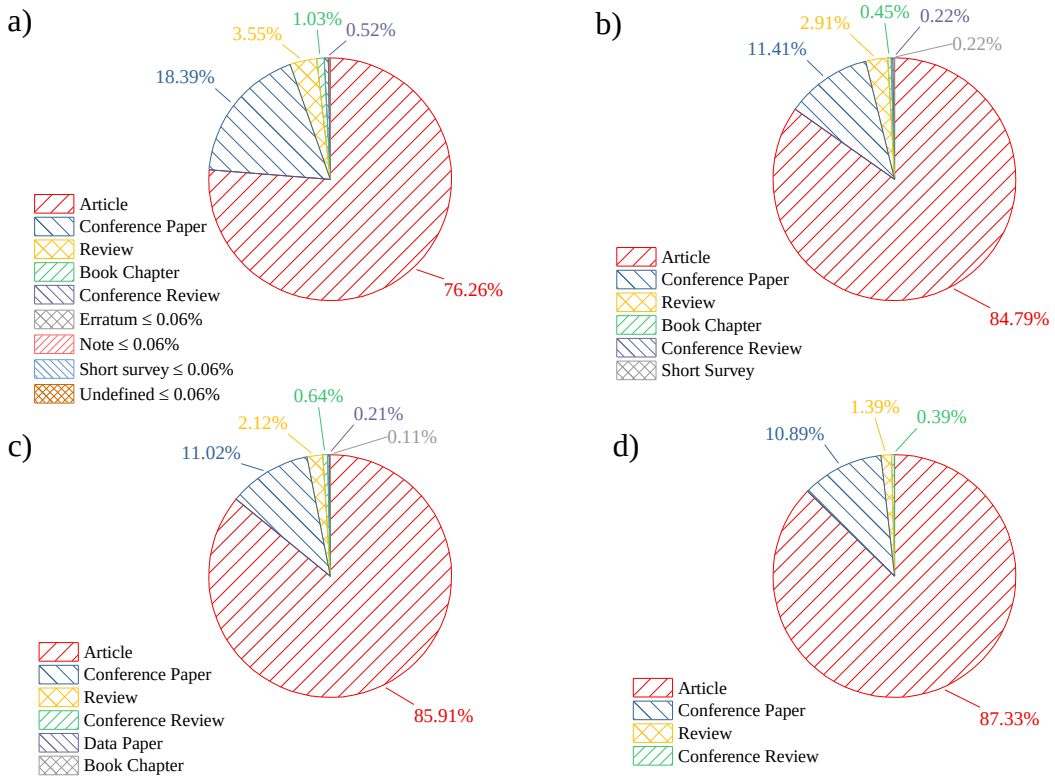

Fig. 9. Document type for a) CS-PCM, b) CS-OPCM, c) SS-PCM and d) SS-OPCM.

Analysis of the top authors that had published in the containment of organic PCMs was done. **Table 6** present the list of authors, number of publications and citations in the topic, affiliation, country, *h*-index, total of publications and citations by author (includes documents in other topics) for core-shell of organic phase change materials, CS-OPCM. The top authors, according to number of documents, that research in CS-OPCM are Xiaodong Wang (9 publications), Dezhen Wu (9 publications), Cemil Alkan (8 publications) and Manuel Carmona (8 publications). Even tough, when analyzing the number of citations of these documents it can be notice that Spanish authors as Paula Sánchez (6 publications, 640 citations), J.F Rodriguez (6 publications, 629 citations) and Manuel Carmona (585 citations) are the most cited compared with other researchers with more number of publications as Xiaodong Wang (420 citations), Dezhen Wu (420 citations) or Cemil Alkan (297 citations). This bibliometric index of number of citations indicates that those authors present a higher

scientific impact in the field despite of the number of published documents, as stated by Waltman et al. **[85]** having more citations does not always coincide with having more impact, but here the number of citations is taken as an "on average" index, without ignoring that there are many factors that have to be taken into account to assess the scientific impact of an author. The same analysis was performed for shape-stabilization of organic phase change materials, SS-OPCM, as it can be seen in **Table 7**. Authors with the major number of publications in the topic were Ahmet Sari (23 publications), Yibing Cai (21 publications) and Qufu Wei (15 publications) and the most cited authors were Yibing Cai, Ali Karaipekli and Alper Biçer with 2104, 1995 and 852 citations, respectively.

Table 6. Top authors publishing in CS-OPCM.

Author	Documents of CS-OPCM	Citations of CS-OPCM	Affiliation	Country	*h*-index	Total documents	Total citations
Wang, X.	9	420	Beijing University of Chemical Technology	China	34	151	3856
Wu, D.	9	420	Beijing University of Chemical Technology	China	34	246	4061
Alkan, C.	8	297	Gaziosmanpaşa Üniversitesi	Turkey	30	73	3146
Carmona, M.	8	586	Universidad de Castilla-La Mancha	Spain	25	83	2128
Fan, J.	6	79	China Academy of Engineering Physics	China	7	50	246
Rodríguez, J.F.	6	629	Universidad de Castilla-La Mancha	Spain	31	179	3554
Sánchez, P.	6	640	Universidad de Castilla-La Mancha	Spain	31	121	3226
Yang, W.	6	79	Southwest University of Science and Technology	China	14	127	657
Zhang, K.	6	79	China Academy of Engineering Physics	China	9	53	329
He, F.	5	79	Southwest University of Science and Technology	China	7	35	165
Sánchez-Silva, L.	5	385	Universidad de Castilla-La Mancha	Spain	24	82	2252
Su, J.F.	5	157	Tianjin Polytechnic University	China	27	75	2089
Bryant, S.J.	4	157	University of Colorado at Boulder	USA	36	125	7151
Fabra, M.J.	4	81	CSIC - (IATA)	Spain	30	105	2647
Fang, G.	4	228	Nanjing University	China	35	89	3361
Feng, Q.	4	82	Southwest Petroleum University	China	6	24	60
Hong, Y.	4	111	University of Central Florida	USA	8	13	245
Kalaiselvam, S.	4	228	Anna University	India	21	71	1527
Legarón, J.M.	4	82	CSIC - (IATA)	Spain	53	282	9035
Paksoy, H.	4	188	Çukurova Üniversitesi	Turkey	21	65	1529
Rodriguez, J.F.	4	190	Universidad de Castilla-La Mancha	Spain	31	179	3554
Sari, A.	4	56	Karadeniz Teknik Üniversitesi	Turkey	67	236	14251
Voevodin, A.A.	4	76	Air Force Materiel Command	USA	55	239	9394

Table 7. Top authors publishing in SS-OPCM.

Author	Documents of SS-OPCM	Citations of SS-OPCM	Affiliation	Country	*h*-index	Total documents	Total citations
Sari, A.	23	518	Karadeniz Teknik Üniversitesi	Turkey	67	236	14251
Cai, Y.	21	2104	Jiangnan University	China	28	134	2384
Wei, Q.	15	292	Minjiang University	China	33	336	4244
Kim, S.	14	371	Yonsei University	South Korea	36	168	3736
Huang, Z.	14	347	China University of Geosciences	China	31	414	4059
Min, X.	14	449	China University of Geosciences	China	19	107	1120
Tang, B.	14	482	Dalian University of Technology	China	21	127	1638
Wu, X.	13	341	China University of Geosciences	China	20	162	1487
Fang, M.	12	263	China University of Geosciences	China	19	147	1220
Hu, Y.L.	12	506	U. of Science and Tech. of China	China	75	803	23770
Jeong, S.	12	370	Pennsylvania State University	USA	17	49	891
Karaipekli, A.	12	1995	Çankiri Karatekin Üniversitesi	Turkey	28	40	4314
Liu, Y.	12	321	China University of Geosciences	China	28	258	2470
Wang, G.	12	238	U. of Science and Tech. Beijing	China	32	203	3684
Zhang, X.	12	258	China University of Geosciences	China	12	31	390
Fang, G.	11	435	Nanjing University	China	34	89	3223
Ke, H.	11	126	Minjiang University	China	11	47	472
Wen, R.	11	319	China University of Geosciences	China	13	29	490
Yang, W.	10	579	Sichuan University	China	39	350	5891
Gao, H.	10	216	U. of Science and Tech. Beijing	China	19	71	1049
Song, L.	10	466	U. of Science and Tech. of China	China	58	247	10916
Yang, J.	10	483	Shanghai Polytechnic University	China	11	15	554
Zhang, K.	10	104	China Academy of Engineering Physics	China	9	53	329
Zhang, S	10	461	Dalian University of Tech.	China	36	329	4326
Biçer, A.	10	852	Gaziosmanpaşa Üniversitesi	Turkey	18	31	1405

In addition, using VOSviewer 1.6.13 software **[86]** the co-authorship networks as well as their evolution during time in the topics were analyzed. The analysis was performed using fractional counting **[87]**. For instance, in **Fig. 10** a co-authorship map is presented for the CS-OPCM, were the lines indicates links when exist co-authoring of a publication with another researcher. Is noticeable that there is little, almost none, collaboration between countries, only China present a small network with USA and even inside countries is difficult to find networks between different universities as it can be seen with Spain, India or Turkey. Colors represent the evolution during time of the topic and who has been published recently. Authors in yellow represent that they have been working recently in the topic and authors in dark blue represent works from 2012. China (He, F., Fan, J., Feng, Q., among others), Turkey (Biçer, A., Hussein, H.M.), India (Beemkumar, N.) and Ittaly (Pegoretti, A.) are the countries that present authors with more recent publications. Contrary to some Spanish, Indian and American authors that presented investigations only until 2015.

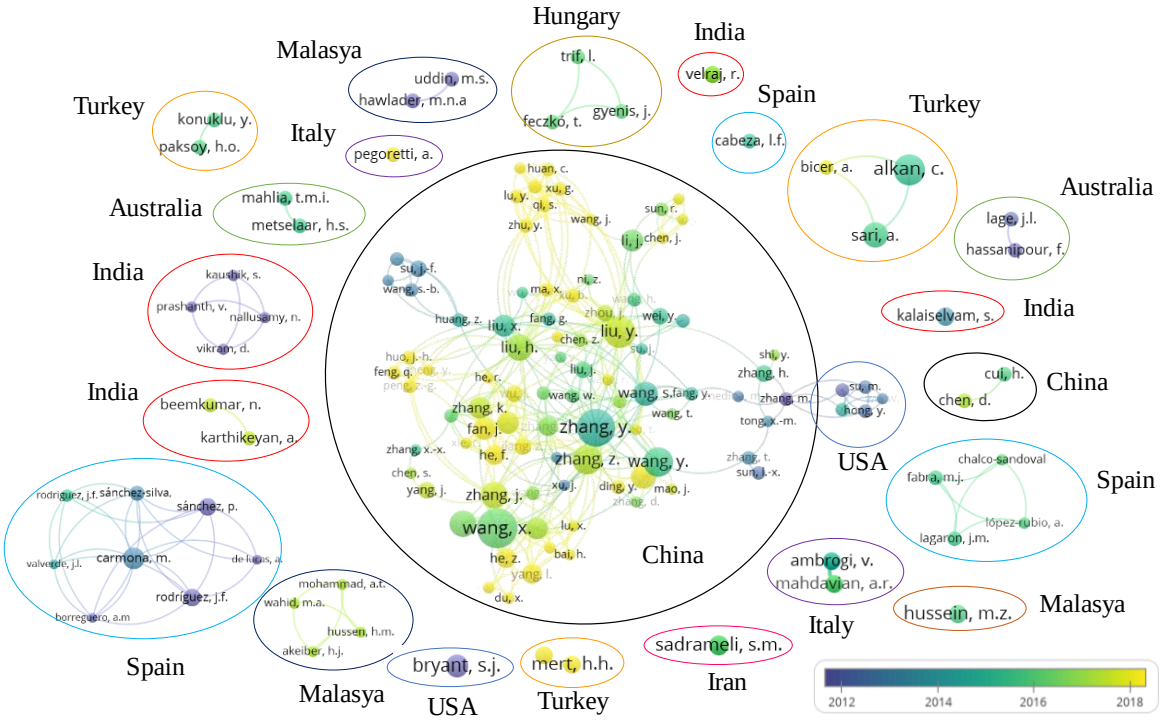

Fig. 10. Co-authorship networks for CS-OPCM.

Similarly, the co-authorship network for SS-OPCM was constructed. As shown in **Fig. 11**. Collaboration between countries seems bigger for this topic compared to the analysis made

for CS-OPCM. Australia showed a network with China, Turkey with Saudi Arabia and South Korea with USA and Japan. The authors that are currently working in the topic are from China (Chen, Y., Gao, J., Liu, Y., among others), Australia (Sanjayan, J., Ramakrishnan, S.) and Saudi Arabia (Al-Sulaiman, F.). A big network can be observed between Chinese authors.

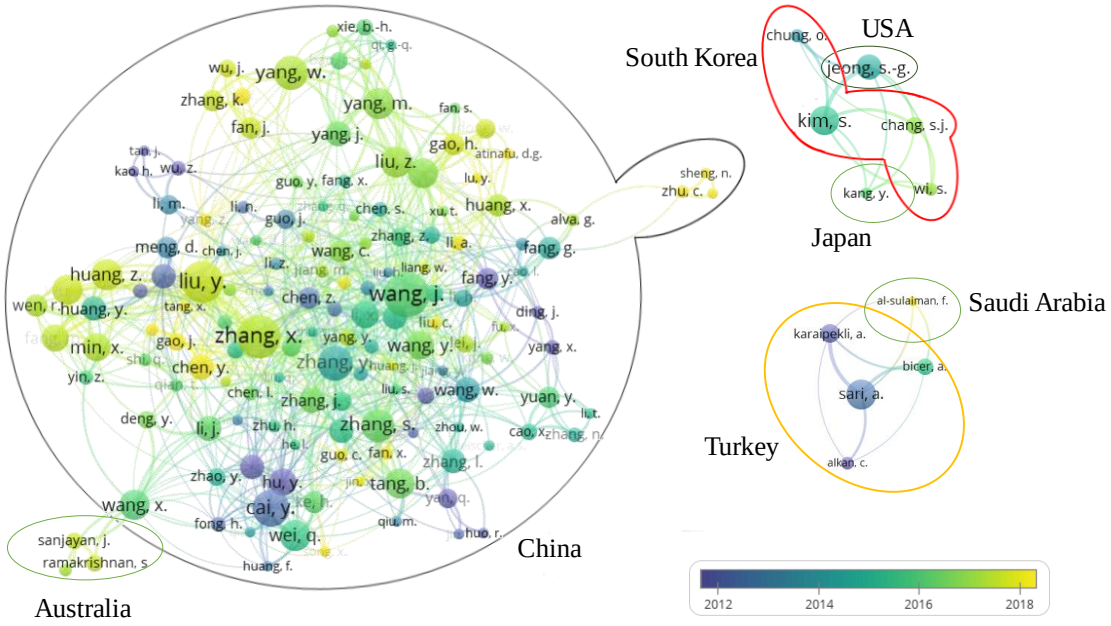

Fig. 11. Co-authorship networks for SS-OPCM.

Finally, two keyword maps were constructed for CS-OPCM and SS-OPCM using as well the VOSviewer software. Some general keywords as storage, energy, heat transfer, flux or thermal stability were obviated from the map, as well as specific characterization techniques (DSC, FTIR, TGA, SEM, etc.), applications (heat exchangers, air conditioning, buildings, etc.) and thermal properties (heat capacity, enthalpy, phase changes, etc.). The number of occurrences selected was 10 for CS-OPCM and 13 for SS-OPCM, meaning the minimum number of times a word is repeated.

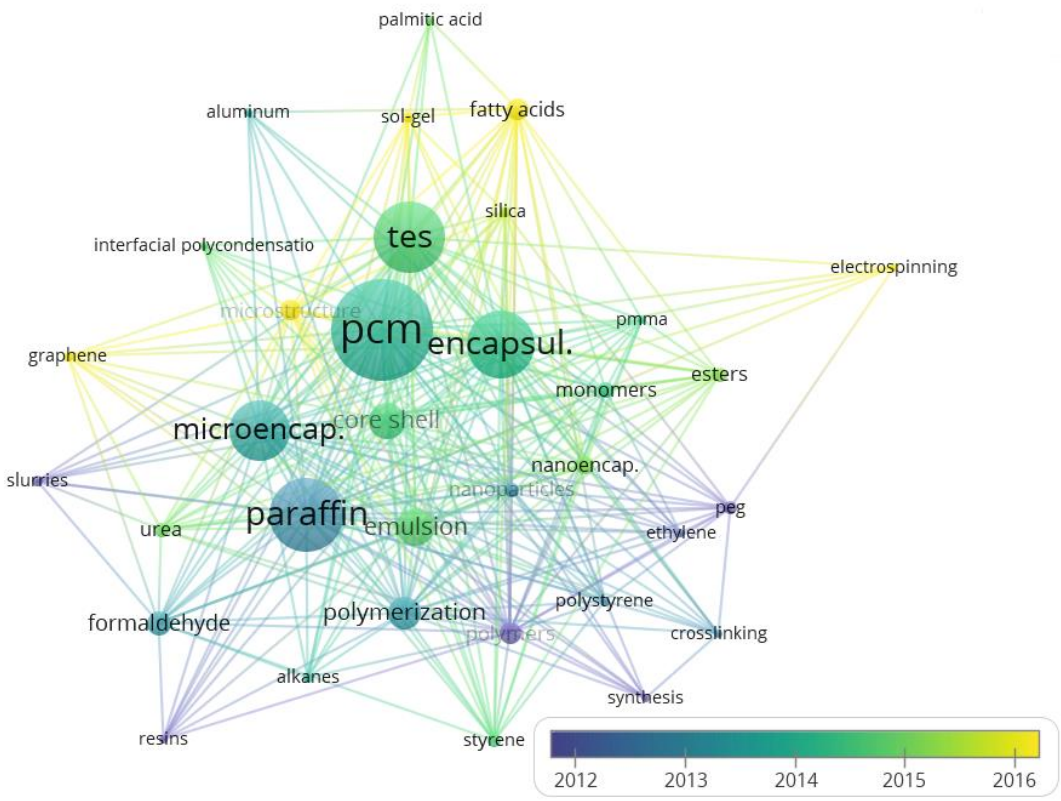

Fig. 12. Keyword map for CS-OPCM.

The keyword map for CS-OPCM (**Fig. 12**) showed that encapsulation of PCM for thermal energy storage have been used mainly for paraffins and the processes has been focused in microencapsulation. The oldest investigations were conducted on encapsulation of polyethylene glycol using chemical synthesis involving crosslinking and probably polymeric shells as polystyrene and ethylene. Then, around 2013, the paraffin encapsulation was performed via polymerization (mini emulsion, in situ, interfacial, etc.) with shells of melamine formaldehyde or urea formaldehyde resines. One inconvenient of these processes are the production of harmful byproducts as formaldehydes. Around 2016, the newest investigations, has been focus in encapsulation of fatty acids, mainly palmitic acid, through sol-gel and silica shells. It can be notice the prescence of graphene in new investigations as a material used to improve the thermal conductivity of the systems. Other encapsulation techniques found in the keyword map were interfatial polycondensation and emulsions, and most new electrospinning. Nanoencapsulation is a method that is still under research, as the size of the circle in the map is not that big and the color is in accordance with investigations after 2015.

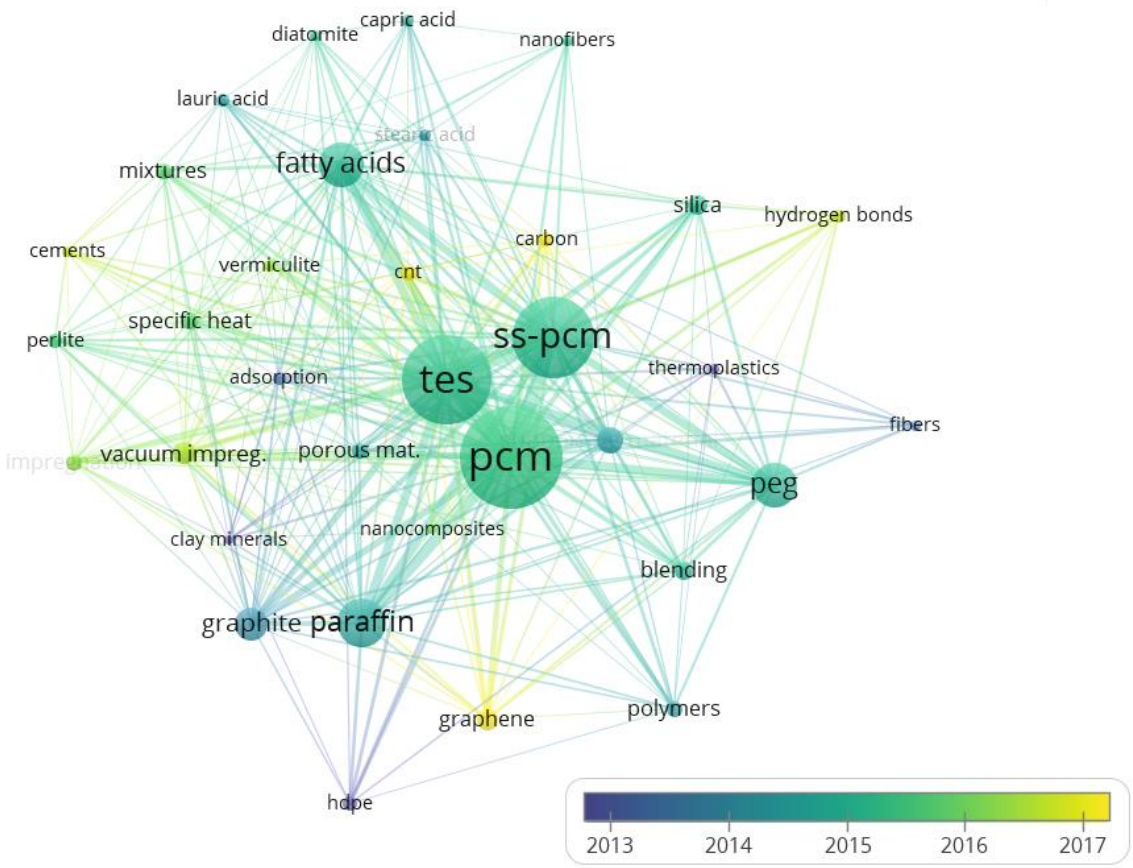

Fig. 13. Keyword map for SS-OPCM.

On the other hand, the keyword map for SS-OPCM (**Fig. 13**) showed that paraffin was the most used PCM for shape-stabilization, as well was found for CS-OPCM. The use of carbon-based materials as carbon nanotubes, graphite and graphene were used for the improvement of thermal conductivity of the SS-OPCM, being the use of graphene and carbon nanotubes newer than the use of graphite. The support materials used for shape-stabilization include porous materials as clays, particularly vermiculite, diatomite and perlite for fatty acids and paraffins, and some polymers as high-density polyethylene and thermoplastics for polyethylene glycol. Cement is another material that appeared in the map in recent investigations as well as fibers. The most used fatty acids were capric acid, lauric acid and stearic acid. The techniques found for shape-stabilization were direct impregnation and vacuum impregnation.

A more detail discussion of the materials and methods found in literature for SS-PCM and CS-PCM is shown below.

1.4. Core-Shell phase change materials (CS-PCM)

Encapsulation is one of the most used methods to improve the handling of phase change materials, particularly those that change from solid to liquid. In this method a core-shell system is achieved as shown in **Fig. 14**. When a CS-PCM is obtained then can be easily use for different applications such construction and building materials **[82,88]** or even in food industry **[22,23]**. Some advantages of the capsules/shells are **[89]**: isolate the PCM from the surroundings, avoiding degradation and acting as a barrier that protects the material from the environment; increase the surface area improving in turn the thermal conductivity of the TES system; increase the compatibility of PCMs with other materials, reduce corrosion, and help to control the volume change of the PCM during phase change.

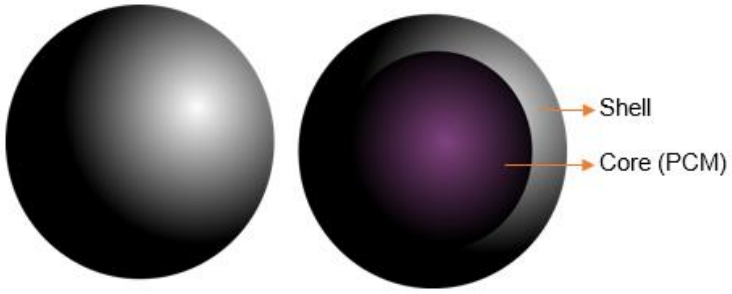

Fig. 14. Typical representation of a CS-PCM.

Encapsulation can be classified according to the capsule size as macroencapsulation, microencapsulation and nanoencapsulation for diameters from 1 mm to 1 cm, 1 μm to 1 mm and less than 1 μm, respectively **[89]**. However, the most investigated size reported in the literature is in the range of microcapsules, which may present different morphologies as presented in **Fig. 15**, being the most common spherical and irregular **[90]**.

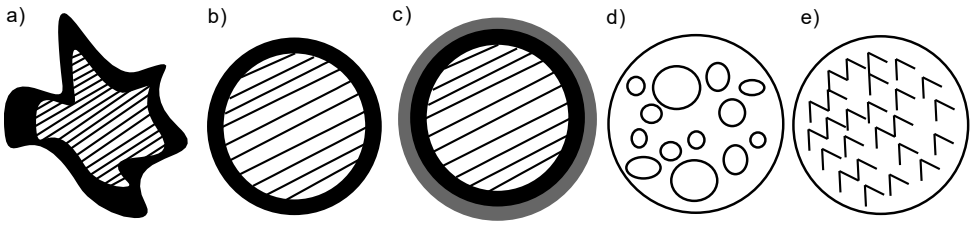

Fig. 15. Possible morphologies of microcapsules a) irregular shape, b) simple, c) multi-wall, d) multi-core, and e) matrix type, adapted from **[90]**.

The selection of the shell material is also important and depends on several factors as the desired temperature of application, thermal conductivity, encapsulation process,

permeability, toxicity and compatibility with the core (PCM) and the surrounding environment where it is going to be incorporated. Therefore, suitable materials must be selected carefully. Next section is a general look about different types of materials (shells) that have been used to encapsulate PCMs (core).

1.4.1. Shell materials used for CS-PCM

Authors such as Giro-Paloma et al **[90]** report that there are about 50 different known polymers that can be used as capsules, both naturally occurring and synthetic. Among polymeric materials are polystyrene **[91]**, polyurethane **[92]**, and polymethyl methacrylate **[93]**. However, little attention has been given to other types of materials **[89]** such as silica **[94]**, calcium carbonate **[95]**, metals (nickel, steel, chromium-nickel), silicates or other inorganic materials which can also be used to encapsulate PCMs. In general, the materials used to encapsulate PCMs can be classified as inorganic and organic, the latter being the most reported in the literature since they have good chemical and mechanical stability, nevertheless, it has been observed that some of them, such as urea-formaldehyde and melamine-formaldehyde **[96–98]** can produce harmful compounds for the environment and for humans, as well as having low thermal conductivity preventing the PCM core from being effective at the time of energy transfer. Because of this, some authors have studied the use of non-polymeric materials that are environmentally friendly, exhibit good thermal conductivity and are inflammable **[95,99,100]**. The little research reported of non-polymeric, mostly inorganic, shell materials present an opportunity for the scientific community to research more about these materials and the encapsulation methods that can be used for PCMs.

For some inorganic PCMs, particularly hydrated salts, an additional difficulty exists when selecting the shell material as well as the encapsulation process because their water content can be lost, present high surface polarities and edge alignment effects **[82,101]**. A good example of technological advances in this field is the development of an inorganic-organic copolymer called ORMOCER® developed by the Fraunhofer-Institut für Silicatforschung **[101]**.

In general, the following characteristics can be listed as desired design factors when choosing a shell material: good mechanical strength, flexibility, corrosion resistance, thermal stability,

high thermal conductivity, structural stability, easy handling, chemical compatibility and non-reactive with the core (PCM), non-hygroscopic, good availability, and non-toxicity.

1.4.2. Encapsulation methods for CS-PCM

The techniques to encapsulate PCMs are divided into physical, chemical and physical chemical methods as shown in **Fig. 16 [35,81,90]**. Most of these methods have been employed to encapsulate organic PCMs and few to encapsulate inorganic PCMs. Examples of methods for encapsulating organic PCMs are suspension polymerization, dispersion, coacervation, electrostatic encapsulation, spray-drying and supercritical CO_2-assisted methods **[82]**. The methods that have been used to encapsulate inorganic PCMs are emulsion polymerization, in situ polymerization, interfacial polymerization and sol-gel process **[82]**. In general, it has been observed that in the encapsulation processes as the emulsion velocity increases, smaller capsule particle sizes are obtained, and as the core to shell ratio increases the efficiency of the microencapsulation decreases **[35]**.

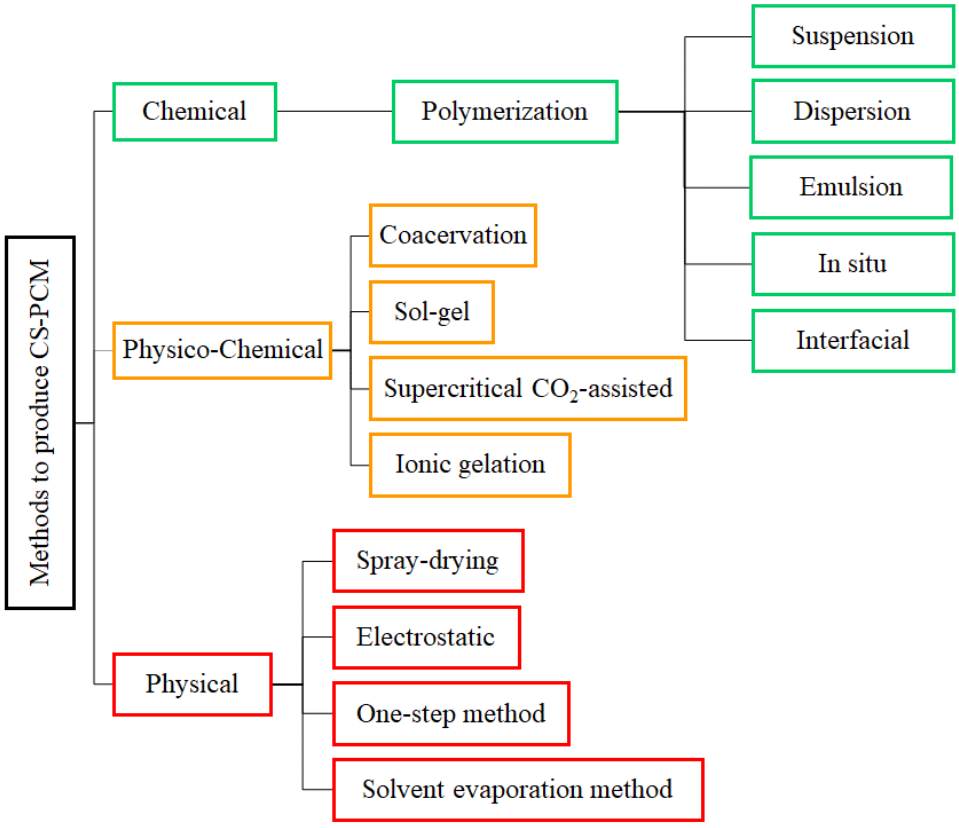

Fig. 16. Methods to produce CS-PCM.

These methods present several advantages and disadvantages which have been tried to be summarized in **Table 8**. The final selection of one method or another should be guided by the type of PCM to be encapsulated, the cost that the process entails, the encapsulation efficiency, the thermal stability of the system and the availability of the reagents.

Table 8. Comparison of different encapsulation methods.

	Advantages	**Disadvantages**
Suspension polymerization	• Environmentally friendly products **[102]** • Used to encapsulate organic PCM **[35]** • Large particles size can be obtained with high PCM content **[35]** • Good heat control of the reaction **[90]**	• High energy consumption and high production costs on a large scale **[35]** • Few monomers are water soluble. Size around 2 – 4000 μm **[90]** • Not used for inorganic PCM **[82]**
In situ polymerization	• Used to encapsulate organic PCM **[35]** • Used to encapsulate inorganic PCM **[82]** Large particles size can be obtained with high PCM content **[35]** High encapsulation efficiency **[35]** • Inorganic shells may be used **[35]** • Uniform coating **[90]**	• It may be obtained substances that are harmful for the environment **[102]** • Size between 1 and 2000 μm **[90]**
Interfacial polymerization	• Used to encapsulate organic PCM **[35]** • Used to encapsulate inorganic PCM **[82]** • High reaction speed **[90]** • Its products have low permeability **[90]** • Versatile, good properties in size, degradability, mechanical resistance **[90]**	• It may be obtained substances that are harmful for the environment **[102]**
Emulsion polymerization	• Used to produce nanocapsules **[35]**. • Used to encapsulate organic and inorganic PCM **[82]**.	• High energy consumption and high production costs on a large scale **[35]**
Sol-gel	• Used to encapsulate organic PCM **[35,82]** • Used to encapsulate inorganic PCM **[82]** • Inorganic shells may be used **[35,90]**	• Not reported **[90]** • Highly cost precursors
Coacervation	• Used to encapsulate organic PCM **[35,82]** • Two methods **[90]** • Versatile **[90]** • Good control of the particle size and thickness **[90]**	• Agglomeration **[90]** • Difficult to scale-up **[90]** • Not used for inorganic PCM **[82]**
Solvent evaporation method	• Used to encapsulate inorganic PCM **[35]**	• Low encapsulation efficiency **[35]**
Spray-Drying	• Rapid method **[81]** • Low-cost commercial process **[90]** • Easily scaled-up **[81,90]** • Production of homogenous microcapsules is achievable **[81]** • Suitable for heat-sensitive materials **[90]**	• Could be agglomerated and uncoated particles **[81,90]** • Not used for inorganic PCM **[82]**

1.5. Shape stabilization of phase change materials (SS-PCM)

On the other hand, shape-stabilized phase change materials, sometimes found in literature as form-stable (FS-PCM), are composites where the PCM in its molten phase is retained by another material, generally porous, by capillarity **[33,82]**, as shown in **Fig. 17**. Thus, shape-stabilization depends largely on the porosity of the support. Moreover, this encapsulation technique can take advantage of natural occurring porous materials as some clays, hierarchical porous material fabricated by templating methods and even some fibers. Thus, shape stabilization could be considered a cheaper method of containment compared to encapsulation and presents less processing steps **[33]**.

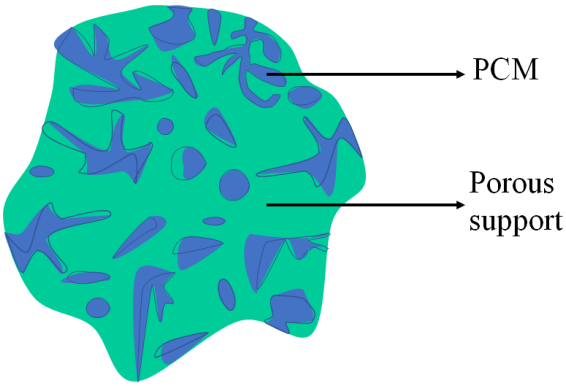

Fig. 17. Typical representation of a SS-PCM.

The study of natural minerals as porous supporting matrices for organic PCMs is limited to investigations of pure mineralogical phases and are just a few of them, as diatomite, vermiculite, perlite, kaolin, bentonite, pumice or sepiolite. Similarly, polymeric supports include polyethylene, polyurethane or acyclic resins. Mineral supports are used mainly to contain organic PCMS, while polymeric supports are used to contain both organic (mainly paraffins) and inorganic PCM. The choice of the porous material or support depends on several factors as porosity, thermal conductivity, mechanical resistance, availability, chemical compatibility with the PCM and the production process. The principal materials and methods use to shape-stabilized phase change materials are described below.

1.5.1. Synthetic supports used for SS-PCM

Polyethylene (PE) has a good chemical affinity to paraffins so is widely used to produce SS-PCM. Polyethylene, low density polyethylene (LDPE) and high density polyethylene (HDPE) are used as a support materials that form three-dimensional network structure where the PCM can be dispersed **[33]**. Chen & Wolcott **[103]** study HDPE, LDPE and linear low-density polyethylene (LLDPE) founding that are partially miscible with paraffin, being the

weakest the HDPE, however in other study **[104]** found a slower leakage of the PCM in HDPE, compared with LDPE or LLDPE.

Acrylic matrixes are used as support. The advantage of this material is that is commercially available and easy to process, like poly(methyl methacrylate) PMMA **[33]**, that presents high impact strength and chemical resistance. For instance, Alkan & Sari **[105]** evaluated the encapsulation of fatty acids in an array of PMMA achieving a SS-PCM useful for latent heat TES systems.

Polyurethane (PU) foam is an excellent thermal insulating material, is rigid, with superior specific mechanical properties and low density **[106]**. It can be used with PCM by direct incorporation or by the incorporation of already encapsulated PCMs as explained by Yang et al. **[106]** in their review. **Fig. 18** shows a PU foam containing microencapsulated *n*-octadecane with a polymer as shell material.

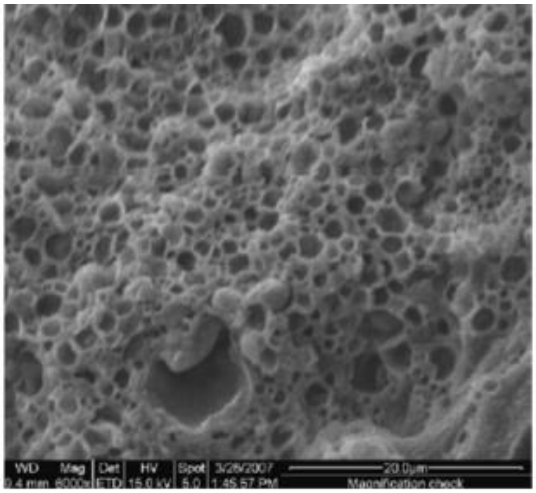

Fig. 18. SEM micrograph of a PU foam containing *n*-octadecane **[106]**.

Another synthetic support, used with n-octadecane, was a hierarchically porous TiO_2 obtained through a soft-template method **[107]**. They found that the crystallization of the PCM is influenced by the different pore structures present in the support (micro, meso and macropores) as shown in **Fig. 19**. As well, they analyzed the durability of the system after 800 melting/solidifying cycles founding an excellent thermal reliability.

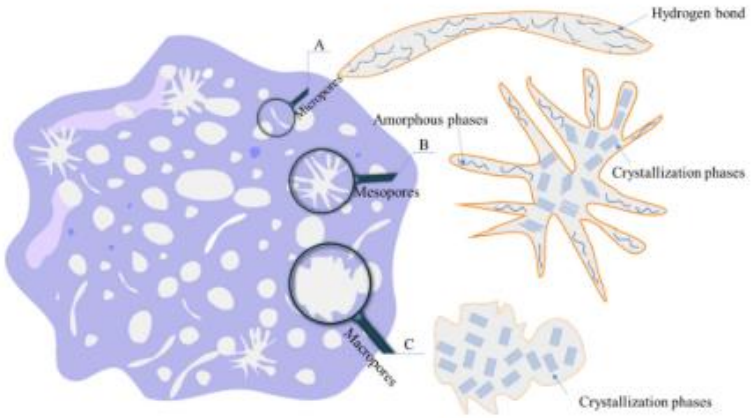

Fig. 19. SS-PCM of n-octadecane in a TiO_2 porous support **[107]**.

The composite of fibers and PCMs is also considered as SS-PCM. This kind of systems consist in fibers that contain PCM. Some of the polymers that have been reported in literature are polylactic acid (PLA) **[108]**, polyethylene terephthalate (PET) **[109,110]** (**Fig. 20**) and polyacrylonitrile (PAN) **[111]**.

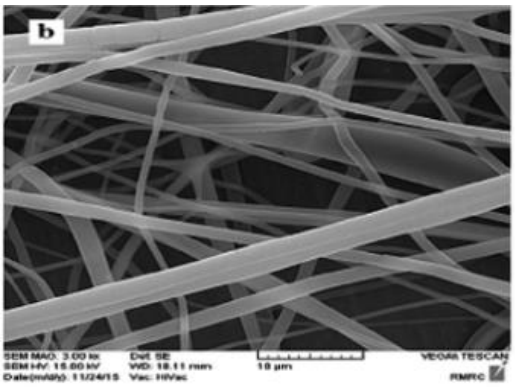

Fig. 20. Composite fiber of fatty acid and PET **[110]**.

Porous silica matrices have been used as well as supports for SS-PCM as they can present high specific area, large pore volume, chemical inertness and good adsorption capacity. Silica matrices can be found naturally in the form of diatomite, or can be designed as silica nanosheets, silica microspheres, silica gel and even as synthetized ordered porous silica like Santa Barbara USA (SBA-15) or Mobil Crystalline Materials (MCM-41). Three silica supports were engineered by Zhang et al. **[112]** to contain paraffin, they concluded that the pore array of the silica supports can immobilized by capillary force and interfacial

interactions the paraffin, even more, a 1000-cycle thermal test was performed and no degradation was found.

1.5.2. Natural supports used for SS-PCM

Many of the naturally occurring clay materials have a porous structure and considerable specific surface area. Thus, absorption capacity of some clays is excellent and the PCMs can be supported within this kind of materials. The interactions between PCM and clay materials are mainly capillary force, surface tension, hydrogen bond, Van der Waals' force (VDW) and so on. The interactions can restrict the leakage of PCM within the clay-based shape stabilized PCM **[113]**, with additional advantages as natural availability and moderate prices.

Between the natural supports found in the literature for SS-PCM, sepiolite, perlite, vermiculite, and diatomite are the most common (**Fig. 21**). Sepiolite is a fibrous phyllosilicate that contains magnesium **[114]**. In their work, Konuklu and Ersoy **[115]** studied the preparation of sepiolite-based PCMs nanocomposites, using organic PCMs as paraffin and fatty acids. The production of these composites was made by the direct impregnation method and probe that sepiolite can be used as a feasible support for shape-stabilization of organic PCMs. On the other hand, expanded perlite present the advantages of high porosity, spherical shape, good acoustic insulation, low water content, low density, high surface area, good chemical stability, and compatibility with the PCMs. As disadvantages, perlite present limited availability in mines in the world and can present low heat transfer **[76,116,117]**. The heat transfer can be solved by adding materials with high thermal conductivity, such as expanded graphite. Comparably, expanded vermiculite present the advantages of high porosity, lightness, economy, good chemical stability, compatibility with PCM and the disadvantage of low thermal transfer, just like expanded perlite, the vacuum impregnation method is usually used **[76,116,118]**.

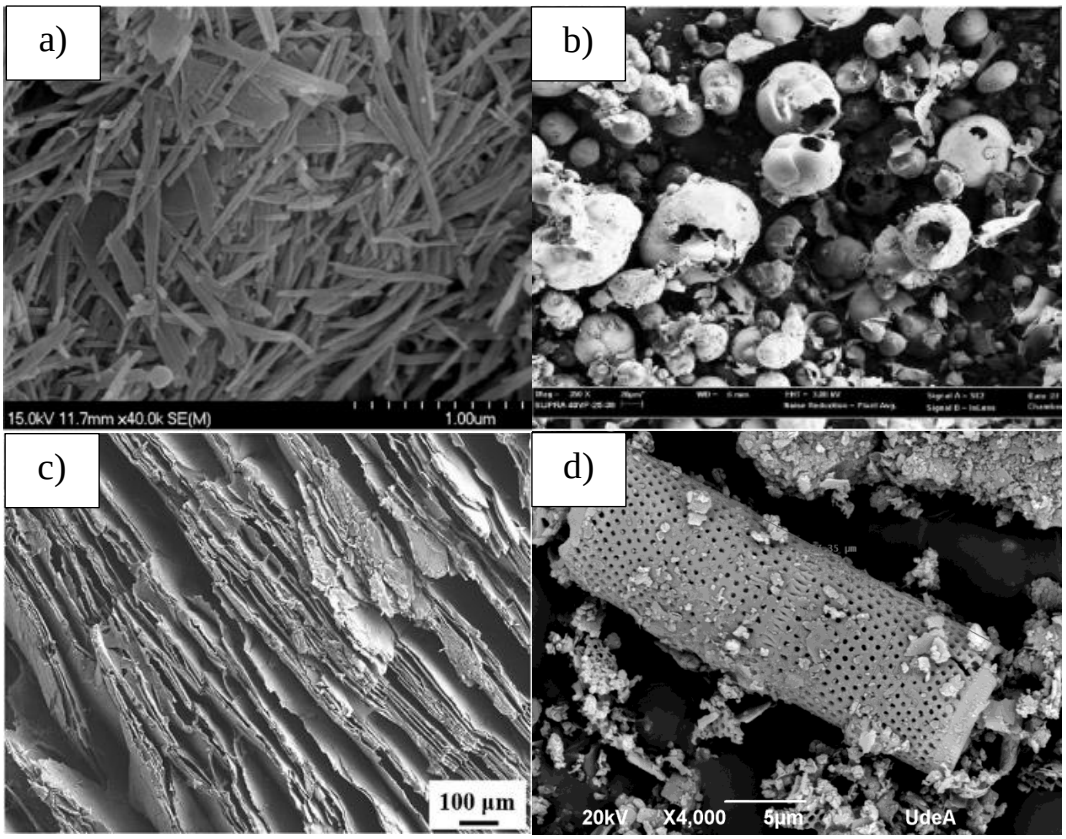

Fig. 21. SEM images of a) sepiolite **[119]**, b) expanded perlite **[120]**, c) expanded vermiculite **[76]**, and d) diatomite (this work).

Among the natural supports, diatomite possesses unique properties as highly porous structure, excellent absorption capacity and good thermal stability. Diatomite, $SiO_2 \cdot nH_2O$, is a natural amorphous siliceous mineral that is well recognized for its uses as catalyst, filters and sorbents as it possesses unique properties as highly porous structure, excellent absorption and thermal stability **[121]**. Biologically, diatomite is the porous silica cell wall (frustules) of the phytoplanktonic (microalgae) unicellular organisms called diatoms, that includes over 250 genera and 10^5 marine and freshwater species **[122]**. The variety of species can be evidence in the diversity of shapes and pore patterns present in diatomite, as evidenced by Haeckel in his book "Art forms in nature" (**Fig. 22**). Most of the studies of SS-PCM based in diatomite have been carried in purified samples**[121,123–126]**, where diatoms are the 99% of the content. As well, the studies have centered in the shape-stabilization of organic PCMs **[33,121,125,127,128]**.

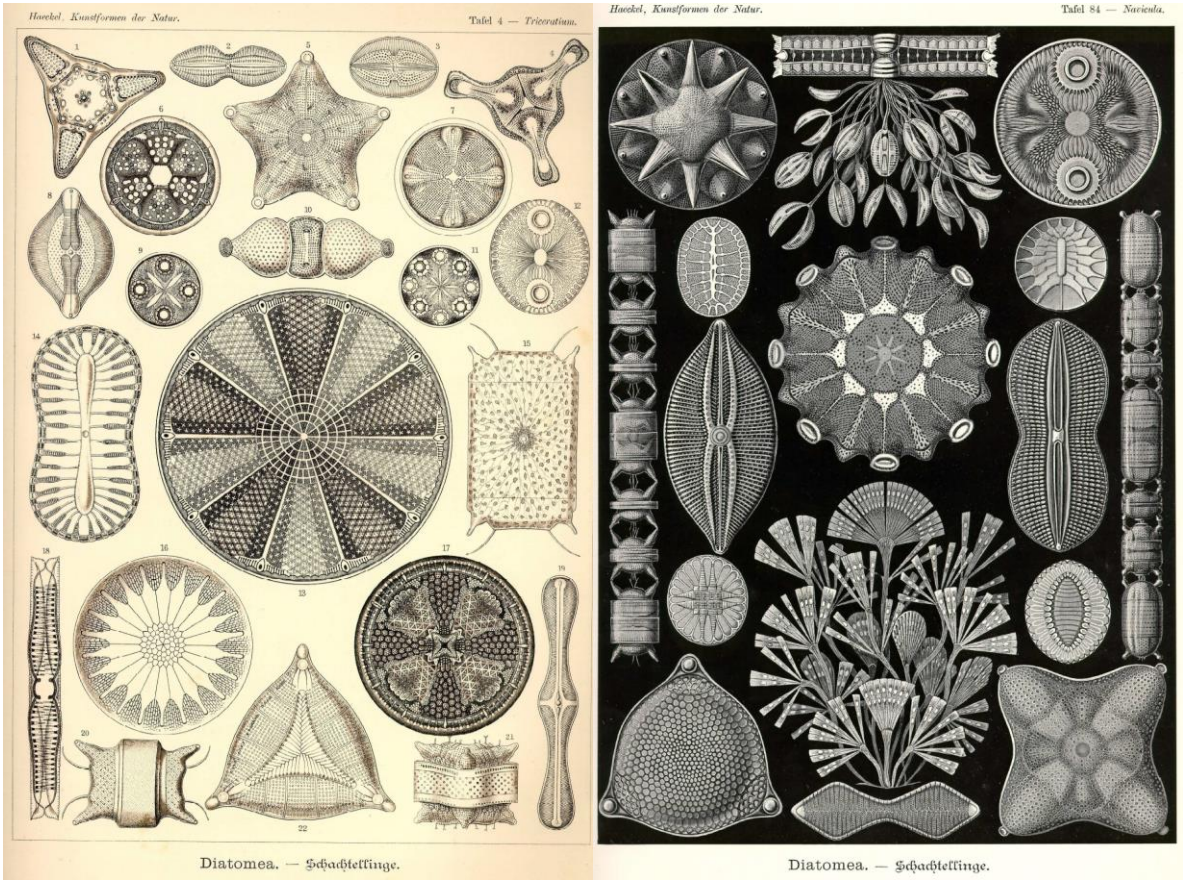

Fig. 22. Diatoms from Haeckel's *Kunstformen der Natur* (Art forms in nature) **[129]**.

Other feasible supports for SS-PCM found in literature are attapulgite, bentonite **[130,131]**, pumice **[131]**, kaolin **[113,132–135]**, halloysite nanotubes **[136]**, carbon foam, expanded graphite **[137,138]** and silica fume.

1.5.3. Encapsulation methods for SS-PCM

The methods reported in literature to produce SS-PCM (**Fig. 23**) are fewer and simpler than the methods reported to produce CS-PCM. In general, most of the methods are of physical nature as absorption/adsorption. In addition, the use of methods as templating to produced hierarchical porosity and methods for fiber fabrication as electrospinning and centrifugal spinning, allowed new possibilities to the technological development of SS-PCM.

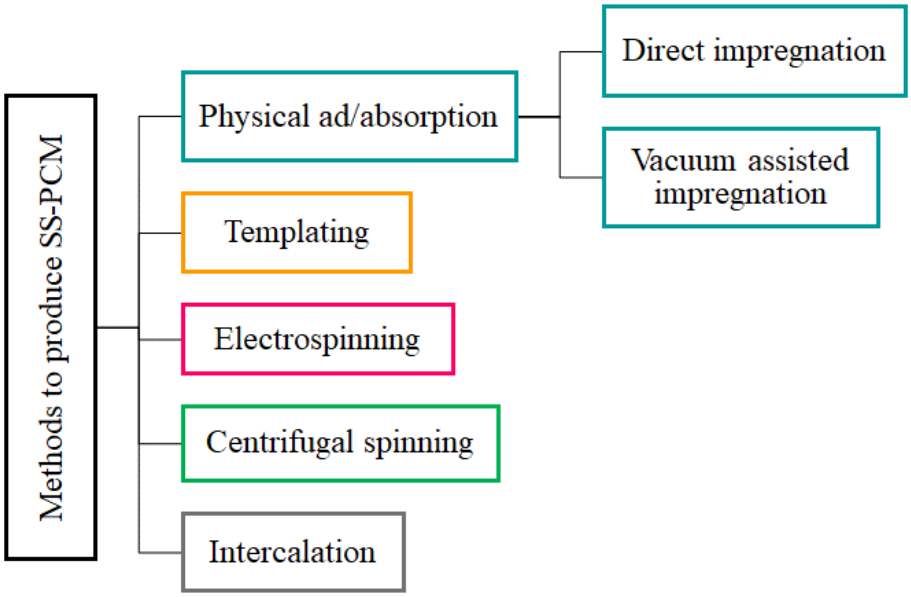

Fig. 23. Methods to produce SS-PCM.

One of the simple methods, yet very effective and more found in literature, to obtained SS-PCM is vacuum-assisted impregnation **[131]**, where vacuum conditions are used to force the PCM in liquid phase to be infiltrated in the porous support. The method is simple and not that expensive. Some authors report direct impregnation techniques where no vacuum is used, and only natural infiltration occurs. It has be proven **[139]** that vacuum impregnation method produced SS-PCMs with more amount of PCM incorporated than direct impregnation. Despite the simplicity of the technique, recently authors as Chang et al. **[140]** developed a vacuum impregnation equipment based on the existing vacuum impregnation method to improve the efficiency of the SS-PCM production and decrease infiltration times.

Some works have studied SS-PCM prepared by intercalation techniques, where basal spacing of layered materials are used. The principal supports found in literature are clay supports and graphite supports **[141]**. For instance, lauric acid was absorbed into intercalated kaolinite **[132]** obtaining a SS-PCM due to hydrogen bonds, capillary and surface tension forces between the fatty acid and the organically modified kaolinite. Works with paraffins have been reported as well using intercalated montmorillonite **[142]**.

Fabrication of PCM-polymeric fibers are mainly achieved by electrospinning **[108,110,143]** as shown in **Fig. 24** or by centrifugal spinning **[111]**. Being novel studied techniques in the field of thermal energy storage. Some authors discus that disadvantages of electrospinning are low productivity, need of high voltage electric field and required an accurate control of the solution properties. Compared to this, centrifugal spinning looks cheaper and with a higher productivity due to the high-speed rotation involved. However, other authors **[143]** sustained that electrospinning is an economic and versatile technique.

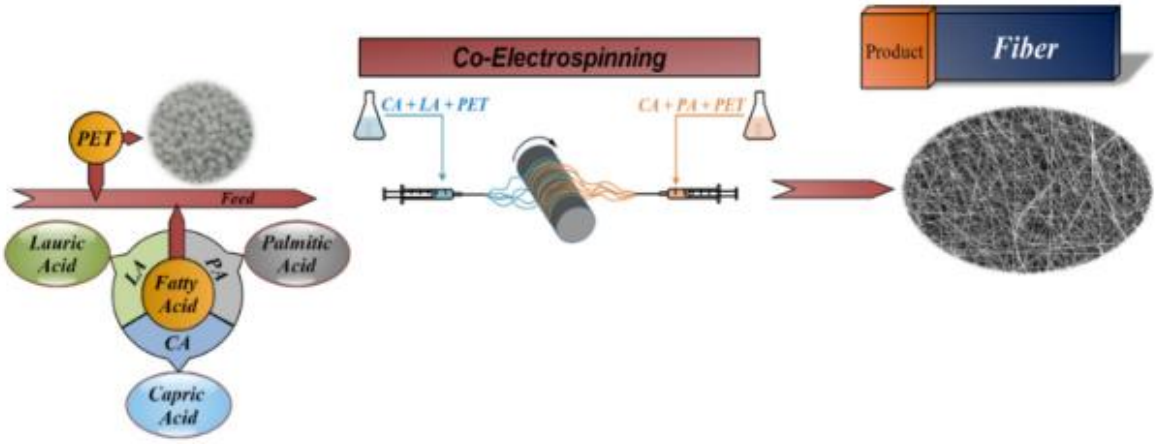

Fig. 24. Composite fibers produced by co-electrospinning **[110]**.

Finally, the use of templating techniques offers a great opportunity to design hierarchical porous matrices, where the structure consists of interconnected pores on different lengths scales, making the method very versatile for shape-stabilization of PCMs. Templating method could be divided in hard templating, soft templating, sacrificial templating and other categories based on the type of template **[144]**.

1.6. Discussion

As stated during this section, all materials and processes must be chosen in accordance to the final application and use. Each encapsulating technology, CS-PCM or SS-PCM, present some strengths and weakness that must be considering when designing solutions for thermal energy storage. In **Table 9** is summarized some of the advantages and disadvantages of core-shell phase materials versus shape-stabilized phase change materials.

Table 9. Comparison of core-shell PCM and shape-stabilized PCM.

	Advantages	**Disadvantages**
CS-PCM	• High Surface area for heat transfer • Reduce reactivity with the surrounding, less corrosion • Control of volume change during the phase transformation • Small particle size that could make more efficient the system	• Expensive process and reagents • Must obtained a non-permeable capsule to prevent leakage • Some methods for production can present harmful by-products • Many steps to be produced
SS-PCM	• Cost-effective production process • Large particle size, it may be easier to handle for certain applications • Porous materials are found in natural inorganic supports • Hierarchical porosity can be obtained by templating methods • May increase thermal conductivity • Few steps for the production • Different morphologies can be achieved as fibers, amorphous particles or rounded particles	• PCM can diffuse to the surface and gradually be lost if the process is not optimized • Limit in the amount of PCM that can be contained • Is difficult to obtain nanoscale particles • More contact between the PCM and the surroundings, leading sometimes to corrosion or not desirable reactions

According to the systematic review performed, it could be notice that research in materials, both for CS-OPCMs and SS-OPCMs, is moving towards investigations that uses carbon-based materials such graphene or nanotubes. Usually they are employed to increase thermal conductivity, and in some cases, as porous supporting materials. Thermal conductivity plays a key role in heat transfer as govern the charge-discharge of the TES system, being important when scaling-up. Some problems to overcome with the use of carbon-based additions are the possible aggregation of the particles, the heterogenous dispersion over the matrix, changes in the viscosity of the PCM and increases in cost of the system. Besides, some discussions in literature **[72]** can be found about suitable techniques for measuring thermal conductivity in TES systems as there is no standard for this kind of materials. Thus, there is still a gap in thermal conductivity enhancement of the TES systems, that includes measurement techniques and the study of new materials or methods to improve this property.

As well, encapsulation techniques as sol-gel and electrospinning are attracting attention in the CS-PCMs field. Sol-gel is a relatively simple and well known method for encapsulating **[145]** at relative low temperature based on wet chemistry processes, is versatile and there is no need to use special or expensive equipment. On the other hand, electrospinning is a novel

method used in the TES field that would increase the range of applications as explore new morphologies as fibers.

Regarding SS-OPCMs, the incorporation of these composites in construction and building materials as cement-based materials or gypsum is still under studying and more work is need it to increase the knowledge about the mechanical performance of the final material, the measurement of the thermal properties, thermal conductivity, percentage of leakage, thermal cycling and durability.

Investigations during the past five years have been selected and summarized for future researchers as a guide in **Table 10**, **Table 11**, and **Table 12**. Each table correspond to core-shell (CS-OPCM), shape-stabilization (SS-OPCM) and a special selection made by fiber-based (FB-OPCM) organic phase change materials, respectively. Each table present the core/PCM, shell/supporting material, diameter of the composite, latent heat, phase change temperature, thermal conductivity, leakage percentage and thermal cycling. It can be inferred, as stated above, that thermal conductivity, leakage percentage and thermal cycling are properties that need more attention for future works, as well, none of these studies consider heat capacity of the materials.

Table 10. Summary of CS-OPCM in literature.

Core	Shell	Diameter (μm)	Synthesis method	Encapsulation efficiency (wt.%)	Latent Heat (J/g)	Melting temperature (°C)	Thermal conductivity (W/m·K)	Leakage (%)	Thermal cycling (cycles)	Ref.
Butyl stearate	Polyurethane	10-35	Interfacial polymerization	-	77.1-80.6	21.7-22.3	-	4.65-8.49	-	**[92]**
Cetyl alcohol	Polyethylene dimethacrylate	758	Suspension polymerization	53.1	89.6	41.65	-	-	1000	**[146]**
Caprylic acid	Polystyrene	-	Emulsion polymerization	15.7-41.78	11.77-79.21	(-5.4)-13.07	-	-	500	**[91]**
Coconut oil	Calcium alginate	2200	Interfacial coacervation/ crosslinking	81.1	84.7	24.65	-	-	2	**[147]**
Myristic acid	Ethyl cellulose (EC)	3, 6, 40	Emulsification–solvent evaporation	35-62	69.10-122.61	54.10-55.33	-	-	100	**[148]**
n-hexadecane	Polymethyl methacrylate + poly (butyl acrylate-co-methyl methacrylate)	60-210	Suspension polymerization	30.0	19.3-63.1	16.9-20.4	-	-	500	**[93]**
n-eicosane	ZnO	4-8	In-situ precipitation reaction and O/W emulsion	40-60	50-130	38-40	-	-	500	**[149]**
n-docosane	ZnO/SiO_2	2.5-4.5	Emulsion-templated interfacial polycondensation	60-80	139.5	45.0	-	Anti-osmosis experiment	200	**[150]**
Octadecyl acrylate	Chitosan	0.29-4.05	Coacervation	49.82-68.99	92.9-131.4	26.4-39.9	-	-	-	**[151]**
Paraffin	Calcium carbonate	1-5	Self-assembly method.	55.7-59.4	-	25-50	0.73-0.93	Qualitative	-	**[152]**
Paraffin	Polyethylene dimethacrylate	994	Suspension polymerization	75.6	132.6	54.55	-	-	1000	**[146]**
Paraffin	SiO_2	0.2-0.7	In situ emulsion interfacial hydrolysis and polycondensation	11.0	13.0	49.00	-	-	-	**[153]**
Paraffin	Polymethyl methacrylate	0.2-0.4	One-step interfacial polymerization	52.95	64.93	21.42	-	-	-	**[154]**
Paraffin	Urea formaldehyde resin	5.7	In situ polymerization	66.54	85.69	35.85	-	-	100	**[155]**
PEG	SiO_2	0.3	Stöber method	61.0	66.24	20-21	-	-	-	**[156]**
Stearic acid	SiO_2	0.02-0.08	In-situ emulsion interfacial hydrolysis and polycondensation	23.0	46.0	71.00	-	-	-	**[153]**
Stearic acid	TiO_2	-	Sol-gel	34.75-55.74	81.67-105.1	65.87-68.70	-	-	3	**[157]**
Stearic acid	Polymethyl methacrylate	0.11-0.36	Emulsion polymerization	26.5-38.9	50.0-63.3	60-85	-	-	-	**[158]**

Table 11. Summary of SS-OPCM in literature.

PCM	Support	Impregnation method	Loading (wt.%)	Latent Heat (J/g)	Melting temperature (°C)	Thermal conductivity (W/m·K)	Leakage (%)	Thermal cycling (cycles)	Ref.
Capric acid	Bentonite	Vacuum-assisted	38.9	74.08	30.07	0.43	-	1000	**[130]**
Capric acid	Kaolin	Vacuum-assisted	10-30	27.23	30.71	0.17-0.23	12.5	1000	**[134]**
Capric/palmitic acid	Pumice	Vacuum-assisted	10-50	56.45	23.13	-	16	3000	**[131]**
Decanoic acid	Sepiolite	Direct	50	35.69	28.65	-	0.01	-	**[115]**
Dodecanol	Bentonite	Vacuum-assisted	31.3	67.55	22.61	0.48	-	1000	**[130]**
Dodecanol	Pumice	Vacuum-assisted	10-50	67.32	23.27	-	19	3000	**[131]**
Heptadecane	Bentonite	Vacuum-assisted	17.8	38.42	22.07	0.35	-	1000	**[130]**
Heptadecane	Kaolin	Vacuum-assisted	10-30	34.63	22.08	0.20-0.29	13.5	1000	**[134]**
Heptadecane	Pumice	Vacuum-assisted	10-50	72.38	22.18	-	18	3000	**[131]**
Lauric/myristic acid	Clay mineral	Vacuum-assisted	25-40	29.63-56.59	35.39-36.36	-	0.1-4.9	2	**[126]**
Myristic/stearic acid	N-doped carbon	Direct	70-90	144.02-164.33	48-65-49.45	0.29-0.37	Qualitative	100	**[159]**
Octadecanol	Expanded perlite	Vacuum-assisted	30-65	73.73-170.38	58.87-59.57	0.37-0.42	0.67-10.85	-	**[160]**
Paraffin	Kaolin	Vacuum-assisted	60	119.49	62.4	0.413	Qualitative	-	**[161]**
Paraffin	Palygorskite	Direct	143	126.08	23.1	-	-	500	**[162]**
Paraffin	Sepiolite	Direct	50	62.08	40.02	-	0.05	-	**[115]**
PEG	Bentonite	Vacuum-assisted	41.6	56.72	4.03	0.39	-	1000	**[130]**
PEG	Diatomite	Vacuum-assisted	30-60	53.8-62.9	7-8	0.26-0.29	42.8-53.0	500	**[78]**
PEG	Flower-like TiO_2 nanostructure	Direct	50.2	93.68	53.6	-	Qualitative	200	**[163]**
PEG	Halloysite	Vacuum-assisted	45	71.3	33.6	0.73-0.9	-	2000	**[136]**
PEG	Kaolin	Vacuum-assisted	10-30	32.80	5.16	0.18-0.27	9	1000	**[134]**
PEG	Triamide-linked polymer	Direct	50-85	70.9-155	51-54	-	Qualitative	50	**[164]**
Stearic acid	Exp. vermiculite	Vacuum-assisted	63.12	134.31-148.39	67.12-67.67	0.34-0.52	Qualitative	200	**[76]**

Table 12. Summary of FB-OPCM in literature.

PCM	Supporting material	Fiber diameters (μm)	Production method	PCM (wt.%)	Latent Heat (J/g)	Melting temperature (°C)	Thermal conductivity (W/m K)	Leakage (%)	Thermal cycling (cycles)	Ref.
Capric/lauric acid	SiO_2	-	Electrospun	82.0	90.4	22.7	-	-	-	**[165]**
Capric/lauric acid + capric/palmitic acid	Polyethylene terephthalate	-	Co-electrospinning	50-120	65-95	20.85	-	-	-	**[110]**
Capric/lauric/myristic acid	SiO_2	-	Electrospun	79.1-81.3	100.9	21.7	-	-	50	**[166]**
Capric/lauric/palmitic acid	Polylactic acid	0.5-0.8	Co-electrospun-electrospray	80.0	7.45-24.28	17.0-21.4	Qualitative	-	-	**[108]**
Capric/myristic acid	SiO_2	-	Electrospun	83.7	99.8	24.7	-	-	-	**[165]**
Capric/palmitic acid	SiO_2	-	Electrospun	84.2	108.6	28.1	-	-	-	**[165]**
Capric/stearic acid	SiO_2	-	Electrospun	83.1	99.8	30.0	-	-	-	**[165]**
Lauric/stearic acid	Carboxy methyl cellulose	50000	Direct impregnation	66-70	107.4-114.6	32.2	-	-	100	**[167]**
Myristic/lauric acid	Polyester	-	Direct impregnation	25.3-27.1	40.3-43.2	29.4-30	0.07-0.14	-	100	**[168]**
Myristic/stearic acid	Polyester	-	Direct impregnation	28.5-30.8	53.9-58.2	34.2-36.7	0.07-0.14	-	100	**[168]**
Polyethylene glycol	Polyamide 6	0.06-0.08	Coaxial electrospinning	36-70	90-120	23.0-33.3	-	-	-	**[143]**
Polyethylene glycol	Polyacrylonitrile	0.57	Centrifugal spinning	10.0	45.61-81-56	39.19-55.95	0.187-0.334	Qualitative	200	**[111]**

1.7. Conclusions

The first part of this chapter has provided an overview of core-shell and shape-stabilization of organic phase change materials, based on 952 publications retrieved from Scopus database. The evolution of these publications over the past forty years has been revised as well as the evolution per authors and per country. Moreover, the interaction between co-authorship, countries and time of publication was analyzed, and, in the same manner, two keyword maps were constructed. Researches about CS-PCM and SS-PCM has growing for the last two decades and continue rising due to new materials and production methods. China, North America and some European countries are the current leaders in these fields, but it is noticeable that more international collaborations are required. Research in thermal energy storage in Latin-America in is still unmatured and just a few papers are published in the field. Particularly, research on this topic is very incipient in Colombia, and no research about shape-stabilization of organic phase change materials has been done until this work.

The systematic review showed that CS-PCM and SS-PCM imply several technological steps that ultimately depend on the intended application. First, the choice of the shell/support material and the core/PCM that must be chemically compatible between them and the surroundings, and with an adequate phase change temperature. Second, the fabrication of the composite should be selected according to the desired morphology, environmental impact, production cost and yield. Third, the measurement of properties as latent heat, phase change temperature, permeability/leakage, durability and thermal conductivity. Further steps, as improving percentage of leakage, thermal reliability, thermal conductivity, thermal cycling and durability, transfer from laboratory scale to pilot plant or taking into service, are still missing in literature. Few investigations comprise topics beyond the third step.

Microencapsulation of PCMs is the most common process studied in literature as can be achieved by several synthesis routes and materials. Depending of the selected route could be expensive and even environmentally dangerous due to some by-products. In comparison, shape-stabilization of PCMs (SS-PCMs) in natural porous supports seem as a less expensive and more easy technique to carry out.

Consequently, this thesis try to increase the knowledge in latent heat thermal energy storage (LHTES) systems based on organic phase change materials (OPCMS) by means of the study of SS-PCMs due to the several advantages that presents, the comparatively less expensive cost, the exploitation of natural minerals found in Colombia that can serve as supports and the use of PCMs from renewable sources as fatty acids.

CHAPTER II.

Selecting an adequate PCM for LHTES systems

2.1. Organic phase change materials: Fatty acids

As stated in Chapter I, organic phase change materials (OPCM) are divided in paraffins and non-paraffins like fatty acids, esters, polyethylene glycol and alcohols. Non-paraffin PCMs can be a sustainable choice because of the renewable source of these materials, compared to petroleum-based paraffins, besides are non-toxic, present no-subcooling and are abundant. Particularly, fatty acids are a promising solution for low temperature (<100 °C) thermal energy storage components given that are safe materials derived from vegetable oils and natural fats, commonly used for food processing purposes **[169]**. The availability of vegetable oils and natural fats make them financially competitive with paraffins and salts in the PCM market **[170]**. The composition of various vegetable oils and animal fats are presented in **Table 13**, showing that are natural sources of saturated and unsaturated fatty acids. The different fatty acids are characterized by the carbon chain length, typically from 8 to 24 carbon atoms, and the carbon-carbon bonds. For instance, caprylic, capric, lauric, myristic, palmitic, stearic and arachidic acids are saturated fatty acids as are composed only by a single bond. When fatty acids are composed for more than a single bond are called unsaturated. One disadvantage of fatty acids is that they can degrade from contact with oxygen, water or microbial contamination **[171]**, thus it is recommended to encapsulate them for extend time applications, even though, saturated fatty acids oxidation stability is much higher than of unsaturated fatty acids. Hence, in this work five saturated fatty acids were chosen as sustainable phase change materials given their good availability and low reactivity when in contact with oxygen or water. The chosen fatty acids were capric acid (decanoic acid), lauric acid (dodecanoic acid), myristic acid (tetradecanoic acid), palmitic acid (hexadecenoic acid) and stearic acid (octadecanoic acid).

Table 13. Average composition of fatty acids in some vegetable oils and natural fats **[169,172,173]**.

		Caprylic Acid (C8:0)	Capric Acid (C10:0)	Lauric Acid (C12:0)	Myristic Acid (C14:0)	Palmitic Acid (C16:0)	Stearic Acid (C18:0)	Oleic Acid (C18:1)	Linoleic Acid (C18:2)	Linolenic Acid (C18:3)	Arachidic Acid (C20:0)
Vegetable oils	Corn	-	-	-	1%	10%	3%	19-50%	34-62%	trace	-
	Soybean	-	-	-	trace	9-12%	3-5%	23-26%	49-53%	5-11%	-
	Sunflower	-	-	-	-	6%	1-4%	20-33%	55-66%	trace	2-5%
	Palm	-	-	-	-	41%	6%	43%	7%	-	-
	Copra	10%	8%	50%	16%	7%	2%	5%	1%	-	-
	Cocoa butter	-	-	-	trace	26-30%	30-34%	32-34%	1-5%	-	-
	Jatropha	-	-	-	-	11-16%	6-8%	30-48%	30-37%	-	-
	Cotton	-	-	-	-	27%	3%	17%	48%	-	-
	Olive	-	-	-	trace	7%	2%	84%	5%	-	-
Natural fats	Pork lard	-	-	-	1%	24%	9%	47%	10%	-	-
	Beef tallow	-	-	-	6%	27%	14%	49%	-	-	-

In this way, capric acid (CA, $C_{10}H_{20}O_2$ purity > 98%), lauric acid (LA, $C_{12}H_{24}O_2$, purity > 99%), myristic acid (MA, $C_{14}H_{28}O_2$, purity > 99%), palmitic acid (PA, $C_{16}H_{32}O_2$, purity > 98%) and stearic acid (SA, $C_{18}H_{36}O_2$, purity > 97%), were purchased from Merck and their thermal properties were analyzed. Phase change temperature and latent heat were measured by means of differential scanning calorimetry (DSC) (TA Instruments Q200 DSC) at a heating/cooling rate of 5 °C/min, using a N_2 atmosphere, flowing at 50 mL/min. Values reported were obtained after 2 heating/cooling cycles. The uncertainties of this DSC system are typically 1.16 J/g for latent heat and ±0.29 °C for the maximum peak of the phase change temperature. As well, the temperature of degradation of these pure fatty acids was determined by means of thermogravimetry analysis (TGA) (TGA 2950 Hi-Re, TA Instruments) from room temperature up to 330 °C with a heating rate of 10 °C min^{-1}.

Heat flows of pure fatty acids, CA, LA, MA, PA and SA during melting/cooling cycle are shown in the DSC curves in **Fig. 25**. From these curves can be observed that the phase change transitions for the selected fatty acids occurred from moderate to low temperatures, i.e. <100 °C.

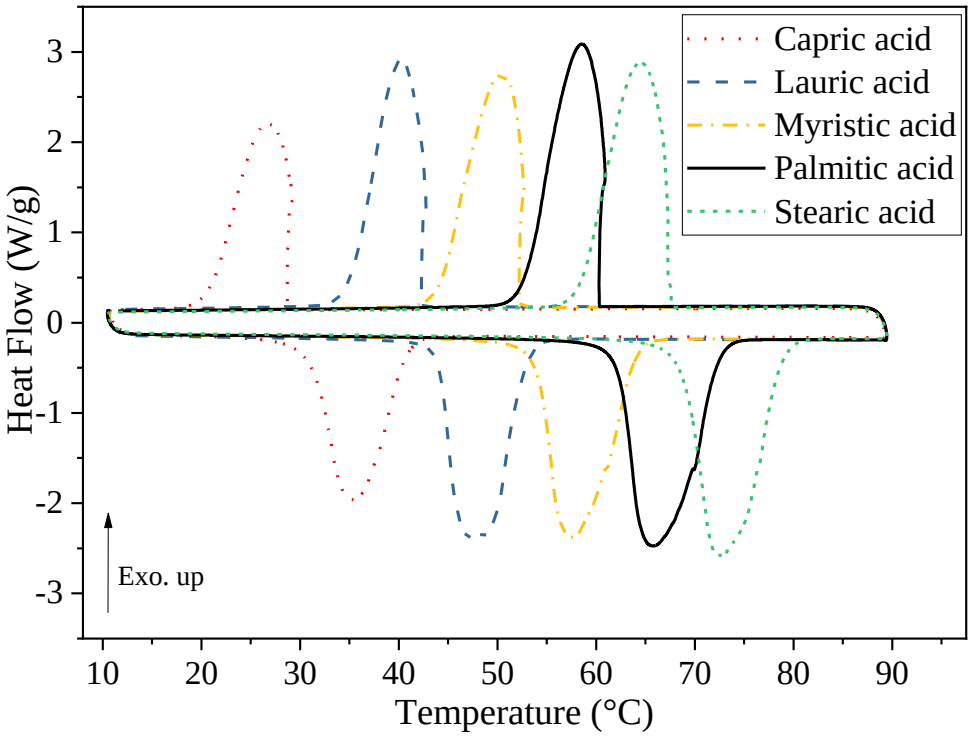

Fig. 25. DSC curves for capric, lauric, myristic, palmitic and stearic acid.

The corresponding data of the onset melting temperature ($T_{m,\ onset}$), maximum melting peak temperature ($T_{m,\ peak}$), latent heat of fusion (ΔH_m), onset solidification temperature ($T_{s,\ onset}$), maximum solidification peak temperature ($T_{s,\ peak}$), latent heat of solidification (ΔH_s) are presented in **Table 14**. As expected, as the chain length of the fatty acid increases, the phase change temperature, and latent heat, increases. Being the CA the one with the lowest melting temperature and latent heat (31.22°C, 147 kJ/kg) and SA the one with the highest (68.81 °C, 209 kJ/kg). As can be noticed in the curves (**Fig. 25**) and in the tabulated data (**Table 14**), there is a difference between the phase change temperatures of melting and solidification, in particular for these kind of materials, this is due to a kinetic phenomenon as the solidification process depends on factors such purity of the sample and nucleation rates due to large molecular weights. The obtained results confirm previous evidence found in literature **[42,43]**.

Table 14. Thermal properties of pure fatty acids.

Sample	Melting			Solidification		
	$T_{m,\ onset}$ (°C)	$T_{m,\ peak}$ (°C)	ΔH_m (kJ/kg)	$T_{s,\ onset}$ (°C)	$T_{s,\ peak}$ (°C)	ΔH_s (kJ/kg)
CA	31.22	35.37	147.0	28.73	26.75	148.5
LA	44.03	47.57	177.2	42.72	40.24	180.2
MA	54.06	57.50	187.3	52.74	50.33	186.8
PA	62.30	65.76	199.9	60.93	58.54	201.7
SA	68.81	75.53	209.1	67.30	64.53	211.7

Besides analyzing the thermal properties, it is important to study thermal degradation of the fatty acids. Through TGA technique is possible to obtain curves as shown in **Fig. 26**. It can be observed that the chain length is directly proportional to the temperature at which the fatty acids were decomposed. Thus, the temperature of initial degradation, defined in this thesis as the temperature where the fatty acid losses 0.01 %/°C, increases with the chain length.

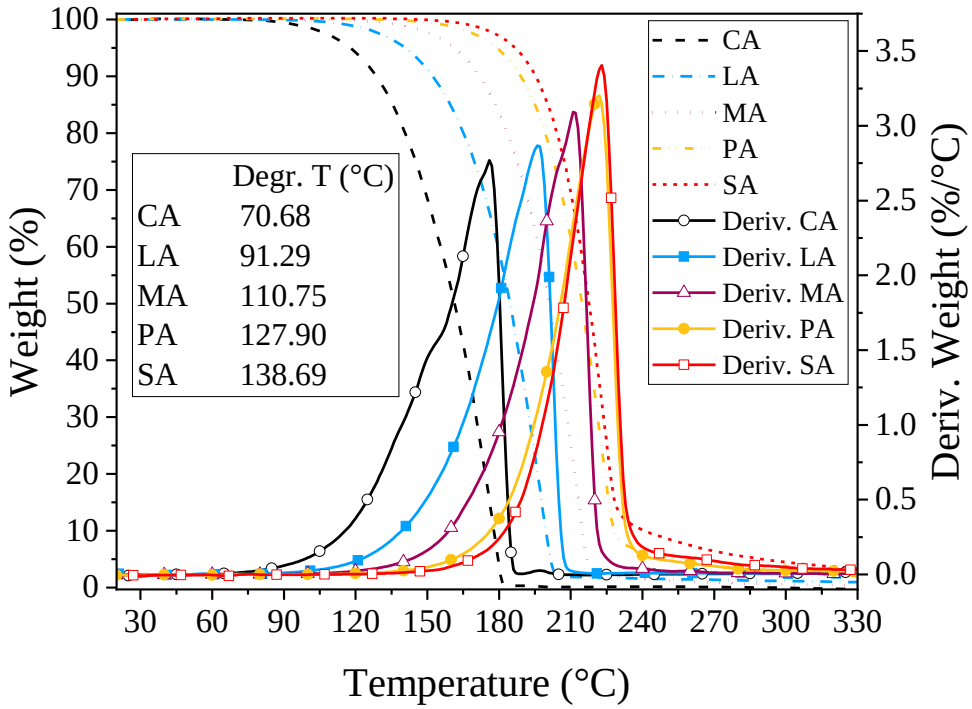

Fig. 26. Thermogravimetric analysis of pure fatty acids (CA, LA, MA, PA, SA) and their degradation temperatures (Degr. T).

In practice this means that degradation temperature cannot be exceed in order to keep the thermal properties of the selected PCMs. Degradation temperatures obtained were 70.68 °C, 91.29 °C, 110.75 °C, 127.90 °C and 138.69 for CA, LA, MA, PA and SA, respectively.

The results obtained of phase change temperatures, latent heat and thermal degradation of capric, lauric, myristic, palmitic and stearic acid corroborate that these PCMs can be used for low to moderate temperature applications in thermal energy storage systems, as stated widely by other authors in literature. However, phase change temperatures are still higher for some applications and thus eutectic mixtures are proposed as an approach to produce at least three PCMs with temperatures between 20 °C and 54 °C, looking for a wide temperature range for multipurpose applications.

2.2. Fatty acid eutectic mixtures

After analyzing five pure fatty acids, capric-myristic (CA/MA), lauric-myristic (LA/MA) and palmitic-stearic (PA/SA) binary eutectic mixtures were chosen due to their wide range of temperatures that could work for different applications, for instance, CA/MA could be used for passive cooling in buildings, LA/MA for food industry and low temperature solar heating, and PA/SA for domestic water heating. To the extent of our knowledge, there is a lack of complete experimental data of these materials in literature. In this section the preparation, phase diagrams, phase change temperatures, latent heats, specific heat capacities and thermal degradation of CA/MA, LA/MA and PA/SA is presented. Moreover, thermal conductivity and thermal reliability (thermal cycling) of the eutectics were measured as well and are presented in Chapter V.

To determine the eutectic composition of each mixture a prediction method was used based on theoretical calculation and plot of its phase diagram. The Schröder equation **Eq. (7)** was used to calculate the phase change temperature **[128,174,175]** as follows:

$$T_m = \left[\frac{1}{T_i} - \frac{RlnX_i}{H_i}\right]^{-1} \quad (i = A, B) \qquad \textbf{(7)}$$

Where A, B are the phase change material A and phase change material B; T_m is the melting temperature of the mixture A:B, [K]; T_i is the melting temperature of the ith component, [K]; X_i is the mole fraction of the ith component, H_i is the latent heat of the ith component, [J/mol] and R the gas constant, 8.315 J/mol·K. By means of the above equation, the phase diagram of binary eutectic can be drawn, and corresponding eutectic points can be determined. Thus, the solid–liquid equilibrium of CA/MA, LA/MA and PA/SA calculated according to **Eq. (7)**

showed a simple eutectic phase diagrams, as seen in **Fig. 27**. The eutectic composition found for CA/MA, LA/MA and PA/SA was 73.20% (w/w) CA and 26.80% (w/w) MA, 60.50% (w/w) LA and 39.50% (w/w) MA and 58.58% (w/w) PA and 41.42% (w/w) SA, respectively.

Latent heat of fusion of the eutectics can be estimated as well by **Eq. (8)** when the molecular weight of every component is big enough, **[176]**.

$$H_m = \sum_{i=1}^{n} \left(\frac{X_i H_i}{T_i}\right) \qquad \textbf{(8)}$$

$$(i = A, B)$$

Where H_m is the latent heat of the mixture A:B, [J/mol] and H_i is the latent heat of the i[th] component, [J/mol]. Thus, the theoretical melting temperature and latent heat of fusion were 24.30 °C, 33.43 °C and 53.41 °C, and 143.78 kJ/kg, 167.83 kJ/kg and 190.96 kJ/kg, for CA/MA, LA/MA and PA/SA, respectively. These values increased with the increased of the chain length of the binary fatty acid mixtures.

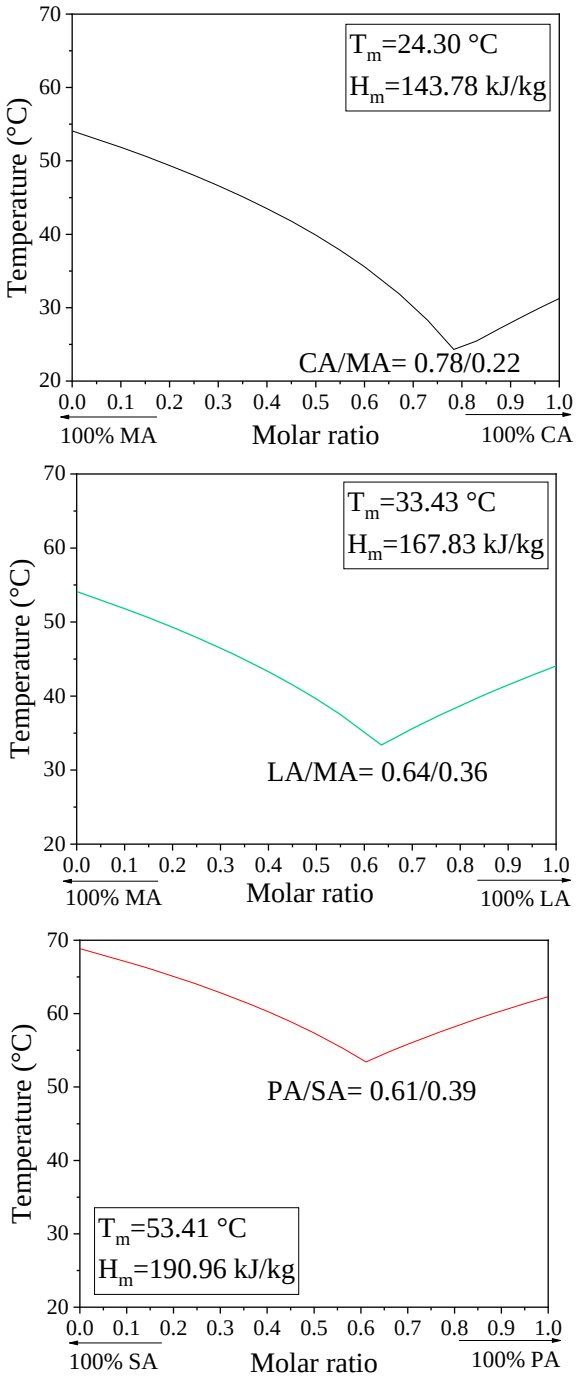

Fig. 27. Calculated phase diagrams, latent heat and phase change temperature of CA/MA, LA/MA and PA/SA.

After calculations, CA/MA, LA/MA and PA/SA eutectics were prepared experimentally in the laboratory by melting the pure fatty acids in a thermostatic bath, using the mixing proportions mentioned above. The thermostatic bath was put at 60 °C to obtain CA/MA and LA/MA, and at 70 °C for PA/SA. The phase change temperatures and latent heats of the binary eutectic mixtures formed were measured through Modulated Temperature DSC (MDSC) using the same DSC instrument described in the pure fatty acids section. Samples were measured in a N_2 atmosphere (50 mL/min), with a heating rate of 1°C/min, a modulation period of 100 seconds, and a modulation amplitude of ±0.5 °C.

Results for phase change temperatures and enthalpies of the eutectics are shown in **Table 15**. The melting temperatures obtained were 24.49 °C, 35.53 °C and 56.92 °C, for CA/MA, LA/MA and PA/SA, respectively. In **Fig. 28**, the calorimetry curves are shown. As can be observed each eutectic presented just one peak for melting and one peak for solidification, indicating that the mixing proportions of pure fatty acids were adequate in order to obtain eutectics.

Table 15. Thermal properties of CA/MA, LA/MA and PA/SA.

Sample	Melting			Solidification		
	$T_{m,onset}$ (°C)	$T_{m,\,peak}$ (°C)	ΔH_m (kJ/kg)	$T_{s,\,onset}$ (°C)	$T_{s,\,peak}$ (°C)	ΔH_s (kJ/kg)
CA/MA	21.88	24.49	139.8	21.35	19.82	143.4
LA/MA	33.81	35.53	149.7	33.37	32.85	178.6
PA/SA	54.24	56.92	183.0	55.18	53.90	200.3

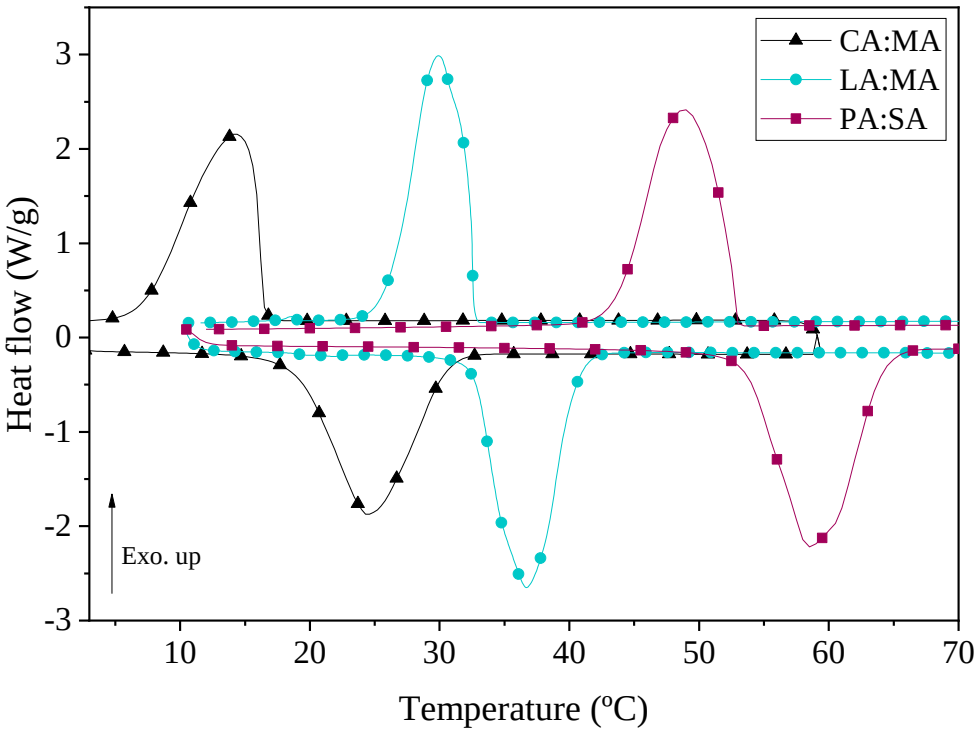

Fig. 28. DSC curves for CA/MA, LA/MA and PA/SA.

Difference between theoretical and experimental values of T_m and ΔH_m were below 6.2%. A survey in literature presented in **Table 16** showed the differences in the thermal properties for CA/MA, LA/MA and PA/SA calculated and measured by different authors. It can be noticed that there is no complete agreement in the values, this is likely due to the choice of T_m values of the pure fatty acids ($T_{m,onset}$, $T_{m,peak}$ or values from the datasheet of the producer) to perform the calculations leading to different molar ratios for the eutectic point. Besides, the measurements from the different research groups were made at different heating rates, atmospheres, equipment and are associated with different experimental errors, in addition to the impurity of the fatty acids used. Even though, the calculation of melting temperature and enthalpy of fusion by means of **Eq. (7)** and **Eq. (8)** were good approximations to the values obtained through DSC analysis with a deviation less than 10%.

Table 16. Literature values for thermal properties of CA/MA, LA/MA and PA/SA.

Eutectic	Composition (wt.%)	Molar ratio	T_m (°C) (Th*)	T_m (°C) (Exp*)	H_m (kJ/kg) (Th*)	H_m (kJ/kg) (Exp*)	Heating rate (K/min)	Gas	Flow rate (mL/min)	DSC Instrument	Ref.
CA/MA	80.0/20.0	-	-	24.06	-	131.09	2	N_2	20	4000 PerkinElmer	**[177]**
	-	0.79:0.21	25.00	-	156.91	-	-	-	-	-	**[178]**
	78.0/22.0	0.82:0.18	-	20.50	-	153.00	2	He	25	TA Instruments Q200	**[179]**
	73.2/26.8	0.78:0.22	24.30	24.49	143.78	139.8	1	N_2	50	TA Instruments Q200 (MDSC)	This study
LA/MA	-	0.66:0.34	33.40	33.62	166.80	164.50	-	-	-	-	**[180]**
	62.4/37.6	-	32.37	32.85	-	-	2-5	N_2	static	Mettler Toledo STAR[e]	**[181]**
	66.0/34.0	-	-	34.20	-	166.8	5	N_2	-	DuPont 2000	**[182]**
	-	0.66:0.35	34.00	-	183.21	-	-	-	-	-	**[178]**
	60.5/39.5	0.64:0.36	33.43	35.53	167.83	149.7	1	N_2	50	TA Instruments Q200 (MDSC)	This study
PA/SA	64.2/35.8	-	53.20	-	-	-	5	N_2	-	204 Netzsch	**[123]**
	64.2/35.8	-	-	52.30	-	181.7	5	N_2	-	DuPont 2000	**[183]**
	-	0.62:0.38	53.00	-	208.70	-	-	-	-	-	**[178]**
	58.6/41.4	0.61:0.39	53.41	56.92	190.96	183	1	N_2	50	TA Instruments Q200 (MDSC)	This study

*Th=theoretical, Exp=Experimental

In addition to calorimetry analysis, thermogravimetric analyses (TGA) were performed to determine the temperature of degradation of the eutectic binary mixtures, the TGA equipment used was the same described before for the pure fatty acids. In **Fig. 29** can be observed that the degradation temperatures found were 94.00 °C, 110.68 °C and 156.96 °C for CA/MA, LA/MA and PA/SA, respectively. The same trend as for pure fatty acids can be seen for the binary eutectics, as longer the chain length of the acids, higher the degradation temperature. Degradation temperatures should be taken as performance limits for the different applications that involves these binary eutectic mixtures.

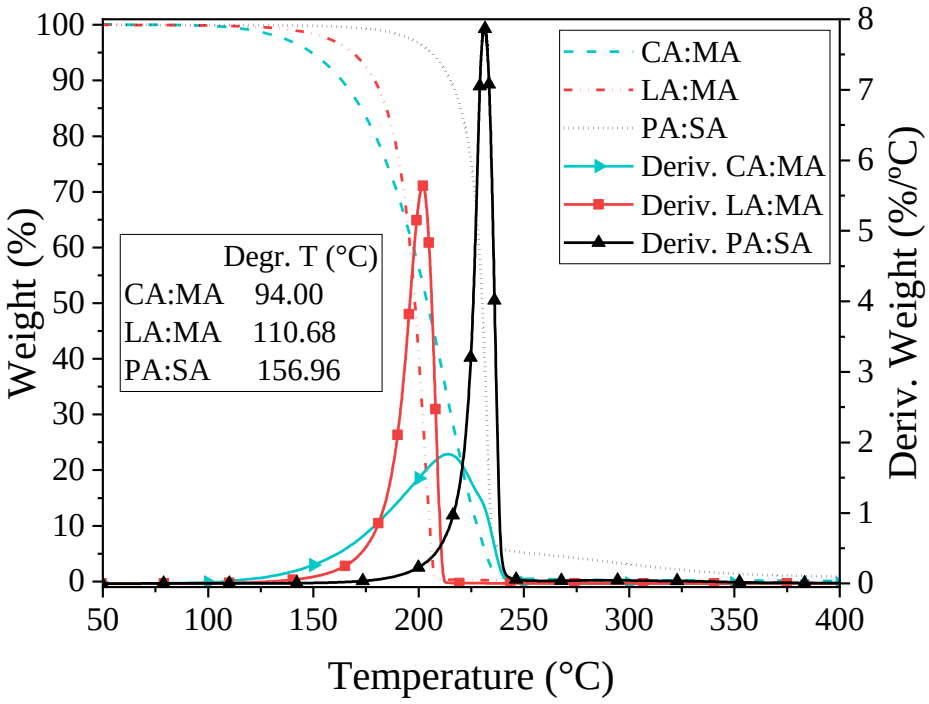

Fig. 29. Thermogravimetric analysis for the eutectics CA/MA, LA/MA and PA/SA.

One novelty of this research is regarding to specific heat capacity, C_p. This is an important, and not always measured **[184]**, thermal property useful for the selection of the PCMs for diverse applications and to perform many chemical engineering calculations. Experimental data for C_p reported in literature include pure fatty acids **[185]** and prediction models for organic PCMs based in group contribution methods **[186–189]**. Ceriani et al. **[188]** performed a survey about experimental heat capacities found in literature to develop a simple contribution method, but the data was limited to liquid phases. Nazir et al. **[43]** focused their

attention in the experimental study of eutectic mixtures based in LA, MA, SA, PA and PT68, but his study did not include CA/MA, LA/MA and PA/SA mixtures. Thus, there is a lack of information about experimental and theoretical calculations of C_p for binary fatty acid mixtures.

As well, in literature, the most common technique to determine heat capacity, C_p, is through conventional differential scanning calorimetry (DSC), either following standards **[187,190,191]** or by methodologies proposed by some authors **[192,193]**. However, with modulated temperature DSC (MDSC or MTDSC) **[194–197]** it is possible to improve the resolution and sensitivity of the measurement, to obtained the individual heat flow components separately to analyze complex transitions, and to performed direct measurement of C_p. Hence, through MDSC, the binary eutectic mixtures produced were characterized and the results obtained are shown below.

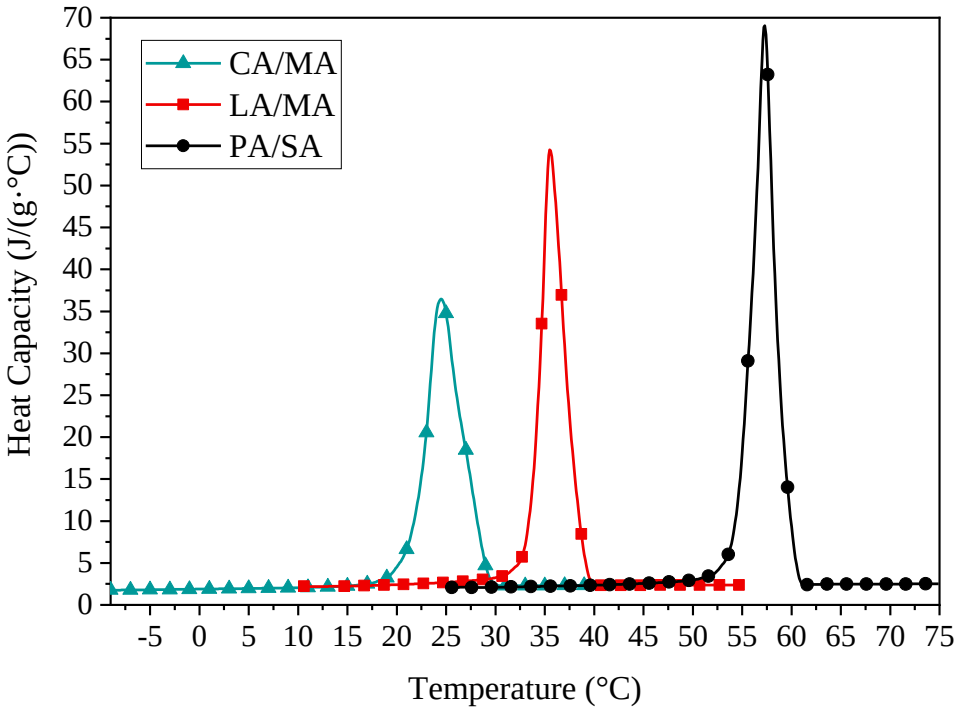

Fig. 30. Heat capacity for CA/MA, LA/MA and PA/SA.

As can be noticed in **Fig. 30** specific heat capacities as a function of temperature of CA/MA, LA/MA and PA/SA eutectic mixture presented large peaks. The value of C_p can be significantly increased during phase transition because the extra energy is required to transit

a low temperature structure to a high temperature structure in materials during phase change transition **[198]**, creating an apparent high value for C_p, as shown in the curves. Thus, the three binary eutectic mixtures presented clear peaks in the temperature region attributable to the respective phase change transition **[199,200]**. From the solid and liquid regions, i.e. before and after the phase change transition.

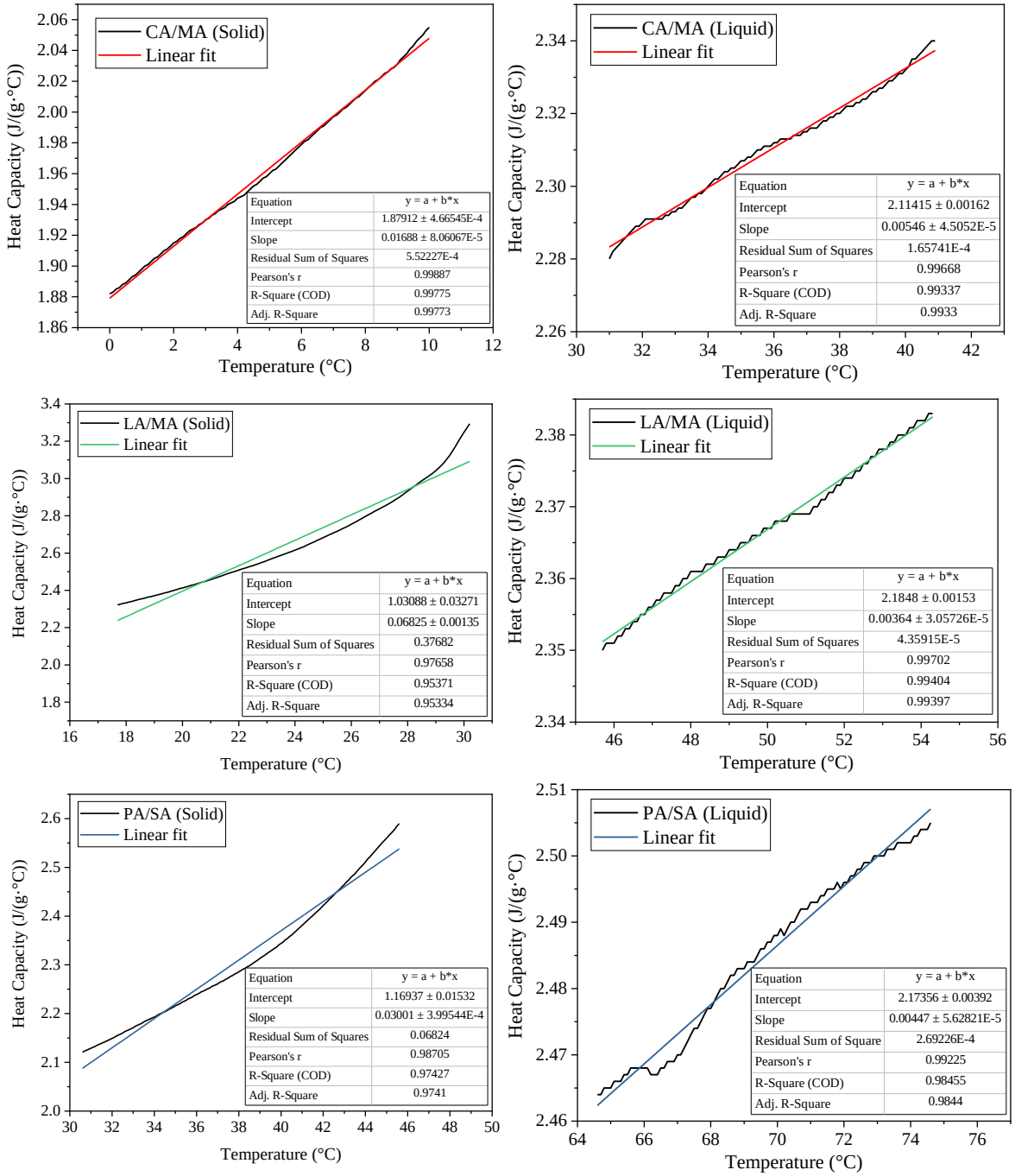

Fig. 31. Heat capacity in the solid and liquid regions for CA/MA, LA/MA and PA/SA.

The temperature dependence of C_p was modeled trough semi-empirical fitting of experimental data. The equations obtained are presented in the insets in **Fig. 31**. All the adjusted equations correspond to linear equations with R-squared greater than 0.95, indicating good agreement in the fitting. From the equation values can be noticed that changes in C_p with temperature are small and, according to Persons's r coefficient, there is a positive correlation between C_p and temperature. Assuming that C_p changes are small, the binary eutectics presented average values in the solid phase of 1.97 J/g·°C, 2.54 J/g·°C and 2.40 J/g·°C and in the liquid phase of 2.31 J/g·°C, 2.40 J/g·°C and 2.50 J/g·°C, for CA:MA, LA:MA and PA:SA, respectively.

The empirical equations obtained are useful to improve the design of thermal energy storage (TES) systems and to develop better simulations, as many authors just work with general theoretical equations, that in most of the cases are not particularly useful for PCMs.

2.3. Morphology of the eutectics CA/MA, LA/MA and PA/SA.

The microstructure of the obtained eutectics was explored through scanning electron microscopy, using a JEOL JSM-6490LV with an accelerating voltage of 20 kV. This analysis technique was performed as an initial exploration of the morphological information of the eutectic mixtures as there was not found in the literature and can serve as a guide for subsequent analysis of other samples as the SS-PCMs. The SEM images are shown below.

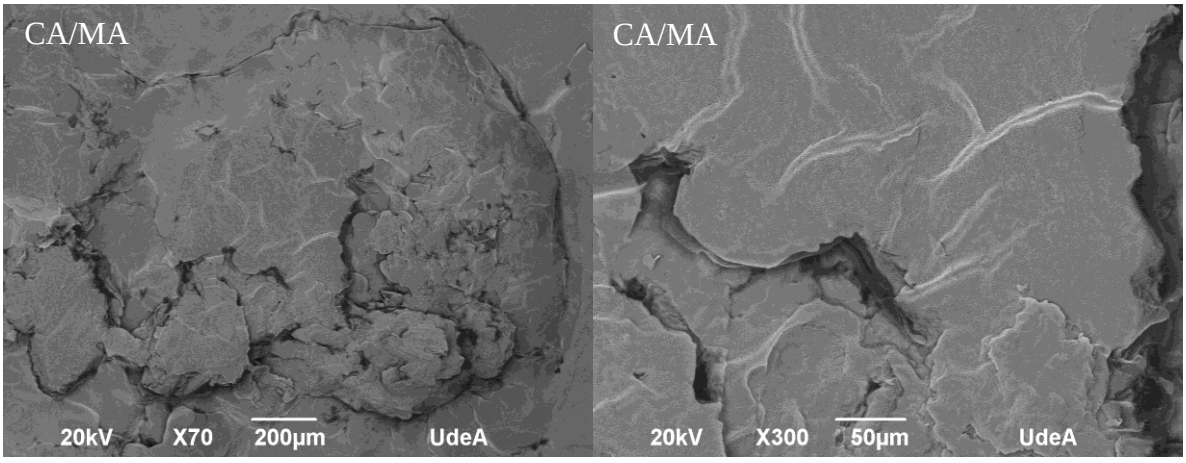

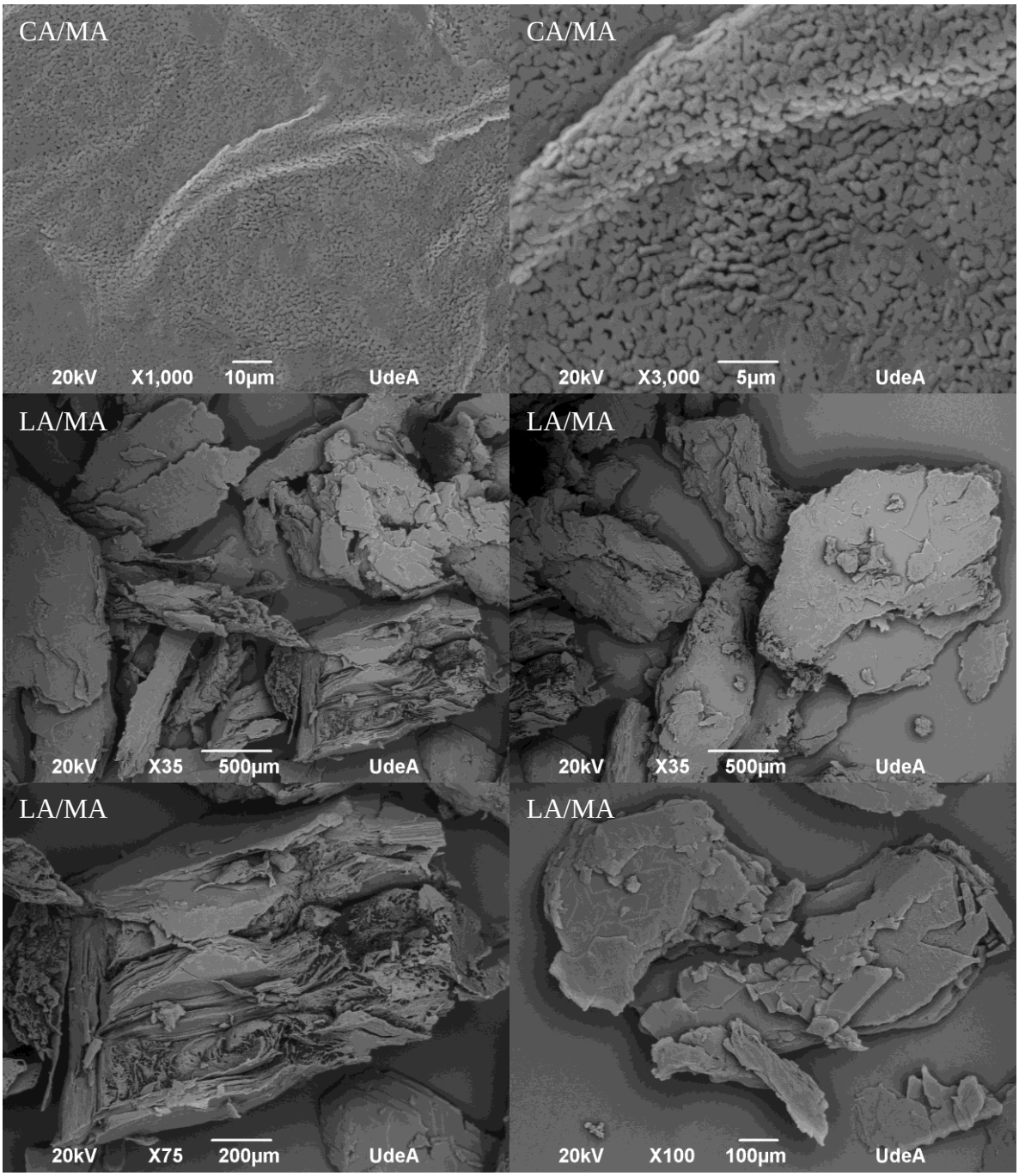
CA/MA
20kV X1,000 10µm UdeA
CA/MA
20kV X3,000 5µm UdeA
LA/MA
20kV X35 500µm UdeA
LA/MA
20kV X35 500µm UdeA
LA/MA
20kV X75 200µm UdeA
LA/MA
20kV X100 100µm UdeA

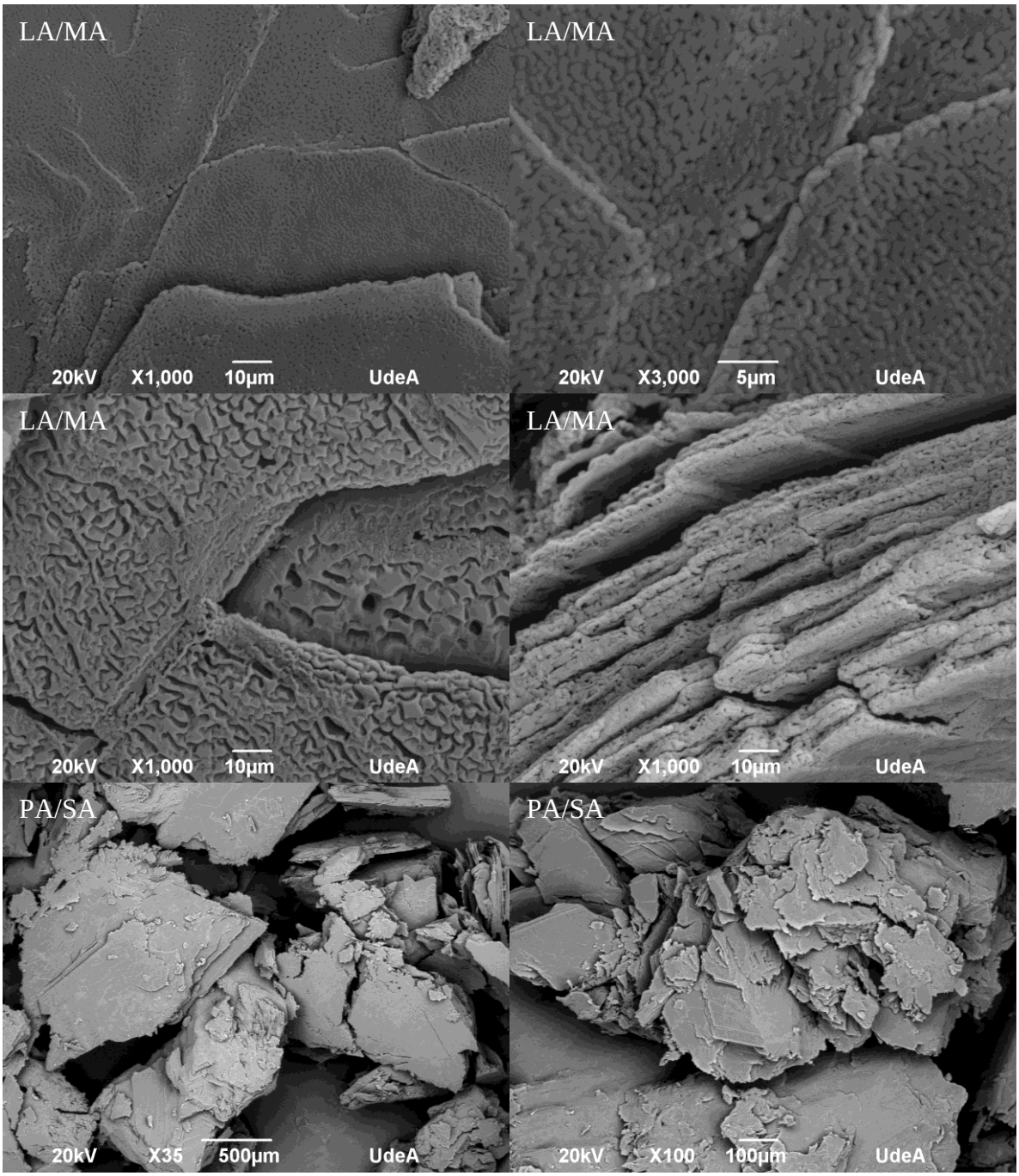
LA/MA
20kV X1,000 10µm UdeA
LA/MA
20kV X3,000 5µm UdeA
LA/MA
20kV X1,000 10µm UdeA
LA/MA
20kV X1,000 10µm UdeA
PA/SA
20kV X35 500µm UdeA
PA/SA
20kV X100 100µm UdeA

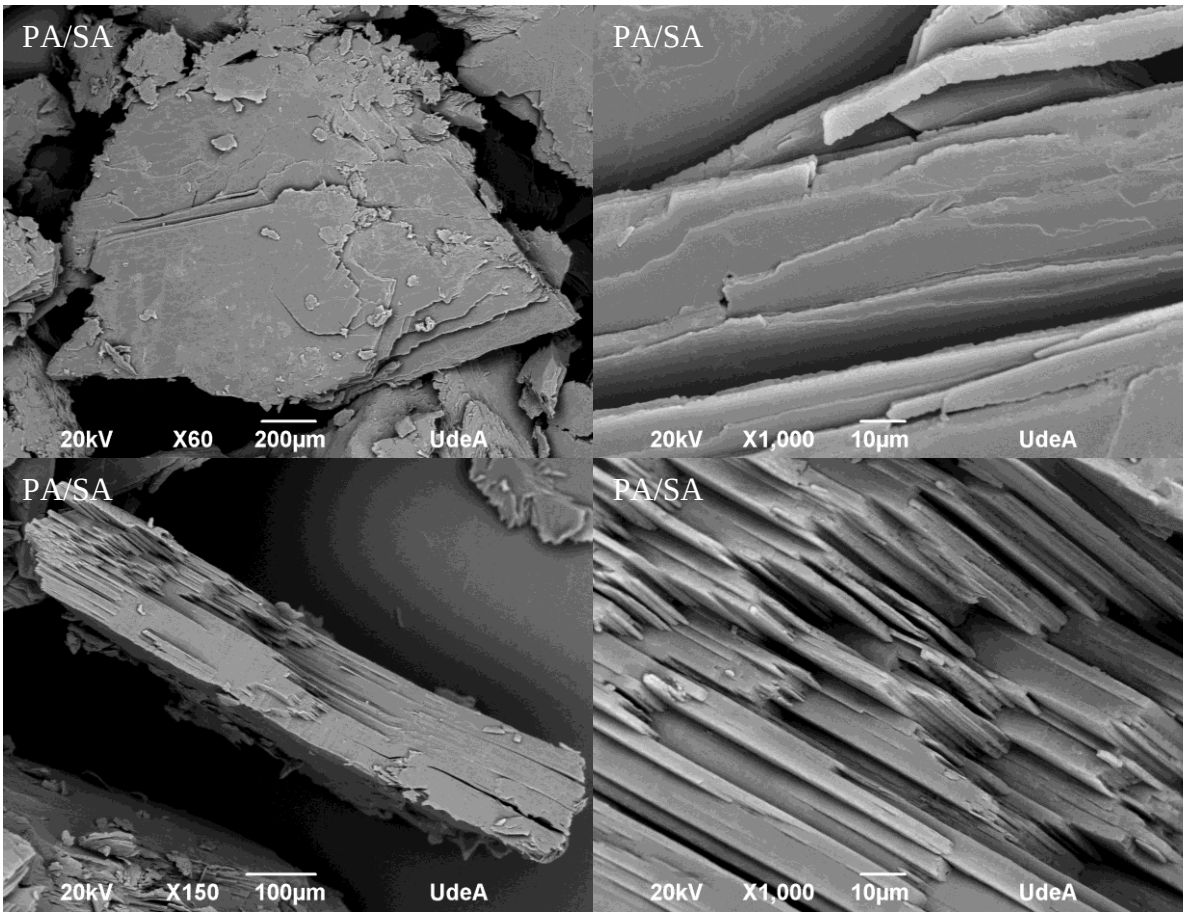

Fig. 32. SEM images of CA/MA, LA/MA and PA/SA.

It could be seen that the eutectics CA/MA, LA/MA and PA/SA presented a sheet-like morphology, indicating that the solidification process of these fatty acids occurs layer by layer. One difference can be noticed in the SEM images under 1000X between PA/SA and the other eutectics. The CA/MA and LA/MA eutectics showed a microstructure composed of a sort of grain pattern and voids. Probably this is due to their relative low melting temperature which made that the electron beam heat the samples during the SEM image acquisition and began to melt them more easily than for PA/SA.

2.4. Conclusions

This section is an attempt to examine and wider the knowledge of organic PCMs as fatty acids, particularly of capric, lauric, myristic, palmitic and stearic acid as they are sustainable (come from renewable sources), available and their phase change temperatures are suitable for low to moderate thermal energy storage systems. However, phase change temperatures

are still higher for some applications and thus eutectic mixtures are proposed as an approach to produce at least three PCMs with temperatures between 20 °C and 54 °C, looking for a wide temperature range for multipurpose applications. The eutectic mixtures accomplished were CA/MA (capric/myristic), LA/MA (lauric/myristic), and PA/SA (palmitic/myristic), with melting phase change temperatures of 21.88 °C, 33.81 °C and 54.24 °C, respectively. For instance, CA/MA could be used for passive cooling in buildings, LA/MA for food industry and low temperature solar heating, and PA/SA for domestic water heating.

The results showed in this section add to a growing body of literature on thermal properties that are poorly described for the binary eutectic mixtures CA/MA, LA/MA, and PA/SA. Thermal properties included melting and solidification enthalpies, phase change temperatures, thermal degradation and specific heat capacity as a function of temperature for both solid and liquid phases. The microstructure of the eutectics was studied and found to be a sheet-like morphology. Moreover, thermal conductivity and thermal reliability were measured as well, and will be presented in the following sections.

CHAPTER III.

Selecting a support for shape-stabilization of PCMs

The containment of PCMs in porous materials, known as shape-stabilization **[184]**, is a reported technique in literature that take advantage of the porosity of several materials to produce shape-stabilized PCMs (SS-PCMs) composites with low leakage and good thermal behavior. Within these materials can be found porous clay minerals **[201]** such diatomite **[78]**, sepiolite **[115]**, kaolinite **[132]**, bentonite **[130]**, besides others. Porous clay minerals can be good supports for SS-PCMs as present a cost-effective production process, are found in nature and depending on the composition, can increase thermal conductivity of the system.

However, most studies have only focused on purified minerals, that present just one mineralogical phase, and there are just a few of them. For instance, there are some papers about diatomite **[121,123,125,128]**, expanded vermiculite and perlite **[76,116]**, kaolin **[113,132,133,135]**, bentonite, pumice **[131]**, and sepiolite **[115]**. With this on mind, this section proposes the study of a Colombian clay mineral composed by several mineralogical phases, as a new and promising support for shape-stabilization of organic PCMs. To the best of our knowledge, no PCM shape stabilization has been carried out in literature with a mineral mixture as the one proposed in this work. The clay mineral contained mainly diatomite, kaolin, illite and quartz, being the former well recognized for its uses as catalyst, filters and sorbents **[127]** as it possesses unique properties as highly porous structure, excellent absorption capacity and thermal stability.

3.1. Physicochemical methods for characterization of the support

The clay mineral was characterized through different techniques in order to quantify the crystalline and non-crystalline phases that coexist in the sample. The raw sample supplied and industrially processed by Sumicol S.A.S (Colombia), is shown in **Fig. 33**, before and

after grinding. The final material used in this work was in powder form with a Dv50 value of 10.60 µm.

Fig. 33. Clay mineral before (left) and after (right) a grinding process.

The chemical composition of the raw mineral was determined by an X-ray fluorescence spectrometer (XRF) (AxiosmAX Minerals, Panalytical).

For the identification of the mineralogical phases of the support several techniques were used. First, the grinded mineral was calcined in a laboratory box furnace (Naber D-2804) at three different temperatures 600 °C, 900 °C and 1100 °C to observe its mineralogical phase evolution. Each sample was calcined independently with a heating rate of 10 °C/min and holding time of 1.0 h for each temperature. These temperatures were chosen after the SiO_2 phase transition temperatures according to its phase diagram (**Fig. 34**). After thermal treatments, the samples were naturally cooled to room temperature.

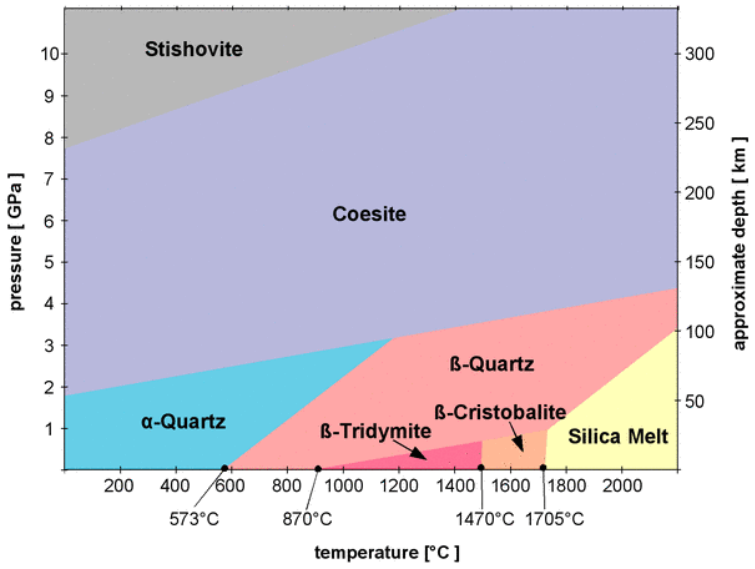

Fig. 34. Phase diagram of silica **[202]**.

X-ray diffraction (XRD) (Panalytical 2012) measurements were carried out to determine the phase composition and crystallinity of the raw and calcined samples (600 °C, 900 °C and 1100 °C). The patterns were collected at 40 kV and 40 mA by means of a solid-state detector (Pixcel 3D) using a monochromatic Co-Kα radiation (λ=1.79 Å). Cobalt radiation was chosen instead of copper radiation to avoid misinterpretation due to fluorescence **[203]**. The data were collected over a range of 2.5° to 70.0° 2θ with a step of 0.026 °/s. The XRD measurements were performed in a Bragg-Brentano geometry. Identification and quantification of the phases present in the samples were carried out using the Rietveld refinement method in the PANalytical X'Pert High Score V.3.0 software in conjunction with the Inorganic Crystal Structure Database (ICSD). Moreover, to quantify the amorphous phases in the sample, 20%wt of a rutile standard was added to the sample.

Surface morphology and microstructure of samples were observed using a scanning electron microscope (SEM) (JEOL JSM-6490LV), with an accelerating voltage of 20 kV, and a Phentom Pro X desktop SEM with and accelerating voltage of 15 kV. Additionally, an electron transmission microscope (TEM) (Tecnai G2-F20, FEI), and high-resolution electron transmission microscope (HRTEM) were used. The TEM was operated at 200 keV.

Thermogravimetry analysis (TGA) (TGA 2950 Hi-Re, TA Instruments) was carried out for all mineral samples from room temperature up to 900°C with a heating rate of 10 °C/min.

Finally, some standard minerals were studied, under the same conditions as for the raw support, by means of XRF, TGA and SEM. Besides measurements of particle size, porosity, thermal conductivity, heat capacity and heat flow were performed. Particle size distribution was measured by a laser particle analyzer Mastersizer 3000, Malvern. As well, textural properties (pore volume, pore width, surface area) and porosity of the samples were assessed by N_2 adsorption-desorption isotherms, using the Brunauer-Emmet-Teller (BET) theory and the average pore diameters and pore volume were evaluated using the Barrett-Joyner-Halenda (BJH) model, through a Micromeritics Instrument, Gemini V2380. Thermal conductivity was measured by means of the transient hot wire technique. The equipment used was the KD2 Pro Thermal Properties Analyzer (Decagon devices) with the sensors KS-1. As a qualitative quality indicator, given by the equipment, a dimensionless measure of the goodness of fit of the model to the data is taken as the error. Thus, only results with less than 0.001 of error were analyzed. Furthermore, thermal conductivity was measured as a function of temperature and for each temperature 5 to 6 measurements were performed. Heat flow was measured by differential scanning calorimetry (DSC) (TA Instruments Q200 DSC) at a rate of heating and cooling of 5 °C/min, in a N_2 atmosphere, flowing at 50 mL/min, after 2 heat-cooling cycles. The uncertainties of this DSC system are typically 1.16 J/g for latent heat and ±0.29 °C for the maximum peak of the phase change temperature. Heat capacity was measured with the same equipment but in the modulated mode, using a N_2 atmosphere (50 mL/min), with a heating rate of 1°C/min, a modulation period of 100 seconds, and a modulation amplitude of ±0.5 °C.

3.2. Chemical composition of the support

The chemical composition of the mineral support, calculated as oxides, is presented in **Table 17**. The analysis reveals a great amount of silica (65.94%), followed by alumina (17.20%) and iron oxide (5.53%). Other minor oxides (<2%) are presented as well like potassium oxide, titania and magnesium oxide.

Table 17. Chemical composition of the raw mineral sample by XRF.

Component	SiO_2	Al_2O_3	Fe_2O_3	TiO_2	CaO	MgO	Na_2O	K_2O	BaO	P_2O_5	SO_3	LOI*
Content (wt. %)	65.94	17.20	5.53	0.52	0.20	0.45	0.08	1.60	0.08	0.15	0.15	8.10

*(110-1000°C)

As expected, the clay support presented an alumino-silicate mineral composition, with 8.10% loss-of-ignition (LOI) due to adsorbed and absorbed water. The relatively high amount of iron oxide corroborates the reddish color of the clay seen by inspection (**Fig. 33**).

3.3. Crystalline and amorphous phases present in the support

After thermal treatments at 600 °C, 900 °C and 1100 °C, x-ray diffraction was performed. XRD patterns (**Fig. 35**) showed that the raw mineral has a clayey nature as it contained illite ($(K,H_3O)(Al,Mg,Fe)_2(Si,Al)_4O_{10}[(OH)_2,(H_2O)]$), I, kaolinite ($Al_2Si_2O_5(OH)_4$), K, and quartz ($SiO_2$), Q. Moreover, the XRD pattern of the raw sample revealed some amorphous phase.

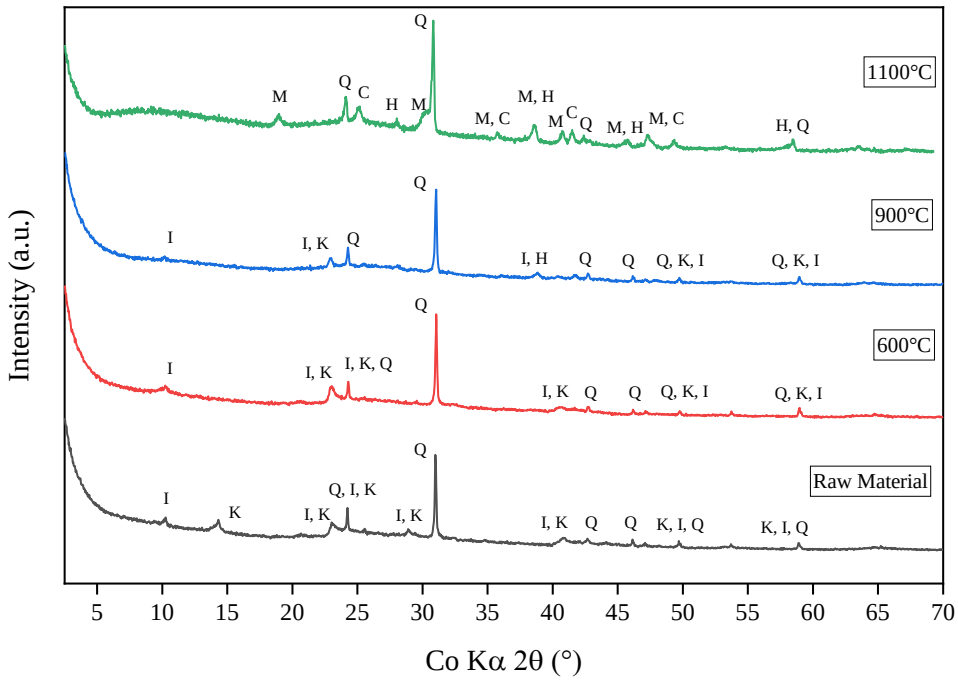

Fig. 35. XRD patterns showing the mineralogical phase evolution of the sample after thermal treatments at 600 °C, 900 °C and 1100 °C. The characters stand for: I-Illite, K-Kaolinite, Q-Quartz, H-Hematite, and M-Mullite.

The quantitative analysis of the crystalline and amorphous phases was subsequently performed by the Rietveld method for the raw sample and for the samples after thermal treatments at 600 °C, 900 °C and 1100 °C. The calculated patterns resulting from the Rietveld fitting procedure closely match with the measured patterns, as it can be seen in

Table 18, with the weighted R profile (R_{wp}) values less than 10% and the goodness of fit (GOF) less than 4, showing good agreements indices of acceptance **[204]**.

Table 18. Agreement indices for the Rietveld fitting procedure.

Sample	Weighted R Profile, R_{wp} (%)	Goodness of Fit, GOF
Raw Material	5.2895	1.7892
600°C	4.9091	1.3519
900°C	5.2784	1.3626
1100°C	5.1860	1.3146

The quantitative analysis of the XRD spectra is presented in **Table 19**. Here, it can be found that the raw sample contained 19.76% of kaolinite (K), 11.91% quartz (Q) and 10.76% of mica/illite (I). Thermogravimetric analysis corroborated the presence of kaolinite with a weight loss around 460°C (**Fig. 36**). The 1.09% of hematite (H) reported by the Rietveld analysis is lower than the 5.53% in the XRF analysis (**Table 17**), this is probably because there is an iron phase missing in the form of goethite, a hydrated phase of iron oxide that cannot be seen easily in the XRD. Decomposition of goethite can be identified more easily from the TGA analysis around 250°C (**Fig. 36**). In addition, a broad diffraction hump in the XRD pattern resulting from the amorphous phase of the raw sample is exhibited and quantified as 56.49%.

Table 19. Quantitative Rietveld analysis of the raw sample and sample after 600 °C, 900 °C and 1100 °C thermal treatments.

Mineralogical phase	Raw sample	Sample 600 °C	Sample 900 °C	Sample 1100 °C
Amorphous	56.49	75.52	77.46	55.97
Kaolinite (K)	19.76	8.94	3.40	0.00
Mullite (M)	0.00	0.00	0.00	23.83
Quartz (Q)	11.91	10.12	9.10	12.19
Cristobalite (C)	0.00	0.00	0.00	4.51
Mica/Illite (I)	10.76	5.42	7.75	0.00
Hematite (H)	1.09	0.01	2.29	3.51

The raw sample after the thermal treatment at 600 °C showed an increase of the amorphous phase of 19.03% and a decreased of kaolinite and mica/illite of 10.82% and 5.34%, respectively. Quartz remained almost the same and the hematite continues to be low, almost 0.00%. The rise of the amorphous phase can be explained by the formation of metakaolin and for the dihydroxylation of the illite. Metakaolin is a phase formed after the

dehydroxylation of kaolinite between 400°C and 600°C (**Fig. 36**). At this temperature some illite is still present, some authors have studied that the onset temperature for illite dihydroxylation is 525 °C in static air but these reactions depends on many factors such test conditions, particle size, structure of the species and even the Al/Si ratio or the vacant type **[205]**, so even at 600 °C it is possible to have illite without dehydroxylation. On the other hand, it is expected that goethite become hematite at 600 °C, but some studies probed that the dehydroxylation of the goethite, as well as for the illite, can be incomplete. Some residual OH groups remained even at 900-1000 °C preventing the formation of the crystalline structure of hematite **[206]**.

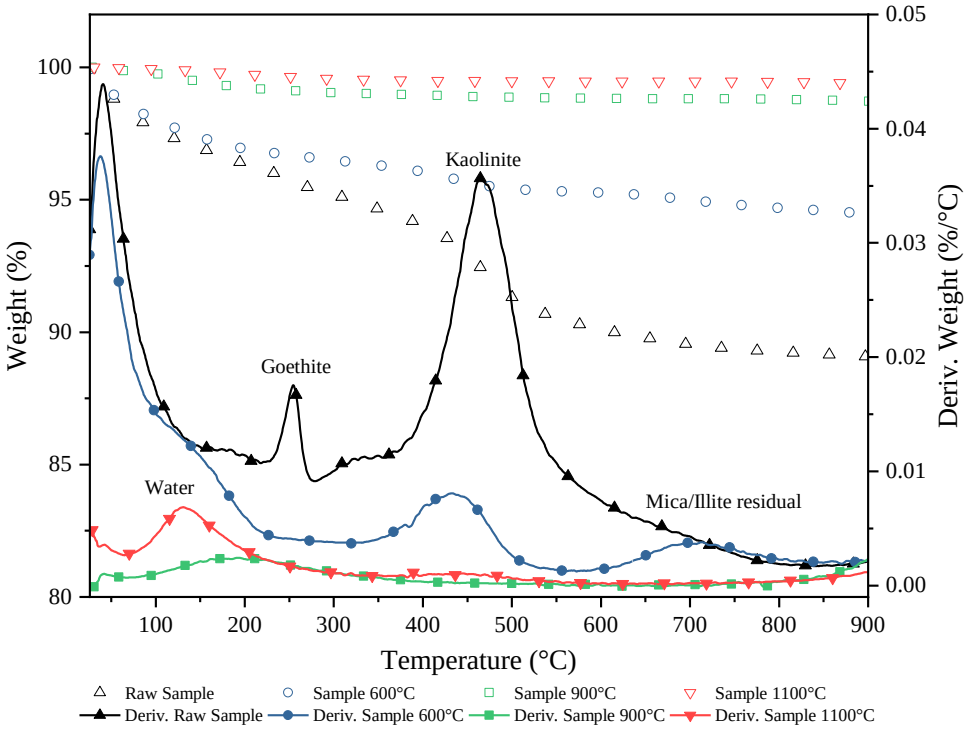

Fig. 36. Thermogravimetric analysis (TGA) curves of raw sample and samples calcined at 600 °C, 900 °C and 1100 °C.

At 900 °C, the sample was approximately as amorphous as sample at 600 °C. The kaolinite continued decreasing forming more metakaolin and 2.29% of hematite appears. At 1100 °C, the sample showed a decrease of the amorphous phase (55.97%), reaching almost the same amount found in the raw sample. At this temperature new crystalline phases appear such 23.83% of mullite, 12.19% of β-quartz (hexagonal), 4.51% of β-cristobalite (cubic) and the

hematite increases to 3.51%. The quartz present in the raw sample, the sample at 600 °C and that at 900 °C correspond to α-quartz (trigonal).

After chemical, mineralogical and thermogravimetric analyses, the structure of the samples was examined by electronic microscopy. SEM images of the raw mineral sample are shown in **Fig. 37**. Once the samples were observed it was confirmed the presence of diatomite as the images presented visible frustules and organized structures, in the geometric sense **[122]**, that through XRD could not be seen. This is due to diatomite is an amorphous silica mineral that present no long-range ordering **[207]** being difficult to identify it through conventional XRD techniques, even more so when it is in the presence of other minerals. As well, the overall images showed quartz and kaolin, as expected from the XRD analyses. Other amorphous phases are detected as heterogenous materials in the images.

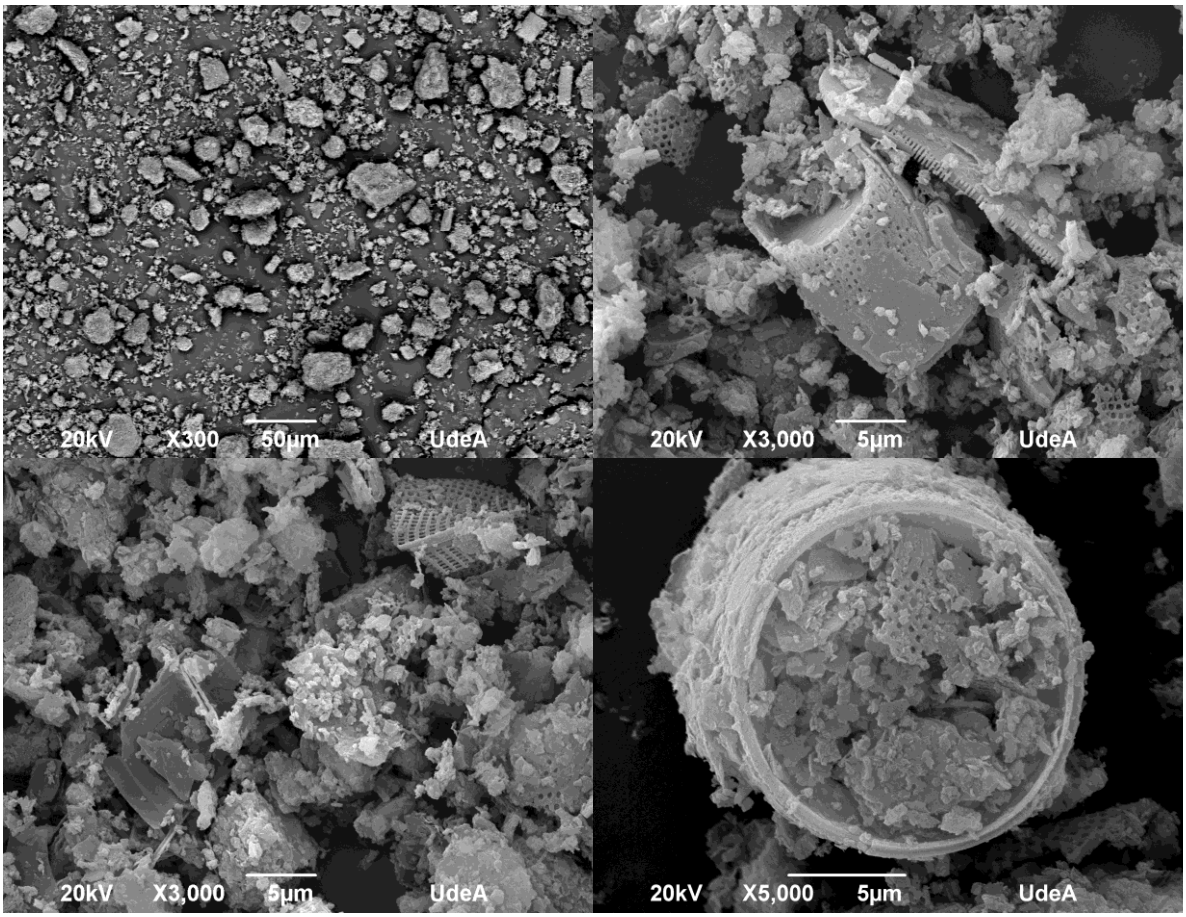

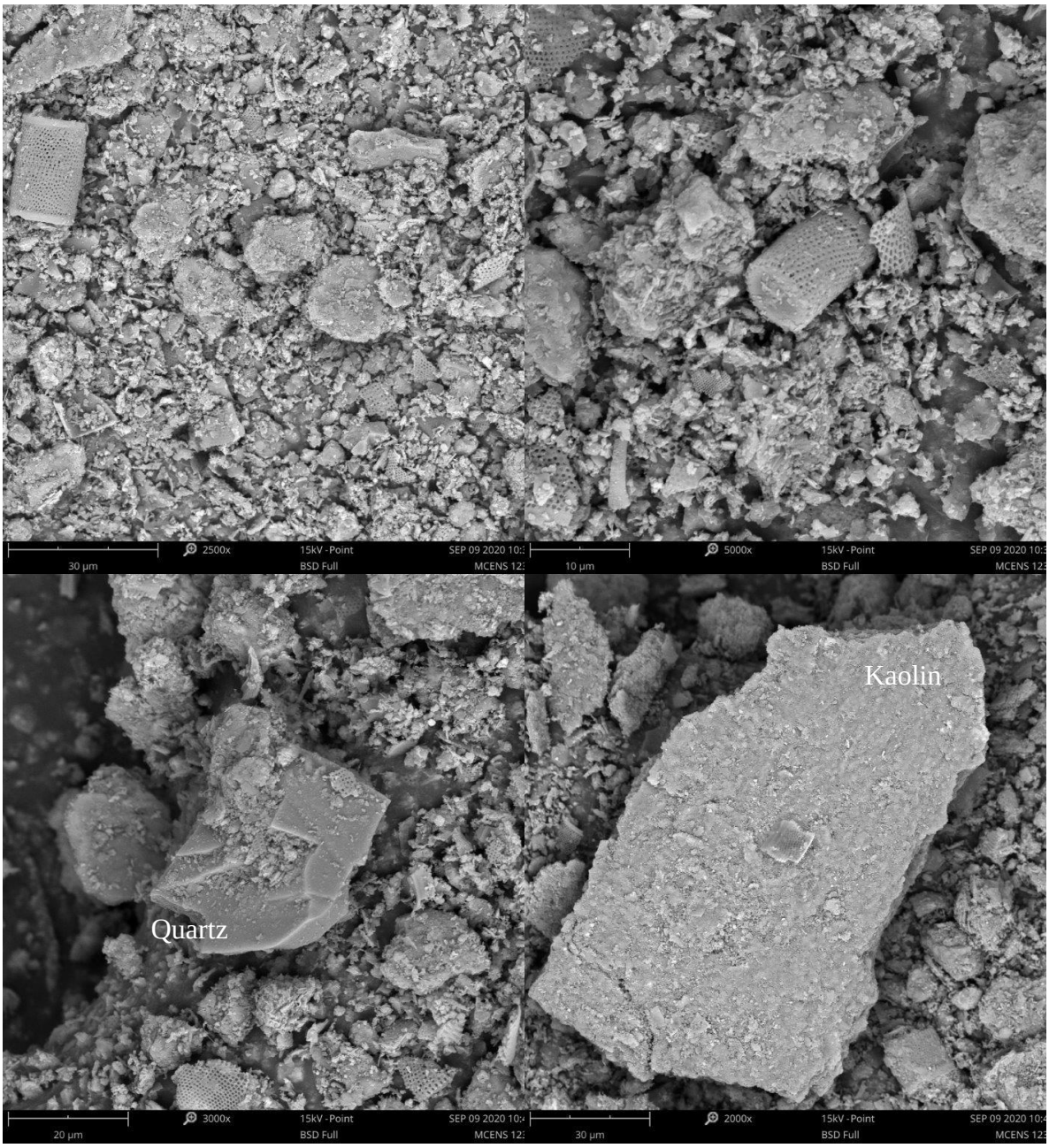
2500x 15kV - Point SEP 09 2020 10:
30 µm BSD Full MCENS 12
5000x 15kV - Point SEP 09 2020 10:
10 µm BSD Full MCENS 12
Quartz
3000x 15kV - Point SEP 09 2020 10:
20 µm BSD Full MCENS 12
Kaolin
2000x 15kV - Point SEP 09 2020 10:
30 µm BSD Full MCENS 12

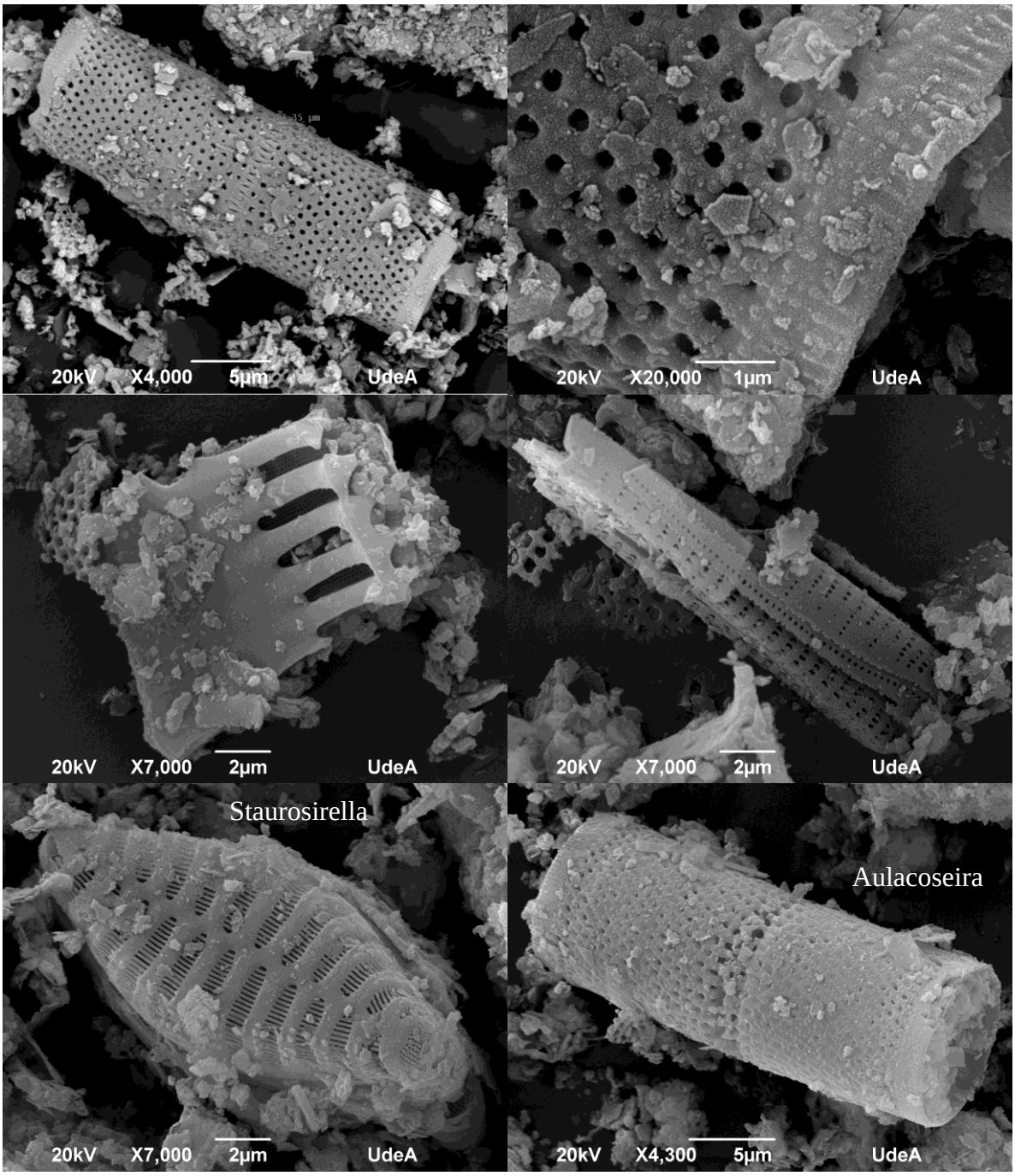

Fig. 37. SEM micrographs of the raw mineral support, showing quartz, kaolin and different types of diatomite such Staurosirella and Aulacoseira genus.

Particularly, in the Colombian sample studied in this work a mixture of several diatomite types appeared, as an example Staurosirella and Aulacoseira genus are presented, being the most common the Aulacoseira (**Fig. 37**). These diatomites had lengths about 17 µm to 30 µm, with macropore between 60 nm to 300 nm.

From a macroscopic point of view, after heat treatments, morphology of the minerals in the sample like diatomite and quartz remained the same, even at 1100 °C, but others like kaolin changed phase, as stated above in the XRD analysis. The SEM images of samples calcined at 600 °C and 1100 °C are shown in **Fig. 38** and **Fig. 39**, respectively.

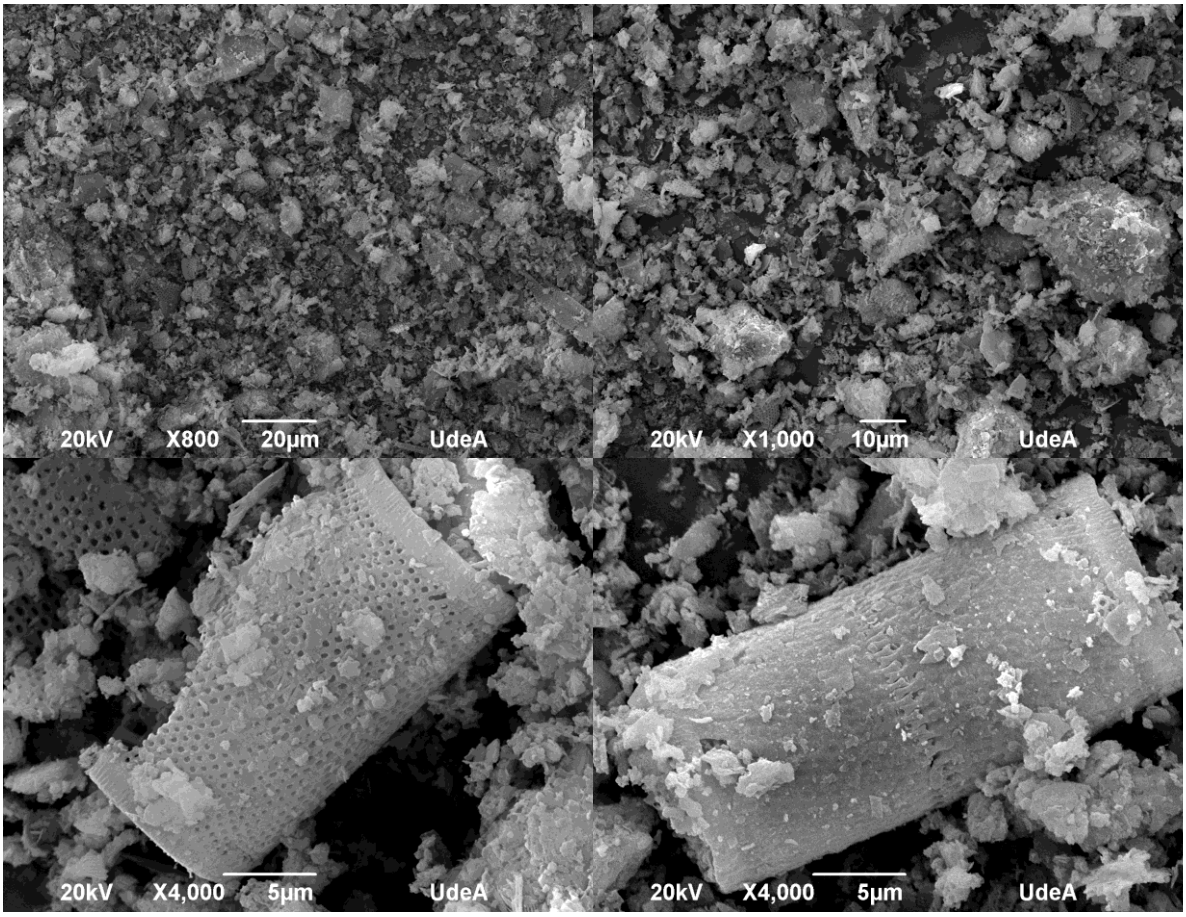

Fig. 38. SEM images of the mineral sample after heat treatment at 600 °C.

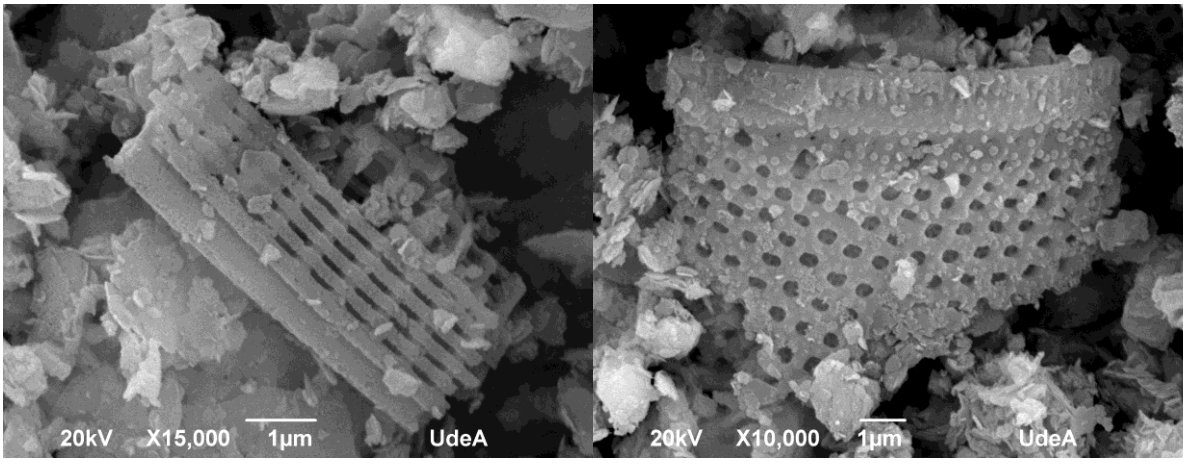

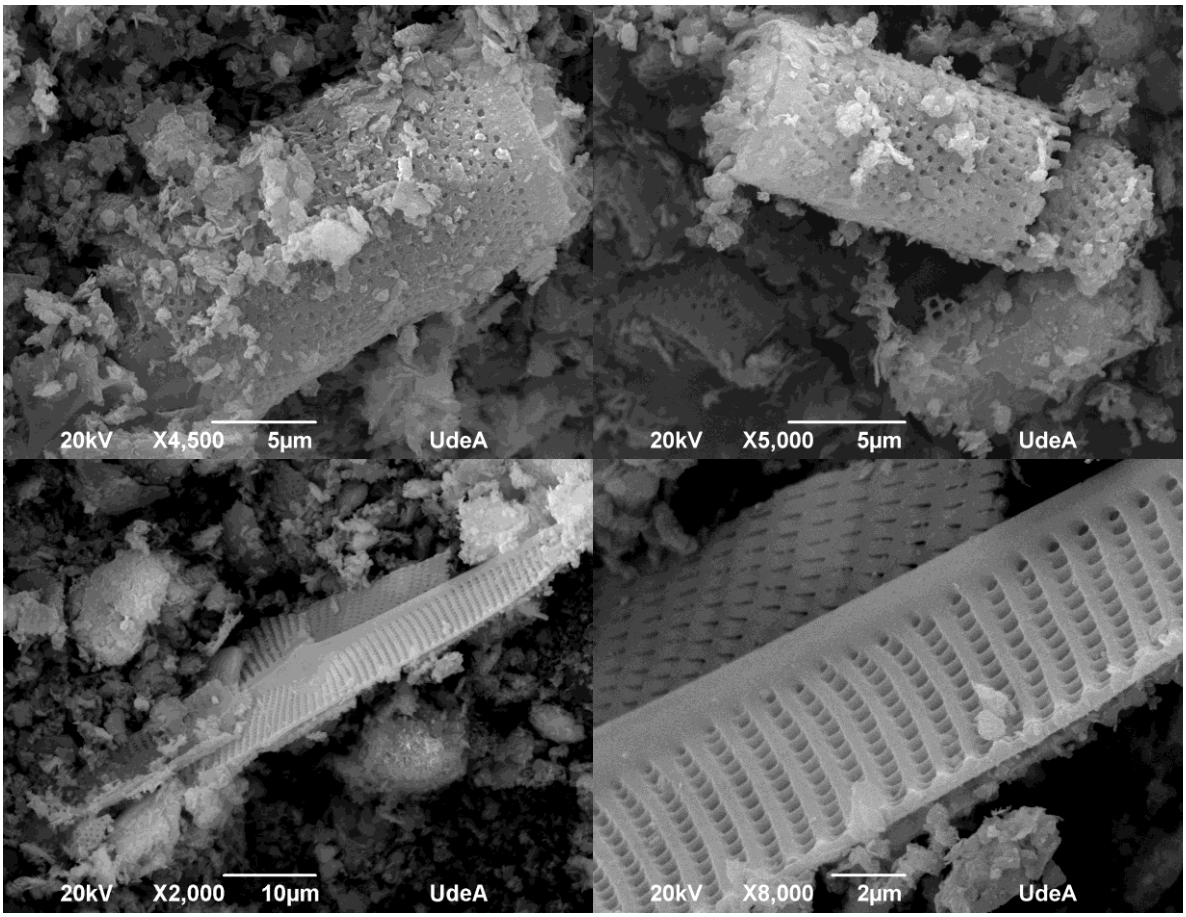

Fig. 39. SEM images of the mineral sample after heat treatment at 1100 °C.

Morphological characterization of the diatomites was complemented with TEM analysis. Images of the raw mineral are shown in **Fig. 40**. In this sample the pores of some types of diatomite where not through-holes but had a sort of inner wall, meanwhile others presented empty holes. These kind of porous can further influence the absorption rate of the sample, being better for the empty holes. Nevertheless, the cylindrical form of the most common diatomite genus found in the studied samples had to be taking in account for the absorption analysis.

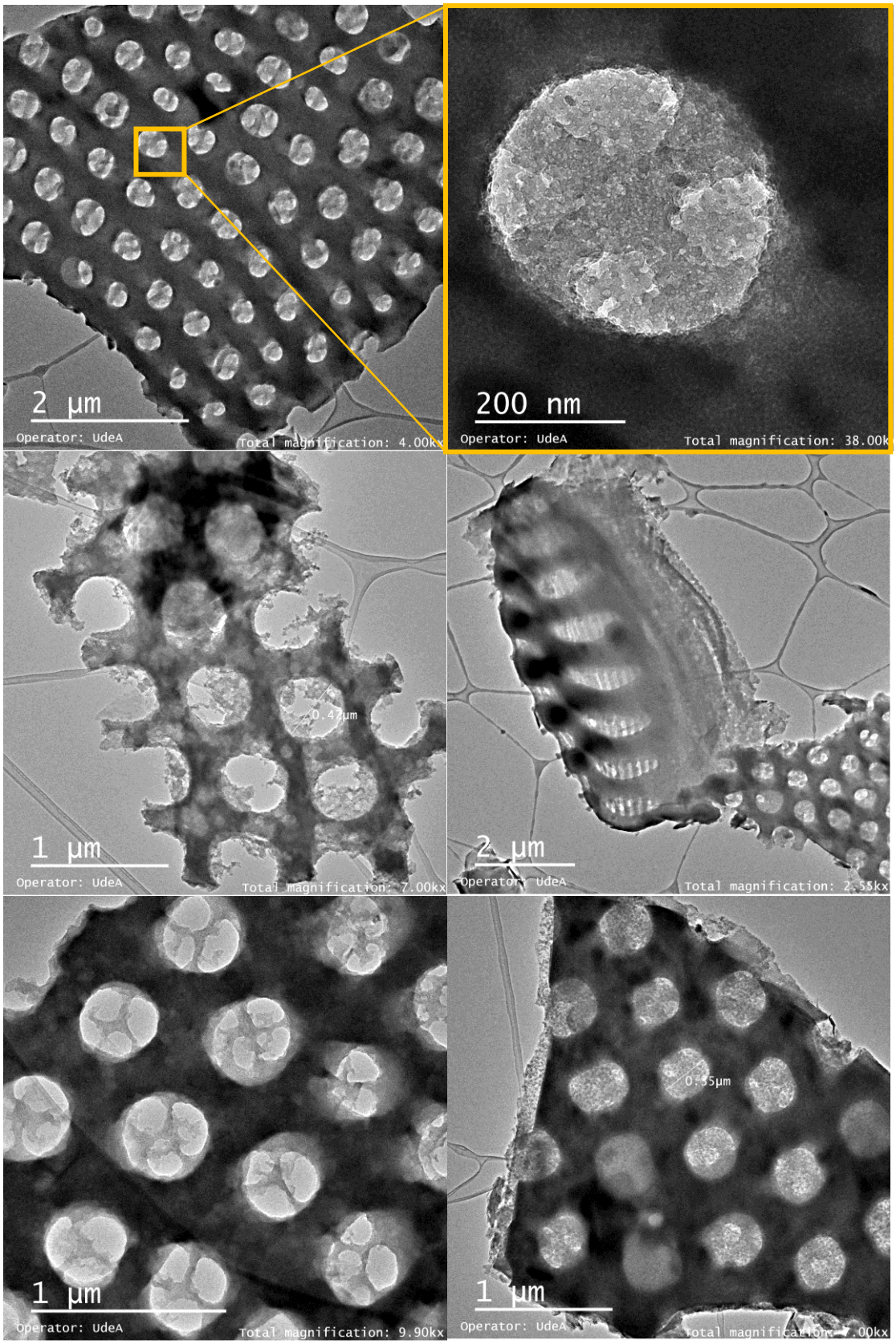

Fig. 40. TEM micrographs of diatomites in the raw mineral sample.

The TEM micrographs of diatomites in the samples with treatments at 600 °C, 900 °C and 1100 °C showed similar morphologies as the diatomites found in the raw sample. Some images can be seen in **Fig. 41** and **Fig. 42**. After heat treatments, the diatomites presented less impurities around and within.

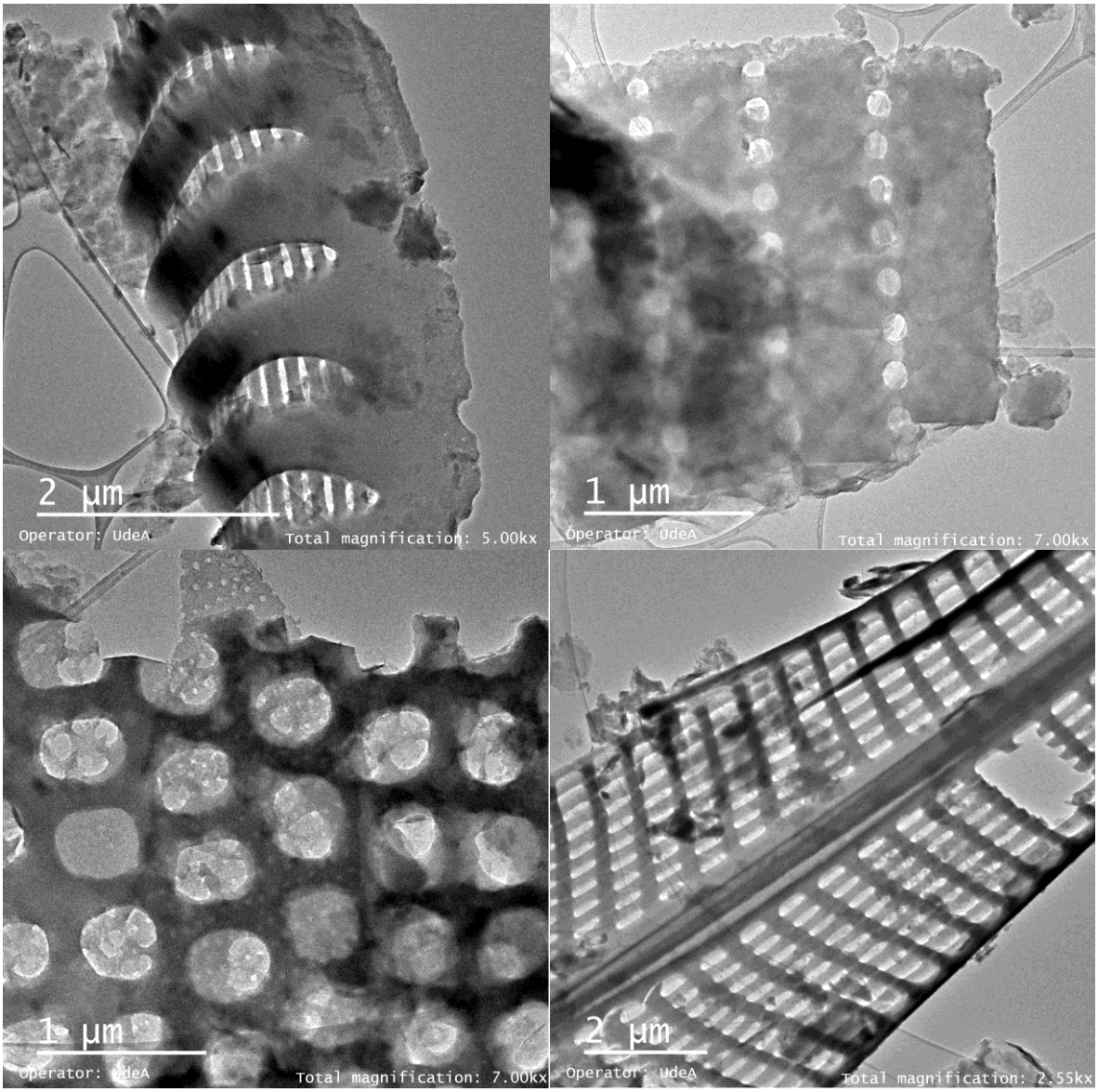

Fig. 41. TEM micrographs of diatomite portions in the sample calcined at 600 °C.

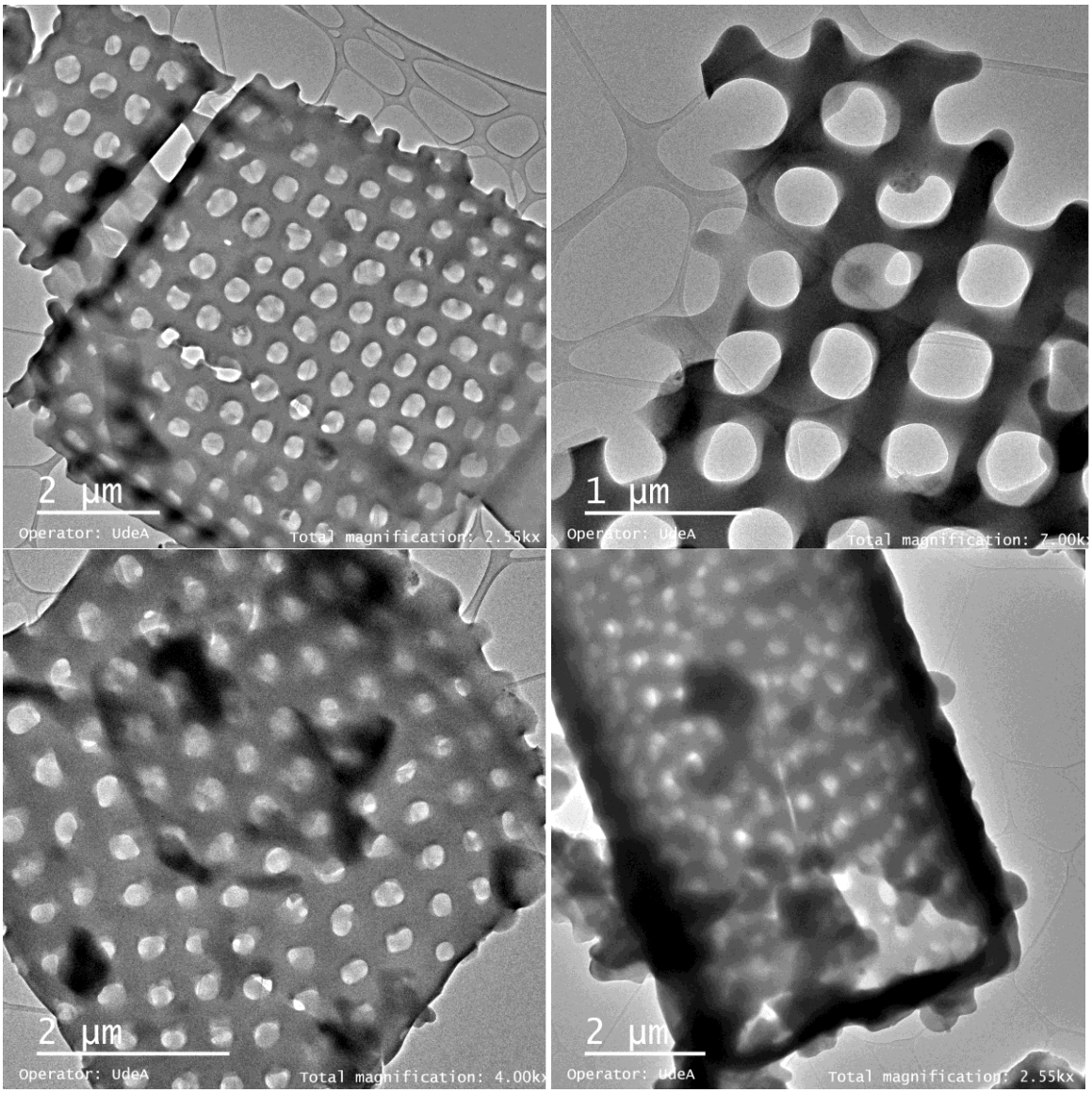

Fig. 42. TEM micrographs of diatomite portions in the sample calcined at 1100 °C.

Complementary selected area electron diffraction, SAED, and HRTEM analysis were performed to several diatomites in all samples. The fast Fourier transform, FFT, was done in the HRTEM images for a better understanding of the crystallinity of the diatomites. The SAED images (**Fig. 43**. **b)**) of diatomite in the raw sample revealed a polycrystalline sample, the rings showed weak reflections probably associated to one of the following:

- Calcedonia, a cryptocrystalline form of silica **[208]**,
- Opal-A, a silica polymorph highly disordered **[209]**,

- Opal-CT, composed of disorder microcrystals of α-cristobalite in an amorphous silica matrix **[209]**
- Opal-AN, a network structure similar to a glass **[207]**.

HRTEM micrographs (**Fig. 43. c)**) corroborated the presence of small crystals within the amorphous matrix. As stated before, the sample contained several kinds of minerals being not pure diatomite, then to confirm that the SAED and HRTEM analyses where done just in the diatomite particles and not in other minerals, energy-dispersive X-ray spectroscopy, EDX, was made and is presented in **Fig. 44**. The results probed that the analyzed sites correspond mainly of 44-46% of Si, 50-55% of O and, in a minor extent, 0.5-2.8% of Al. Thus, the results of TEM, HRTEM and SAED showed that the mineralogical phase, existing in diatomite, is not entirely amorphous and present a short-range order that through conventional XRD technique cannot be determined, the same findings were observed in different diatomites in the other samples. Thus, it was demonstrated that cryptocrystals or microcrystals are present in the amorphous silica matrix of diatomite, even without thermal treatments, contrary to some reports **[210]**. As well, some d-spacings from the SAED patterns were measured, showing a correlation with crystalline phases of cristobalite/tridymite-like crystals.

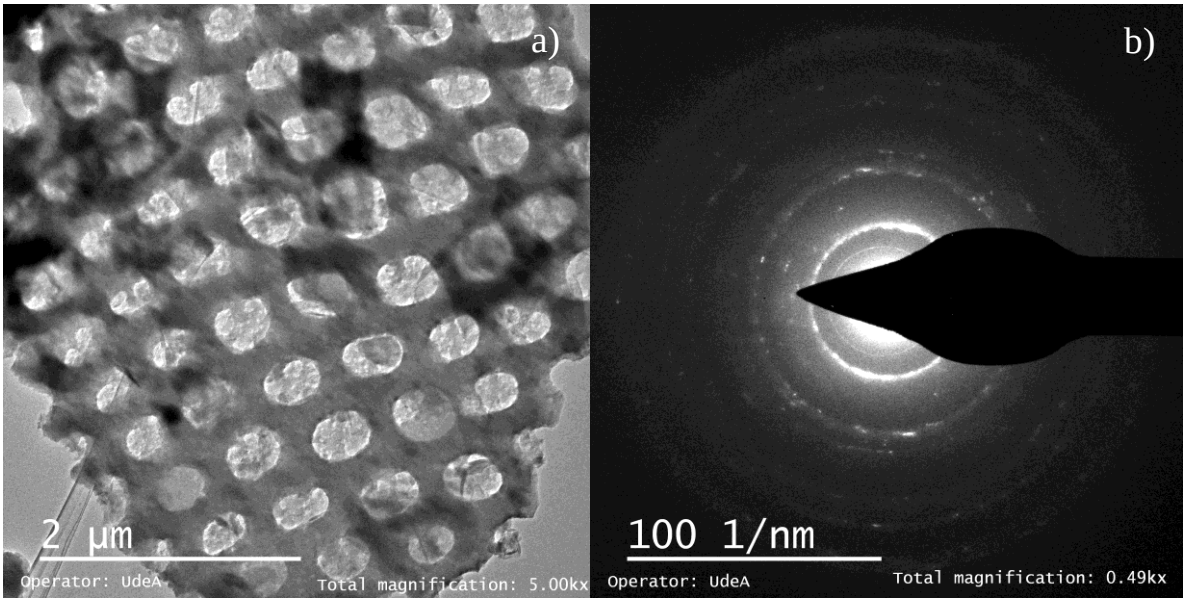

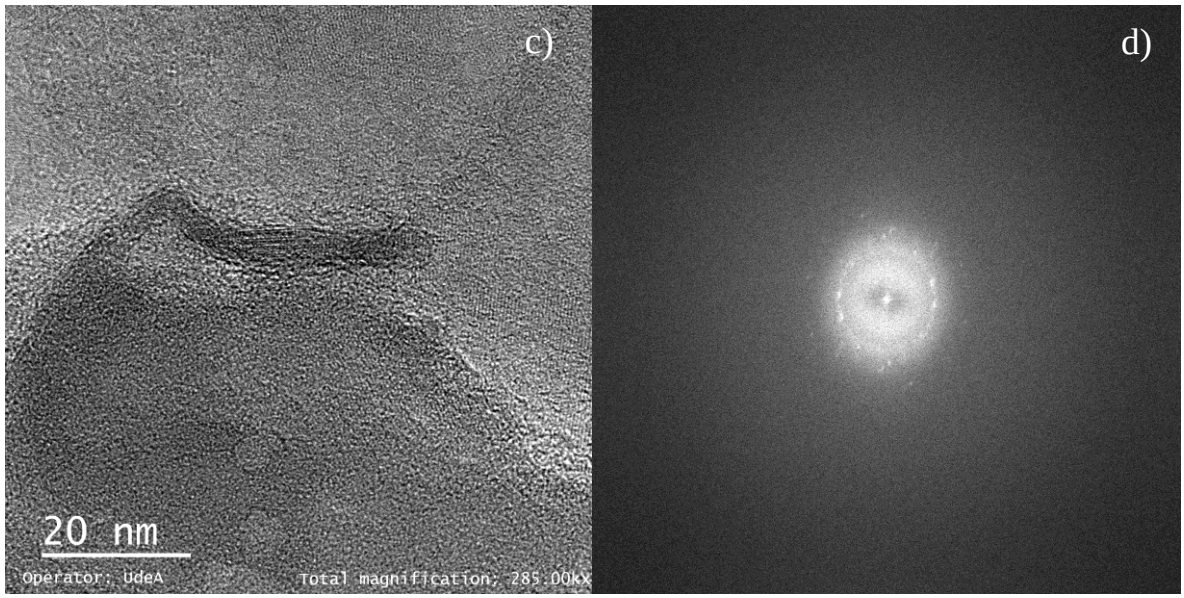

Fig. 43. TEM micrograph a), SAED image b), and HRTEM c) with its FFT image d) of a diatomite in the raw sample showing some crystalline planes.

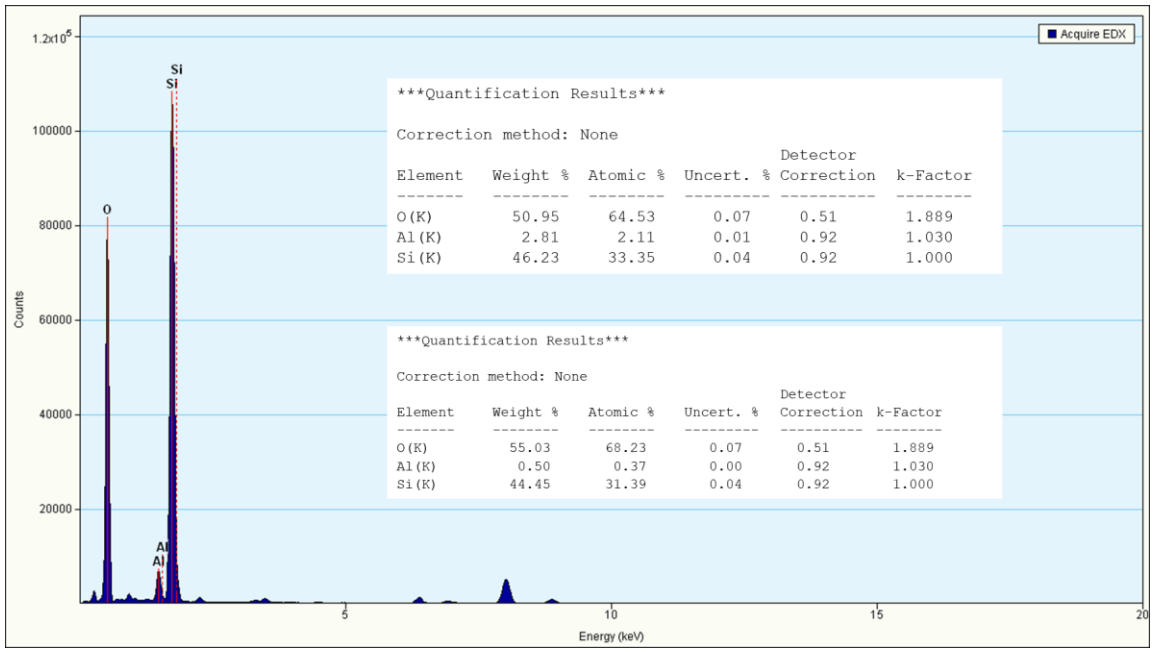

Fig. 44. Energy dispersive X-ray spectroscopy (EDS) analysis for diatomite.

It is important to highlight that even at 1100 °C diatomite remained amorphous as no high values of cristobalite were found **[39],** this is in accordance to Yuan et al. **[211]**, who studied the hydroxyl species and acid sites on diatomite surfaces and proposed a model to understand the dehydration process, and supported on the work of Bogdan et al. **[212]**, who reported

that silica with microporous or mesoporous structure has the hydroxyl groups on the inner wall of pores arranged and preferred to form H-bonded hydroxyl groups than isolated ones, making therefore the condensation temperature generally high. It can be presumed that most of the survival H-bonded silanols remain in those mesopores even after treatment at 1100 °C, favoring the diatomite thermal resistance.

As diatomite is an amorphous silica is hard to quantified it through conventional XRD techniques, but still some theoretical analysis can be done to approximate its value within the sample. As seen in **Table 20**, the XRD quantification of the crystalline phases that contains SiO_2 is shown, as well as the total amount of SiO_2 contained in each phase. The SiO_2 value was calculated from the stoichiometry composition of each mineralogical phase. The maximum total amounts of SiO_2, coming from crystalline phases, are 27.50% in the raw sample and 23.42% in the sample at 1100 °C. Comparing these values with the 65.94% of SiO_2 of the XRF analysis (**Table 17**) it can be concluded that at least in the amorphous phases are around 38% to 42% of SiO_2. Moreover, as no peaks appeared in the TGA (**Fig. 36**) related with other phases than goethite, kaolinite or illite, it can be assumed that the sample contained approximately 40% of diatomite.

Table 20. Quantitative XRD analysis of the crystalline phases containing SiO_2 and stoichiometry calculations.

	Raw sample		Sample 600 °C		Sample 900 °C		Sample 1100 °C	
Mineralogical phase	%XRD	%SiO_2*	%XRD	%SiO_2*	%XRD	%SiO_2*	%XRD	%SiO_2*
Kaolinite (K)	19.76	9.78	8.94	4.42	3.40	1.68	0.00	0.00
Mullite (M)	0.00	0.00	0.00	0.00	0.00	0.00	23.83	6.72
Quartz (Q)	11.91	11.91	10.12	10.12	9.10	9.10	12.19	12.19
Cristobalite (C)	0.00	0.00	0.00	0.00	0.00	0.00	4.51	4.51
Mica/Illite (I)	10.76	5.81	5.42	5.42	7.75	4.19	0.00	0.00
Total	42.42	27.50	24.48	17.47	20.26	14.97	40.52	23.42

*Calculated from the stoichiometry composition of the mineral phases found in **[213]**.

The identification of the mineralogical phases and clay group minerals using the X-ray diffraction method is supported mainly in the spacings of the basal planes, hence the identification among the members of a group is greatly hindered by this technique. Then, it is important to combine several methods as XRF, TGA, SEM, TEM, XRD, Rietveld

refinement and stoichiometry calculations for a complete identification in complex minerals as the one studied in this work. Finally, the complete composition, including the crystalline and amorphous phases, of the raw sample is shown below.

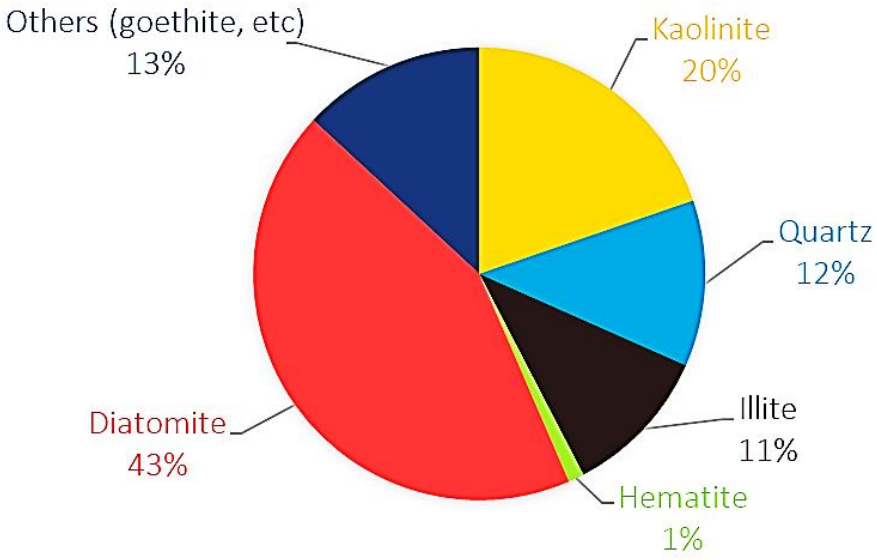

Fig. 45. Mineralogical composition of the raw natural support.

Moreover, as a potential support for phase change materials, the presence of different minerals can suppose some advantages compared to supports that present a single mineralogical phase, for instance kaolin and diatomite are absorbents, and quartz and cristobalite presents good thermal conductivity. Advantages and disadvantages of the minerals are shown in **Table 21**. Thus, natural supports offer some properties that can be exploited for shape-stabilization of phase change materials.

Table 21. Advantages and disadvantages of the minerals present in the mineral sample.

Mineral	Advantages	Disadvantages
Kaolin	Good absorbent Flame retardant	Low thermal conductivity
Quartz	Good thermal conductivity	Low absorbent
Mica	Absorbent	Thermal insulator
Cristobalite	Good thermal conductivity	Not an absorbent
Diatomite	Good absorbent	Low thermal conductivity

3.4. Influence of the mineralogical phases of the support in the porosity, thermal conductivity, heat capacity and other thermal properties

As stated above, the raw mineral support was composed of several mineralogical phases, each of one having different properties. To study the effect of these on the support, some mineral standards were acquire. Silica (98.2% purity) and kaolin (94.94% purity) were supplied by Sumicol S.A.S (Colombia). Illite IMT-2 (85-90% purity) was purchased from the Clay Minerals Society (USA). Illite structure, according to the supplier is $(Mg_{0.09}\ Ca_{0.06}\ K_{1.37})\ [Al_{2.69}\ Fe(III)_{0.76}\ Fe(II)_{0.06}\ Mg_{0.43}\ Ti_{0.06}][Si_{6.77}\ Al_{1.23}]O_{20}(OH)_4$. The X-ray fluorescence, XFR, of the minerals is shown in **Table 22**. The chemical composition by XRF confirmed the purity of the minerals.

Table 22. Chemical composition by XRF of raw support, kaolin, silica and illite.

Content (wt. %)	SiO_2	Al_2O_3	Fe_2O_3	TiO_2	CaO	MgO	Na_2O	K_2O	P_2O_5	SO_3	LOI*
Raw support	65.9	17.2	5.53	0.52	0.20	0.45	0.08	1.60	0.15	0.15	8.1
Kaolin	45.6	37.5	1.82	0.58	0.011	0.19	-	0.42	0.04	0.02	13.9
Silica	98.2	1.23	0.08	0.04	0.01	0.06	-	0.03	-	-	0.4
Illite	57.7	20.1	5.97	0.73	0.41	2.16	-	7.64	0.02	0.08	0.07

*(110 °C – 1000 °C)

Although these standard minerals could differ from the ones in the support, especially regarding size and, for kaolin, crystallinity degree, this section's purpose is to give an overview of the incidence of these minerals in the absorption capacity and thermal properties of the support. Particle size distribution of the samples is presented in **Fig. 46**. The cumulative volume indicated that the Dv_{50} for kaolin, silica and illite was 14.60 µm, 7.59 µm and 7.02 µm, respectively. Meanwhile, the raw support Dv_{50} was 10.60 µm. The particle size distribution of the minerals is shown for having a notion of the particle sizes of the samples studied.

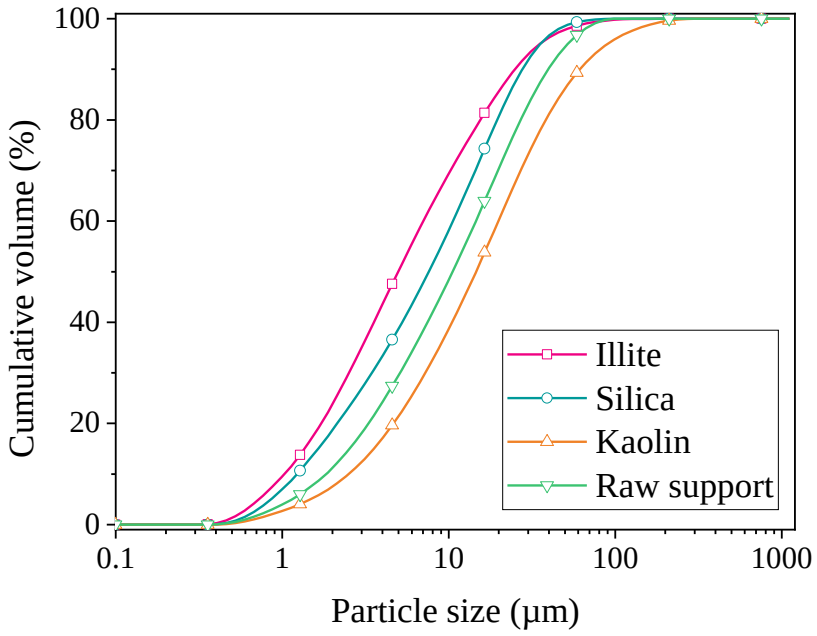

Fig. 46. Particle size distribution of illite, silica, kaolin and the raw mineral support.

While macroscopic sizes of the standard minerals could differ from the minerals of the raw support, other properties can be similar such porosity, calorimetry curves and thermal conductivity. For instance, textural properties as pore volume, pore width and surface area (**Table 23**) of the samples were measured by N_2 adsorption-desorption isotherms (**Fig. 47**).

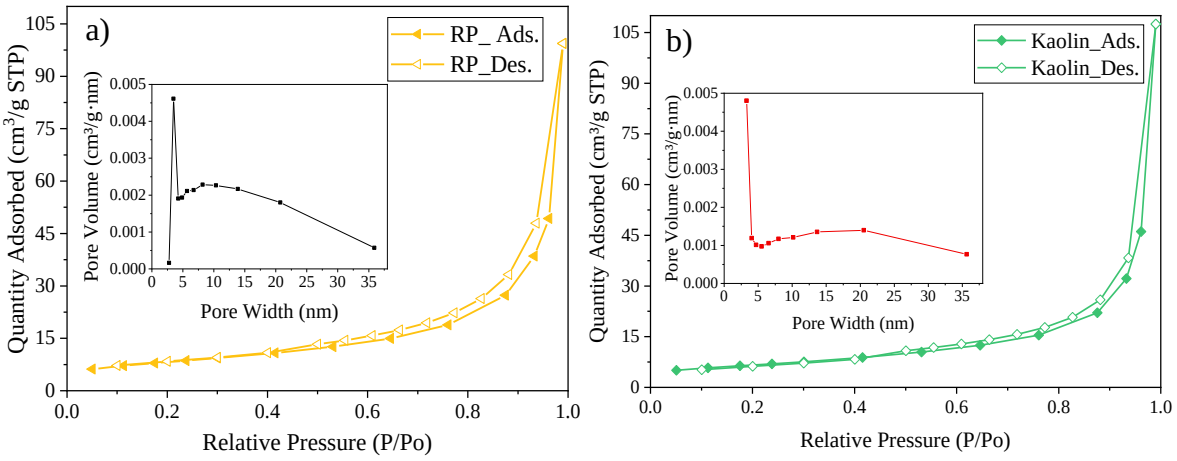

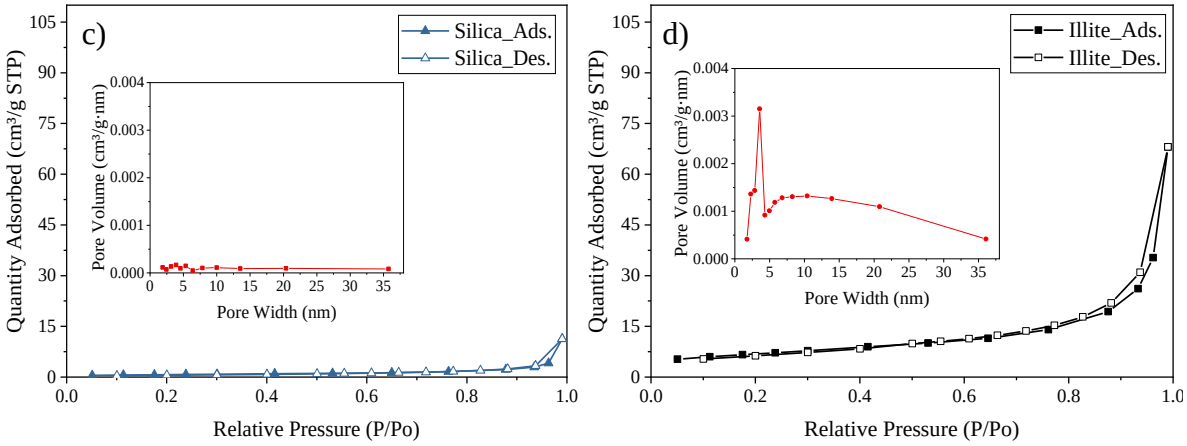

Fig. 47. N_2 adsorption-desorption isotherms for a) the raw support (RP), b) kaolin, c) silica (quartz), and d) illite. Inset shows the BJH desorption dV/dw pore volume distribution for the same materials.

The classification of the type of isotherms and hysteresis used was in accordance to the IUPAC **[214]**, as well as the classification of the pores, being micropores (< 2 nm), mesopores (2-50 nm) and macropores (> 50 nm). The kaolin (**Fig. 47**. **b)**) and illite (**Fig. 47**. **d)**) appear to exhibit Type-II curves with H3-type hysteresis loops. Type-II isotherms are the result of unrestricted monolayer-multilayer adsorption. The beginning point of the linear section is considered as the point where completion of monolayer coverage is achieved. The increase when $P/P_0=1$ indicates the formation of an adsorbed nitrogen multilayer, usually due to the existence of macropores. From the respective insets, corresponding to the BJH desorption dV/dw pore volume distribution, it could be notice that the pore widths are in the mesopore scale, and there are none or very low amount of micropores in the samples. The H3-type hysteresis loop correspond to non-rigid aggregates of plate-like particles **[214]** and demonstrate the presence of mesopores that are filled and empty by capillary condensation **[215]**. These results indicate that in these samples the main size of pores are mesopores and the more likely type of pores are slit-shaped pores. Meanwhile, silica (**Fig. 47**. **d)**) presented a very low amount of N_2 adsorbed compared to the other minerals, indicating that is a non-porous mineral, this is in accordance with the pore volume distribution shown in the inset. The isotherm for the raw support (RP) (**Fig. 47**. **a)**) presented, as well, a Type-II curve with H3-type hysteresis loop. This agrees with the presence of kaolinite and illite/mica in the support. Besides, the BJH desorption dV/dw pore volume distribution of the RP is larger than

for the pure kaolinite, illite or silica, most probably due to the presence of diatomites in the support. Hence, the porosity of the natural mineral support RP is governed by the presence of diatomite, kaolinite and illite/mica.

Table 23. Surface area, pore volume and pore size of raw support, illite, silica and kaolin.

		Raw support	Illite	Silica	Kaolin
Surface Area	BET Surface Area (m^2/g)	29.12	24.17	2.70	23.48
	BJH Adsorption cumulative surface area of pores (between 1.7 nm and 300 nm width) (m^2/g)	28.69	21.80	2.54	24.03
	BJH Desorption cumulative surface area of pores (between 1.7 nm and 300 nm width) (m^2/g)	33.19	23.92	2.88	30.23
Pore Volume	BJH Adsorption cumulative volume of pores (between 1.7 nm and 300 nm width) (cm^3/g)	0.15	0.10	0.02	0.17
	BJH Desorption cumulative volume of pores (between 1.7 nm and 300 nm width) (cm^3/g)	0.15	0.11	0.02	0.17
Pore Size	Adsorption average pore width (4V/A by BET) (nm)	21.12	17.42	25.86	28.32
	BJH Adsorption average pore width (4V/A) (nm)	21.32	19.01	27.15	27.63
	BJH Desorption average pore width (4V/A) (nm)	18.58	17.69	24.01	22.04

Regarding the heat accumulated by these minerals, **Fig. 48** shows the DSC curves for kaolin, illite, silica and the raw support, from 13 °C to 57 °C. As can be noticed, none of these minerals presented any latent heat storage, as in this temperature range the minerals do not reach the temperature of fusion. Thus, the minerals than compose the raw support RP do not contribute to the latent heat of fusion/solidification.

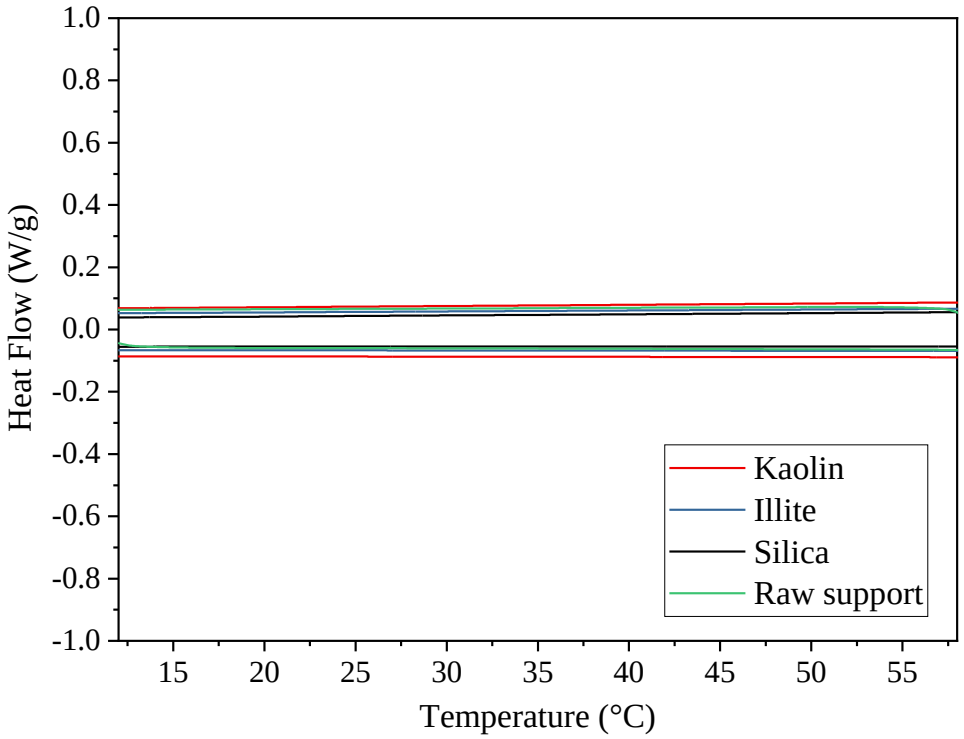

Fig. 48. DSC curves for the raw support, kaolin, silica and illite.

On the other hand, sensible heat contribution of the minerals can be observed in **Fig. 49** as the specific heat capacity, C_p. The dependence of specific heat capacity of the kaolin, illite and silica as a function of temperature from 5 °C to 74 °C showed a linear behavior with a positive slope, which implies that when temperature increases, heat capacity increases. At 5 °C heat capacities of kaolin, illite, and silica were 1.12 J/(g·°C), 0.88 J/(g·°C), and 0.48 J/(g·°C), and at 74 °C were 1.23 J/(g·°C), 1.07 J/(g·°C), and 0.81 J/(g·°C), respectively. The specific heat capacity increased about 9.8%, 21.6% and 68.8% for Kaolin, illite, and silica, respectively, in this interval. The specific heat capacity of the raw support behaved as for the minerals, with a heat capacity increase about 14% in this temperature interval, from 1.14 J/(g·°C) to 1.30 J/(g·°C). These results proved that, between the studied minerals, kaolin presented the higher heat capacity, being similar to the heat capacity of the raw support. Probably, kaolin governed the heat capacity of the support.

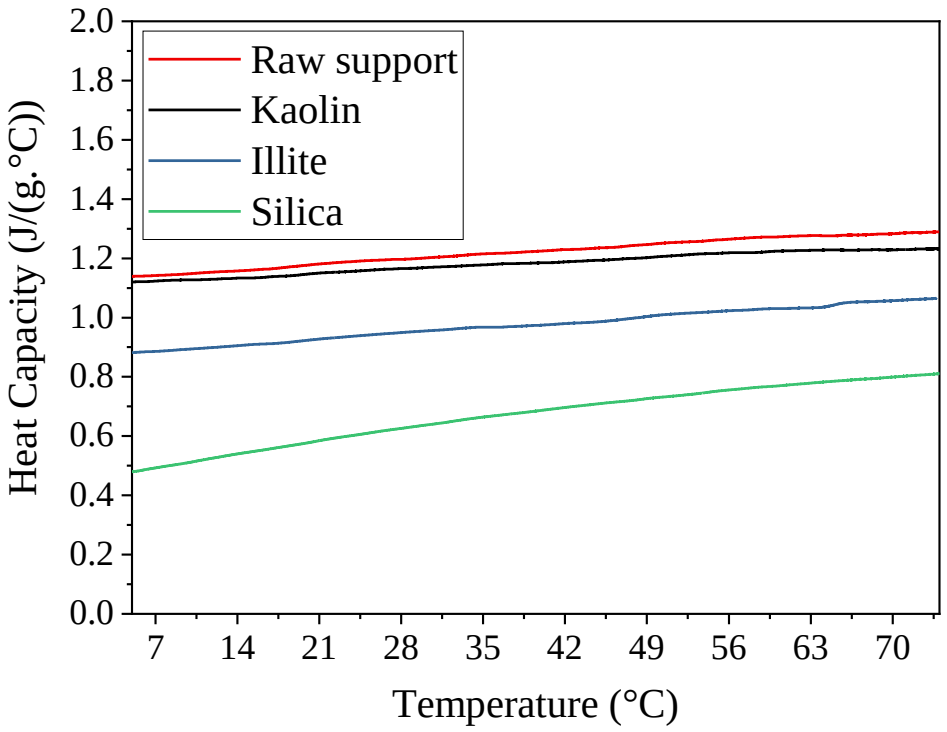

Fig. 49. Specific heat capacity as a function of temperature for the raw support, kaolin, silica and illite.

As well, the temperature dependence of the thermal conductivity of illite, silica, kaolin and the raw support is shown in **Fig. 50. a)**. Thermal conductivity of the minerals remained almost constant throughout the temperature range (5°C to 70°C). Illite presented the higher conductivity values (0.240 ± 0.004 W/m·K), followed by the kaolin (0.160 ± 0.003 W/m·K) and the silica (0.070 ± 0.002 W/m·K). The raw support presented the lower thermal conductivity of all the materials (0.050 ± 0.001 W/m·K).

For estimation of the influence of each mineral (mass fraction) in the thermal conductivity of the support, the linear rule of mixtures approximation **[216]** was used, assuming that each phase is contiguous, with no assumed shape and that they are randomly dispersed respect to the heat flow. Knowing that the support is constituted by 4.61% illite, 8.60% silica, 7.60% kaolin, 15% air (according to the pore volume of the sample), the remaining 64.19% corresponds mainly to amorphous minerals such diatomite and metakaolin. Then, by applying the rule of mixtures, **Fig. 50. b)**, can be found that kaolin and illite contribute to

0.012 W/m·K and 0.011 W/m·K, respectively; silica, in the quartz form, contributes to 0.006 W/m·K, the air contributes to 0.003 W/m·K, and the other minerals with 0.015 W/m·K.

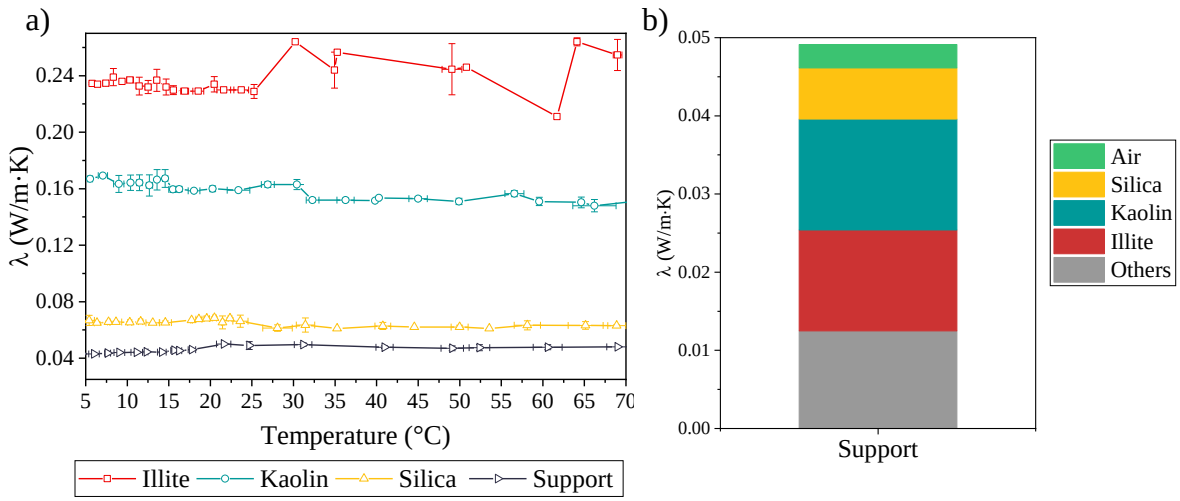

Fig. 50. Thermal conductivity of a) illite, silica, kaolin, and the raw support, and b) mixing rule for the raw support.

Hence, for the raw support, kaolin represented 26.14% of thermal conductivity, illite 23.76%, amorphous 31.52%, silica 12.07%, and air 6.5%. Thus, between the studied minerals, kaolin governed thermal conductivity of the raw support.

In summary, the results obtained for the thermal properties of the minerals that compose the raw support indicate that kaolin and illite governed properties as heat capacity and thermal conductivity. The overall porosity of the support is due to the presence of diatomite, kaolin and illite. Silica is the mineral with the less contribution to thermal properties within the support.

3.5. Conclusions

The identification of the mineralogical phases and clay group minerals using the X-ray diffraction method is supported mainly in the spacings of the basal planes, hence the identification among the members of a group is greatly hindered by this technique. Then, it is important to combine several methods as XRF, TGA, SEM, TEM, XRD, Rietveld refinement and stoichiometry calculations for a complete identification in complex minerals as the one studied in this work. The results of TGA, XRF, XRD and SEM indicate that the

mineral presented different mineralogical phases as kaolinite (19.75%), illite (10.75%), quartz (11.88%), and diatomite (40.00%). High-resolution electron transmission images and selected area electron diffraction analysis showed that the diatomite was not entirely amorphous and presented a short-range order that through conventional XRD technique could not be determined. The diatomite confers a porous structure to the mineral and therefore can be considered as a feasible support for containing PCMs, moreover, the presence of laminar phases as kaolinite and illite might match or even improve the loading amount of PCM into the support compared to the investigations of pure diatomite supports found in literature.

The findings of this research allow to improve the understanding of complex minerals containing diatomite through the implementation of different characterization techniques for its adequate phase determination and quantification, as well to demonstrate that this Colombian clay mineral is suitable as a porous support for shape-stabilized organic phase change materials as fatty acids.

CHAPTER IV.

Production of shape-stabilized phase change materials

The objective of this section is to present the shape-stabilization process of the eutectic phase change materials produced, CA/MA, LA/MA and PA/SA, into the raw porous support to obtain a thermal energy storage system. As stated in the theoretical framework, one of the simple methods yet very effective, to obtained SS-PCM is vacuum-assisted impregnation **[131]**, as it presents the advantage **[131,139,140,184,217]** of improving the absorption of the PCM (liquid phase) into the support by removing the air trapped in the pores. Furthermore, the properties of the obtained SS-PCMs are presented, as leakage percentage, phase change temperatures, latent heat, heat capacity, and morphology.

4.1. Preparation of SS-PCMs by vacuum assisted impregnation method

The SS-PCM composites were prepared by the setup shown in **Fig. 51** consisting in a heating mantle, a vacuum mixer and a vacuum pump. Some samples, due to availability, were heated using a thermostatic bath (**Fig. 52**) controlled by a cartridge heater and a thermocouple instead of the heating mantle. A typical vacuum mixer consists in a stainless-steel vessel with a lid that have a seal-ring to ensure a good seal, as well, the lid have a mixing agitator, and a hole to connect the vacuum pump. The mixing agitator is coupled to a drill that have variable speed control. The advantage of this setup, compared with others found in literature, is the mixing control and the temperature homogeneity.

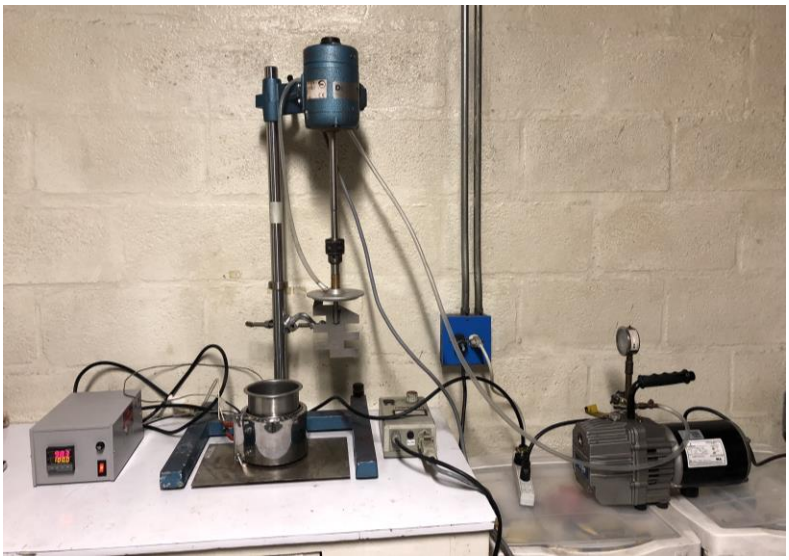

Fig. 51. Experimental setup of vacuum impregnation method using a heating mantle.

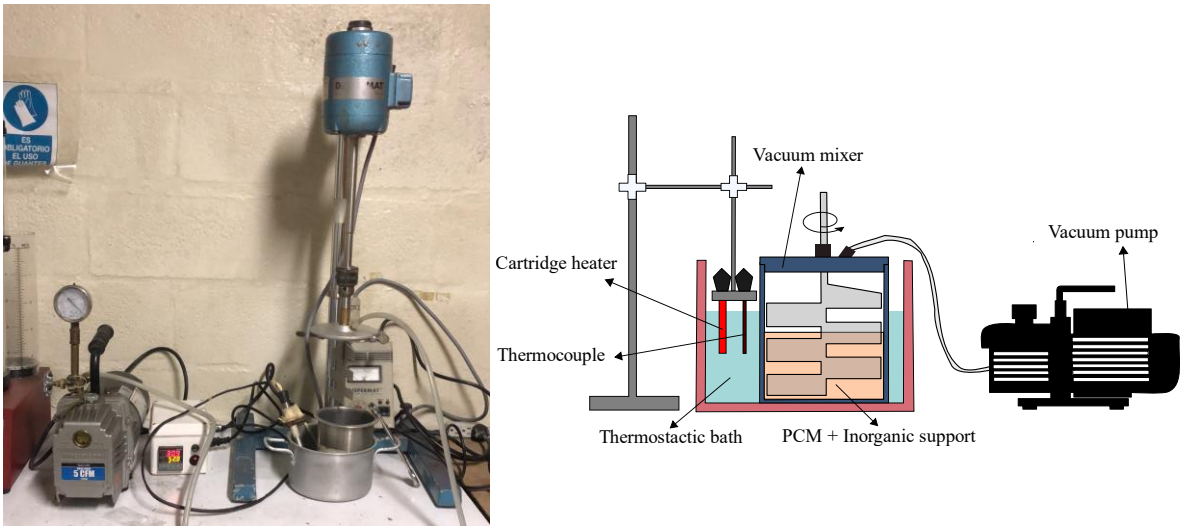

Fig. 52. Experimental setup of vacuum impregnation method using a thermostatic bath.

After a literature survey, and some preliminary experiments, the setup conditions (vacuum and exposure time) were chosen. In literature, it was found several setups with different conditions, when reported. Some of them are summarized in **Table 24**. The vacuum conditions vary from 0.3 bar and 1 bar, and the exposure time between 30 min and 90 min.

Table 24. Vacuum conditions found in literature for SS-PCMs.

Vacuum (bar)	Exposure time (min)	Ref.
0.3	90	**[160]**
0.65	90	**[78]**
0.88	30	**[218]**
1	30	**[131]**

Three preliminary impregnations, to establish the vacuum parameter, were obtained using LA/MA eutectic (40% wt.) and the raw support. The SS-PCMs were produced at atmospheric pressure, 0.09 bar, and 0.6 bar. The leakage behavior, calculated as explained in the next section, was measured as the response variable. **Fig. 53** shows the comparison of producing SS-PCMs with different vacuum pressure. As can clearly be seen, the use of vacuum decreases de leakage percentage of the composites. At a vacuum of 0.09 bar and 0.6 bar, the leakage decreases 25.46% and 56.47%, respectively, compared with direct impregnation (no vacuum assistance). Thus, the vacuum condition chosen for the experiments was 0.6 bar during 30 min.

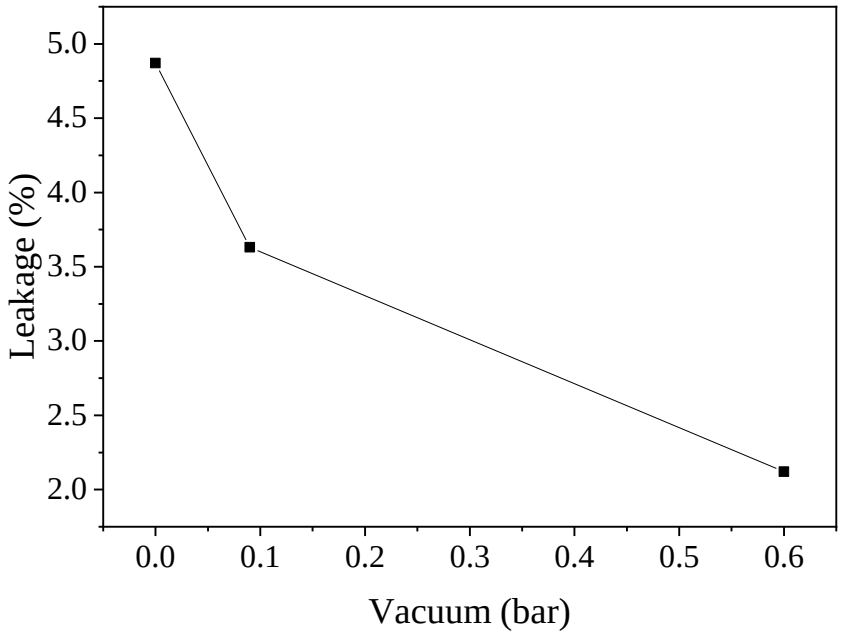

Fig. 53. Comparison between vacuum and direct (0 bar) impregnation method.

The production of the SS-PCMs composites consisted in four steps, shown in **Fig. 54**:

1. The desired weight amount of PCM, in solid phase, is added to the stainless-steel vessel.

2. The heater (thermostatic bath or heating mantle) is turned on and set at a greater temperature than the melting temperature of the respective PCM. The next step is executed only when the PCM is completely melted.

3. The support is then added to the melted PCM, and the lid of the vessel is closed. In this moment, the mixer agitator and the vacuum pump are turned on, at 20 RPM and 0.6 ± 0.14 bar, respectively. In this point the 30 min countdown begin.

4. After half an hour, the lid is opened, allowing the air to enter the vessel, and an additional mixing is performed. In this step, the SS-PCM is obtained.

The phenomenon after the vacuum assistance can be summarized in three parts. First, the vacuum removes the air trapped in the pores of the support. Second, the superficial tension of the PCM can decrease under vacuum condition as the intermolecular forces decreases, and thus, the cohesive force decrease, and capillarity increases. Third, when the vacuum mixer is opened to allow the air to enter, forced the liquid to penetrate the pores. In this way, shape-stabilization using vacuum assistance improves the impregnation of PCMs in porous supports.

Fig. 54. Images showing the steps for SS-PCM production.

The produced SS-PCM consisted in 9 samples, as stated in **Table 25**. All the samples were produced at 0.6 bar for 30 min, using the raw mineral as the support, and a temperature of 40 C for CA/MA and LA/MA composites, and 70°C for PA/SA composites.

Table 25. SS-PCMs produced by the vacuum assisted method, using the raw support.

Sample name	Eutectic type	% Impregnation (wt.)	% Support (wt.)
SS-CA/MA-25	CA/MA	25	75
SS-CA/MA-35	CA/MA	35	65
SS-CA/MA-40	CA/MA	40	60
SS-LA/MA-25	LA/MA	25	75
SS-LA/MA-35	LA/MA	35	65
SS-LA/MA-40	LA/MA	40	60
SS-PA/SA-25	PA/SA	25	75
SS-PA/SA-35	PA/SA	35	65
SS-PA/SA-40	PA/SA	40	60

4.2. Leakage percentage of the SS-PCMs

The leakage behavior of the nine composites (**Table 25**) was evaluated by a test based on the filter paper method **[78,219,220]**, as presented in **Fig. 55**. The SS-PCM was put on a circular template of 1.4 cm x 0.2 cm upon a filter paper and then was placed in an oven at 60 °C for 120 min. The template was removed, and the sample and the filter paper were weighted, before placing the sample in the oven. Then the samples along with the filter paper were cooled down to room temperature and weighted again.

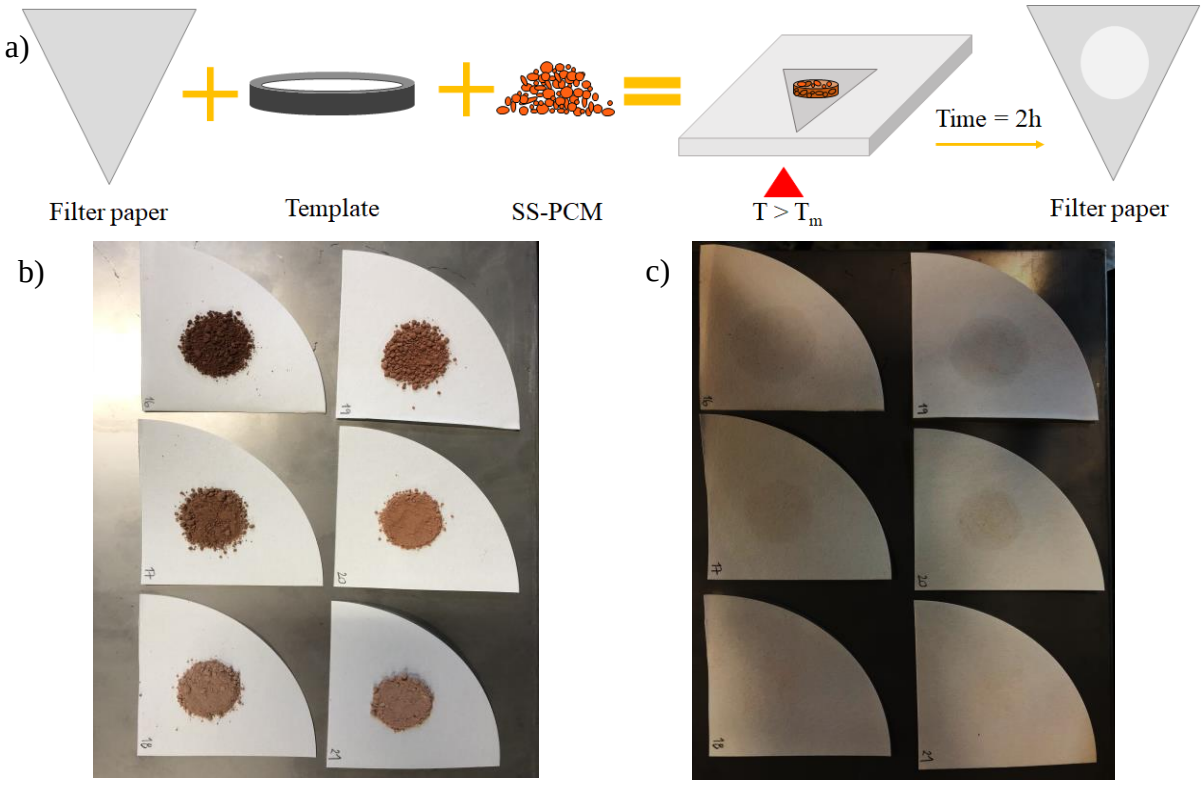

Fig. 55. Scheme of the filter paper method used to measure the leakage of the SS-PCM, a), and images of some samples before, b), and after the leakage test, c).

Thus, the weight loss of the sample, and therefore the leakage percentage, was calculated by **Eq. (9)**.

$$\%\ Leakage\ (weight\ loss) = \frac{\Delta_{wt} Paper}{wt\ sample} \times 100 \qquad \textbf{(9)}$$

Where $\Delta_{wt} Paper$ is the weight difference of the filter paper after and before the test, and $wt\ sample$ is the initial weight of the SS-PCM sample. Three measurements were done for each sample and are shown in **Fig. 56**. The results indicate that as the percentage of PCM increases, the percentage of leakage increases. For each percentage of PCM, the leakage is similar despite the differences in the molecular weights, except for the 40% of impregnation where SS-CA/MA40 presented the lower leakage, probably due to its low molecular weight compared to SS-LA/MA40 and SS-PA/SA40.

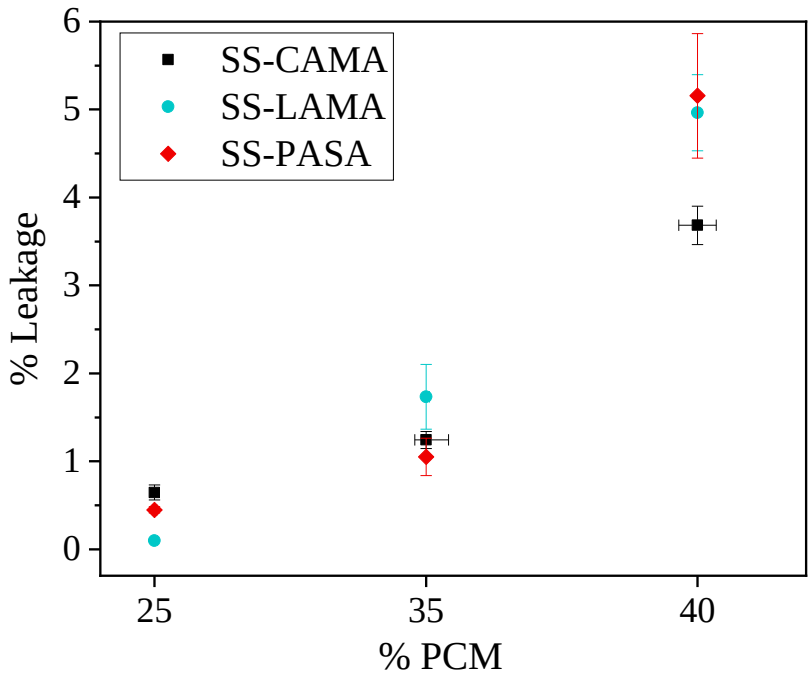

Fig. 56. Leakage test of SS-CA/MA, SS-LA/MA and SS-PA/SA with 25%, 35% and 40% impregnation ratio. Composites shape-stabilized with the raw support.

Some authors **[220]** considered that leakages below 4% are accepted as adequate for SS-PCMs, even though, there is a lack of consensus in literature about leakage evaluation as most of the works only report qualitative analysis by inspection, without presenting numbers **[121,132,215,221,222]**, or present diameter measurements of the leakage trace in filter papers

[125] accepting some leakage as normal but without reporting values. In this thesis, a leakage below 2% is accepted to maximize the energy storage efficiency of the system. Thus, composites with 35% of PCM impregnation were considered stable as the leakage percentage were 1.2%, 1.7% and 1.0% for SS-CA/MA-35, SS-LA/MA-35 and SS-PA/SA-35, respectively, indicating a good fatty acid retention ability of the support. Composites with 25% of PCM impregnation were not considered as the latent heat of fusion was low compared to 35% of PCM impregnation, as it can be seen in the next section.

It is worthy to noticed that the mineral used as support in this work, that is not a single mineralogical phase but several, presented good absorption capability compared to pure diatomite supports that are reported to have an optimum impregnation ratio between 30% and 40% **[124]**. Even more, some studies report that commercially obtained diatomaceous earth impregnated with hexadecane presented leakage losses of around 20% **[139]**, five times higher than the results obtained for these composites.

4.3. Phase change temperature and latent heat of the SS-PCMs

For an initial exploration, complete characterization was performed to the SS-LA/MA composites, and then, guided by the results obtained, the other composites, SS-CA/MA and SS-PA/SA were studied. Phase change temperatures and latent heats of the SS-LA/MA composites were determined through differential scanning calorimetry (DSC) (Q200, TA Instruments) at a rate of heating and cooling of 5 °C/min, in a nitrogen atmosphere, flowing at 50 mL/min, after 2 melt-freeze cycles.

DSC analysis were performed to understand the thermal properties of the three SS-LA/MA composites obtained. Comparison curves of eutectic LA/MA, raw support and the SS-LA/MA composites fabricated with the three different impregnation ratios are presented in **Fig. 57**. As expected, the area under the curves decrease with decreasing the amount of LA/MA present in the composite, indicating that the latent heat of fusion and latent heat of solidification decreases. The raw powder material, acting as a porous support of the PCM, do not present phase changes in the studied temperatures, demonstrating that all the thermal properties are due to the eutectic phase change material added. Besides, the difference in the

phase change temperatures of the composites and the pure eutectic can be explained by the partial restriction of the free movements of PCM molecules into the porous support **[131]**.

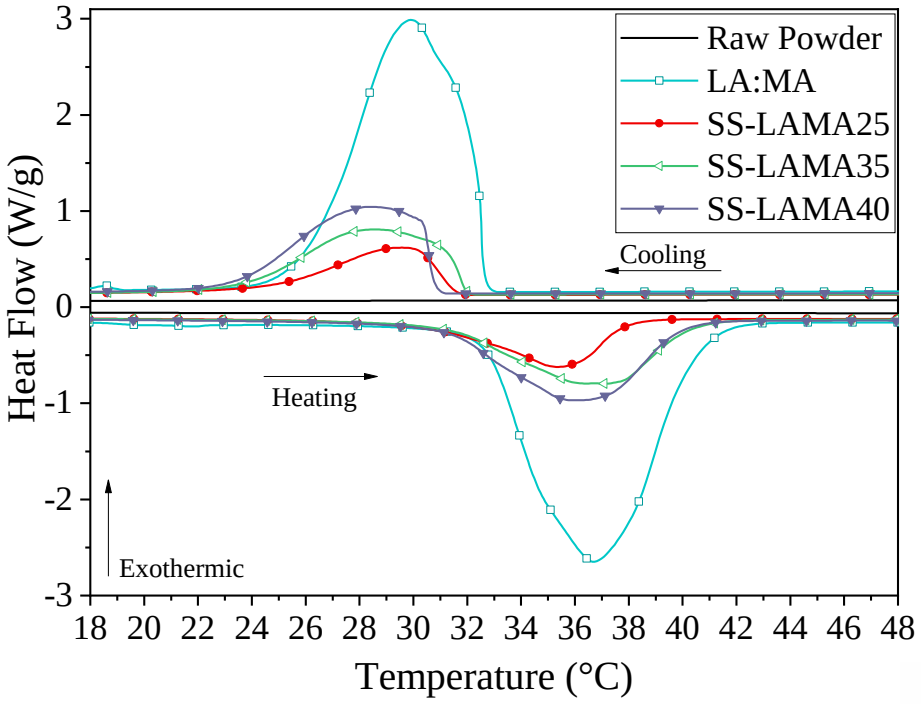

Fig. 57. DSC curves of eutectic LA/MA, raw powder support, SS-LA/MA25, SS-LA/MA35, and SS-LA/MA40.

The composites SS-LA/MA-25, SS-LA/MA-35, and SS-LA/MA-40 presented latent heats of fusion (ΔH_m) values of 29.63 kJ/kg, 51.57 kJ/kg, and 56.59 kJ/kg and latent heats of solidification (ΔH_s) values of 27.78 kJ/kg, 48.55 kJ/kg, and 55.99 kJ/kg, respectively. These values are comparable to the heat storage capacities of similar composites reported in literature **[124,125,223]** or even higher **[221]**. The onset melting phase change temperatures ($T_{m,onset}$) were similar for the three composites, being 31.14 °C, 31.00 °C, and 31.12 °C, and the maximum peak melting temperatures ($T_{m,peak}$) were 35.39 °C, 36.35 °C, and 36.17 °C for the SS-LA/MA25, SS-LA/MA35, SS-LA/MA40, respectively. The solidification data ($T_{s,onset}$ and $T_{s,peak}$) presented a larger range probably due to that nucleation is a statistical effect and is not well defined. The data for melting and solidification of the composites is summarized in **Table 26**. These results are in agreement with the data reported in literature **[181,224]**.

Table 26. Thermal properties of SS-LA/MA-25, SS-LA/MA-35, and SS-LA/MA-40 composites shape-stabilized with the raw support.

Sample	Melting			Solidification		
	$T_{m,\ onset}$ (°C)	$T_{m,\ peak}$ (°C)	ΔH_m (kJ/kg)	$T_{s,\ onset}$ (°C)	$T_{s,\ peak}$ (°C)	ΔH_s (kJ/kg)
SS-LA/MA-25	31.14	35.39	29.63	31.57	29.57	27.78
SS-LA/MA-35	31.00	36.35	51.57	31.97	28.65	48.55
SS-LA/MA-40	31.12	36.17	56.59	30.76	28.62	55.99

According to the obtained values of enthalpies, phase change temperatures and leakage, the most promising composite for thermal energy storage was the SS-LA/MA-35, as the thermal values obtained were similar to the SS-LA/MA-40 but with less leakage loss. These data showed that the SS-LA/MA composites fabricated in this research have considerable TES potential for low thermal applications particularly for industrial uses during production, transport or storage of food, beverages, fermentation processes, pharmaceutical products or cooked food **[23,24,225]** as the maximum peak phase change temperature is around 36 °C.

From the results of SS-LA/MA and considering that the three eutectic mixtures behavior should be alike, composites with 35% of impregnation, SS-CA/MA-35 and SS-PA/SA-35, were selected for further characterization. The phase change temperatures and latent heats measured through DSC are shown in **Fig. 58** and presented in **Table 27**. The peak and onset values of melting and solidification temperatures were similar to the values obtained for the binary eutectics, with differences below 3 °C. These variations are considered low, meaning that the support did not change considerable the phase change temperatures of the binary eutectic mixtures. These shifts can be attributed to physical interactions among the components of the composite, i.e., the support and the PCM **[130]**.

Table 27. Thermal properties of SS-CA/MA-35 and SS-PA/SA-35 composites, shape-stabilized with the raw support.

Sample	Melting			Solidification		
	$T_{m,\ onset}$ (°C)	$T_{m,\ peak}$ (°C)	ΔH_m (kJ/kg)	$T_{s,\ onset}$ (°C)	$T_{s,\ peak}$ (°C)	ΔH_s (kJ/kg)
SS-CA/MA-35	19.99	22.63	39.81	20.53	19.04	38.21
SS-PA/SA-35	51.83	54.96	50.35	52.16	50.92	50.94

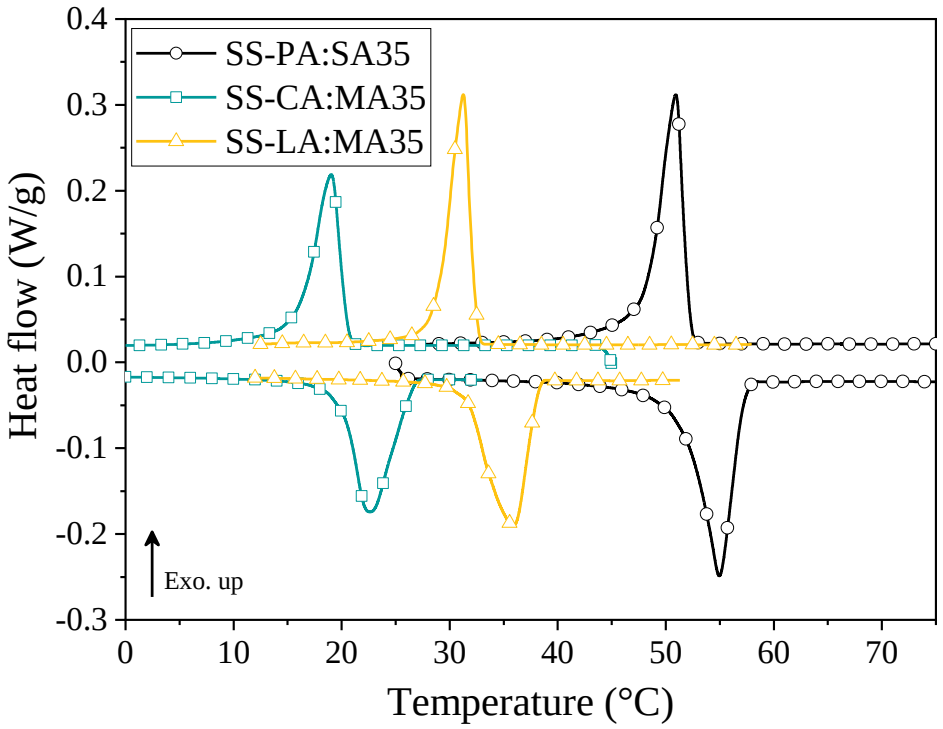

Fig. 58. DSC curves of SS-CA/MA-35, SS-LA/MA-35, and SS-PA/SA-35 composites shape-stabilized with the raw support.

Regarding the enthalpy, the composites SS-CAMA-35 and SS-PASA-35 presented 39.81 kJ/kg and 50.35 kJ/kg, respectively. The obtained values are comparable to the latent heats of similar composites reported in literature **[123,125,130,132]**. Moreover, should be considered that SS-PCMs enthalpy measurements include the weight of the support (65 wt.%) plus the weight of the eutectic (35 wt.%). The enthalpy change of the support material is equal to zero as not thermal changes may occur in the temperature range of the measurement. The decrease of enthalpy of the SS-PCMs compared to the pure PCM (**Fig. 28**), is about 7% (approx. 7 kJ/kg), that is a manageable change. Furthermore, other advantages of the produced SS-PCM must be considered as an ease handling for several applications, phase change temperatures in a wide range (23 °C to 55 °C) that allow different kind of uses and leveraging of local natural occurring minerals.

4.4. Heat capacity of the SS-PCMs

Modulate differential scanning calorimetry, MDSC, was used for measured specific heat capacity of SS-PCMs composites, with the same conditions stablished for the heat capacity

measurements of the eutectic binary mixtures. The specific heat capacity signal was calibrated using a sapphire disk. The samples were run in temperature range from -10 °C to 45 °C, 10 °C to 60 °C, and 25 °C to 80 °C, for samples containing CA/MA, LA/MA and PA/SA, respectively.

Specific heat capacities as a function of temperature, $C_p(T)$, of the support, the binary eutectic mixtures and the SS-PCMs composites (35% of PCM) were measured (**Fig. 59**). The measurement of C_p during phase change transition is complicated as two phenomena (C_p and phase change) are occurring simultaneously and contribute to the modulated heat flow amplitude, creating an apparent high value for C_p, as shown in the curves. Thus, the three SS-PCM-35 composites, as well as the three binary eutectic mixtures, presented clear peaks in the temperature region attributable to the respective phase change transition.

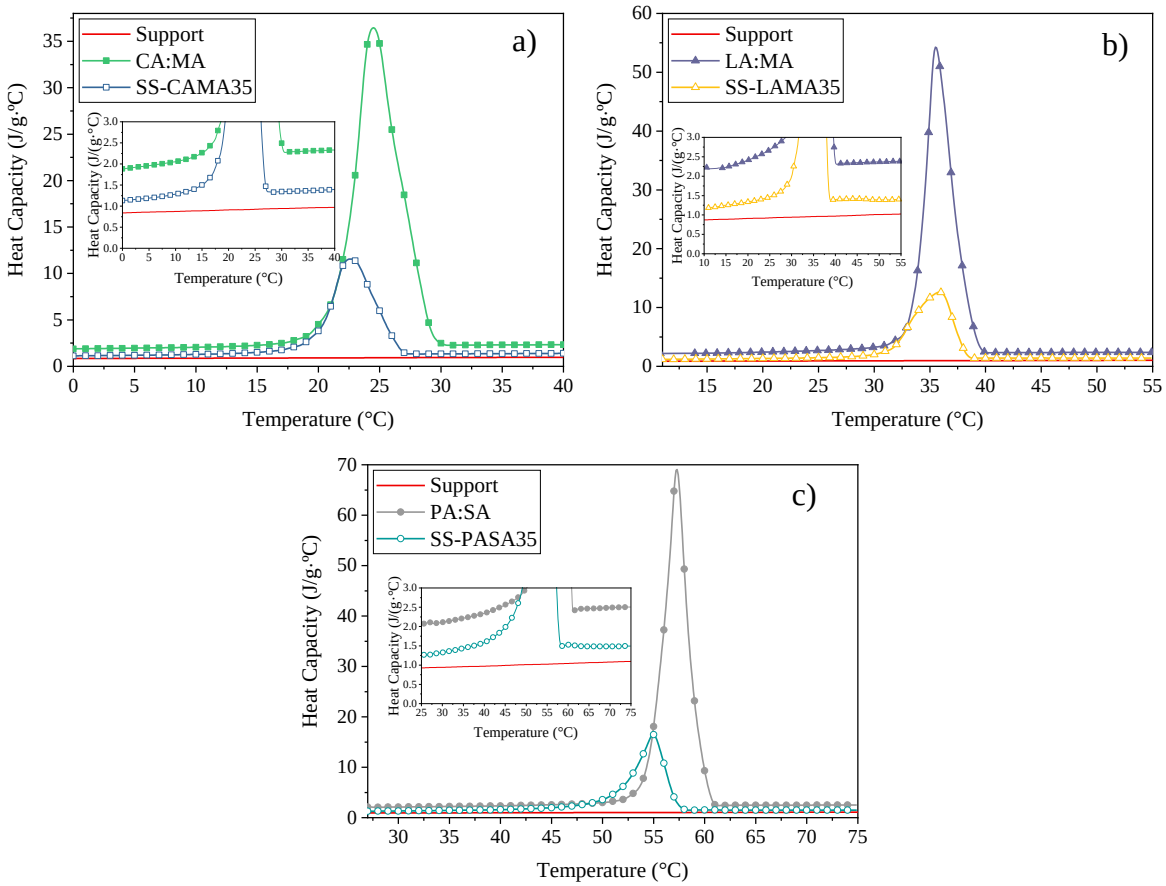

Fig. 59. Heat capacities as a function of temperature of a) the support, CA/MA, SS-CAMA-35, b) LA/MA, SS-LAMA-35, and c) PA/SA, SS-CAMA-35. The inset shows a detail in the region under 3.0 J/g·°C.

Nevertheless, values obtained for C_p were accurate in the liquid and solid regions (before and after the phase change transition). The temperature dependence of C_p was model trough semi-empirical fitting of experimental data. The equations obtained for the SS-PCMs and the raw support are presented in **Table 28** and **Table 29**, equations for the binary eutectic mixtures are presented in Chapter II. The temperature interval at which these equations are valid is presented as T_i and T_f. All the adjusted equations correspond to second grade and third grade polynomial equations with R-squared greater than 0.95, indicating good agreement in the fitting. The importance of having more proposed empirical models for specific heat capacity in the literature lies in that some of the existing ones **[185]** are limited and do not accomplished complex systems as binary eutectics or SS-PCMs.

Table 28. Equations of heat capacity for the solid phase of SS-CA/MA-35, SS-LA/MA-35, SS-PA/SA-35 produced with the raw support. $\boldsymbol{C_p(T) = B_0 + B_1 \cdot T + B_2 \cdot T^2}$.

Sample	B_0	B_1	B_2	*RSS*	R^2	*Adj.* R^2	T_i (°C)	T_f (°C)
SS-CA/MA-35	1.15	5.19E-4	1.40E-3	1.07E-2	0.992	0.992	0	15
SS-LA/MA-35	1.54	-4.26E-2	1.60E-3	7.19E-3	0.994	0.993	15	28
SS-PA/SA-35	3.81	-16.10E-2	2.67E-3	4.20E-2	0.990	0.990	30	45
Support	0.84	3.56E-3	-1.54E-6	7.78E-3	0.998	0.998	-10	80

Table 29. Equations of heat capacity for the liquid phase of SS-CA/MA-35, SS-LA/MA-35, SS-PA/SA-35 produced with the raw support. $\boldsymbol{C_p(T) = B_0 + B_1 \cdot T + B_2 \cdot T^2 + B_3 \cdot T^3}$.

Sample	B_0	B_1	B_2	B_3	*RSS*	R^2	*Adj.* R^2	T_i (°C)	T_f (°C)
SS-CA/MA-35	1.33	-3.03E-3	1.17E-4	-	4.83E-5	0.997	0.997	30	40
SS-LA/MA-35	-21.29	1.44	-3.01E-2	2.14E-4	5.70E-4	0.954	0.953	42	52
SS-PA/SA-35	-5.89	0.34	-5.18E-3	2.64E-5	3.30E-5	0.969	0.968	64	74

The C_p of the raw support presented slight changes during the temperature range measurement (inset **Fig. 59**), with heat capacities values between 0.8 and 1.0 J/g·°C. The binary eutectics, as stated in Chapter II, presented average values in the solid phase of 1.97 J/g·°C , 2.54 J/g·°C, and 2.40 J/g·°C, and in the liquid phase of 2.31 J/g·°C, 2.40 J/g·°C, and 2.50 J/g·°C, for CA/MA, LA/MA, and PA/SA, respectively. Likewise, the heat capacity average values for the SS-PCMs were 1.22 J/g·°C, 1.41 J/g·°C, and 1.68 J/g·°C for the solid phase, and 1.38 J/g·°C, 1.40 J/g·°C, and 1.50 J g^{-1} $°C^{-1}$, for the liquid phase, for SS-CA/MA-35, SS-LA/MA-35 and SS-PA/SA-35, respectively. As it can be notice, the support is

diminishing the heat capacity of the SS-PCMs systems as C_p of the binary eutectics, both solid and liquid, is higher than the C_p of the SS-PCMs. As an assumption, some atomic vibrations at the eutectics could be limited by the support itself at the interphase scale due to strong interaction with the fatty acids, reducing the average value of kinetic energy into the system and thus reducing heat capacity. As an overall value, the supports seem to reduce a 40% of the heat capacities of the pure binary eutectics, but it has to be take into consideration that the SS-PCMs only contain 35% of the pure binary eutectic, then, theoretically, every gram of the SS-PCM might consist of 65% of the support and 35% of the PCM. Thus, the final heat capacity of the SS-PCMs are increasing, in average, a 0.7%, 0.6% and 0.9%, for SS-CA/MA, SS-LA/MA and SS-PA/SA, respectively, compared to having 0.35 of the heat capacities of the pure binary eutectics.

4.5. Morphology of the SS-PCM

Morphology and microstructure of SS-CA/MA-35, SS-LA/MA-35 and SS-PA/SA-35 were analyzed through a scanning electron microscope (SEM) (JEOL JSM-6490LV), with an accelerating voltage of 20 kV. Images are shown in **Fig. 60**, **Fig. 61**, and **Fig. 62**. As it can be noticed, the SS-PCMs presented rounded morphologies due to the production process that included a mechanical mixing around an axis. Surprisingly, although the support used for shape-stabilized the PCMs was the same for the three composites, differences in the particle size distribution of the obtained composites can be observed. SS-CA/MA-35 exhibit smaller particle size distribution than SS-LA/MA-35 and SS-PA/SA-35, being the last the one with the largest particle size. Difference in particle size could be due to the molar volumes of the binary eutectic mixtures. CA/MA have the smallest molar volume, and PA/SA the biggest, thus, the aggregates should be larger for the eutectics with the greatest molar volume.

Despite the differences in the particle size distribution of the SS-PCMs, the leakage percentage remain similar among the composites (< 2%) indicating that the impregnation and the capillary forces are comparable between them. In the SEM images can be noticed that the eutectics filled the diatomites and agglomerate the non-porous particles of the mineral support. Given that these findings are based on the observation of the SS-PCMs in the solid

phase, further analysis, probably by in-situ SEM technique, could be done to fully understand the morphology of the SS-PCMs when change to the liquid phase.

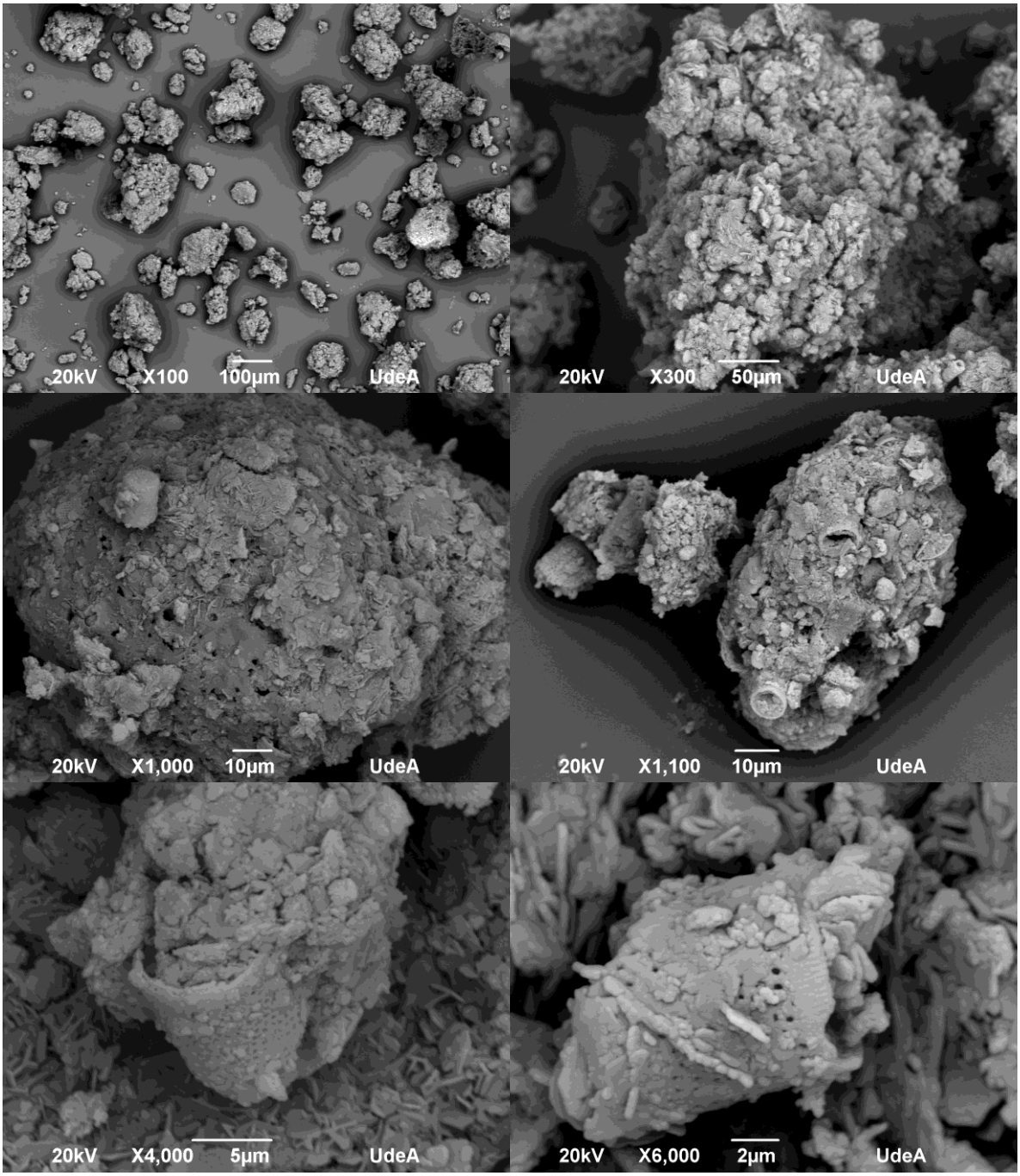

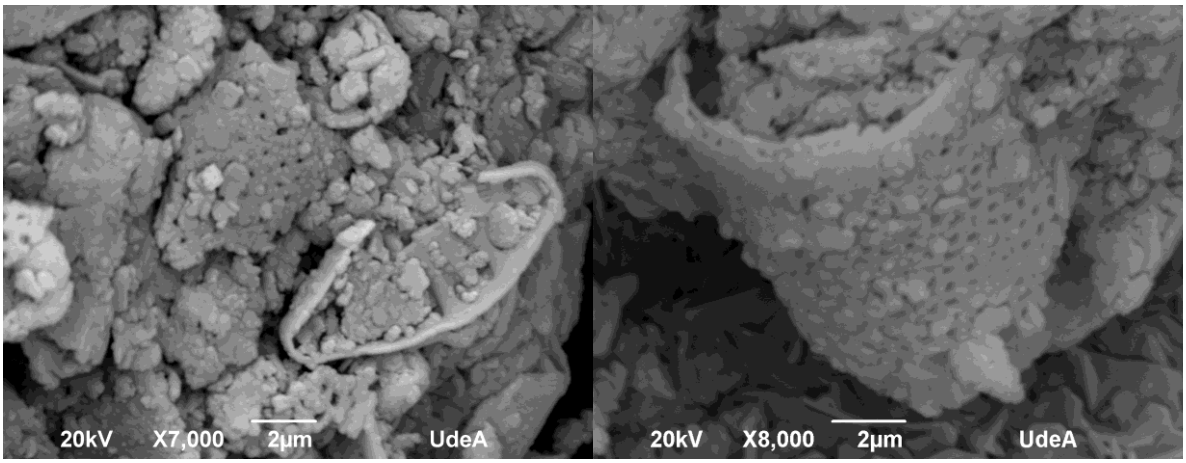

Fig. 60. SEM images of SS-CA/MA-35.

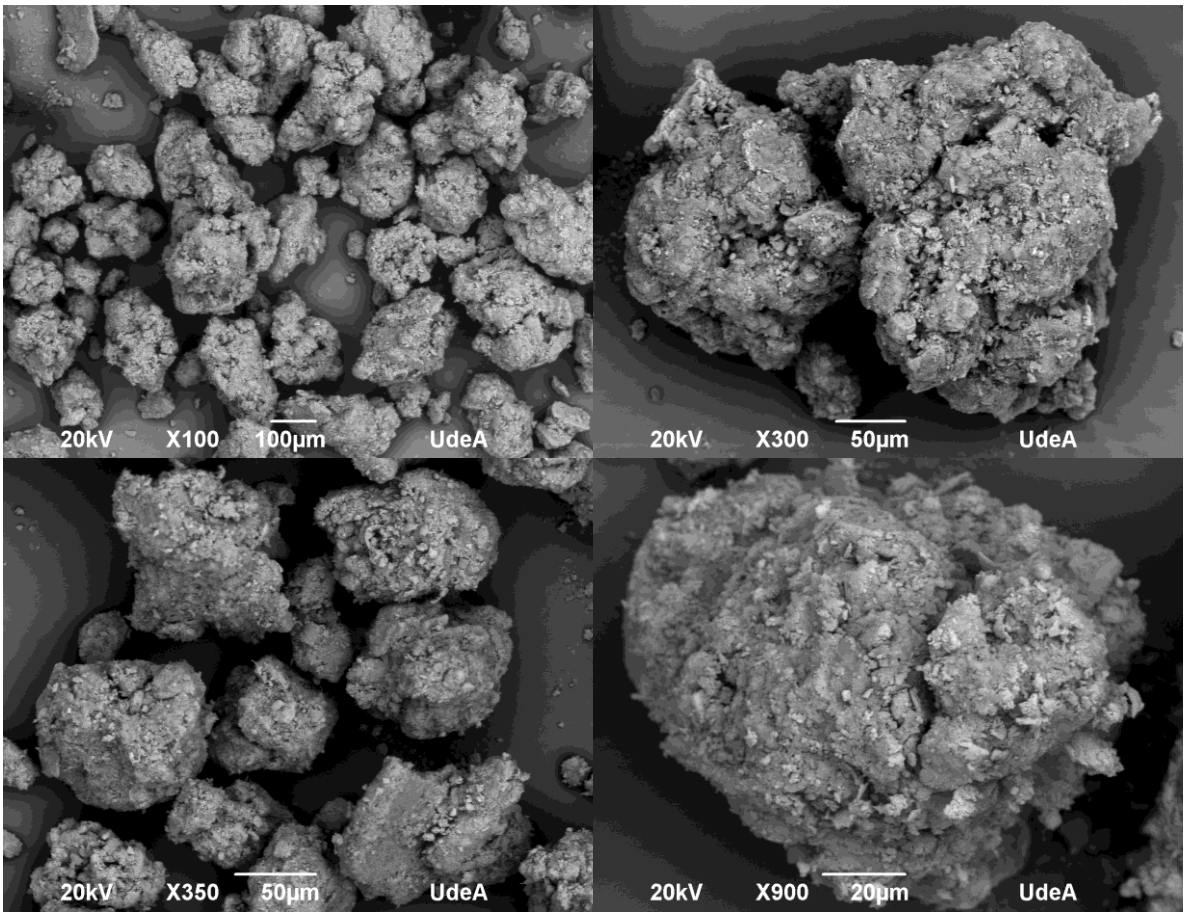

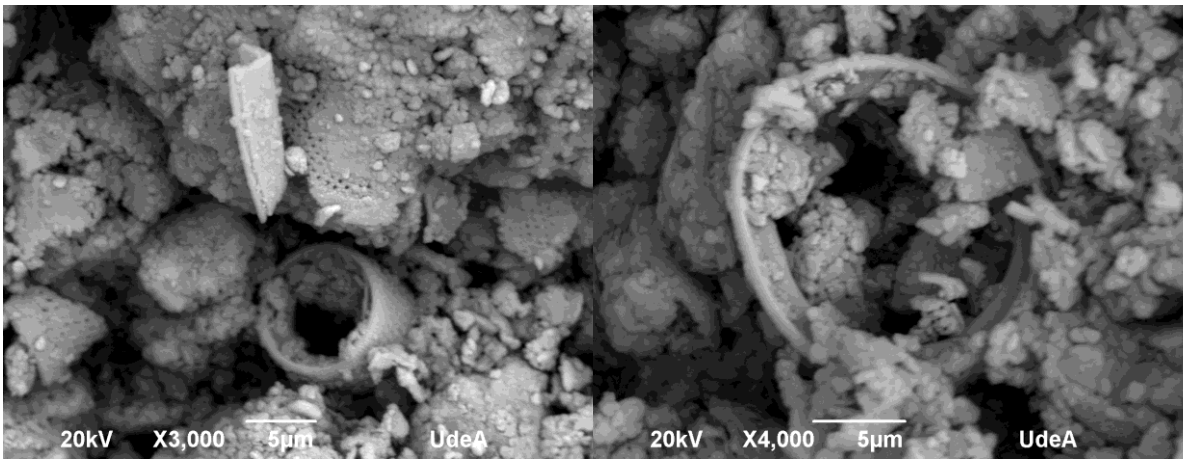

Fig. 61. SEM images of SS-LA/MA-35.

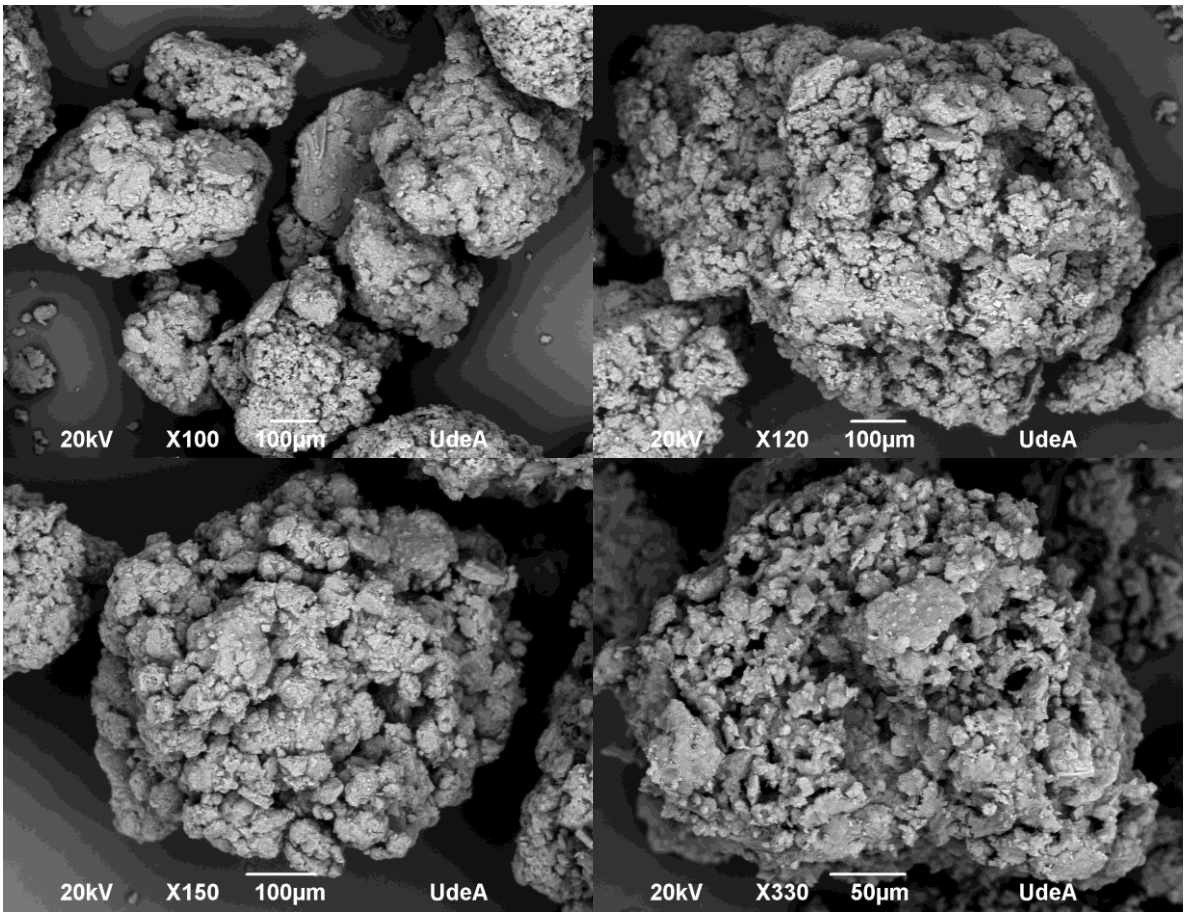

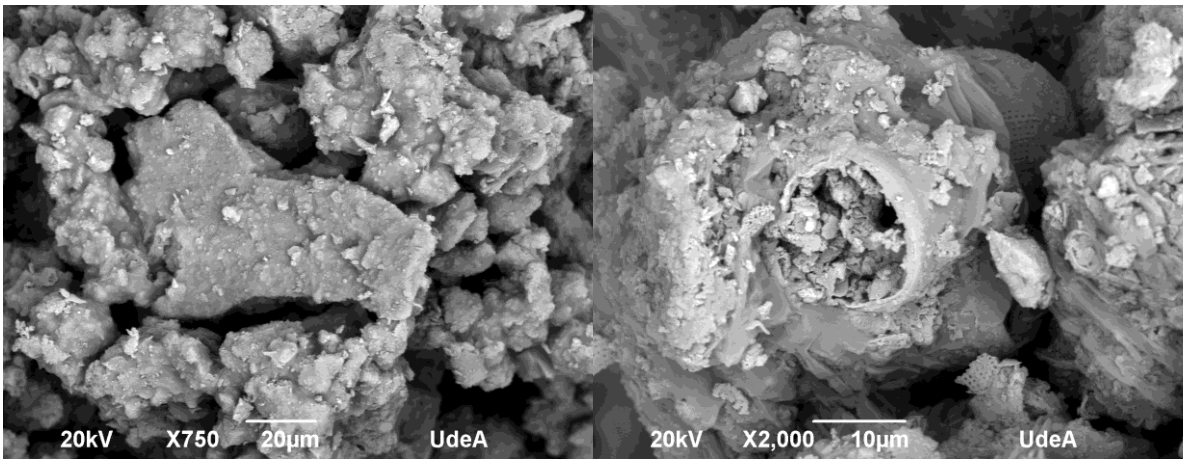

Fig. 62. SEM images of SS-PA/SA-35.

4.6. Conclusions

Taken together, these results suggest that the production of SS-PCMs through the vacuum assisted impregnation method was successfully address for CA/MA, LA/MA and PA/SA using the raw mineral support. The best composites obtained were SS-CA/MA-35, SS-LA/MA-35 and SS-PA/SA-35, using 35% of PCM impregnation, with melting temperatures of 23 °C, 36 °C and 55 °C, respectively. The wide range of temperatures offered by these composites are intended for diverse applications as in construction (SS-CA/MA-35), food industry (SS-LA/MA-35) and domestic hot water tanks (SS-PA/SA-35). Leakage was less than 2% for all the SS-PCMs, indicating a good performance of the systems compared to other similar composites found in literature, probably as a result of the inorganic support used for shape-stabilization as comprises several mineralogical phases that together can be more effective to absorb organic PCMs as fatty acids than pure mineralogical phases. Melting enthalpies were between 40 kJ/kg, and 50 kJ/kg, and average heat capacities of 1.4 J/g·°C.

Likewise, empirical equations for specific heat capacity as a function of temperature were obtained for the SS-PCMs in the solid and liquid region. These models are useful to improve the design stage of TES systems and to develop better simulations regarding solid and liquid phases. This information is not widely available in literature for binary fatty acids eutectic mixtures, nor for SS-PCMs.

CHAPTER V.

Physical and chemical modifications of the support

Improvement of the support material to achieve better shape-stabilized PCMs in terms of thermal properties were performed. Physical and chemical processes were proposed to modify or to functionalize the support and improve the bond between the fatty acid eutectics and the inorganic support. In this way, higher PCM loading and a lower leakage can be reached.

Particularly, the influence of three kind of modifications on the absorption and thermal properties of the clay mineral support used for shape-stabilization of the PCMs were studied:

- Effect of granulation: the powder support was granulated until forming fine granules and coarse granules.
- Effect of thermal treatments: the support was calcined at 400 °C, 500 °C, 600 °C, 900 °C, and 1100 °C in order to study their surface area, pore volume, and pore size through Brunauer-Emmet-Teller (BET) and Barrett-Joyner-Halenda (BJH) analysis.
- Effect of interlayer grafting: the powder support was chemically modified by intercalation of dimethylsulphoxide (DMSO) and grafting of 3-aminopropyltrietoxysilane (APTES).

After these modifications, the obtained supports were used to prepare shape-stabilized phase change materials, that were compared in terms of leakage percentage and thermal properties with the SS-PCMs stabilized with the raw support.

5.1. Granulation and thermal treatments of the support

Textural properties, as pore volume, surface area, and pore size, are physical properties that describe the morphology of porous materials. Different materials can present identical

particle sizes but complete distinct textural properties, leading to different properties and so, final applications. Particularly, the loading amount of phase change materials (PCM) within shape-stabilized phase change materials (SS-PCMs) depend, to some extent, on the porosity of the support employed. Hence, the supports of the SS-PCMs can be optimized by improving their textural properties to increase the loading amount of PCM, and so, obtain better thermal storage properties. Changes of the porosity of a clay support can be achieved through heat treatments, chemical reactions or physical modifications. The following sections provide an overview of granulation and heat treatments performed to the raw clay support, as well, as the thermal properties when used those modified supports for shape-stabilization of PCMs.

5.1.1. Granulation process

The granulated samples were obtained from the powder raw support, through a granulation process in an Eirich Lab High Intensity Mixer (Approx. 10 L), with and inclined pan mixer, as shown in **Fig. 63**. The mixer consists in a stainless-steel pan and rotor, 315 mm diameter pan x 245 mm deep (approximately), with a 5.5 HP High speed rotor, variable speed, that runs both directions. The powder support was mix with a commercial water-based binder to help the granules to form. Two kind of granulated materials were obtained, a fine granulated and a coarse granulated material, as presented in **Fig. 64**.

Fig. 63. Eirich lab high intensity mixer.

The particle size distribution of the powder was measured by a Malvern Mastersizer 3000 particle size analyzer. For determining the particle size distribution of the granulated materials, a set of Tayler test sieves stacked vertically with mesh sizes ranging from 325 mesh (45 µm) to 4 mesh (4750 µm) were used **[226]**. The resulting particle size distribution curves are shown in **Fig. 65**. The median diameter Dv.50 for the powder sample, fine granulated, and coarse granulated samples, were 10.60 µm, 350 µm, and 1050 µm, respectively. By visual inspection, it can be notice that the particle size of the powder increases after granulation, as well, the morphology of the granulated samples is round-shaped due to the high intensity mixer process.

Fig. 64. Powder raw support, fine granulation and coarse granulation (from left to right).

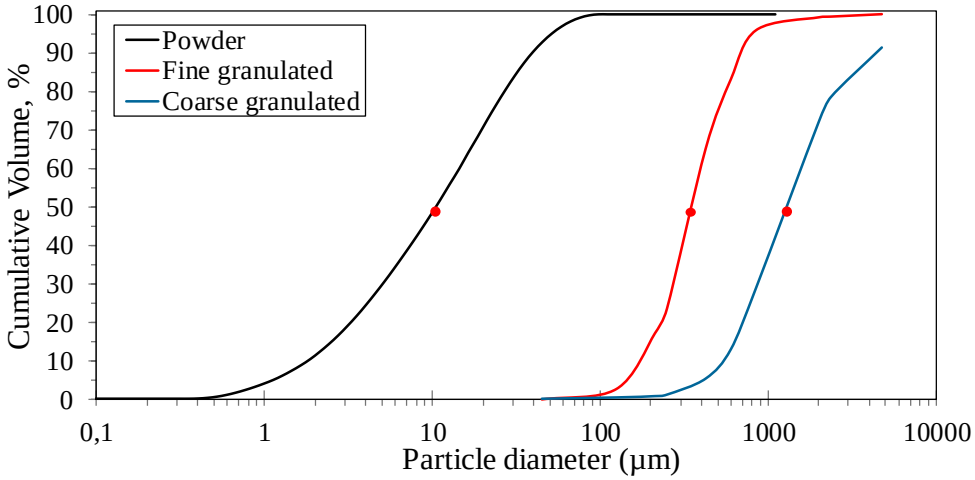

Fig. 65. Particle size distribution of the powder support, fine granulated, and coarse granulated materials.

5.1.2. Heat treatments

After the granulation, the supports were calcined in a laboratory box furnace (Naber D-2804) at several temperatures (**Fig. 66**). The cooling was done naturally after the furnace was off. The final samples were named according to the calcination temperature, and the granulation process, as powder (P), fine granulated (G) or coarse granulated (CG). Description of the samples is presented in **Table 30**.

Table 30. Sample description of the powder, fine granulated and coarse granulated supports.

Sample	Particle size description	Heat treatment (°C)
RP	Powder	None
P4	Powder	400
P5	Powder	500
P6	Powder	600
P9	Powder	900
P11	Powder	1100
RG	Fine granulated	None
G6	Fine granulated	600
G9	Fine granulated	900
G11	Fine granulated	1100
CG	Coarse granulated	None
CG6	Coarse granulated	600
CG9	Coarse granulated	900
CG11	Coarse granulated	1100

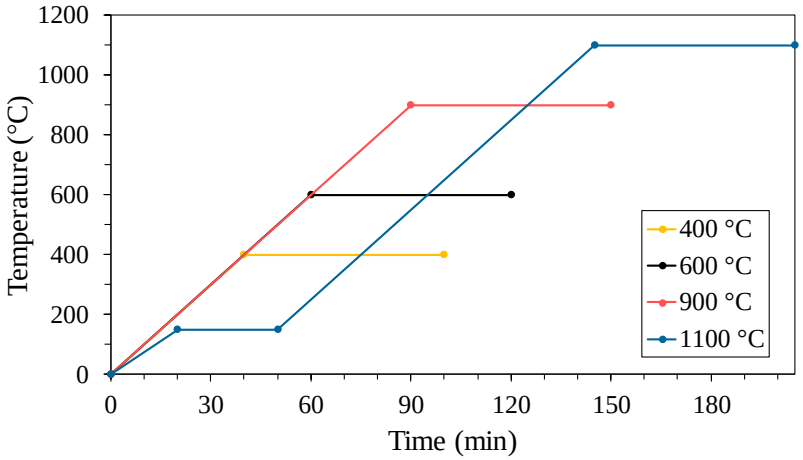

Fig. 66. Temperature ramp rates used for the heat treatments.

The mineralogical phases of the calcined supports were studied and presented in previous chapters.

5.1.3. Porosity of the supports

The porosity of the supports was assessed by N_2 adsorption-desorption isotherms using the Brunauer-Emmet-Teller (BET) theory, and the average pore diameters and pore volume were evaluated from the desorption branch using the Barrett-Joyner-Halenda (BJH) model, through a Micromeritics Instrument, Gemini V2380. The isotherms of the powder supports are shown in **Fig. 67**, the classification of the type of isotherms and hysteresis used in this study was in accordance to the IUPAC **[214]**, as well as the classification of the pores, being micropores (< 2 nm), mesopores (2-50 nm) and macropores (> 50 nm). **Fig. 67** shows that isotherms of RP, P4, P5, P6, and P9 supports appear to exhibit Type-II curve with H3-type hysteresis loop. Type-II isotherms are the result of unrestricted monolayer-multilayer adsorption. The beginning point of the linear section is considered as the point where completion of monolayer coverage is achieved. The increase when $P/P_0=1$ indicates the formation of an adsorbed nitrogen multilayer, usually due to the existence of macropores. From the respective insets, it could be noticed that the pore widths are in the mesopore scale, and there are none or very low amount of micropores in the samples. The H3-type hysteresis loop corresponds to non-rigid aggregates of plate-like particles **[214]** and demonstrates the presence of mesopores that are filled and empty by capillary condensation **[215]**. These results indicate that in the RP, P4, P5, P6, and P9 supports the main size of pores are mesopores and the more likely type of pores are slit-shaped pores. Such features are in accordance with the presence of kaolinite, mica/illite, and diatomite in the supports, as studied in previous chapters. The support P11 presented a very low amount of N_2 adsorbed compared to the other supports, indicating a low porosity that is in accordance with the pore volume distribution shown in the inset.

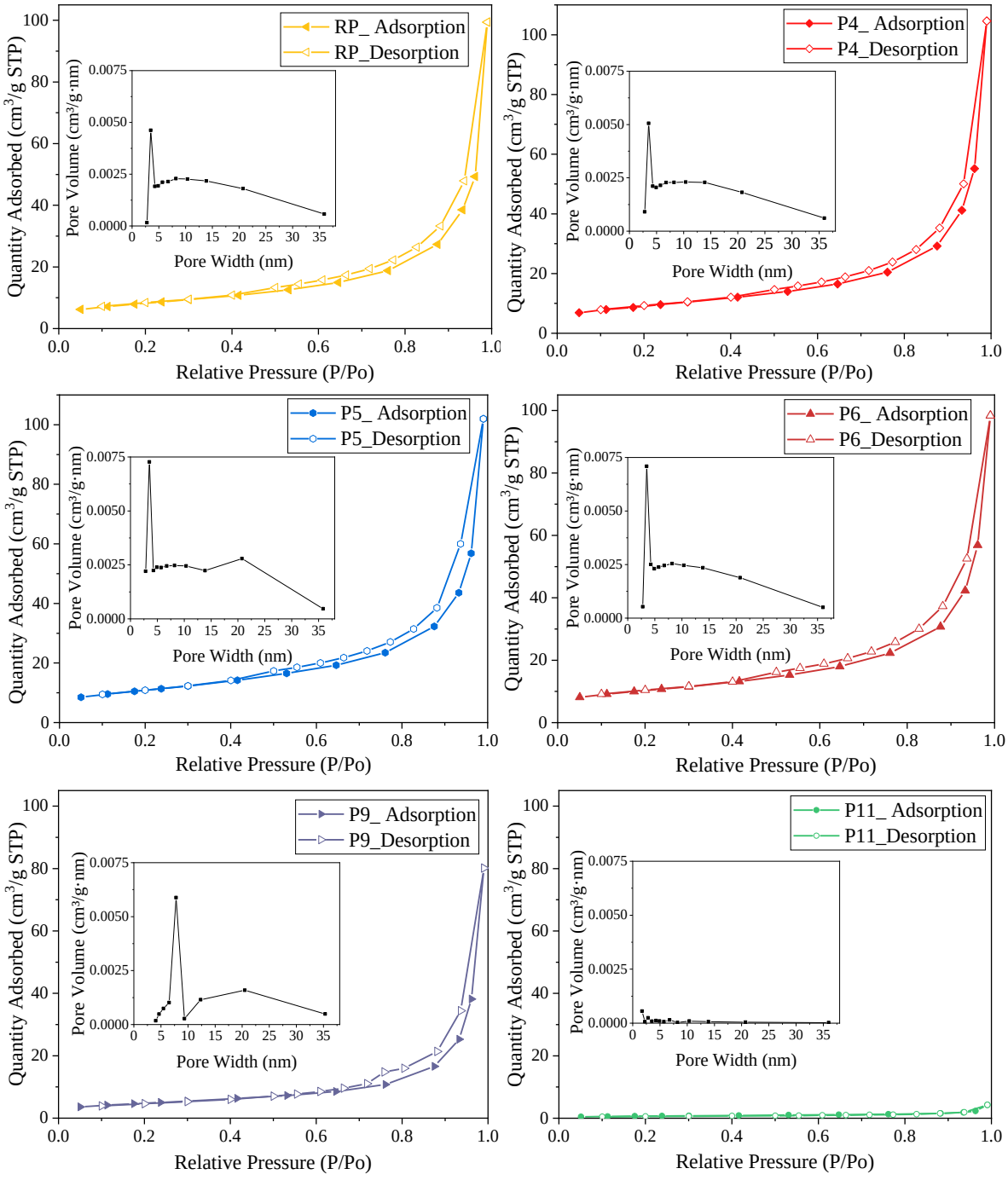

Fig. 67. N_2 adsorption-desorption isotherms for the powder supports RP, P4, P5, P6, P9, and P11. Inset shows the BJH pore size distribution for the same materials.

Regarding the calcination temperature of the powder supports, as the temperature increases the BJH desorption cumulative volume of pores, V_{pore}, remain almost the same (0.156 ± 0.0042 cm^3/g) until 900 °C (0.124 cm^3/g), then a drastic decrease occurs at 1100 °C

reaching 0.007 cm^3/g, as shown in **Fig. 68**. The BJH desorption average pore width, d_{BJH}, was the same for the RP (18.58 nm) and P4 (18.38 nm) supports, while there was a slight decreased of 2.3 nm when the temperature was around 500 °C (15.85 nm) and 600 °C (16.47 nm). At 900 °C the pore size increased to 22.43 nm and then at 1100 °C the smallest size appeared (12.47 nm). The BET surface area, S_{BET}, started growing up from the RP support (29.12 m^2/g), followed by P4 (32.33 m^2/g) until reaching 500 °C and 600°C, where the surface areas were 37.88 m^2/g and 35.48 m^2/g, respectively. Then, at 900°C the surface area decreases almost half, 16.99 m^2/g, to finally reached 2.49 m^2/g for the P11 support. The trends observed here are in good agreement with the sintering phenomena **[227]** and mineralogical phase changes that occur when the temperature increases for clay minerals, as the supports studied in this work, containing kaolinite, mica/illite, and diatomite. In general, in the first stage, below 500 °C dehydration occurs, coordination water is lost, organic material is degraded and some holes in the diatomite appeared to be open, due to the loss of some impurities **[121]**, increasing the total BET surface area, then, at 600 °C – 900 °C, some structures collapses (e.g. kaolinite) due to dehydroxylation processes and the few existing mesopores disappear and finally, with temperatures as high as 1100 °C, sintering occurs, leading to a low pore volume and nearly zero pores. It is worthy to note that some works **[228]** that presented pure diatomite supports found surface area values of 11.09 m^2/g and 16.12 m^2/g and pore sizes of 9.42 nm and 7.54 nm, being values presented in this study almost double. This could be an indication that the studied supports showed good morphological properties that can be used for shape-stabilization of PCMs.

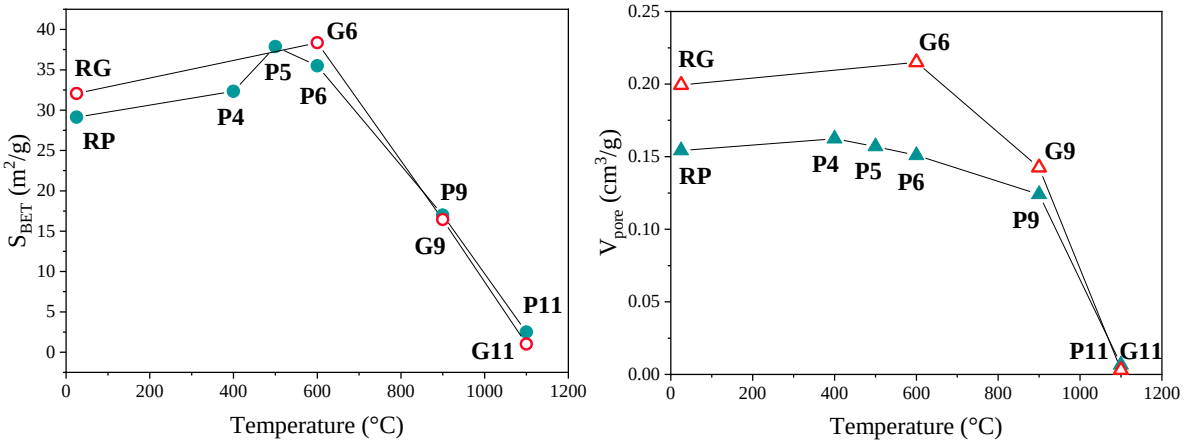

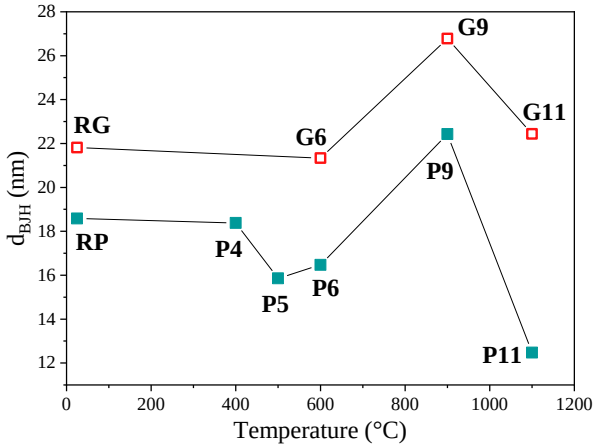

Fig. 68. Textural properties of the supports as a function of calcination temperature, for the fine granulated (G) and, powder (P) supports.

A similar analysis can be conducted for the fine granulated supports, G. The surface area, pore volume, and pore width are illustrated in **Fig. 68**. The textural properties of these supports followed the same trend with temperature as the powder supports. The BET area is similar between the P and G supports, except at 25 °C and 600 °C, being 3 m^2/g higher for RG and G6, compared to RP and P6, respectively. Even though the BET area seems comparable within the P and G supports, the pore volume and pore width exhibit major changes. For instance, the pore volume for RG, G6, and G9 increased a 29.2%, 42.5% and 14.8%, respectively, compared with RP, P6, and P9. This was expected as the granulated supports contained a bigger pore network between the particles due to the granulation process. For 1100 °C temperature the pore volume decreased for the G11 support, matching the P11 support, indicating that this calcination temperature governs the pore volume despite the size of the supports. This is in accordance with the sintering explanation given before for the powder supports. As for the pore widths, the G supports showed bigger pore sizes than the P supports. The maximum pore width was 26.8 nm for the G9 support, followed by 22.4 nm for the G11. The RG and G6 presented the smaller pore widths, 21.8 nm, and 21.3 nm, respectively.

In **Fig. 69**, the N_2 isotherms for RG, G6, G9, and G11 are presented. The isotherm curves presented the same isotherm type as for the P supports, Type-II with H3-type hysteresis loop, besides the behavior of the isotherms with temperature remains similar. The difference lies in the amount of N_2 adsorbed, which for the G supports is higher. This agrees with the textural

properties of the supports previously discussed. The insets showed a predominant mesopores range for all supports, except for the G11, that like P11, exhibited nearly zero pore volume and almost no quantity adsorbed of N_2.

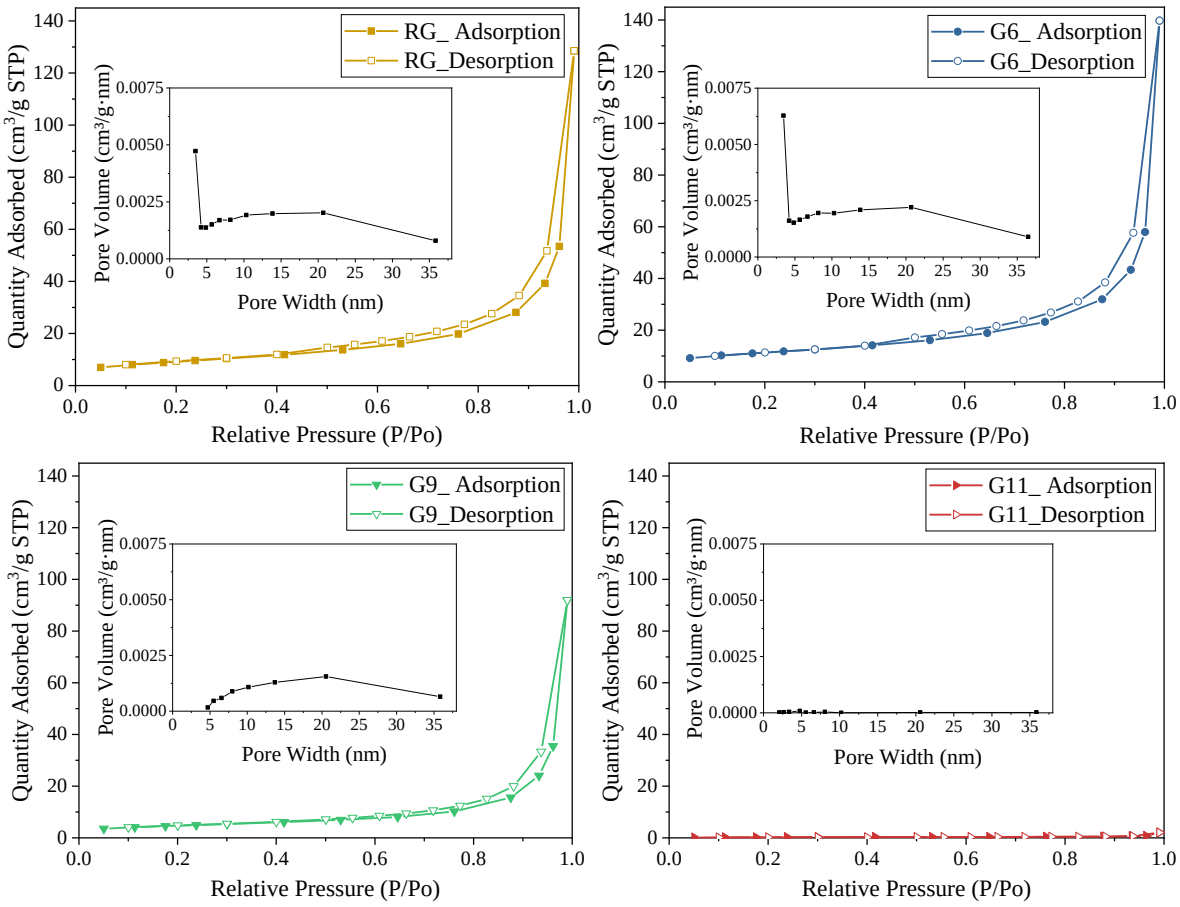

Fig. 69. N_2 adsorption-desorption isotherms for the fine granulated supports RG, G6, G9, and G11. Inset shows the BJH pore size distribution for the same materials.

The N_2 isotherms obtained in this study are in agreement with the results presented in literature about pure diatomite **[215,228]**, illite **[229]**, and kaolinite **[230]** samples. Minerals that contained those mineralogical phases are most likely to present the same sorption characteristics. It should be borne in mind, however, that adsorption-desorption isotherms only considered porosity up to 50 nm, then by SEM inspection, as shown in previous chapters, it could be seen that the minerals of the supports, particularly the diatomite, present macropores in the 200-300 nm range. Moreover, the pore network geometry and topology, especially for the granulated G supports, can be difficult to characterize due to the wide range of length scales **[231]**.

In the same manner, the porosity of the coarse granulated (CG) particles was analyzed by N_2 adsorption-desorption isotherms (**Fig. 70**), as well as their textural properties (**Fig. 71**). In general, the coarse granulated supports presented the same trends observed and discussed previously, including the type of isotherms. The raw coarse granulated support, compared to the fine granulated support, presented a pore volume increase for the pore width between 8 nm and 16 nm. The CG6 and CG9 showed a pore volume increased, as well, between 15 nm and 25 nm, compared to the G6 and G9 supports, respectively. The support calcined at 1100 °C, CG11, displayed a low curve, indicating a low absorption/desorption of nitrogen, just like P11 and G11. These findings suggest that the coarse granulated supports have bigger pore widths that the fine granulated and powder supports, and that heat treatments up to 1100 °C, despite the size of the particles, generate an almost non-porosity materials regard macropores (> 50 nm).

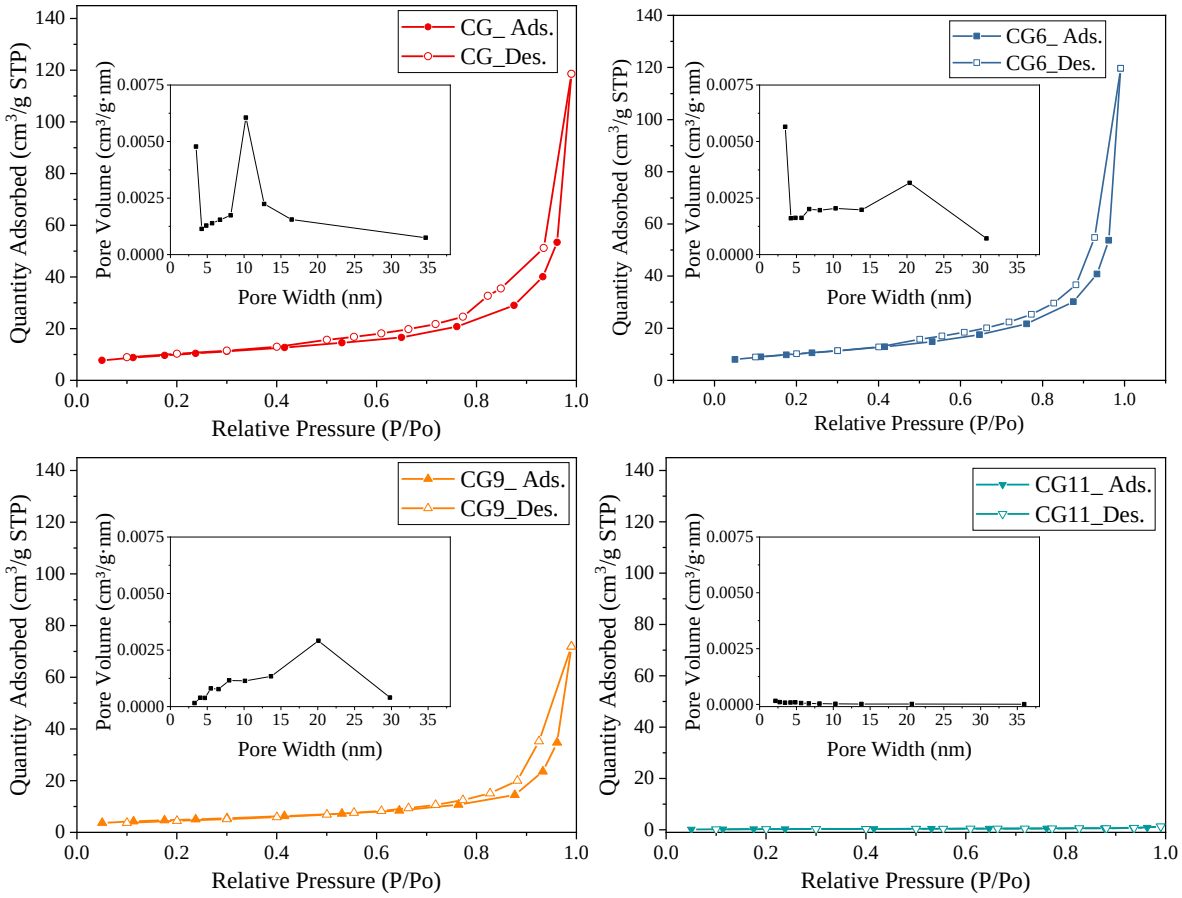

Fig. 70. N_2 adsorption-desorption isotherms for the coarse granulated supports CG, CG6, CG9, and CG11. Inset shows the BJH pore size distribution for the same materials.

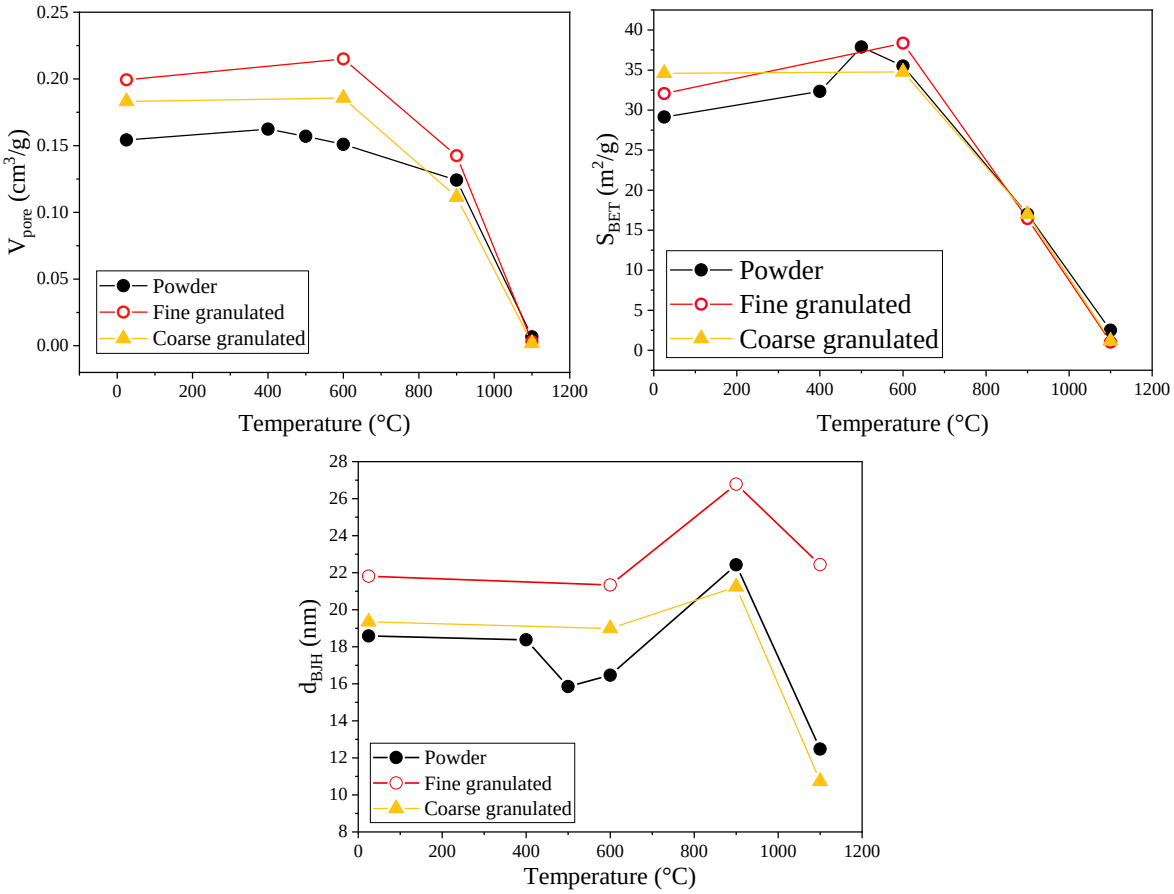

Fig. 71. Textural properties of the supports as a function of calcination temperature, for the powder (P), fine granulated (G), and coarse granulated (CG) supports.

Hence, in general, the powder and granulated supports comprises mesopores between 3 nm to 5 nm and macropores ten times higher, around 200 nm to 300 nm, besides, for the granulated supports, a pore network is present as the particles are agglomerated. The morphology of RP, P6 and P11 supports was examined by scanning electron microscope as shown in **Fig. 72**. The samples selected for SEM inspection were those with the lowest (**Fig. 72. a)**), intermediate (**Fig. 72. b)**), and highest (**Fig. 72. c)**) calcination temperature, that allowed to examined morphology changes. As the temperature increases, the structures of the minerals present in the clay support began to collapse, and even to sintered at 1100 °C. The result of calcination is a low order structure for minerals as kaolinite and illite, and the appearance of amorphous phases such metakaolin. A detailed discussion about mineralogical changes of the clay support was presented in Chapter III.

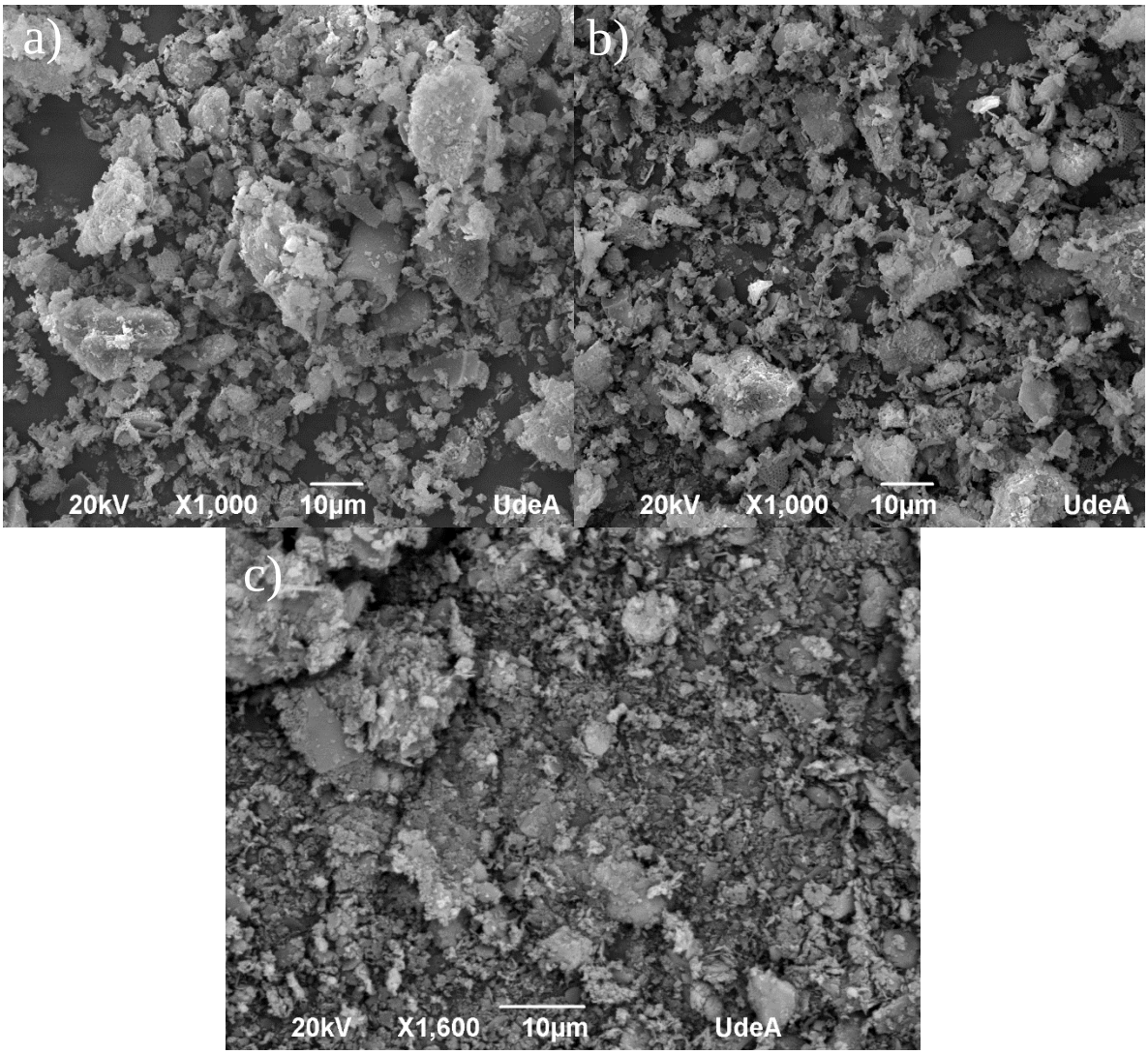

Fig. 72. The SEM images of a) RP, b) P6, and c) P11.

5.1.4. Thermal conductivity of the supports

Hot wire method was performed in order to analyze the incidence of the calcination temperature of the support in the thermal conductivity. The hot wire method was selected to as it is recommended for liquids, soils, granular and porous materials. The single-needle method is used here, where the probe consists in a heater with a temperature sensor inside. While a current passes through the heater the system monitors the temperature over time, t. The algorithm used to analyze the measurement consist in two equations that compute temperature of the needle during the heating (**Eq. (10)**) and the cooling (**Eq. (11)**):

$$T = m_0 + m_2 t + m_3 \ln t \quad \textbf{(10)}$$

$$T = m_1 + m_2 t + m_3 \ln\left[\frac{t}{t - t_h}\right] \quad \textbf{(11)}$$

where m_0 is the ambient temperature during heating, m_2 is the rate of background temperature drift, m_3 is the slope of a line relating temperature rise to logarithm of temperature, m_1 is the ambient temperature during cooling, t_h is the time in which the heat is applied, equal to the time after heating. Finally, the thermal conductivity is computed from **Eq. (12)**:

$$\lambda = \frac{q}{4\pi m_3} \quad \textbf{(12)}$$

where q is the heat per unit length. **Eq. (10)** and **Eq. (11)** can be solved by linear least squares, giving a very fast computation to calculate thermal conductivity of the sample. The equipment used for the measurements was the KD2 Pro Thermal Properties Analyzer (Decagon devices) with the sensors KS-1. As a qualitative quality indicator, given by the equipment, a dimensionless measure of the goodness of fit of the model to the data is taken as the error. Thus, only results with less than 0.001 of error were analyzed. Furthermore, thermal conductivity was measured as a function of temperature and for each temperature five to six measurements were performed

Thermal conductivity of the supports RP, P4, and P6 was measured and the results are presented in **Fig. 73**. The temperature range of measurements was between 5 °C and 70 °C, as thermal conductivity is a temperature-dependent variable **[66]**. From the results, it could be noticed that as temperature increases, the thermal conductivity slightly increases, except for the P6 support. Nevertheless, the values of increment were negligible when analyzing the thermal conductivity scale. Even more, temperatures between 25 °C and 57 °C, which correspond to the phase change temperatures of the eutectic fatty acids studied in this work, showed almost the same curve for the three supports. Thus, changes in temperature between 25 °C and 600 °C do not show increases or decreases in the thermal conductivity of the supports. All the supports presented a low thermal conductivity of 0.05 W/m·K, on average. These results were expected as clay minerals present low thermal conductivity due to their

porosity, textural properties, grain size, grain shape, and mineralogical composition **[232–234]**. The presence of air trapped in the pores diminish the heat transfer in porous materials and thus reduce thermal conductivity. Even though, it is expected that when PCM impregnation occurs thermal conductivity significantly enhances as the pores will be filled and thus heat transfer should increase. For the final intended use of these materials, as part of thermal energy storage systems, it is suggested that some enhancement could be done **[72]** as thermal conductivity controls the charging/discharging rates and, hence, improves the heat transfer.

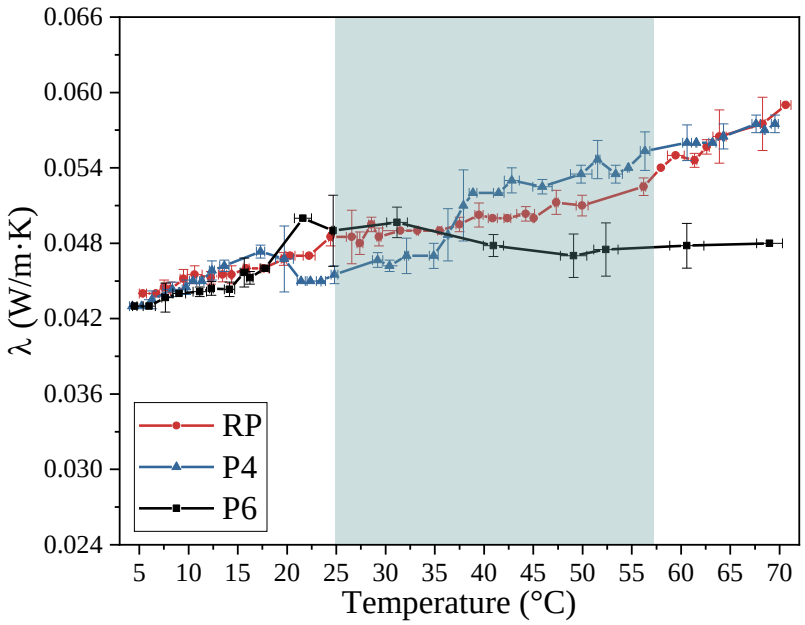

Fig. 73. Thermal conductivity of the treated support at different temperatures.

From the porosity and textural results obtained, the RP, P6, P9, P11, G6, and G9 supports were chosen to study their performance for shape-stabilization of phase change materials as they correspond to a set of dissimilar characteristics as pore volume, pore width, BET area, and particle size.

5.2. SS-PCMs based in the calcined supports

Eighteen SS-PCMs composites, with different percentages of PCM impregnation and different porous supports (RP, P6, P9, P11, G6, and G9), were prepared by the vacuum impregnation method as presented in Chapter IV. The obtained composites are summarized in **Table 31**. The support RG was not used as the mechanical resistance was low and easily

can be damaged during the vacuum impregnation process, hence, calcination was preferred for the granulated supports. In the same way, supports P4, P5, and G11 were not used to shape-stabilized PCMs as supports P6 and P11 were like them in terms of porosities. Coarse granulated supports, CG, were not used as the pore width was too big to retain the liquid PCMs.

Table 31. SS-PCMs produced by vacuum impregnation method using LAMA eutectic.

Sample	Binary eutectic	% Impregnation (% wt. of PCM)	Support
SS-LAMA-RP-25	LA:MA	25	RP
SS-LAMA-RP-35	LA:MA	35	RP
SS-LAMA-RP-40	LA:MA	40	RP
SS-LAMA-P6-25	LA:MA	25	P6
SS-LAMA-P6-35	LA:MA	35	P6
SS-LAMA-P6-40	LA:MA	40	P6
SS-LAMA-P9-25	LA:MA	25	P9
SS-LAMA-P9-35	LA:MA	35	P9
SS-LAMA-P9-40	LA:MA	40	P9
SS-LAMA-P11-25	LA:MA	25	P11
SS-LAMA-P11-35	LA:MA	35	P11
SS-LAMA-P11-40	LA:MA	40	P11
SS-LAMA-G6-25	LA:MA	25	G6
SS-LAMA-G6-35	LA:MA	35	G6
SS-LAMA-G6-40	LA:MA	40	G6
SS-LAMA-G9-25	LA:MA	25	G9
SS-LAMA-G9-35	LA:MA	35	G9
SS-LAMA-G9-40	LA:MA	40	G9

5.2.1. Thermal properties and absorption of the SS-PCMs

The leakage behavior after two hours of the eighteen composites described in **Table 31** is shown in **Fig. 74**. The leakage was evaluated through the filter paper method following the procedure described in Chapter IV. The uncertainty of the data, although small, is shown as error bars in the plot and represents the error propagation of the measurement. The LA/MA eutectic was incorporated in three levels, 25%, 35%, and 40%. As the percentage of LA/MA increases in the support, higher the leakage, as expected. Composites with the best leakage performance were SS-LA/MA-P6=SS-LA/MA-P9 < SS-LA/MA-RP < SS-LA/MA-P11 < SS-LA/MA-G6 < SS-LA/MA-G9. These findings suggest that there is an optimum pore size

along with a pore volume, for a good impregnation of the binary eutectic fatty acid, moreover when only Van der Waals forces exist. If the pore size is around 21 nm (G6), with a pore volume of 0.21 cm^3/g, or if the pore size is around 26 nm (G9), with a pore volume of 0.14 cm^3/g, the molecules of LA/MA can migrate easily to the surface through capillarity, macropores, pore connectivity **[235,236]** and intergranular spaces existing in granulated materials. If the pore size is small, 12 nm (P11), and the pore volume almost negligible, the molecules of LA/MA hardly can be incorporated within the support. Thus, materials that present low pore connectivity, as powders, with mesopore sizes between 16 nm (P6) and 22 nm (P9), and pore volumes around 0.14 cm^3/g plus the typical diatomite macropores, seems to be appropriate to contained effectively the LA/MA eutectic into the support. Analyzing the RP support impregnation, with pores of 18 nm and pore volume of 0.15 cm^3/g, should be as good as the P6 and P9 supports, but the leakage behavior is not as good. Then, the temperature influences the impregnation of the supports by controlling the pore width and volume, and by exposing more silanol groups **[237]** through the dehydration of physisorbed and capping water, leading to a better interaction between the exposed silanols of the support and the fatty acids.

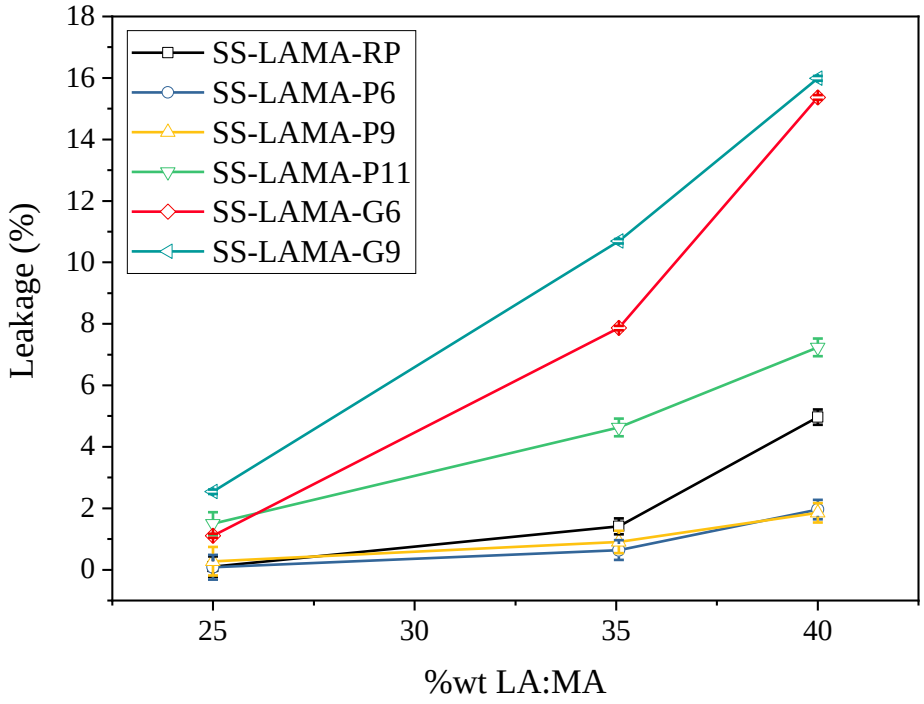

Fig. 74. Leakage test of SS-LAMA with 25%, 35%, and 40% impregnation ratio.

The influence of the porosity on the absorption of the supports can be seen more clearly in **Fig. 75**. The leakage percent as a function of BET surface area, S_{BET}, the volume of pores, V_{pore}, and average pore width, d_{BJH}, were plotted for the SS-LA/MA with 35% of impregnation, as these samples showed the best behavior. In general, can be notice a trend for the powder supports (RP, P6, P9, P11), where, as the surface area, the pore volume and the pore width increases, the leakage decreases. The granulated supports (G6, G9) presented the same trend for surface area and pore volume, but for pore width the trend is reversed. Seems that when the pore width was greater than 23 nm the leakage increases no matter the surface area or the pore volume. It is worth highlighting that the three textural properties act as a set of required conditions and do not should be analyzed separately because can conduct to misinterpretations.

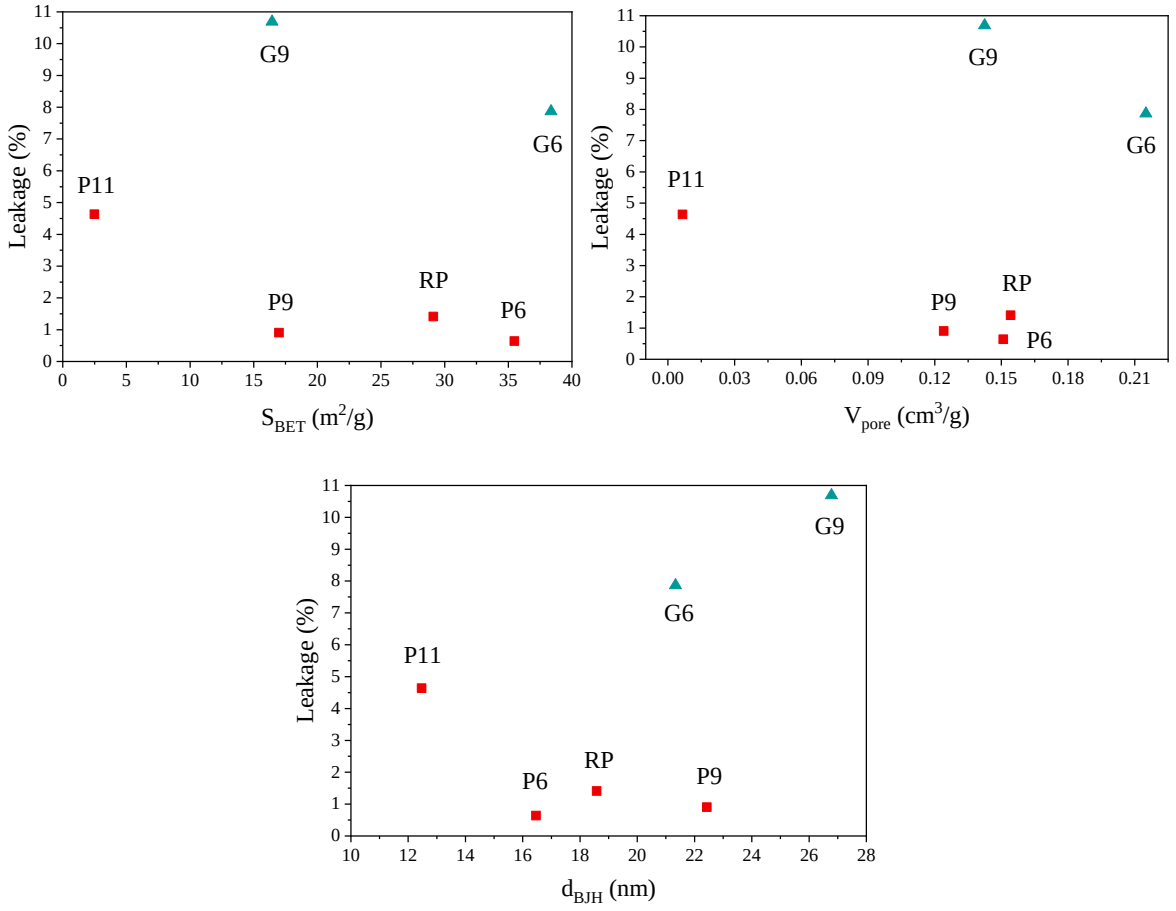

Fig. 75. Leakage as a function of the textural properties for SS-LAMA-35.

As leakage percentage of the SS-LA/MA composites with RP, P6 and P9 supports were the lowest no matter the amount of LA/MA, only these composites were thermally characterized, as shown in **Table 32**. The values of the phase change temperatures and the latent heat of the SS-PCMs were determined through differential scanning calorimetry (DSC) (TA Instruments Q200 DSC) at a rate of heating and cooling of 5 °C/min, in a N_2 atmosphere, flowing at 50 mL/min, after 2 heat-cooling cycles. The uncertainties of this DSC system are typically 1.16 J/g for latent heat and ±0.29 °C for the maximum peak of the phase change temperature. From the results can be seen that as the percentage of LA/MA incorporated increases, the latent heat of fusion (ΔH_m) and solidification (ΔHs) increases, as expected. The latent heat of fusion was on average 29.9 kJ/kg, 51.2 kJ/kg, and 58.4 kJ/kg for SS-LA/MA-25, SS-LA/MA-35, and SS-LA/MA-40, respectively. The peak phase change temperature of melting, $T_{m,\,peak}$, was 36.2 °C, only 0.68 °C above the pure eutectic LA/MA. Besides, the deviation of the measurements between the different supports, for each impregnation percentage, was low and around the standard error of the measurement. The only considerable deviation obtained was for the SS-LA/MA-P9-40, with a deviation of 3.3 kJ/kg for the latent heat, being above the standard error of the measurement by 2 kJ/kg. Even though, these values can be considered negligible. Then, supports RP, P6 and P9 did not affect the thermal behavior of the binary fatty acid eutectic when incorporated in 25%, 35%, or 40%.

Table 32. Phase change temperatures and latent heats for SS-LAMA at 25%, 35% and 40% impregnation, using supports RP, P6, and P9.

	SS-LA/MA-25					SS-LA/MA-35					SS-LA/MA-40				
	RP	P6	P9	$\bar{x}$	σ	RP	P6	P9	$\bar{x}$	σ	RP	P6	P9	$\bar{x}$	σ
$T_{m,\,peak}$ (°C)	35.39	35.56	35.32	35.42	0.12	36.35	36.56	36.13	36.35	0.22	36.17	37.26	37.15	36.86	0.60
$T_{m,\,onset}$ (°C)	31.14	31.53	30.95	31.21	0.30	31,00	30.83	30.94	30.92	0.09	31.12	31.38	31.42	31.31	0.16
$Ts_{,\,peak}$ (°C)	29.57	29.54	29.63	29.58	0.05	28.65	29.24	29.33	29.07	0.37	28.62	28.86	28.81	28.76	0.13
$Ts_{,\,onset}$ (°C)	31.57	32.03	32.13	31.91	0.30	31.97	32.26	32.42	32.22	0.23	30.76	32.27	32.55	31.86	0.96
ΔH_m (kJ/kg)	29.63	29.67	30.46	29.92	0.47	51.57	51.63	50.39	51.20	0.70	56.59	56.37	62.08	58.35	3.23
ΔHs (kJ/kg)	27.78	26.83	28.32	27.64	0.75	48.55	49.12	49.43	49.03	0.45	55.99	55.15	61.25	57.46	3.31

After these analyses, support P6 was selected as the optimum for shape-stabilization of LA/MA, with impregnation of 35% of the PCM, i.e, SS-LA/MA-P6-35. The decision was taken after the low leakage losses (1.26%) of the PCM due to the adequate surface area, pore

volume, and pore width of the support; the range of phase change temperature (36.56 °C) was in the desired operating range (**Table 32**), which matches the pure eutectic; good latent heat of fusion (51.63 kJ/kg) compared with the other percentages; good chemical and physical compatibility observed between the support and the PCM; and the affordability of its production compared with other calcination temperatures (≥ 900 °C). Besides, this composite is non-toxic, non-harmful for people or environment and is non-flammable.

5.2.2. Validation of optimal conditions for the SS-PCMs

For comparison and verification of the best conditions of the chosen support, and based on the chemical similarity between the eutectics CA/MA and PA/SA with LA/MA, two new sets of composites were produced, called SS-CA/MA-P6 and SS-PA/SA-P6, with 25%, 35% and 40% of the corresponding PCM. Comparison was made between eutectics supported in the raw support (RP) and in the support calcined at 600 °C (P6). The leakage behavior after two hours is presented in **Fig. 76**, as well as the error bars corresponding to the standard deviation of the three measurements performed for each sample. For all SS-PCMs, increasing the impregnation amount, increased the leakage percentage. As expected, the leakage of the SS-PCMs-P6 was lower than for the SS-PCMs-RP, demonstrating that the calcined support at 600 °C presented better absorption properties than the raw support. Furthermore, this conclusion can be extended for other eutectic binary fatty acids than LA/MA, as CA/MA and PA/SA.

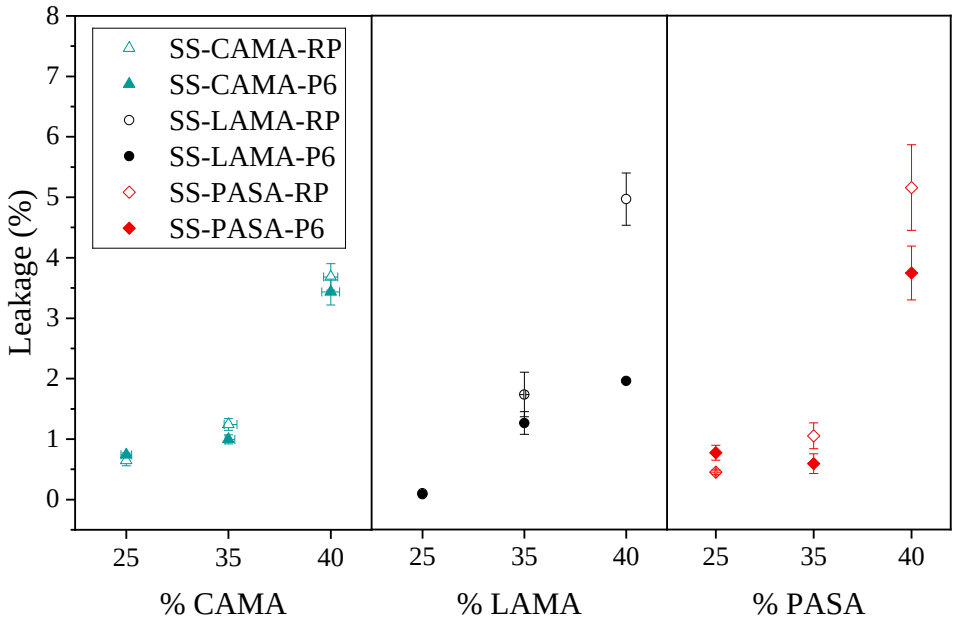

Fig. 76. Leakage test of SS-CA/MA, SS-LA/MA, and SS-PA/SA using the supports RP (hollow symbol) and P6 (filled symbol), with 25%, 35% and 40% of impregnation ratio.

In this thesis, leakage characterization below 2% was considered as a good performance indicator of the absorption capacity of the supports. Thus, SS-CA/MA-P6, SS-LA/MA-P6, and SS-PA/SA-P6 presented the best results with 35% wt. impregnation, with leakage of 0.99%, 1.26%, and 0.59%, respectively. The composites supported in the raw support, SS-CA/MA-RP, SS-LA/MA-RP, and SS-PA/SA-RP, with the same 35% PCM impregnation, presented values of 1.24%, 1.73%, and 1.04%, respectively. Thus, heat treatment of the support at 600 °C decreased leakage in 20.2%, 27.2%, and 43.3%, for CA/MA, LA/MA, and PA/SA, respectively, compared to the raw support. Although initial measurements of leakage are good enough to filter the obtained SS-PCMs, as most of the researchers present in their studies, could be not accurate to evaluate the durability or the performance in time of the composites. Even more, when in literature can be found several leakage analysis, most of them qualitative **[80,107,125,132,223,238]**, some quantitative **[78]**, other studies are unlikely to performed leakage **[128,239,240]** or even mislead the measurement doing thermal cycling **[124,167]**, that with the composite in the same sample holder prevent the real leakage to happen. Thus, we proposed further leakage analysis based on a leakage cycling for the best SS-PCMs produced, as shown in **Fig. 77**. Thus, every two hours the leakage value was

obtained for the samples at 60°C. The error bars included in the plot represents the variability of the three measurements made for each sample.

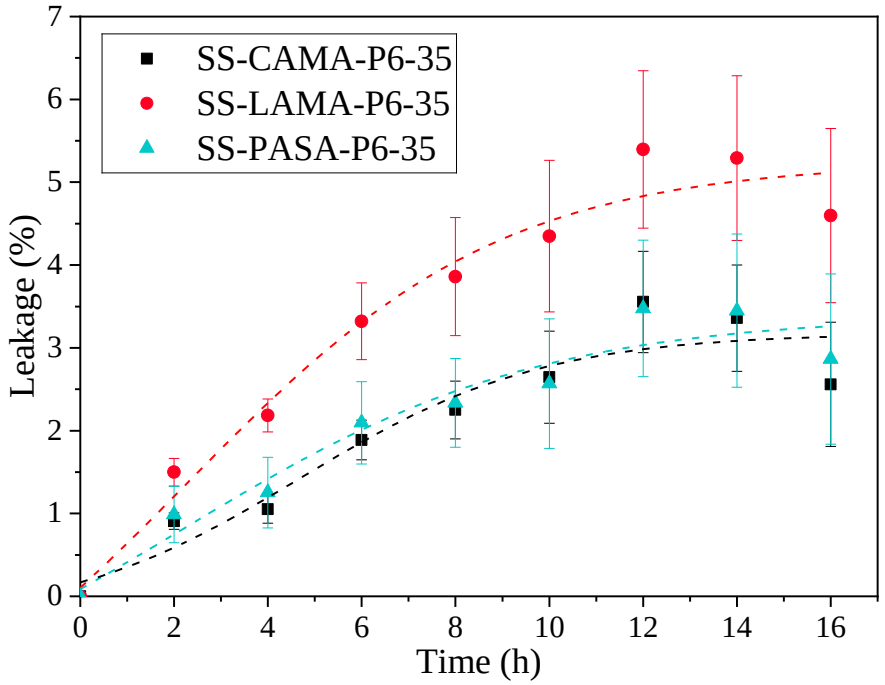

Fig. 77. Leakage cycling (accumulated) for SS-CA/MA-P6-35, SS-LA/MA-P6-35, and SS-PA/SA-P6-35.

The leakage cycling confirmed the hypothesis that a single leakage cycle, for example at 2 h, may not be enough to understand the leakage behavior of the composite. All the SS-PCMs increased their leakage percentage every cycle, i.e. every 2 h, until twelve hours when the leakage curves reach stabilization. The final cumulative leakage, after sixteen hours, was 2.6%, 4.5% and 2.7% for SS-CA/MA-P6-35, SS-LA/MA-P6-35, and SS-PA/SA-P6-35, respectively, indicating that the CA/MA and PA/SA eutectics were more effectively absorbed by the porous supports. Even though, all the leakages were still below 5% that seems a good value compared to a similar analysis conducted by Qu et al **[241]**, who found leakage in their samples (n-octadecane-HDPE) from 8.22% to 44.92% at seven hours, with an impregnation range of 71% to 83% of the paraffin.

Phase change temperature and latent heat of the three composites were measured, as presented in **Fig. 78** and **Table 33**, through modulated temperature DSC (MDSC) (TA Instruments Q200 DSC), using a N_2 atmosphere (50 mL/min), with a heating rate of 1 °C/min, modulation period of 100 seconds, and a modulation amplitude of ±0.5 °C. The

phase change temperatures for SS-CA/MA-P6-35, SS-LA/MA-P6-35 and SS-PA/SA-P6-35 were 22.40 °C, 35.33 °C and 55.73 °C, respectively, these values were similar to the pure binary eutectics. In general, the latent heats for all the composites were 10 kJ/kg lower to having 35% of the latent heats of the pure eutectics. Hence, the support did not change significantly the thermal properties of the PCMs.

Table 33. Thermal properties of SS-CA/MA-P6-35, SS-LA/MA-P6-35, and SS-PA/SA-P6-35.

Sample	Melting			Freezing		
	$T_{m,onset}$ (°C)	$T_{m,peak}$ (°C)	ΔH_m (kJ/kg)	$T_{s,onset}$ (°C)	$T_{s,peak}$ (°C)	ΔH_s (kJ/kg)
SS-CAMA-P6-35	19.62	22.40	39.07	20.61	18.51	37.62
SS-LAMA-P6-35	31.51	35.33	41.74	34.32	32.60	39.88
SS-PASA-P6-35	53.85	55.73	53.85	52.40	51.15	45.15

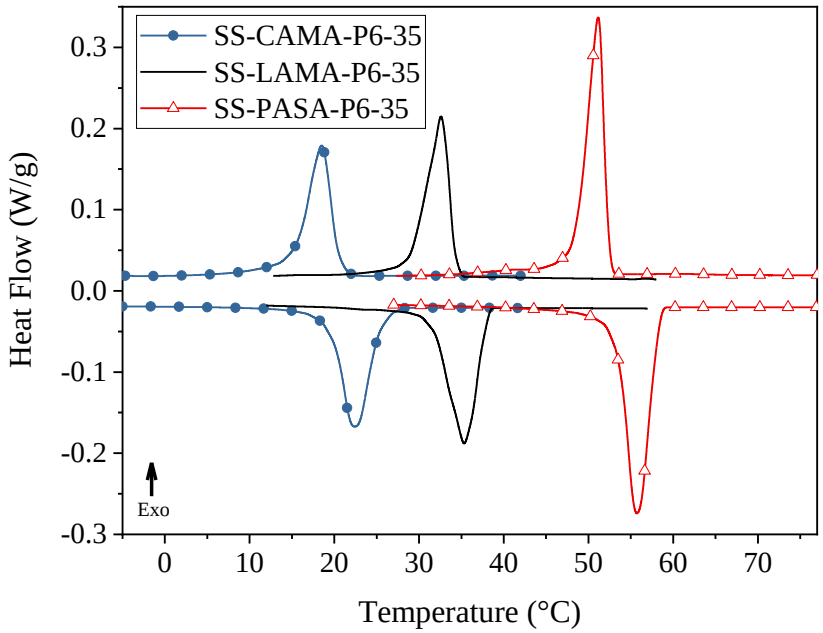

Fig. 78. DSC curves for SS-CA/MA-P6-35, SS-LA/MA-P6-35 and SS-PA/SA-P6-35.

5.2.3. Heat capacity of the SS-PCMs

Heat capacity as a function of temperature, $C_p(T)$, was measured using a MDSC with the same conditions mentioned above, for the P6 support and the SS-PCMs-P6 composites. The curves (**Fig. 79**) clearly showed a peak in the phase change region for the composites. No peaks were seen for the P6 support. As well, empirical equations of $C_p(T)$ for the solid (**Table 34**) and the liquid (**Table 35**) phases were obtained. The equations correspond to

linear fitting, and second and third grade polynomial fittings with R-squared greater than 0.87, indicating good agreement with the experimental data.

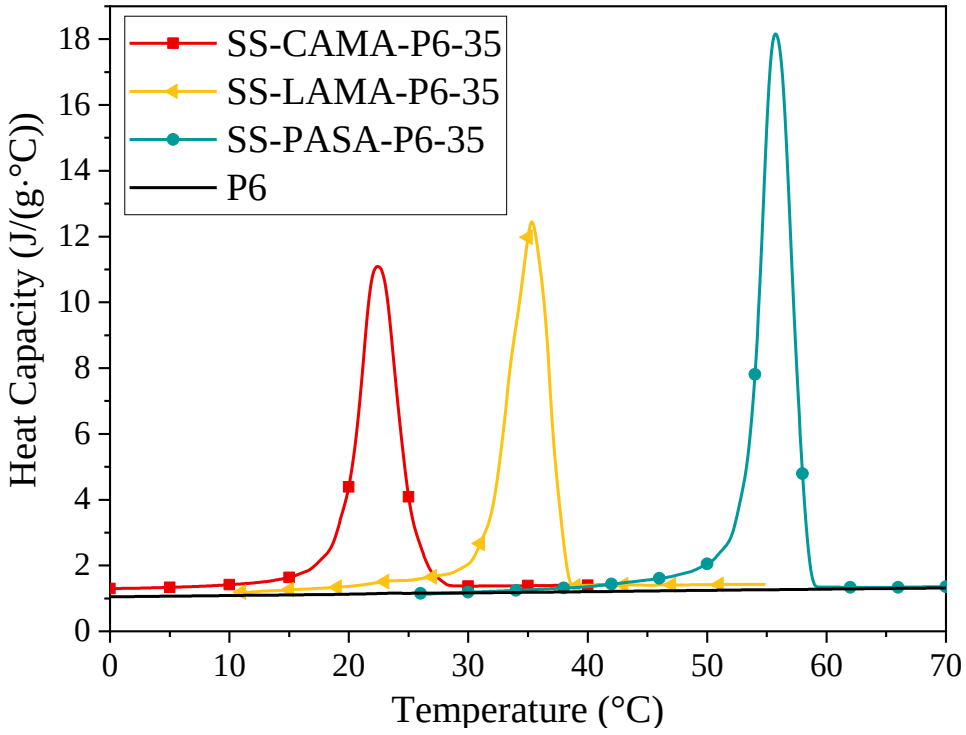

Fig. 79. Heat capacities as a function of the temperature of the P6 support and composites SS-CAMA-P6-35, SS-LAMA-P6-35, and SS-PASA-P6-35.

The average C_p of the P6 support was 1.25 J/(g·°C), and for the raw support 0.95 J/(g·°C) (presented in Chapter III). From this comparison it can be noticed that the calcination temperature increased the heat capacity of the clay mineral support due to a densification effect as presented in the textural properties in **Fig. 68**, being another factor to be considered when choosing the support. In the temperatures where the PCMs were completely liquid or solid, no significant differences could be observed between the heat capacities of the evaluated SS-PCMs. In average, heat capacities were 1.38 J/(g·°C), 1.41 J/(g·°C) and 1.33 J/(g·°C) for SS-CAMA-P6-35, SS-LAMA-P6-35, and SS-PASA-P6-35, respectively. These values were considered equal as their differences were between the standard deviation in the measurement of 2-8% in the temperature region analyzed. As a conclusion, heat capacity of the P6 support increased with the impregnation of the PCM eutectics.

Table 34. Equations of heat capacity for the solid phase. $\boldsymbol{C_p(T) = B_0 + B_1 \cdot T + B_2 \cdot T^2 + B_3 \cdot T^3}$

	B_0	B_1	B_2	B_3	*RSS*	R^2	*Adj.* R^2	T_i (°C)	T_f (°C)
SS-CAMA-P6-35	1.25	0.019	-	-	0.127	0.892	0.891	0	15
SS-LAMA-P6-35	2.60	-0.22	1.1 E-2	-1.55 E-4	0.016	0.992	0.992	15	28
SS-PASA-P6-35	3.46	-0.14	2.2 E-3	-	0.145	0.984	0.984	30	45
P6	1.05	0.003	-	-	0.012	0.998	0.998	-4	77

Table 35. Equations of heat capacity for the liquid phase. $\boldsymbol{C_p(T) = B_0 + B_1 \cdot T + B_2 \cdot T^2 + B_3 \cdot T^3}$

	B_0	B_1	B_2	B_3	*RSS*	R^2	*Adj.* R^2	T_i (°C)	T_f (°C)
SS-CAMA-P6-35	1.295	0.003	-	-	1.5 E+1	0.975	0.975	30	40
SS-LAMA-P6-35	1.248	0.003	-	-	4.32	0.987	0.987	45	52
SS-PASA-P6-35	17.038	-0.687	0.01	-4.7 E-5	6.2 E-5	0.982	0.981	60	75

5.2.4. Thermal stability of the SS-PCMs

Finally, to determine the thermal stability of the composites and thus the temperature of degradation, thermogravimetry analysis (TGA) (TGA 2950 Hi-Re, TA Instruments) was performed from room temperature up to 900 °C with a heating rate of 10 °C/min. Results are presented in **Fig. 80**. The degradation temperatures, here taken at the temperature where weight losses of the samples were 1%, correspond to 110 °C, 125 °C, and 145 °C, for SS-CA/MA-P6-35, SS-LA/MA-P6-35, and SS-PA/SA-P6, respectively. These temperatures indicate a good thermal performance for low and moderate temperature applications in thermal energy storage systems as they were above 100 °C.

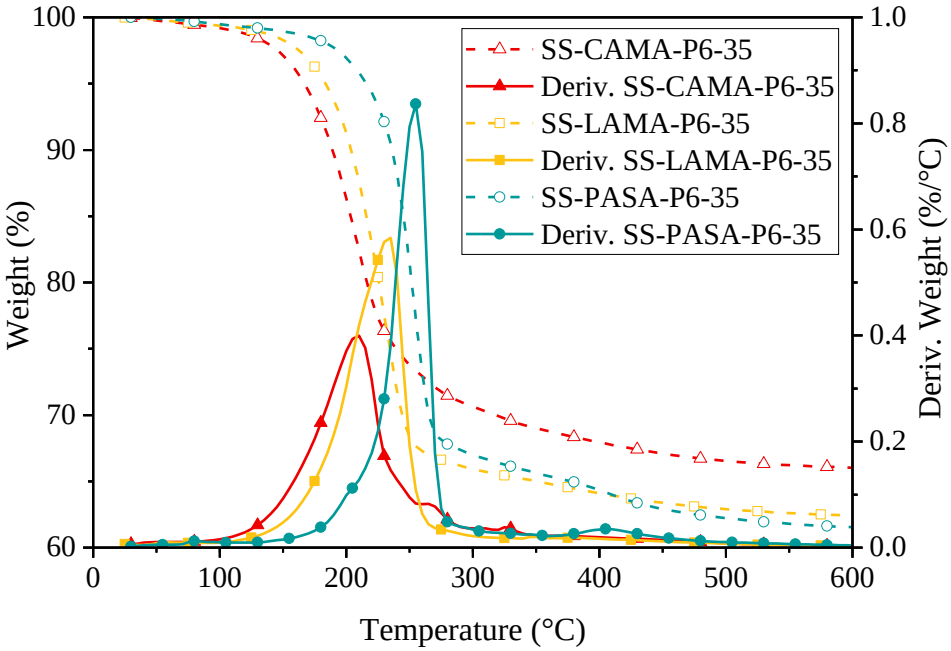

Fig. 80. Thermogravimetric analysis for SS-CA/MA-P6-35, SS-LA/MA-P6-35, and SS-PA/SA-P6-35.

5.2.5. Thermal conductivity of the SS-PCMs and the eutectic PCMs

This section intended to enlarge the experimental studies on the thermal conductivity of binary eutectic mixtures CA/MA, LA/MA, and PA/SA as a function of temperature, and their respective composites SS-CA/MA-P6-35, SS-LA/MA-P6-35, and SS-PA/SA-P6-35. Besides, for comparison, a commercial SS-PCM, GR42 (Rubitherm), was measured as well. Measurements were done with the equipment used KD2 Pro Thermal Properties Analyzer (Decagon devices) with the sensors KS-1 and TR-1. Temperature ranges (5 °C to 70 °C) were selected as the temperatures above and below the phase change temperatures of each material looking forward to having a complete solid and liquid state of the PCMs. To avoid further errors, initial density of the SS-PCMs samples was maintained at 0.790 ± 0.057 g/cm^3 during the measurements.

Results of the thermal conductivity for P6 support, CA/MA, LA/MA, PA/SA, SS-CA/MA-P6-35, SS-LA/MA-P6-35, and SS-PA/SA-P6-35 are shown in **Fig. 81**. As can be noticed, thermal conductivity of the clay support remained almost constant in the whole temperature

range and presented the lowest values around 0.05 W/m·K. This can be explained as the support is porous and there is air trapped in the pores that have low thermal conductivity (~0.024 W/m·K). This porosity resulted in a reduction of thermal conductivity as the heat transfer across the pores is slow and inefficient **[65]**. Besides, in materials where the atomic structure is highly disordered and irregular, like in amorphous ceramics, the phonon scattering is much more effective and thermal conductivity decreases **[65]**.

As for the eutectics and the SS-PCMs, thermal conductivity function turns into a huge increase during the phase change temperature and after the transition, it falls back again to lower values. These increments can be noticed as wide peaks near 20 °C, 35 °C and 53 °C for CA/MA, LA/MA, and PA/SA, respectively. The same peaks can be observed for their respective SS-PCMs, with a slight shifting to lower temperatures, and a decrease in the height of the peak, as the porous support interfere with the phase change of the PCM, as stated in previous works by the authors **[242,243]**. These increases may correspond to second-order like transitions, called λ-transitions, where there is a discontinuity or a vertex at the transition temperature **[244]**, similar to the behavior of heat capacity as a function of temperature. Classical thermodynamics is still unable to present explanations for this kind of transitions **[199]** but has been reported for magnetic systems, superconductors, alloys and order-disorder transitions **[245–247]**. Thus, the understanding of thermal conductivity during phase transition is not well stablished yet **[198]**.

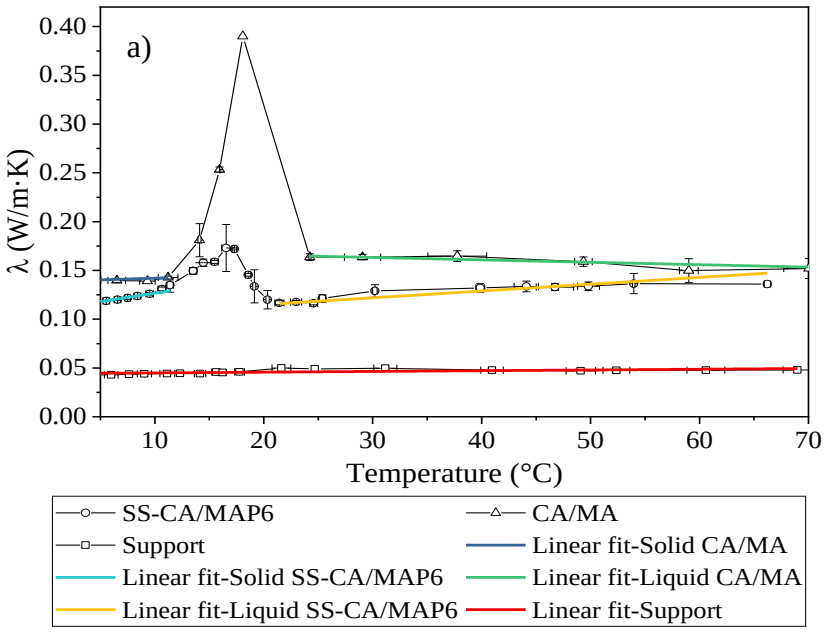

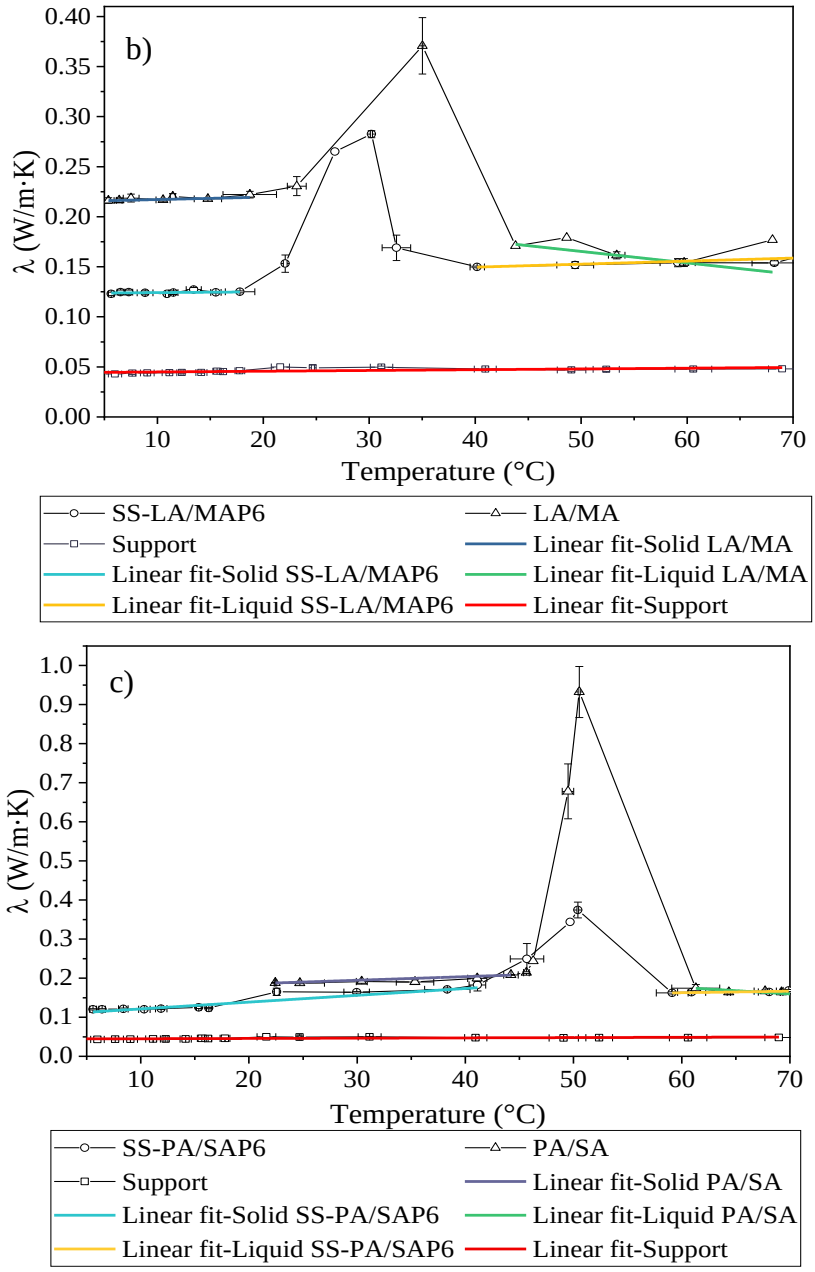

Fig. 81. Thermal conductivity of a) CA/MA and SS-CA/MA-P6-35, b) LA/MA and SS-LA/MA-P6-35, and c) PA/SA and SS-PA/SA-P6-35. Support P6 is shown as reference.

Despite these λ-transitions-like curves, thermal conductivity can be obtained from data before (solid region) and after (liquid region) phase transition of the PCMs and SS-PCMs. Hence, linear regression was used to fit the experimental data. The main fitting parameters obtained are exhibited in **Table 36** for the solid region and in **Table 37** for the liquid region. Adjusted R-square suggests that the models explain most of the variability in the response

variable. Hence, thermal conductivity presented a linear correlation with temperature for all the materials studied in this work.

Table 36. Thermal conductivity fitting parameters for linear regression of the solid phase of eutectics and SS-PCM-P6-35

Sample	Intercept	Slope	RSS	Pearson's r	Adj. R-Square
CA/MA	0.1387 ± 8.1774E-4	3.3610E-4 ± 1.2387E-4	0.4629	0.8868	0.6796
LA/MA	0.2147 ± 0.0012	3.8809E-4 ± 1.0163E-4	1.9963E-8	0.8629	0.6936
PA/SA	0.1670 ± 0.0024	9.2208E-4 ± 8.3210E-5	7.6505	0.9841	0.9606
P6 Support	0.0442 ± 6.8913E-4	7.5522E-5 ± 2.1322E-5	4.9809E-5	0.6629	0.4045
SS-CA/MA-P6-35	0.1094 ± 9.7962E-4	0.0017 ± 1.4725E-4	6.0185	0.9753	0.9443
SS-LA/MA-P6-35	0.1229 ± 0.0012	1.3456E-4 ± 1.1264E-4	1.3456E-8	0.5618	0.2015
SS-PA/SA-P6-35	0.1094 ± 0.0068	0.0018 ± 2.2308E-4	3.2669E-6	0.9381	0.8667

Table 37. Thermal conductivity fitting parameters for linear regression of the liquid phase of eutectics and SS-PCM-P6-35

Sample	Intercept	Slope	RSS	Pearson's r	Adj. R-Square
CA/MA	0.1707 ± 0.0025	-2.4776E-4 ± 7.0549E-5	0.7443	-0.8690	0.6939
LA/MA	0.2227 ± 9.4408E-4	-0.0012 ± 1.6792E-5	0.0012	-0.9997	0.9991
PA/SA	0.2749 ± 0.0407	-0.0017 ± 5.8821E-4	4.0031	-0.8502	0.6304
SS-CA/MA-P6-35	0.1010 ± 0.0020	6.9718E-4 ± 6.9300E-5	4.1974	0.9583	0.9093
SS-LA/MA-P6-35	0.1375 ± 0.0034	3.0259E-4 ± 6.1943E-5	5.5968	0.9425	0.8511
SS-PA/SA-P6-35	0.1382 ± 0.0143	4.0703E-4 ± 2.1788E-4	1.0146	0.7973	0.4536

The thermal conductivity increases with the increase of temperature for the eutectics and the SS-PCMs. However, in the liquid phase, the thermal conductivity of CA/MA, LA/MA, and PA/SA decreases with increasing temperature, but for SS-CA/MA-P6-35, SS-LA/MA-P6-35, and SS-PA/SA-P6-35 is the opposite, and thermal conductivity increases with the increase of temperature. This behavior can be observed from the Pearson correlation coefficient (Person's r) in **Table 36** and **Table 37**. Despite this, the slope variation of thermal conductivity in all materials is very small and thus can be considered almost constant when needed for practical applications. In **Table 38**, the average thermal conductivity in the solid region, λ_{avg_Solid}, and in the liquid region, λ_{avg_Liquid}, for all the samples is presented.

Thermal conductivity values for the SS-PCMs were lower than for the eutectics but higher than for the support. This is due to the filling of the pores of the support with the PCM, which increased the mean free paths for phonon transfer, reduced interfacial thermal resistance, and increased the heat conduction as the density increased (from 0.45 g/cm^3 to 0.79 g/cm^3). Thus, an increase in the heat transfer and thermal conductivity of the composite was observed. Pure eutectics, being homogenous, presented more effective heat transfer than the composite clay/PCM, hence thermal conductivity was higher. The reduction of thermal conductivity of SS-CA/MA-P6-35, SS-LA/MA-P6-35, and SS-PA/SA-P6-35 compared with their respective eutectics, in solid phase, was 12.14%, 43.12% and 30.21%; and in liquid phase was 19.50%, 5.56% and ~0.00%, respectively. On the other hand, the increase of thermal conductivity of SS-PCMs respect to the support was between 59.35% and 69.70%.

Table 38. Average thermal conductivity in the solid and liquid region for the eutectics, the support and the SS-PCMs.

Sample	λ_{avg_Solid} (W/m·K)	λ_{avg_Liquid} (W/m·K)
Support	0.046 ± 0.002	-
CA/MA	0.140 ± 0.002	0.159 ± 0.009
LA/MA	0.218 ± 0.003	0.162 ± 0.010
PA/SA	0.192 ± 0.007	0.164 ± 0.005
SS-CA/MA-P6-35	0.123 ± 0.005	0.128 ± 0.008
SS-LA/MA-P6-35	0.124 ± 0.002	0.153 ± 0.004
SS-PA/SA-P6-35	0.134 ± 0.021	0.165 ± 0.003

The acquire results for the SS-PCMs studied in this work were similar to other composites found in the literature. For instance, Sari et al **[78]** studied a raw diatomite (0.08 W/m·K) and produced SS-PCMs with PEG, with a phase change temperature of 7.86 °C. Thermal conductivity obtained was 0.15 W/m·K for a composite diatomite/PEG (41%). Improvement of these values can be reach by the addition of conductive materials as graphene or CNTs. Furthermore, the commercial SS-PCM GR42 (Rubitherm) was analyzed and in **Fig. 82** the comparative thermal conductivity curves are shown. As can be noticed, the thermal conductivity of the SS-PCMs of this work is higher than GR42, in both solid and liquid phases. The increase of thermal conductivity was between 10.57% and 33.33%. Thus, SS-CA/MA-P6-35, SS-LA/MA-P6-35 and SS-PA/SA-P6-35 exhibit a higher thermal conductivity compared with the commercial SS-PCM GR42.

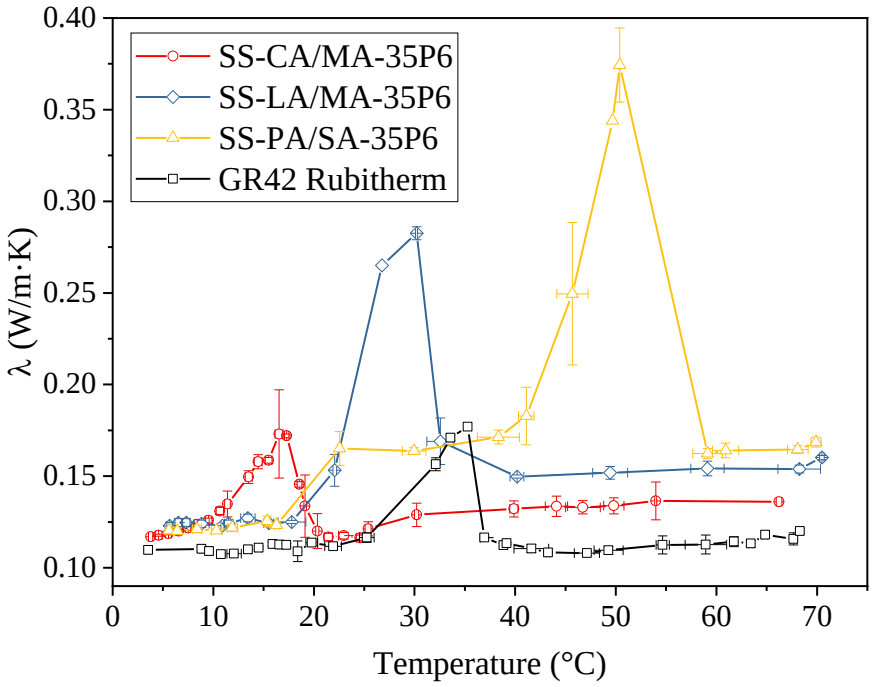

Fig. 82. Temperature dependence of thermal conductivity of SS-CA/MA-P6-35, SS-LA/MA-P6-35, SS-PA/SA-P6-35 and commercial GR42 (Rubitherm).

As stated in Chapter III, the kaolin present in the support accounts for much of the thermal conductivity and heat capacity of the support. In this way, 10%, 20%, 30%, 40% and 50% of a standard kaolin (Dv50=14.60 µm) were added to the composite SS-LA/MA-P6-35 in order to study the effect of this mineral on the thermal conductivity. Complete particle size distribution and chemical composition of the kaolin used here can be found in Chapter III. Illite or other materials with higher thermal conductivity, like carbon-based materials, were not studied at this time as kaolin is a cheap natural occurring mineral that can be easily obtain commercially. With this experiment the authors wanted to attempt another approach different than adding carbon nanotubes (CNTs) or expanded graphite (EG), among others, that are typically expensive, difficult to disperse, and can change the viscosity of the system. In **Fig. 83** results of kaolin additions can be observed, the data were acquired at a single temperature of 19 °C.

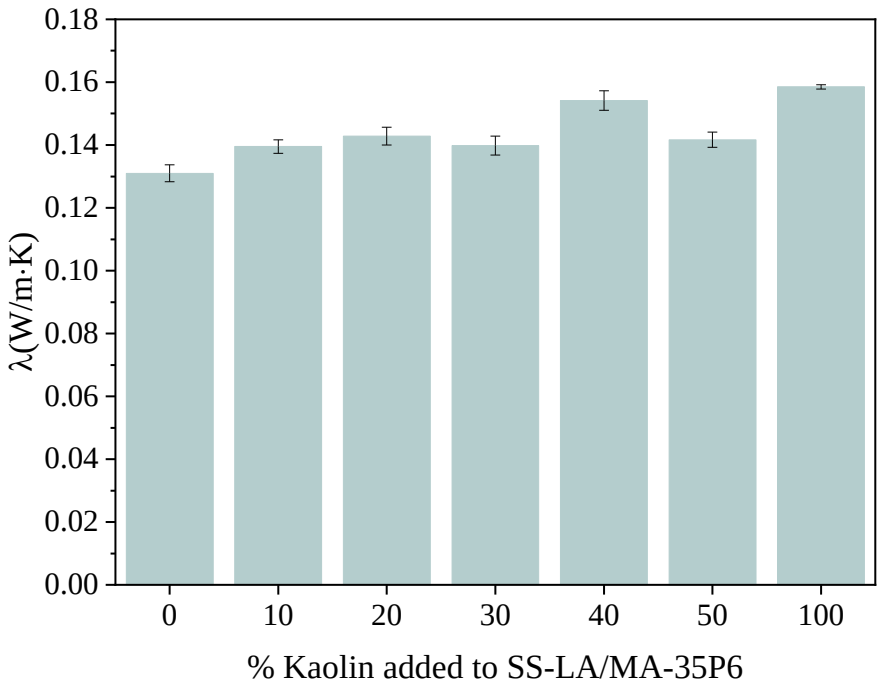

Fig. 83. Thermal conductivity of SS-LA/MA-P6-35 added with kaolin.

Adding kaolin to the composite SS-LA/MA-P6-35 resulted in an increase in its thermal conductivity. The raise in λ was 6.49%, 9.03%, 6.74%, 17.68% and 8.14%, respect to the composite without addition (0% kaolin added), for the 10%, 20%, 30%, 40% and 50% of kaolin added, respectively. Although there was an increment, the absolute value is still low compared with other usual additives employed for thermal conductivity enhancement. For example, conductive additives as graphite, carbon and copper foams can increase thermal conductivity from 1 to 10 times **[67]**. As well, literature about other additives as silica, alumina, diatomite, and kaolin reported increments of around 0.4 to 3 times **[67]**. In this sense, the results from this section showed that adding minerals like kaolin to the composites can accelerate the charging/discharging of the TES system, even though, further investigation must be done, particularly in terms of latent heat and heat capacity, as this experiment was only intended as an initial exploration of the potential of adding natural minerals to increase the thermal conductivity of TES systems. Besides, particle distribution, morphology and mass fractions of the added mineral are other variables to be considered in further investigation. For instance, Lv et al. **[161]** prepared paraffin/kaolin SS-PCMs by the vacuum impregnation method, using different particle sizes of kaolin. They demonstrated that the

thermal conductivity of the SS-PCMs with large kaolin particles is higher than SS-PCMs with small kaolin particles.

5.2.6. Thermal reliability of the SS-PCMs and the eutectic PCMs

The stability of TES systems should be measured in terms of their thermal properties after a repeated thermal cycling (charging and discharging) to ensure that phase change temperature and latent heat remain almost constant and do not degrade during operation performance.

As stated by several authors **[248,249]**, the thermal reliability of LHTES is an important factor for long-term performance. On a daily basis application, as thermal comfort, the LHTES system will experience at least one charge during the day and one discharge during the night. Hence, a complete thermal cycle can occur once per day, and in a period of a year, the LHTES system will be subjected to at least 365 thermal cycles. Operational performance equivalent to 4 years, 10 years, and 30 years corresponds to approximately 1200, 3650, and 10000 thermal cycles. This condition can be replicated in the laboratory with an accelerated thermal cycling test, consisting of repeatedly melting/solidification cycles of the PCM with controlled conditions that reproduce the long-time performance of the TES system in a relatively short time. Typical methods used for thermal cycling include dynamic method **[250]**, where isothermal stages are performed before and after each heating/cooling cycle; and pyramid method **[251]** where no isothermal stages are used. The most used setups to performed these thermal cycles comprehend differential scanning calorimetry **[252]**, thermal cyclers **[253–255]**, equilibrium cell **[256]**, metal baths **[249]**, hot plate **[257]**, and thermal baths **[258]** with a temperature controller, and other experimental setups designed by the authors **[75,259,260]**.

In the literature, investigations about thermal reliability of inorganic PCMs as calcium chloride hexahydrate ($CaCl_2 \cdot 6H_2O$) **[252]** and magnesium chloride hexahydrate ($MgCl_2 \cdot 6H_2O$) **[261]** up to 1000 cycles can be found. Also, there are studies of organic PMCs as paraffins over 200 cycles **[262]**; up to 120 **[256]**, and 4000 **[259]** thermal cycles for capric/lauric binary acid and capric/myristic binary acid and capric/palmitic binary **[259]**; and 120, 560, 850 and 1200 cycles for pure fatty acids (stearic acid, palmitic acid, myristic acid, and lauric acid) **[258]**. Recently, Yang et al. **[249]** reported 10000 accelerated thermal

cycles for lauric acid, myristic acid, palmitic acid, and stearic acid. In **Table 39**, some of the most recent studies found are summarized. Moreover, the thermal stability of phase change materials until 2013 and 2015 can be found in two published review papers **[251,263]**, respectively.

Table 39. Phase change materials found in the literature tested under accelerated thermal cycling.

Type	Material	Number of cycles	Reference
Pure PCM	Calcium chloride hexahydrate	1000	**[264]**
	Magnesium chloride hexahydrate	1000	**[261]**
	Glutaric acid	2000	**[248]**
	Lauric acid	1200	**[265]**
		10000	**[249]**
	Myristic acid	1200	**[265]**
		10000	**[249]**
	Palmitic acid	1200	**[265]**
		10000	**[249]**
	Paraffin	200	**[262]**
	Paraffin wax	200	**[260]**
	PEG	200	**[163]**
	Stearic acid	1200	**[265]**
		10000	**[249]**
Binary PCM	Capric/lauric acid	120	**[256]**
		4000	**[259]**
	Capric/myristic acid	100	This study
		4000	**[259]**
	Capric/palmitic acid	4000	**[259]**
	Lauric/myristic acid	1460	**[266]**
		10000	This study
	Lauric/palmitic acid	1460	**[266]**
	Myristic/stearic acid	1460	**[266]**
	Palmitic/stearic acid	10000	This study
	Stearic acid/1,10-decanediol	100	**[267]**
		500	**[267]**
SS-PCM/CS-PCM	Capric-myristic-stearic acid/vermiculite	200	**[268]**
	Capric-myristic acid/expanded perlite	5000	**[269]**
	Myristic acid/ethyl cellulose shell	100	**[148]**
	Myristic-palmitic acid/PMMA shell	5000	**[270]**
	Paraffin/calcined diatomite	200	**[271]**
	Paraffin/expanded vermiculite	200	**[272]**
	Paraffin/expanded perlite	1000	**[223]**

Type	Material	Number of cycles	Reference
	PEG/TiO_2 support	200	**[163]**
	SS-CA/MA-P6-35 (clay support)	100	This study
	SS-LA/MA-P6-35 (clay support)	10000	This study
	SS-PA/SA-P6-35 (clay support)	10000	This study

Based on the literature survey carried out, it can be noted that few studies have focused on the stability of LHTES systems for long-term applications, for more than 10 years (4000 cycles). Moreover, most of them only have studied pure PCMs and not composites such shape-stabilized phase change materials. Therefore, thermal cycling up to 10000 cycles to the fatty acid eutectic mixtures produced in this thesis and their SS-PCMs, stabilized in the P6 support (clay calcined at 600°C) was performed. As well, the commercial SS-PCM, GR42 (Rubitherm), based on approximately 30% of paraffin and supported in a SiO_2 support **[273,274]**, was cycled. Composite GR42 is the only known commercial product similar to the SS-PCMs developed by the authors, that contains an organic PCM and a mineral support.

5.2.6.1 Thermal cycling test

Thermal cycling test for LA/MA, PA/SA, SS-LA/MA-P6-35, and SS-PA/SA-P6-35 was performed using a GeneQ Thermal Cycler TC-18/H(b) from Bioer Technology Co. LTD. Each sample was evaluated after 10, 100, 1000 and 10000 heating/cooling cycles. The cycles were executed as shown in **Fig. 84**. The lower and higher temperatures were selected to ensure the complete solidification and melting of the PCMs. As 20 °C is the lower limit of the GeneQ Thermal Cycler, the samples CA/MA, SS-CA/MA-P6-35, and GR42 were manually cycled, heated in an oven, and cooled in a fridge. These samples were evaluated after 10 and 100 cycles. The temperatures used were 6 °C and 40 °C for CA/MA and SS-CA/MA-P6-35, and 6 °C and 50 °C for GR42. Temperatures were chosen above and below the phase change temperature of the eutectics.

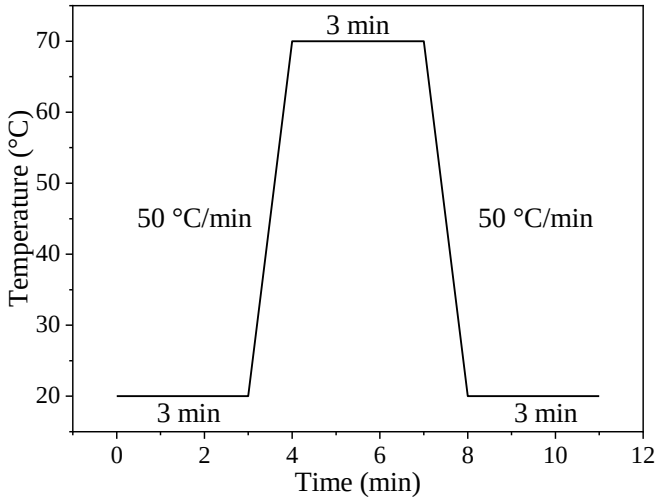

Fig. 84. Dynamic method for thermal cycling used in this study.

5.2.6.2 Chemical characterization (FT-IR)

Fourier transformation infrared spectroscopy (FT-IR), using the attenuated total reflection (ATR) as the sampling technique, was used to characterize the chemical composition of the eutectics, SS-PCMs and the P6 support. The spectroscope used was a FT/IR-6300 type A from Jasco, at a resolution of 4 cm^{-1} in a range from 650 to 4000 cm^{-1}. The spectra for the eutectics CA/MA, LA/MA, and PA/SA are given in **Fig. 85.** The bands at 2917 cm^{-1} and 2850 cm^{-1} correspond to the stretching vibrations of CH_3 and CH_2 groups. The carbonyl group band was observed at 1699 cm^{-1}, corresponding to a stretching vibration of C=O (H-bonded). Specific bands between 1350 cm^{-1} and 1570 cm^{-1} are attributed to the deformation of CH_2 and CH_3 groups due to bending vibrations. The band observed at 931 cm^{-1} correspond to the out-of-plane bending vibration of the O-H functional group and finally, the band at 723 cm^{-1} corresponds to CH_2 rocking vibration. All these bands are indicative of long-chain linear aliphatic structure **[275]**, as expected for eutectic mixtures of fatty acids.

Similarly, the infrared spectra for SS-CA/MA-P6-35, SS-LA/MA-P6-35, and SS-PA/SA- P6-35, are shown as well in **Fig. 85**. The 2917 cm^{-1} and 2859 cm^{-1} bands correspond to the stretching vibrations of CH_3 and CH_2 groups. A C=O (H-bonded) band was observed at 1696 cm^{-1} and around 1430 cm^{-1} a band attributed to bending vibrations of CH_2 and CH_3. A broadband around 1025 cm^{-1} appeared, corresponding to Si-O vibration from the support phase. The band at 795 cm^{-1} corresponds to the vibration band of AlO_4 tetrahedron in

metakaolin **[276]**. Similarly, as the support is not pure metakaolin, and other minerals are present, including kaolinite, other bands can be observed as a small band at 3655 cm^{-1} corresponding to the hydroxyl (OH) stretching vibrations **[276,277]**. Besides, band at 1630 cm^{-1} could be assigned to OH vibrational mode of hydroxyl molecule in water, which is observed in almost all natural hydrous silicates **[277]**. Hence, characteristic bands of the PCM eutectic were observed in each composite, indicating the presence of PCM inside the porous support. No additional bands different from the eutectics or the support appears in the SS-PCMs, meaning that there is no chemical reaction between the PCMs and the mineral support. It is worth to notice that peaks at 2917 cm^{-1}, 2850 cm^{-1}, and 1700 cm^{-1} weaken in the spectrum of the SS-PCMs possibly due to the formation of hydrogen bonds between the eutectic and the support **[268,278]**. These H-bonds may stabilized the PCMs in the composites avoiding leakage, as exposed in previous studies **[126,242]**.

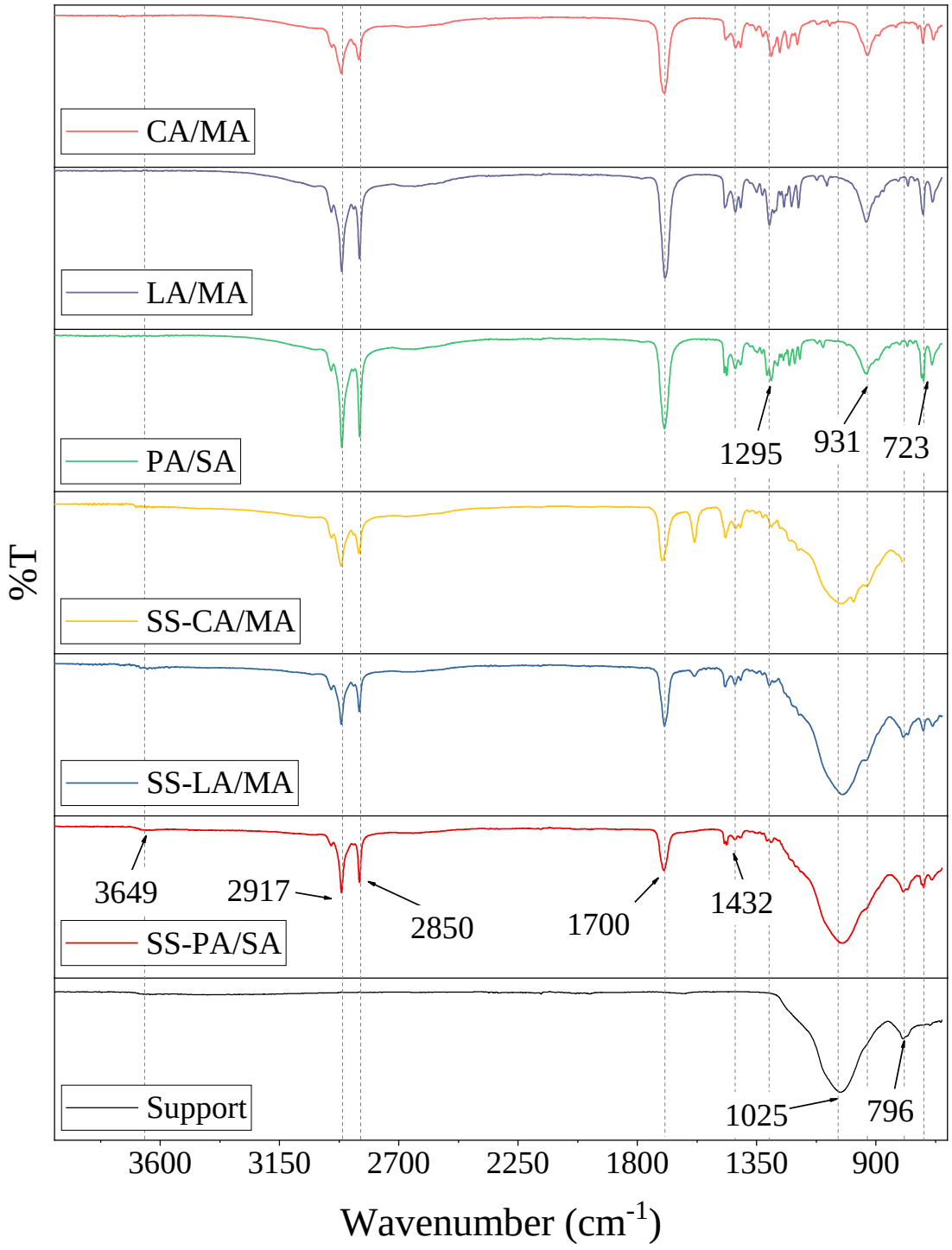

Fig. 85. FT-IR spectra of the support P6, CA/MA, LA/MA, PA/SA, SS-CA/MA-P6-35, SS-LA/MA-P6-35, and SS-PA/SA-P6-35.

5.2.6.3 Chemical changes after thermal cycling

Spectroscopy technique was used to explore if any chemical change occurred during thermal cycling of the binary PCMs and the SS-PCMs. As well, plots with normalized peaks based on the functional group that did not change significantly after cycling are shown next to each spectrum to easily analyzed changes in the functional groups present in the samples after thermal cycling. Functional groups used for normalization were CH_2 (2850 cm^{-1}), CH_2 (722 cm^{-1}), C=O (1698 cm^{-1}), CH_2, CH_3 (1585 cm^{-1}), Al-O (797 cm^{-1}), and Al-O (796 cm^{-1}) for CA/MA, LA/MA, PA/SA, SS-CA/MA-P6-35, SS-LA/MA-P6-35, and SS-PA/SA-P6-35, respectively.

The FT-IR spectra of CA/MA, LA/MA, and PA/SA after thermal cycling are shown in **Fig. 86**. As clearly seen in the spectra, all the peaks fit one another at the same frequency band. No additional peaks appeared for any of the eutectics, indicating that no chemical reaction occurred after cycling. A slight increase in the carbonyl group in CA/MA can be observed as the cycles increase, probably due to a partial oxidation of the fatty acids, as CA/MA is the eutectic with the shortest chain and more likely to present a higher rate of oxidation. No significant changes in LA/MA and PA/SA peaks were observed. Therefore, the chemical structure of the eutectics remained and did not degrade significantly during thermal cycling. This can be confirmed with the normalized plots where no significant increase or decrease of the peaks of each functional groups were observed after 10, 100, 1000, or 10000 cycles. This outcome complement results found in literature as the obtained by Yang et al. **[249]**, who reported a good chemical stability of pure fatty acids (lauric acid, myristic acid, palmitic acid, and stearic acid) after 10000 thermal cycles. Similarly, they are in agreement with Sari et al. **[183]**, who cycled lauric acid-myristic acid eutectic up to 1460 cycles finding a good stability. Thus, with this work, it was proven that eutectic binary mixtures CA/MA, LA/MA, and PA/SA present good chemical stability after 100 cycles for CA/MA, and up to 10000 cycles for LA/MA and PA/SA.

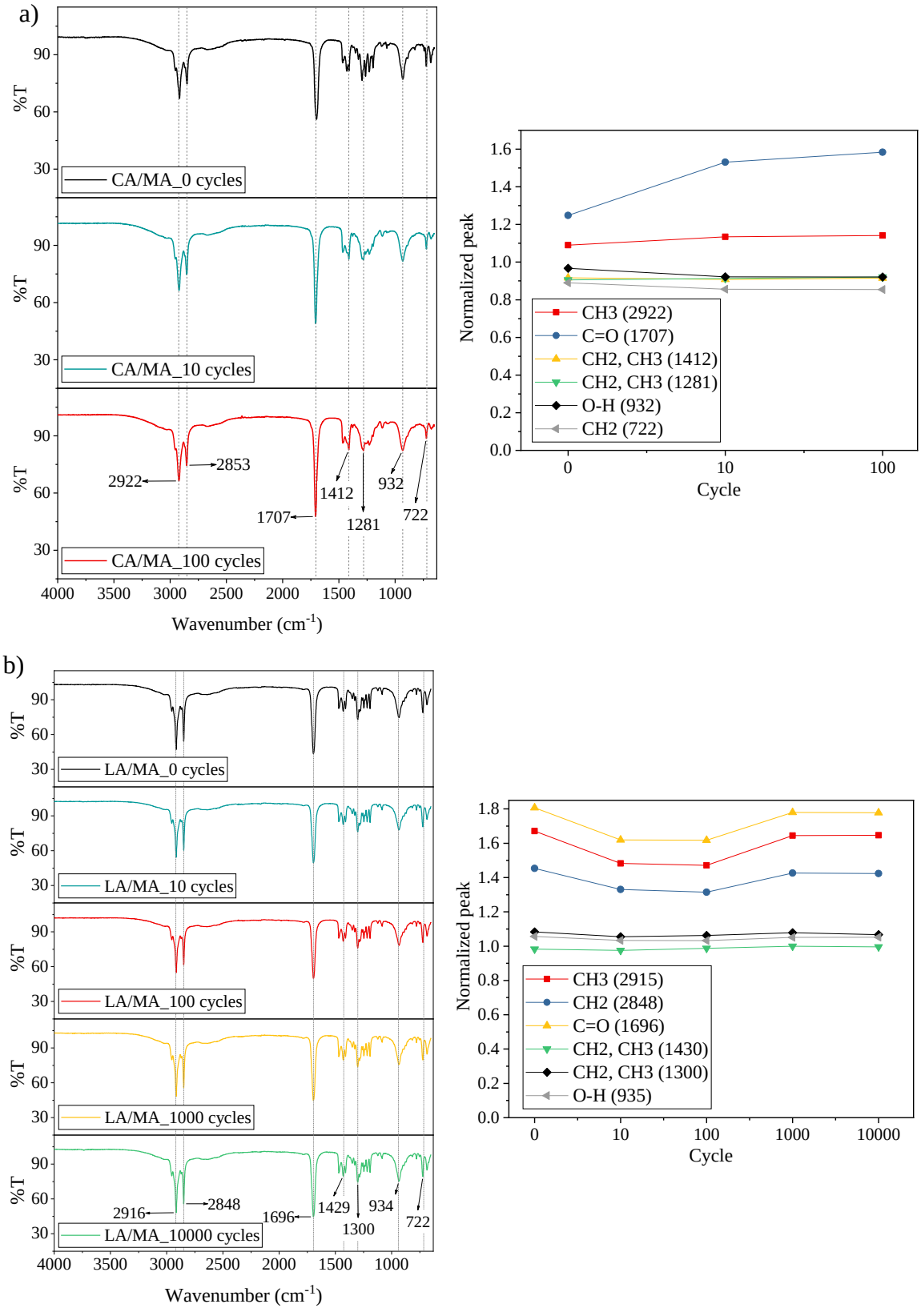
a)
%T
CA/MA_0 cycles
CA/MA_10 cycles
CA/MA_100 cycles
2922
2853
1707
1412
1281
932
722
Wavenumber (cm-1)
Normalized peak
CH3 (2922)
C=O (1707)
CH2, CH3 (1412)
CH2, CH3 (1281)
O-H (932)
CH2 (722)
Cycle
b)
LA/MA_0 cycles
LA/MA_10 cycles
LA/MA_100 cycles
LA/MA_1000 cycles
LA/MA_10000 cycles
2916
2848
1696
1429
1300
934
722
CH3 (2915)
CH2 (2848)
C=O (1696)
CH2, CH3 (1430)
CH2, CH3 (1300)
O-H (935)

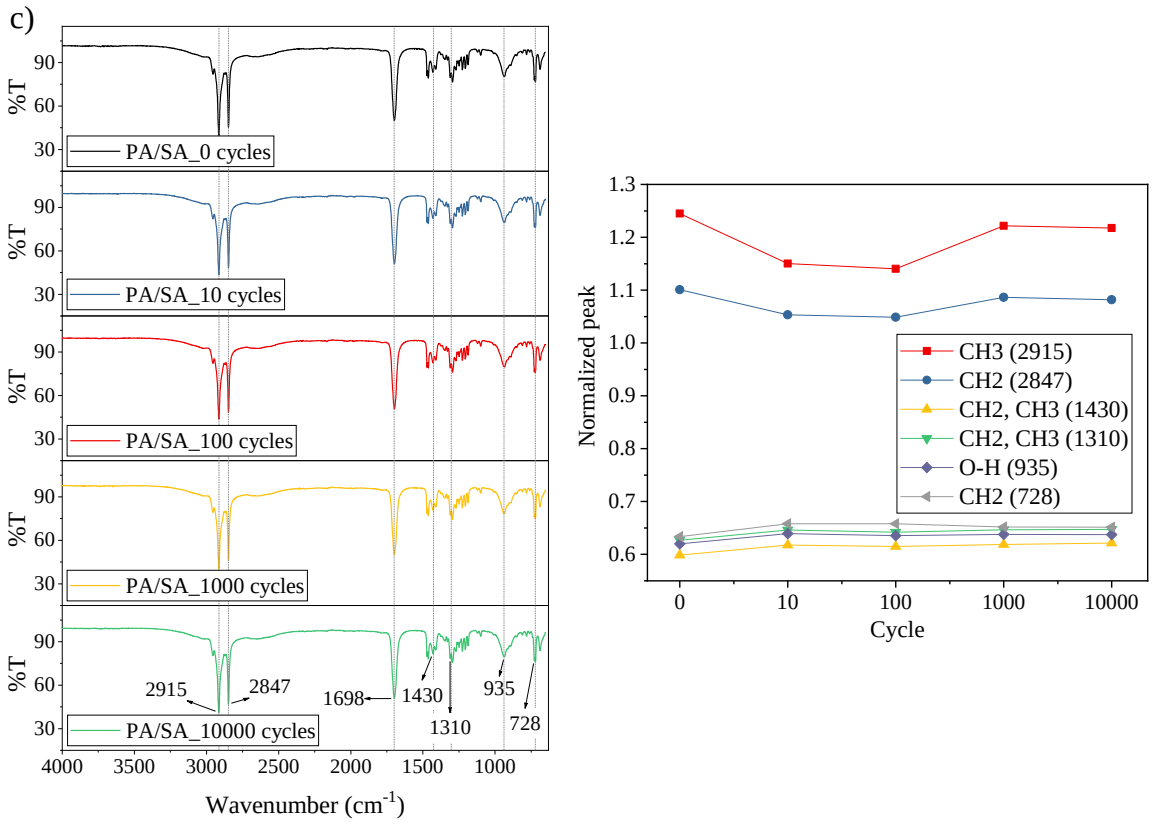

Fig. 86. FTIR Spectra and normalized peak plot of eutectics a) CA/MA, b) LA/MA, and c) PA/SA after 0, 10, 100, and 10000 cycles.

Similarly, SS-PCMs composites were cycled and the spectra are shown in **Fig. 87**, with their respective normalized peak plots. The SS-CA/MA-P6-35 composite cycled up to 100 cycles, presented no significative changes in their bands, except for the Si-O band. Even though, the chemical composition remained the same during cycling. SS-LA/MA-P6-35 peaks fit one another at the same frequency band and no additional peaks appeared, meaning good chemical stability of the composite, even at 10000 thermal cycles. In the same way, SS-PA/SA-P6-35 presented good stability as no new peaks appeared during cycling and no significant changes were observed on most of the functional groups, only an unexpected increment in the Si-O band could be observed.

a)

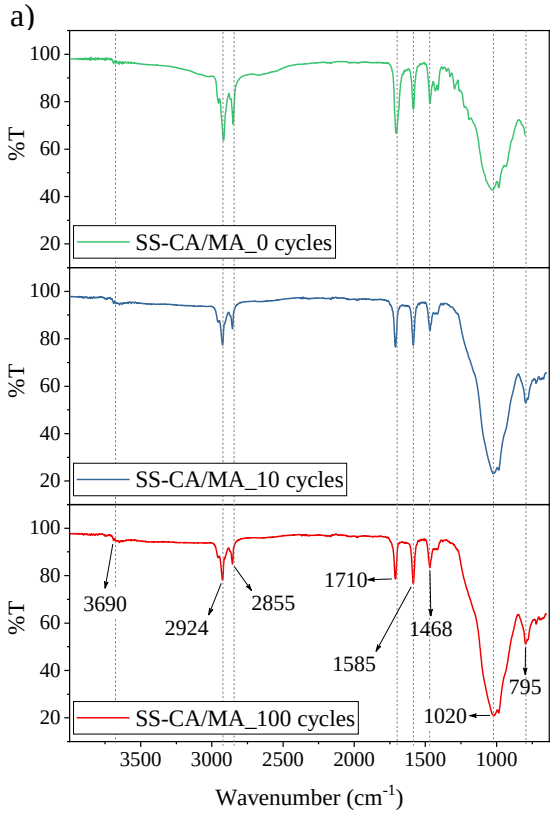
%T
SS-CA/MA_0 cycles
SS-CA/MA_10 cycles
SS-CA/MA_100 cycles
3690
2924
2855
1710
1468
1585
795
1020
Wavenumber (cm-1)

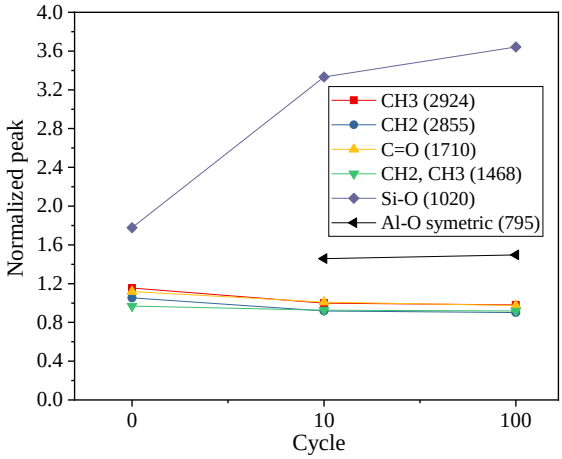
Normalized peak
CH3 (2924)
CH2 (2855)
C=O (1710)
CH2, CH3 (1468)
Si-O (1020)
Al-O symetric (795)
Cycle

b)

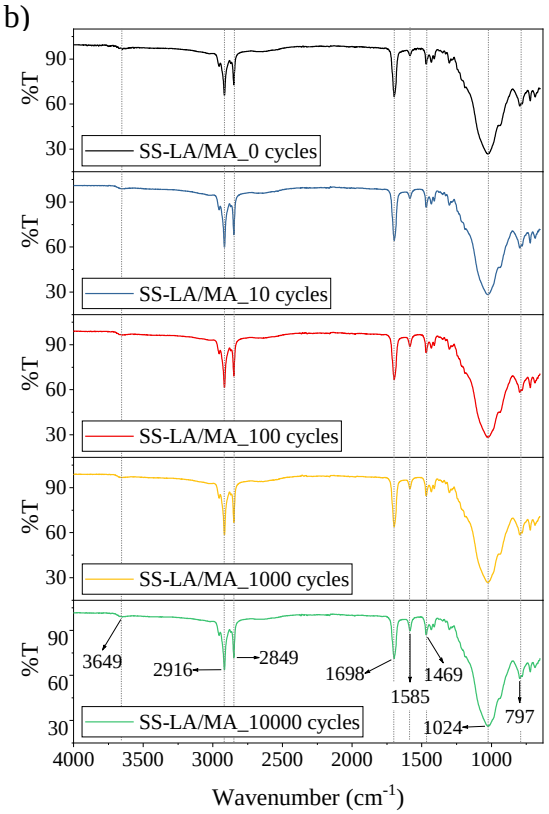
%T
SS-LA/MA_0 cycles
SS-LA/MA_10 cycles
SS-LA/MA_100 cycles
SS-LA/MA_1000 cycles
SS-LA/MA_10000 cycles
3649
2916
2849
1698
1585
1469
1024
797
Wavenumber (cm-1)

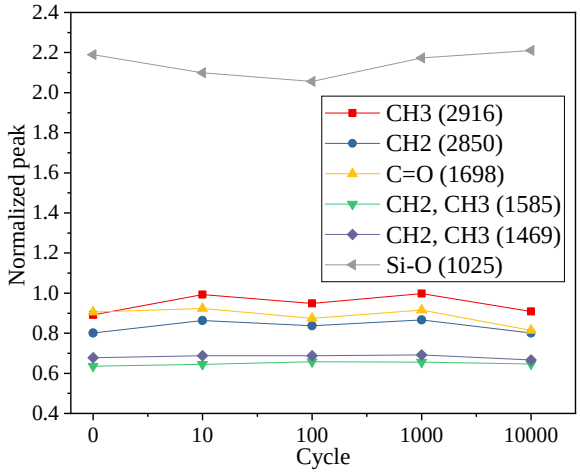
Normalized peak
CH3 (2916)
CH2 (2850)
C=O (1698)
CH2, CH3 (1585)
CH2, CH3 (1469)
Si-O (1025)
Cycle

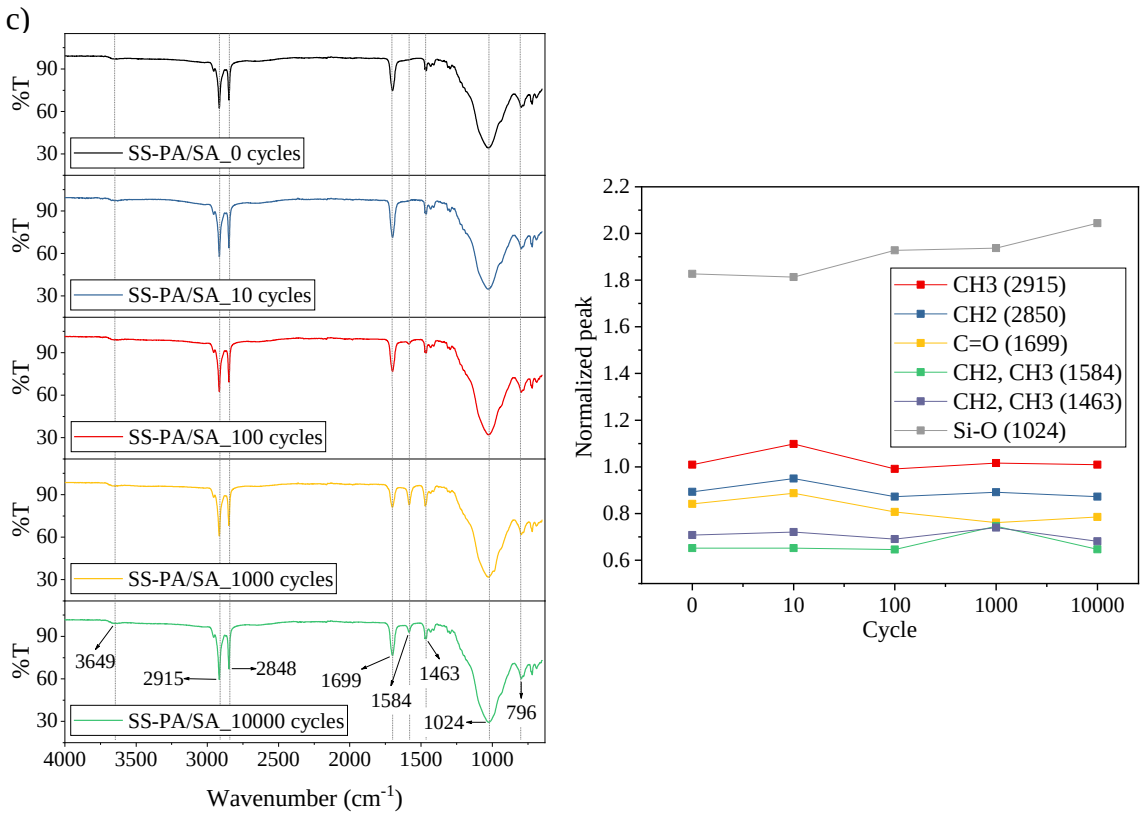

Fig. 87. FTIR Spectra and normalized peak plot of composites a) SS-CA/MA-P6-35, b) SS-LA/MA-P6-35, and c) SS-PA/SA-P6-35 after 0, 10, 100, and 10000 cycles.

The commercial granulated sample GR42 was cycled up to 100 cycles. **Fig. 88** shows the FT-IR spectrum after each cycle, and it can clearly be noticed that no new peaks were formed, nor significant changes of the existing ones was appreciated. Hence, GR42 presented good thermal stability in terms of chemical structure when cycled up to 100 cycles. After measuring this commercial sample, it can be stated that the SS-PCMs produced in this work were as chemically stable as the only commercial SS-PCMs available in the market, to the best of our knowledge, produced with a comparable support.

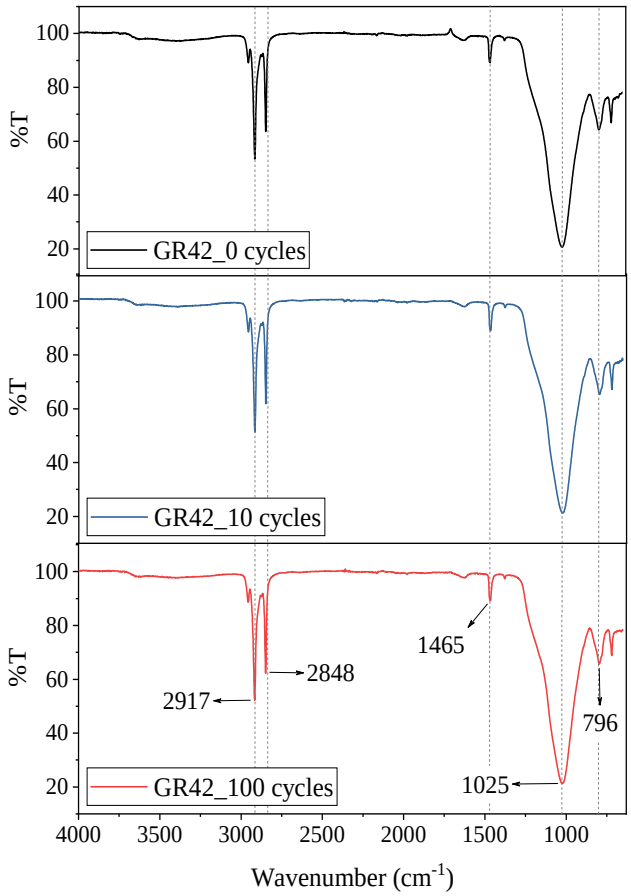

Fig. 88. FT-IR spectrum of GR42 after 0, 10 and 100 cycles.

5.2.6.4 Thermal energy storage properties after thermal cycling

Thermal properties were measured using differential scanning calorimetry (DSC) with a DSC 3+ from Mettler Toledo. Measurements were carried at a heating/cooling rate of 5 °C/min, as lower rates were proven to give the same information for our samples. Samples were measured under nitrogen atmosphere (50 mL/min) and the values reported were obtained after 2 heating/cooling cycles.

Phase change temperatures and enthalpies of the eutectics and the SS-PCMs, after cycling, are shown in **Fig. 89.** The SS-PCMs without thermal cycling (0 cycles) undergo little changes compared to the eutectics for the onset melting temperatures, that differences were of 1.8 °C for CA/MA and SS-CA/MA-P6-35; 1.3 °C for LA/MA and SS-LA/MA-P6-35; and 0.2 °C for PA/SA and SS-PA/SA-P6-35. Changes in the phase change temperature are attributable to the confinement of the PCM inside the porous structure of the support as some pressure

variations in the PCM occur when the phase change and thus modifies the melting temperature **[279]**.

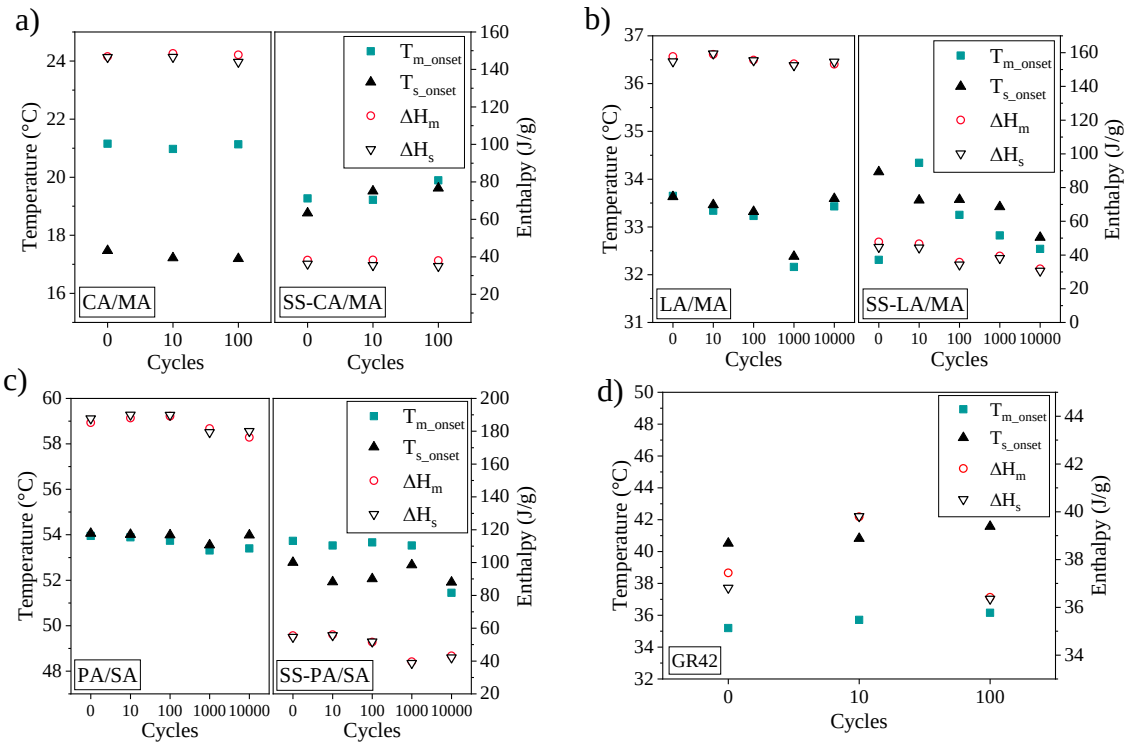

Fig. 89. Thermal properties (phase change temperatures, T, and enthalpies, ΔH, for melting, m, and solidification, s, of a) CA/MA, SS-CA/MA-P6-35, b) LA/MA, SS-LA/MA-P6-35, c) PA/SA, SS-PA/SA-P6-35, and d) GR42.

For CA/MA eutectic (**Fig. 89. a)**), all thermal properties remained the same up to 100 cycles, the melting temperature was around 21.08 ± 0.09 °C and latent heat of fusion/solidification was 147.74 ± 0.84 J/g. Similarly, the SS-CA/MA-P6-35 composite (**Fig. 89. a)**) did not show significant changes between cycles; the melting temperature was 19.46 ± 0.37 °C and latent heat of fusion of 38.20 ± 0.15 J/g. These results indicate that CA/MA and SS-CA/MA-P6-35, besides being chemically stable as discussed previously with the FT-IR analyses, are also thermally stable after cycling.

On the other hand, LA/MA (**Fig. 89. b)**) presented a melting and solidification temperature of 33.40 ± 0.21 °C after 100 cycles, and a decreased of 1.24 °C could be noticed after 1000 cycles, but then, after 10000 cycles increased again up to 33.40 °C. Latent heat of fusion/solidification was 157.46 ± 1.70 J/g after 100 cycles, then after 1000 cycles decreased

4.20 J/g and remained of 153.26 ± 0.18 J/g after 10000 cycles. Composite SS-LA/MA-P6-35 (**Fig. 89. b)**) presented a melting/solidification temperature increase of 2.03 °C after 10 cycles, from 32.31 °C to 34.34 °C, and then began to decrease with each thermal cycle, reaching almost the 0-cycle temperature. The temperature after 100, 1000 and 10000 cycles remained of 32.87 ± 0.35 °C. Latent heat of fusion/solidification was 47.20 ± 0.74 J/g after 10 cycles, then decreased 11.45 J/g and remained of 35.65 ± 3.84 J/g after 10000 cycles. These irregular changes with increasing the number of thermal cycles have been reported by other authors **[182]**. As no significant degradation of the PCM was observed by means of spectroscopy then these changes may be due to some impurities present in the fatty acids **[182,249,258]**. Furthermore, these changes in temperature and enthalpy are not significant and it can be concluded that LA/MA and SS-LA/MA-P6-35 presented a reasonably good thermal reliability after 10000 cycles.

Similarly, PA/SA (**Fig. 89. c)**) presented an average melting temperature of 53.65 ± 0,28 °C and a latent heat of fusion of 184.10 ± 5.23 J/g between 0-cycle and 10000-cycles, indicating a good thermal stability. Composite SS-PA/SA-P6-35 (**Fig. 89. c)**) behaved comparably, with an average melting temperature of 53.18 ± 0.97 °C and a latent heat of fusion of 49.184 ± 7.43 J/g between 0-cycle and 10000-cycles. These deviations are acceptable for PCMs that will be used in latent heat energy storage systems **[258]**. Complete DSC curves for the samples are shown in **Fig. 90**.

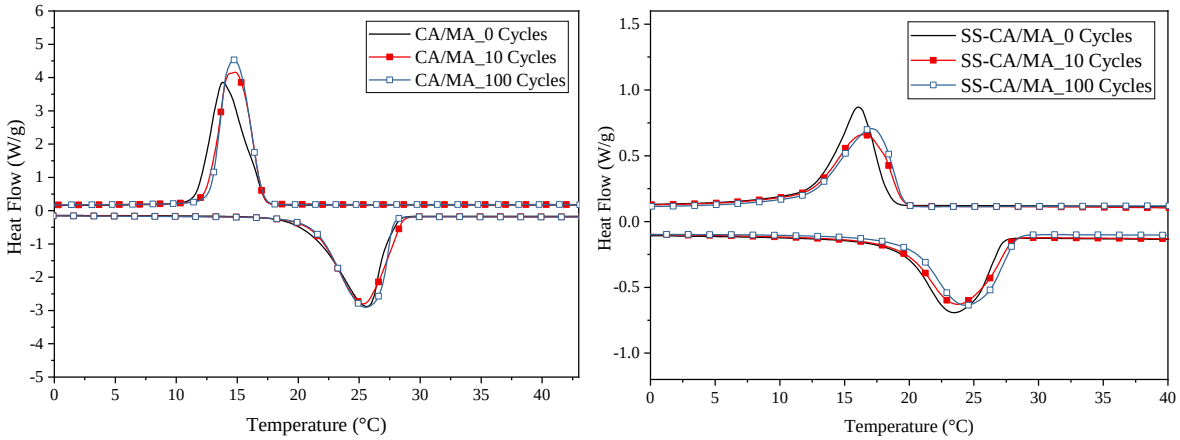

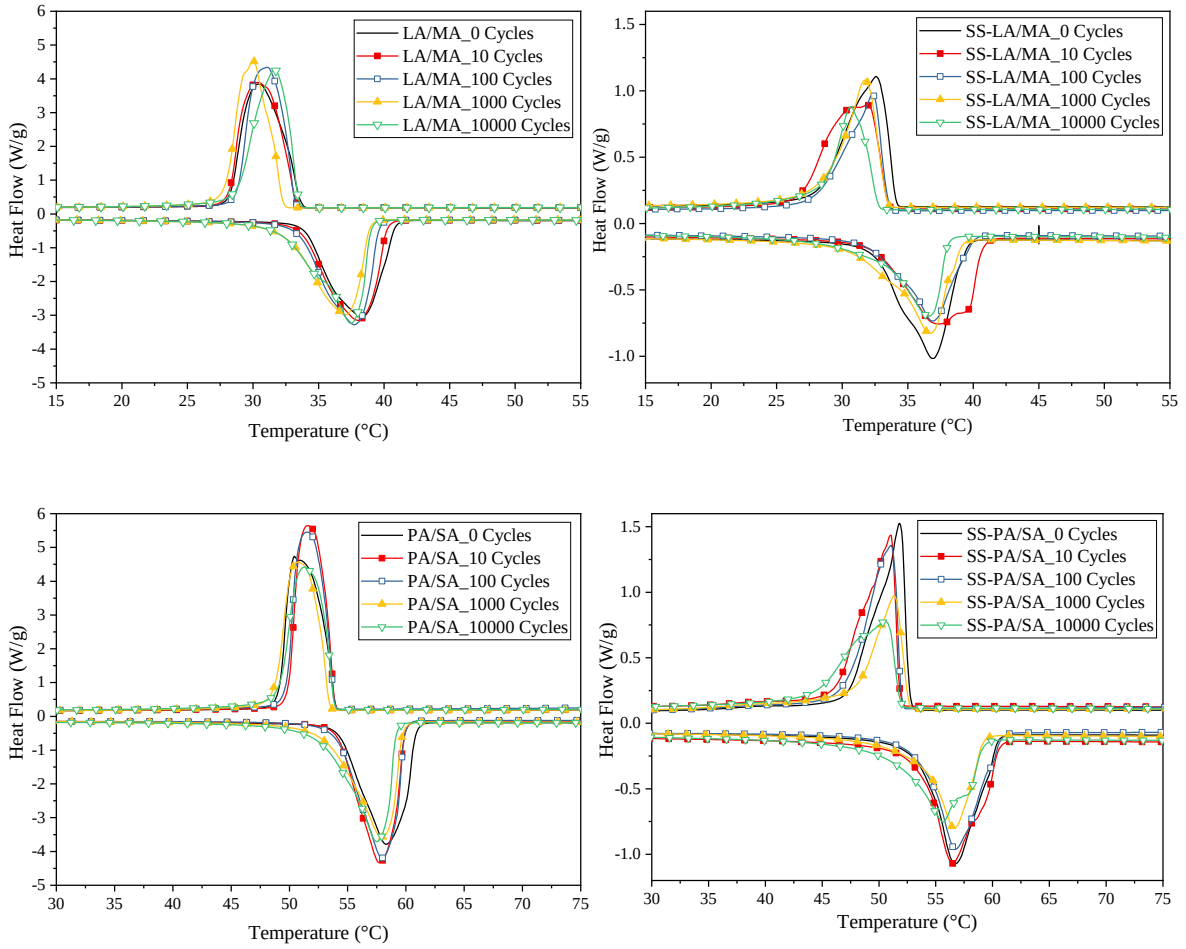

Fig. 90. DSC curves of CA/MA, LA/MA, PA/SA, SS-CA/MA-P6-35, SS-LA/MA-P6-35, and SS-PA/SA-P6-35, after thermal cycling. The curves are drawn with the exothermic peak up.

Commercial SS-PCM, GR42 (**Fig. 89. d)**), maintained a melting temperature of 35.68 ± 0.48 °C and a latent heat of fusion of 37.88 ± 1.72 J/g after 100 cycles. Again, irregular changes in the thermal properties can be notice in the plot along the thermal cycles, but the order of magnitude is not significant, then GR42 presented a good thermal stability up to 100 cycles. It is worth mentioning that differences between onset melting and solidification temperatures, along the thermal cycles, for GR42 are the largest (5.28 °C) compared with SS-CA/MA-P6-35 (0.16 °C), SS-LA/MA-P6-35 (0.44 °C) and SS-PASA-P6-35 (0.99 °C); this parameter can be important when optimizing TES system in the charging/discharging performance. Similarly, Quanying et al. **[280]** studied numerous paraffins and fatty acid mixtures after 500 thermal cycles finding that fatty acids were more

stable than paraffin mixtures as the average change rate of phase change temperature and latent heat were lower.

With this section we prove that the SS-PCMs with 35% of PCM and supported in the clay P6 presented good thermal stability (up to 30 years of working service) and adequate thermal properties. It can be inferred that these TES composites can be used in several applications **[281]**. For instance, SS-CA/MA-P6-35 can be incorporated in buildings for reducing the required power capacity of HVAC systems, to improve their thermal performance, or for free-cooling systems (thermal comfort). Composites SS-LA/MA-P6-35 and SS-PA/SA-P6-35 can be intended for use in as domestic hot water system, heating applications or even for the food industry. As well, these powder SS-PCMs, can be used for low-temperature storage applications such bubbling fluidized beds **[273,274]** as an alternative to conventional packed beds.

5.2.7. Conclusions of granulation and heat treatments

The previous sections were carried out to determine the influence of thermal treatments on the porosity of a powder and granulated clay mineral support. Likewise, this work was intended to help understand how modifying textural properties of a support affects the impregnation and thermal properties of PCMs in SS-PCMs composites. Thus, the following conclusions can be drawn:

- The increase of calcination temperature decreases the leakage of the PCM from the support, up to 900 °C. At 1100 °C some of the clay minerals sinter, drastically decreasing the volume of pores to almost zero, thus increasing the leakage percent.

- It was proved that textural properties as the surface area, pore volume, and pore width act as a set of required conditions and do not should be analyzed separately because can conduct to misinterpretations. When appropriately adjusted, textural properties modification can decrease the leakage of SS-PCMs.

- Powder and granulated supports comprise mesopores between 3 nm and 35 nm, and macropores ten times bigger, around 200-300 nm, besides, for the granulated supports, a pore network is present as the particles are agglomerated.

- The thermal conductivity of the powder support from room temperature up to 600 °C did not showed significant changes.

- Raw support (RP) and supports calcined at 600 °C (P6), and 900 °C (P9) did not affect the thermal behavior of the binary fatty acid eutectic when incorporated in 25%, 35%, or 40% wt.

- Support calcined at 600 °C (P6) was selected as the optimum for shape-stabilization of lauric/myristic acid (LA/MA), with impregnation of 35% wt. The composite SS-LA/MA-P6-35 presented low leakage losses (1.26%) as P6 presented an adequate surface area, pore volume, and pore width. The phase change temperature, 36.56 °C, was in the desired operating range, which matches the pure eutectic. As well, good latent heat of fusion of 51.63 kJ/kg was achieved.

- Validation of the performance of the P6 support with other eutectics, as capric/myristic (CA/MA) and palmitic/stearic (PA/SA) acids, was accomplished successfully. The best impregnation ratio was 35%. The P6 support improved (decreased) the leakage in 20.2%, 27.2%, and 43.3%, for CA/MA, LA/MA, and PA/SA, respectively, compared to the raw support (RP). Besides, heat capacity as a function of the temperature, thermal degradation and a leakage cycling for 16 hours of the composites was obtained.

- Temperature dependence curves of thermal conductivity for the binary eutectic mixtures CA/MA, LA/MA and PA/SA, as well as for their shape-stabilized forms, SS-CA/MA-P6-35, SS-LA/MA-P6-35 and SS-PA/SA-P6-35, was obtained. The values of thermal conductivity for the SS-PCMs (0.128 W/m·K - 0.165 W/m·K) were lower than for the eutectics (0.140 W/m·K - 0.218 W/m·K), but higher than for the support (0.05 W/m·K). The thermal conductivity presented a linear correlation with temperature for all the materials.

- Commercial SS-PCM from Rubitherm, GR42, was compared with the SS-PCMs produced in terms of thermal conductivity. The results showed that SS-CA/MA-P6-

35, SS-LA/MA-P6-35 and SS-PA/SA-P6-35 exhibit higher thermal conductivity than GR42. The increase of thermal conductivity was between 10.57% and 33.33%.

- Additions up to 50% of kaolin were made to the composite SS-LA/MA-P6-35, resulting in an increase on its thermal conductivity. The raise was between 6.49% and 17.68% respect to the composite without addition (0% kaolin added). Even though, further investigation must be done to improve the values as this experiment was only intended as an initial exploration of the potential of adding natural minerals to increase thermal conductivity of TES systems.

- Thermal reliability of CA/MA, LA/MA and PA/SA, as well of their shape-stabilized composites SS-CA/MA-P6-35, SS-LA/MA-P6-35, and SS-PA/SA-P6-35, was determined. Results after thermal cycling test demonstrated good chemical stability after 100 cycles for CA/MA and SS-CA/MA-P6-35, and up to 10000 cycles for LA/MA, PA/SA, SS-LA/MA-P6-35, and SS-PA/SA-P6-35. Thus, the SS-PCMs developed presented thermal stabilities corresponding up to 30 years of operation.

- After thermal cycling, the maximum changes in the phase transition temperature were of 0.09 °C, 0.37 °C, 1.24 °C, 2.03 °C, 0.28 °C, and 0.97 °C; and changes in enthalpy were about 0.84 J/g, 0.15 J/g, 4.20 J/g, 11.45 J/g, 5.23 J/g, and 7.43 J/g for CA/MA, SS-CA/MA-P6-35, LA/MA, SS-LA/MA-P6-35, PA/SA, and SS-PA/SA-P6-35, respectively. Besides, no new functional groups appeared in the FT-IR spectra, indicating an adequate chemical stability through thermal cycling.

The results of sections 5.1 and 5.2 support the idea that controlling and analyzing the textural properties of the supports used for shape-stabilization of PCMs, from a top-down approach, can optimize the absorption capacity of the PCM and thus, the thermal properties of the general system.

5.3. Grafting of silane into the clay support

In this section, chemical modification of the raw clay support was performed by organosilane grafting, particularly by aminopropyltriethoxysilane. This approach was selected as the clay used in this work present siloxane bridges and different kinds of hydroxyl groups, as silanols,

which are key reactive sites for various surface modifications as sylanization **[237]**, as well, aluminol groups are reported as suitable for edge surface grafting reactions **[227]**. These functional groups are mainly present within the clay in the kaolin, illite and diatomite minerals.

Grafting reactions form covalent bonds between reactive surface groups and organic species. In the literature there are stablished three models (**Fig. 91**) of interaction between silane and clays: interlayer grafting, external surface grafting and "broken" edge grafting. This is due to clay minerals are characterized by certain properties as the existence of several types of surfaces **[227]** such as external basal (planar), edge surfaces and internal (interlayer) surfaces. Particularly, the external and internal surfaces can be modified by adsorption, ion exchange, or grafting.

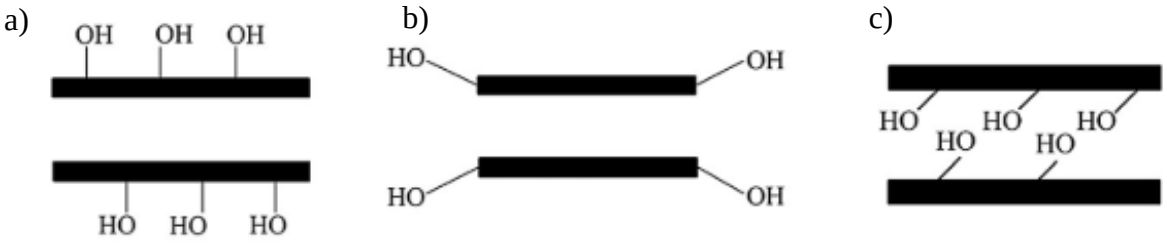

Fig. 91. Possible sites for silylation, a) external surface, b) "broken" edges, and c) internal clay surface **[282]**.

Some authors **[283–285]** sustain that the formation of an intercalation complex as an intermediate step can improve the grafting reaction of the clay. There are mainly three kind of materials used for intercalation. Compounds that form H-bridges (e.g. hydrazine, urea, formamide, amides), compounds with high-dipole moment (e.g. DMSO, pyridine), and compounds as alkyl-ammonium, primary amines, or quaternary ammonium salts. Hence, the previous intercalation of a molecule before sylanization was studied in this work.

Works of intercalation and sylanization of clays reported in the literature are done using pure minerals as kaolinite **[284,286–288]**, montmorillonite **[283,289,290]**, vermiculite **[291,292]**, and just a few, diatomite **[293,294]**. In this thesis, we wanted to go one step further modifying a natural clay that comprises a mixed of minerals such kaolinite, diatomite, quartz and illite. After the surface silylation of the clay, the new modified clays will serve as improved

supports for shape-stabilization of organic PCMs. The good compatibility of organic PCM and the modified clay should improve PCM retention.

5.3.1. Materials

The clay used here to be modified was the powder raw support, called hereafter P, without any heat treatment. The clay was milled (M200) and dried. The reagents used were 3 - aminopropyltriethoxysilane (APTES, Wacker), dimethyl sulfoxide (DMSO, Merk), hydrochloric acid (HCl, 33% purity), isopropanol (Merk, 99.8% purity) and ethanol (Merk). Deionized water was used to prepare solutions.

5.3.2. Silane grafting methods

Two procedures of silane grafting of the P clay were compared. The synthesis methods followed in here are adaptations of the works of Raji et al. **[295]** who studied the silanization with 3-aminopropyltriethoxysilane (APTES) and vinyltrimethoxysilane (VTMS) of montmorillonite, halloysite and sepiolite for a polypropylene/clay nanocomposite. As well, the research conducted by Abou-El-Sherbini et al. **[296]**, in which kaolinite samples were intercalated with dimethylsulphoxide (DMSO). The procedures are shown schematically in **Fig. 92** and are described below.

Procedure I (acid leaching and grafting of APTES): 100 g of P clay was added to a solution of 190 g of deionized water and 302 ml of HCl (5 mol/l). The mixture was refluxed at 80 °C with stirring for 2 h. Then the dispersion was filtered under vacuum and washed several times with deionized water, and finally was dried at 70 °C for 24 h. The resulting material was named P-M1. In a second stage, 5 g of P-M1 was added to a solution of 50 g of APTES and 500 ml of isopropanol. The mixture was refluxed at 82 °C with stirring for 24 h. Then the dispersion was filtered under vacuum and washed several times with isopropanol, and finally was dried at 70 °C for 24 h. The resulting material was named P-M2.

Procedure II (intercalation of DMSO and grafting of APTES): 20 g of P clay was added to a solution of 135 g of DMSO and 15 ml of deionized water. The mixture was refluxed at 70 °C with stirring for 2 h. Then the dispersion was filtered under vacuum and washed several times with ethanol, and finally was dried at 70 °C for 24 h. The resulting material was named P-

M3. Then, 5 g of P-M3 was added to a solution of 50 g of APTES and 500 ml of isopropanol. The mixture was refluxed at 80 °C with stirring for 24 h. Then the dispersion was filtered under vacuum and washed several times with isopropanol, and finally was dried at 70 °C for 48 h. The final material was named P-M4.

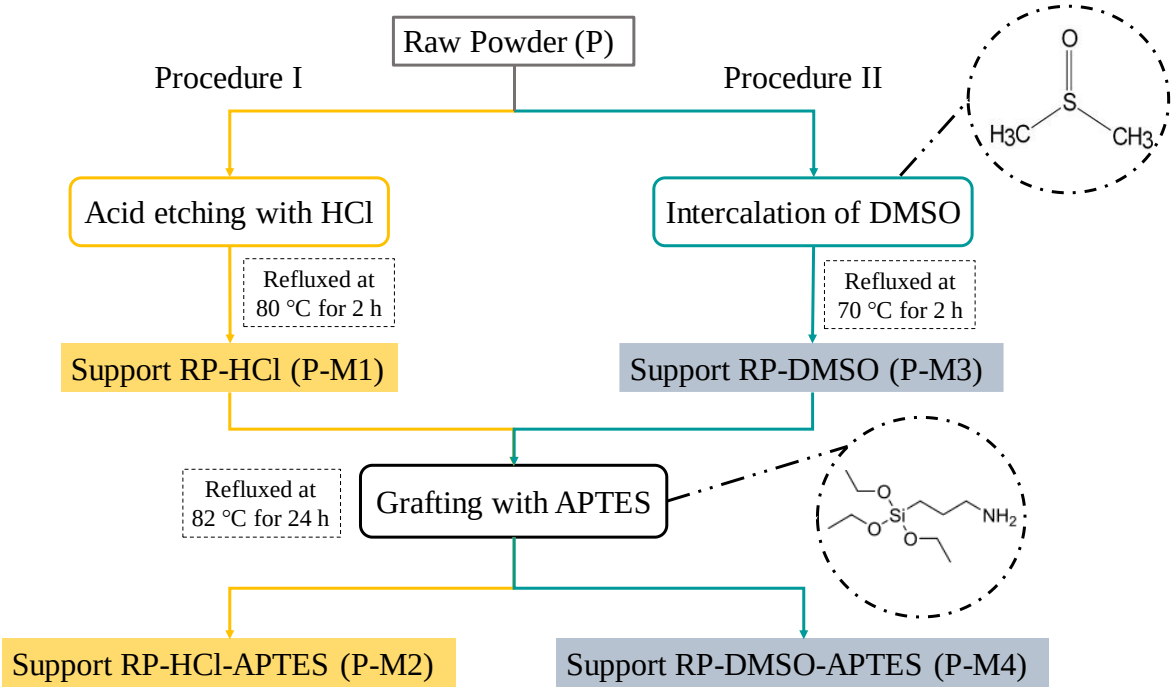

Fig. 92. Schematic representation of the two procedures used for sylanization.

5.3.3. Characterization of the silane-grafted clay

5.3.3.1 X-ray fluorescence (XRF)

Chemical composition of the clay supports was analyzed in a PANalytical AXIOS Max-Mineral X-ray fluorescence spectrometer (XRF) with a Rh-tube. XRF characterization was performed to assess the effect of DMSO, HCl, and APTES treatments in the composition of the P clay. Results of the elemental analysis of samples P, P-M1, P-M2, P-M3, and P-M4 are shown in **Table 40**. In general, treatments of clays with HCl **[297,298]** has proven to remove iron oxides and alumina. Samples P-M1 and P-M2 confirmed this outcome as alumina and iron oxide decreased compared with the untreated sample P. The reduction of iron oxide, additionally, conferred to the sample a less reddish color (**Fig. 103. b)**), here acting the HCl as a bleaching agent. Besides, calcium and phosphorus oxides decreased as well. On the other hand, the incorporation of DMSO increased, as expected, four times the sulfur oxides

compared to the P sample. The other elements remained very similar to the untreated sample. The APTES addition did not affect, according to XRF data, the chemical composition of the samples.

Table 40. Chemical composition of P, P-M1, P-M2, P-M3 and P-M4 samples.

Sample	SiO_2	Al_2O_3	Fe_2O_3	TiO_2	CaO	MgO	Na_2O	K_2O	BaO	MnO	P_2O_5	SO_3	LOI*
P	65.3	17.2	5.73	0.51	0.2	0.40	0.01	1.58	0.07	0	0.15	0.09	8.7
P-M1	72.2	16.0	1.56	0.57	0.06	0.32	0.03	1.58	0.08	N.D.	0.04	N.D.	7.6
P-M2	71.2	14.8	1.46	0.53	0.08	0.30	0.02	1.46	0.06	N.D.	0.04	N.D.	8.0
P-M3	64.4	16.8	5.56	0.50	0.19	0.39	-	1.54	0.07	0.01	0.14	0.36	10.1
P-M4	65.1	16.1	5.31	0.48	0.19	0.37	-	1.47	0.06	0	0.14	0.16	-

*loss of ignition between 110 °C and 1000 °C.

5.3.3.2 Fourier transform infrared spectroscopy (FT-IR)

FT-IR spectroscopy was performed to identify the different functional groups formed during the chemical modifications of the clays. The spectroscope used was a Nicolet 6700 from Thermo Fisher Scientific, at a resolution of 4 cm^{-1} in a range from 500 to 4000 cm^{-1}.

The spectra for P, P-M1, P-M2, P-M3, and P-M4 are given in **Fig. 93**. The assignments of the main vibrations are shown in **Table 41**, and were based on previous reports on clays and chemical modifications with APTES and DMSO **[284,285,288,296,299]**. All the samples displayed typical vibration bands corresponding to the hydroxyl stretching vibration (3653 cm^{-1}, 3651 cm^{-1}, 3620 cm^{-1}), and to the vibration modes of OH deformation of water (1635 cm^{-1}). The bands at 1033 cm^{-1}, 912 cm^{-1}, 798 cm^{-1}, and 695 cm^{-1} represent asymmetric Si-O stretching, Al-OH bending, Si-O-Al, and Si-O bending vibrations, respectively. The bands at 3697 cm^{-1} and 3695 cm^{-1} are attributed to the vibration of interlayer hydrogen-bonded hydroxyl groups, Al-OH. A new band developed near 1560 cm^{-1} for P-M2 and P-M4 corresponding to $N\text{-}H_2$ deformation. This reflected the presence of APTES molecules in those materials. Besides, the relative intensity of the peak related to absorbed water (1635 cm^{-1}) for P-M2 and P-M3 decrease compared to P. This is attributable to a reduction of the absorbed water molecules in the interlaying spacing of the clay that have been replaced by organosilane molecules **[282]**, thus corroborating the silylation of the P support with APTES.

Table 41. Positions and assignments of the IR bands of the P clay and its modification with DMSO and APTES.

Position (cm^{-1})	Assignment
3697, 3695	Inner surface Al-OH stretching
3653, 3651	Inner-surface O-H
3620	Stretching vibration of inner O-H
1635	O-H deformation of water
1560	N-H_2 deformation
1425	CH_3 bending
1033	Si-O asymmetric stretching
912	Al-OH bending
798	Si-O-Al
695	Si-O bending

As well, the APTES-modified supports, P-M2 and P-M4, showed decreasing intensities of the Al-OH stretching (3697 cm^{-1}) suggesting that the modification consumed Al-OH groups. Thus, indicating that grafting occurs between the Al-OH groups and the hydrolyzed APTES **[285]**. As well, the band of the Si-O asymmetric stretching vibration (1033 cm^{-1}) decreased with the incorporation of APTES, indicating that some of the organosilane were attached to the Si-O.

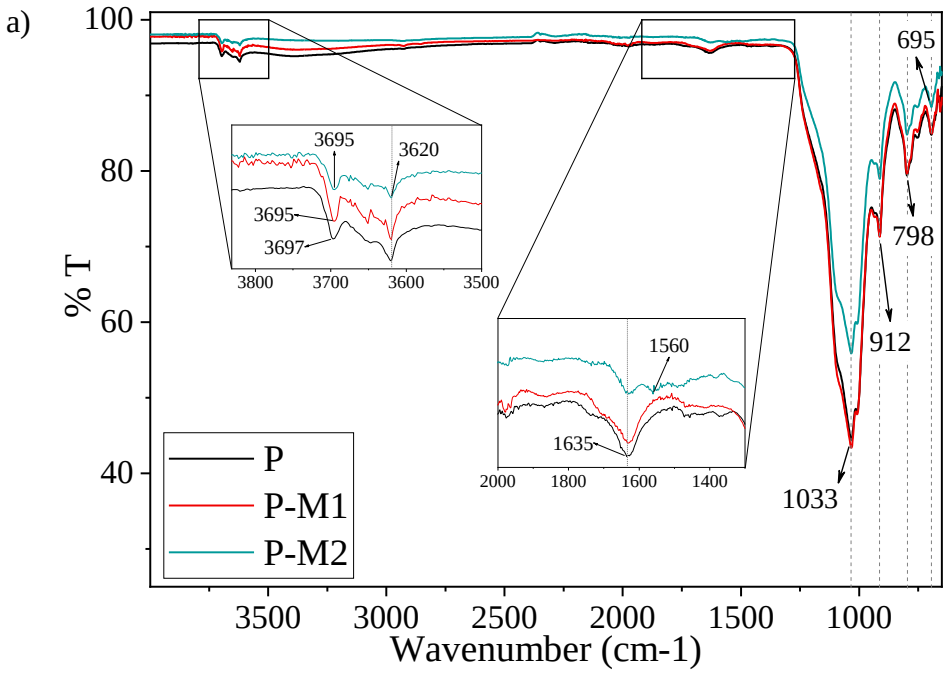

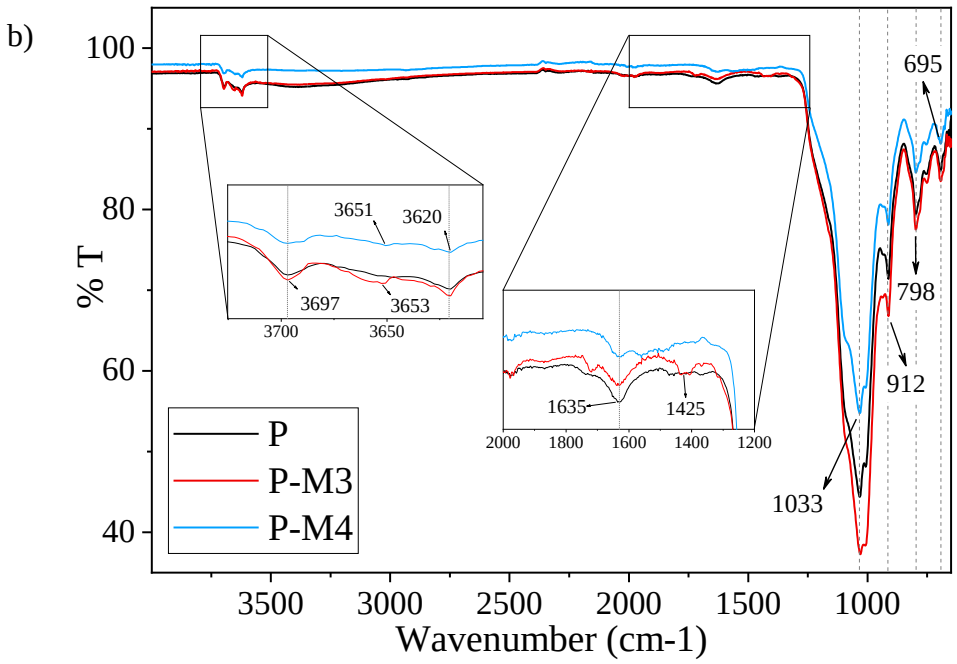

Fig. 93. FT-spectroscopy of the modified clays a) P-M1, P-M2, and b) P-M3, P-M4. The unmodified clay is shown as P.

Intermediate sample, P-M1, treated with HCl, presented a more intense OH vibrations compared with the P sample. As well, a small red shift can be noticed in the band corresponding to the inner surface Al-OH stretching vibration mode. As for the P-M3 sample, treated with DMSO, the spectra showed an increase in the intensity of the Si-O stretching mode band at 1033 cm^{-1}. Additional bands for P-M3 were observed near 1400 cm^{-1}, which are associated with the bending vibration modes of CH_3 groups. The band at 3653 cm^{-1} can be attributed to the hydrogen bonds between the internal OH of the kaolinite sheet and the sulfonyl group in DMSO **[300]** . Thus, the FT-IR results indicate the interaction of DMSO and APTES with the surface of the clays.

5.3.3.3 Thermogravimetric analysis (TGA)

As stated above, FT-IR spectroscopy is a useful technique to obtain qualitative information about the presence of DMSO and grafting of APTES into the clay support. However, to gain further knowledge, thermogravimetry analysis (TGA) were performed. Measurements were carried out by a TGA 2950 Hi-Re (TA Instruments) from room temperature up to 960 °C with a heating rate of 10 °C/min.

In **Fig. 94**, thermogravimetric curves are shown for P, P-M1, P-M2, P-M3, and P-M4 samples. Around 66 °C, all samples lose weight due to the loss of adsorbed water molecules. Between 255 °C- 260 °C a mass loss attributed to goethite (α-Fe^{3+}O(OH)) can be seen. In the samples P-M1 and P-M2 the mass loss of goethite decreased compared to the P, P-M3 and P-M4 samples, due to the chemical attack of the HCl to the iron compounds, as stated in the XRF analysis.

A major mass loss is observed for all samples around 480 °C, that is typical for the dehydroxylation of kaolinite. Moreover, in the samples where APTES is present (P-M2 and PM4), two additional peaks can be seen before and after the kaolinite degradation. The first one, between 300 °C and 400 °C, is attributed to the removal of the nitrogen molecule of the APTES during combustion **[285]**. The second one, is around 600 °C and may be attributed to the decomposition of oxyethyl groups, where a condensation of a C-C-O occurred and the oxyethyl appeared as a degradation product of the APTES.

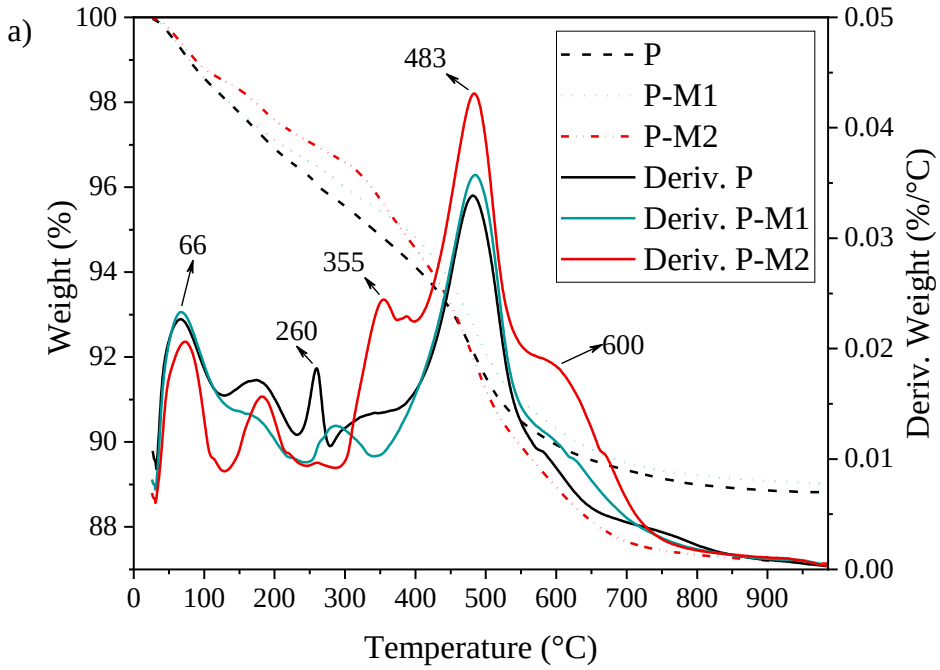

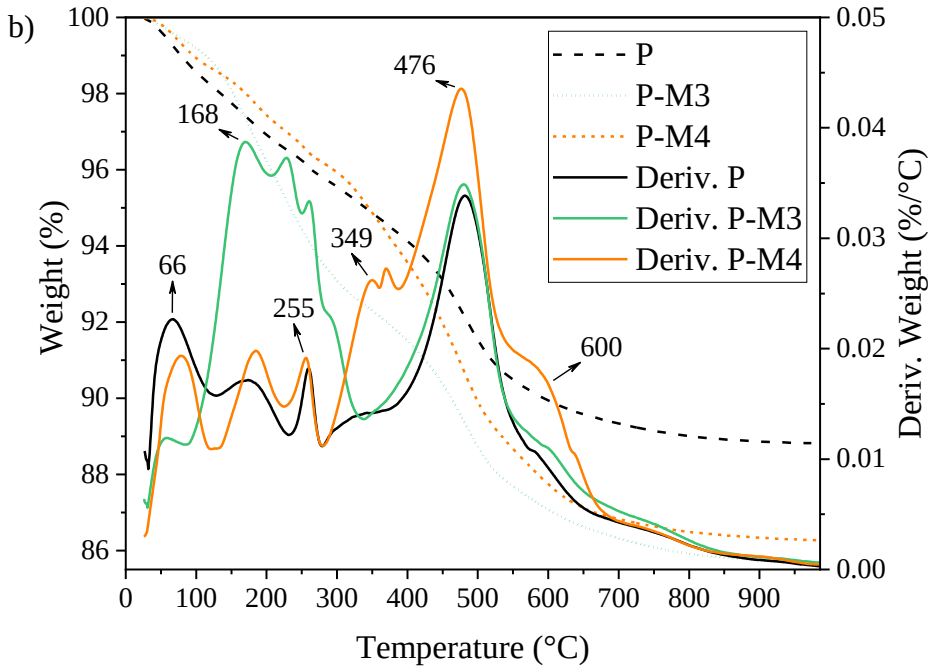

Fig. 94. Thermogravimetric analysis for the modified supports a) P-M1, P-M2, and b) P-M3, P-M4. Unmodified support is shown as P.

Sample P-M3 showed, additionally, a mass loss at about 168 °C attributed to DMSO molecule. According to literature **[296]**, there are two loading mechanism of intercalation of DMSO in phyllosilicates as kaolinite. The first one is known as Type I and consist in the adsorption of the DMSO in the delaminated layers of the clay. The second, Type II, can be adsorbed in the delaminated layers and/or intercalated into kaolinite crystallites. The TGA analysis, due to the temperature of decomposition observed, demonstrated that in our work the DMSO is Type II. The DMSO oxygen is bind to the inner-surface Al-OH groups and presented a higher thermal stability (between 160 °C and 200 °C) than the Type I (around 100 °C). This reaction is in accordance with the FT-IR spectroscopy analysis.

5.3.3.4 X-ray diffraction (XRD)

Diffractometry is the most used technique to probe that an intercalated compound is in fact affecting the interlayer structure of the clay. X-ray diffraction (XRD) measurements were conducted by a PANalytical AERIS XRD diffractometer with monochromatized Cu Kα radiation (λ=1.5418 Å). The patterns were collected at 40 kV and 15 mA over a range of 2.5°

to 70.0° 2θ with a step of 0.02 °/s. The XRD measurements were performed in a Bragg-Brentano geometry.

The XRD patterns of the samples are shown in **Fig. 95**. As expected, all samples presented similar mineralogical phases as illite/mica (M), kaolinite (K), and quartz (Q). The amount of amorphous minerals is considerable as the P sample is largely composed of diatomite (Chapter III).

All samples showed a characteristic reflection (001) of the kaolinite with a d value of 0.714 nm. However, the most noticeable change in the mineralogy is for the P-M3 sample, where the kaolinite increased the basal spacing to 1.11 nm, indicating the effective intercalation of DMSO molecule into the interlayer space of the kaolinite. These values are in accordance with literature where the intercalation of a monolayer DMSO enlarged the basal space up to 1.12 nm **[132,284,300,301]**.

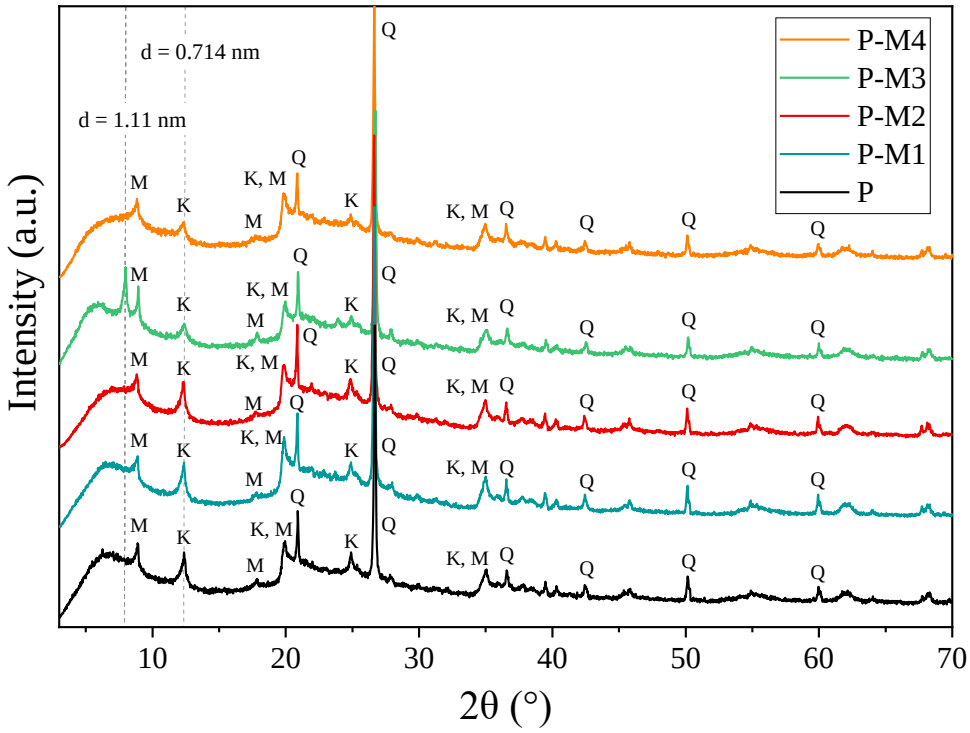

Fig. 95. X-ray diffraction patterns of supports P, P-M1, P-M2, P-M3, and P-M4. The characters stand for: M- Illite/Mica, K-Kaolinite, and Q-Quartz.

Some authors **[288,296]** have calculated the DMSO intercalation efficiency or ratio, I.R, as stated in **Eq. (13)**. Where I_K and I_{K_DMSO} are the intensities of the (001) reflection of the unreacted kaolinite and kaolinite with DMSO, respectively.

$$I.R\ (\%) = \frac{I_{k\_DMSO}}{I_k + I_{K\_DMSO}} \qquad \textbf{(13)}$$

In this work, the intensities of kaolinite in sample P and sample P-M3 were taken for compute the intercalation efficiency. Result showed a 58.81% of efficiency. In literature **[288,296,300]** there are reports form 67% to 96%. Being the value found in this work a little below. However, it is worthy to note that the efficiency ratio is often calculated for pure kaolinite samples with high crystalline order (Hinckley index) **[300]**, where no other minerals are present. In this case, the P sample is a natural mixture of minerals in which only the 19.8% correspond to kaolinite. Thus, a value of around 60% of I.R appear like a good response to the DSMO intercalation in a material with only 20% of kaolinite of probably low crystalline order, with particle distortions.

5.3.3.5 N_2 adsorption/desorption isotherms

Porosity of the supports was assessed by N_2 adsorption-desorption isotherms with a Micromeritics Gemini V2380. Specific surface area was calculated by the Brunauer-Emmet-Teller (BET) model. The mean pore diameter and pore volume were evaluated from the desorption branch using the Barrett-Joyner-Halenda (BJH) model. The samples were degassed during 15 h at 100 °C under nitrogen atmosphere before measurements. The classification of the type of isotherms and hysteresis is in accordance to the IUPAC **[214]**, as well as the classification of the pores, being micropores (< 2 nm), mesopores (2-50 nm) and macropores (> 50 nm).

The N_2 adsorption and desorption isotherms of the clays P, P-M1, P-M2, P-M3, and P-M4 are shown in **Fig. 96.** All clays appear to exhibit Type-II curve with H3-type hysteresis loop. From the respective insets, it could be noticed that the pore widths are in the mesopore scale, and there are none or very low amount of micropores in the samples. The H3-type hysteresis loop corresponds to non-rigid aggregates of plate-like particles **[214]** and demonstrates the presence of mesopores that are filled and empty by capillary condensation **[215]**. Such

features are in accordance with the presence of kaolinite, mica/illite, and diatomite in the supports, as widely studied in Chapter 5, Section 5.1.

P-M2 and P-M4 clays, exhibit an increased in the pore size, between 10 nm and 19 nm, probably because the APTES create an interconnected net with bigger porosity that the clays P, P-M1, and P-M3. Moreover, new mesopores were formed in P-M2 and P-M4, and the APTES fulfilled pores below 10 nm. As well, for both isotherms, of P-M2 and P-M4, the hysteresis increased, probably due to the existence of that bigger mesopores.

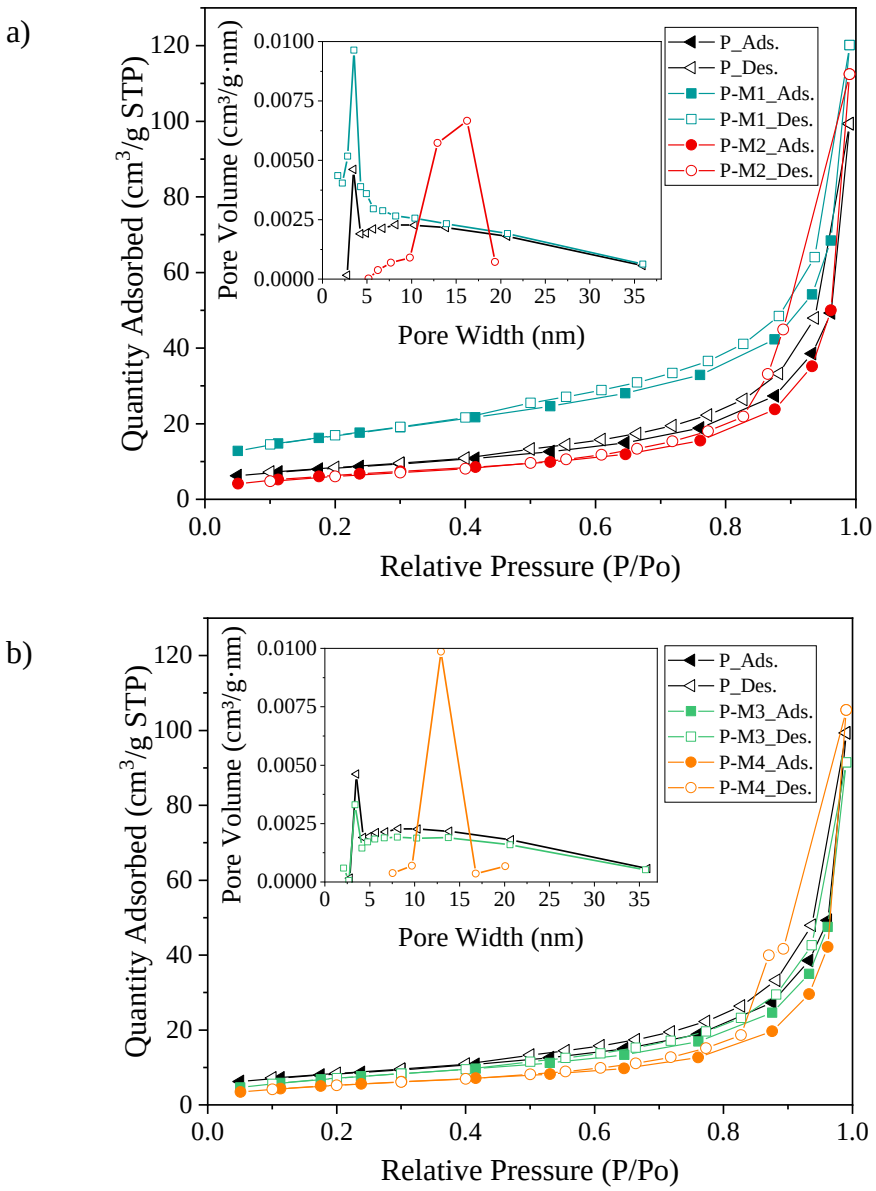

Fig. 96. N_2 adsorption-desorption isotherms of the modified supports a) P-M1, P-M2, and b) P-M3, P-M4. Unmodified support is shown as P. Inset shows the BJH pore size distribution for the samples.

Textural properties, as BJH desorption cumulative volume of pores, V_{pore}, BJH desorption average pore width, d_{BJH}, and BET surface area, S_{BET}, are presented in **Fig. 97**. Clay P - M1 showed an increase of pores < 5 nm (inset for P-M1 in **Fig. 96**) and a decreased in bigger pores. Thus, the BET surface area increased as well. This effect is due to the acid treatment performed in this sample, where more reactive sites in the clay surface are formed (more hydroxyl groups are available) and alumina and iron compounds are lixiviated, thus exposing more pores. Textural properties of sample P-M3 showed a decrease in the BET surface area, compared to P, as a result of DMSO intercalation. P-M3 and P-M4 presented lower BET surface area and larger volume of pores compared with P, due to the APTES presence.

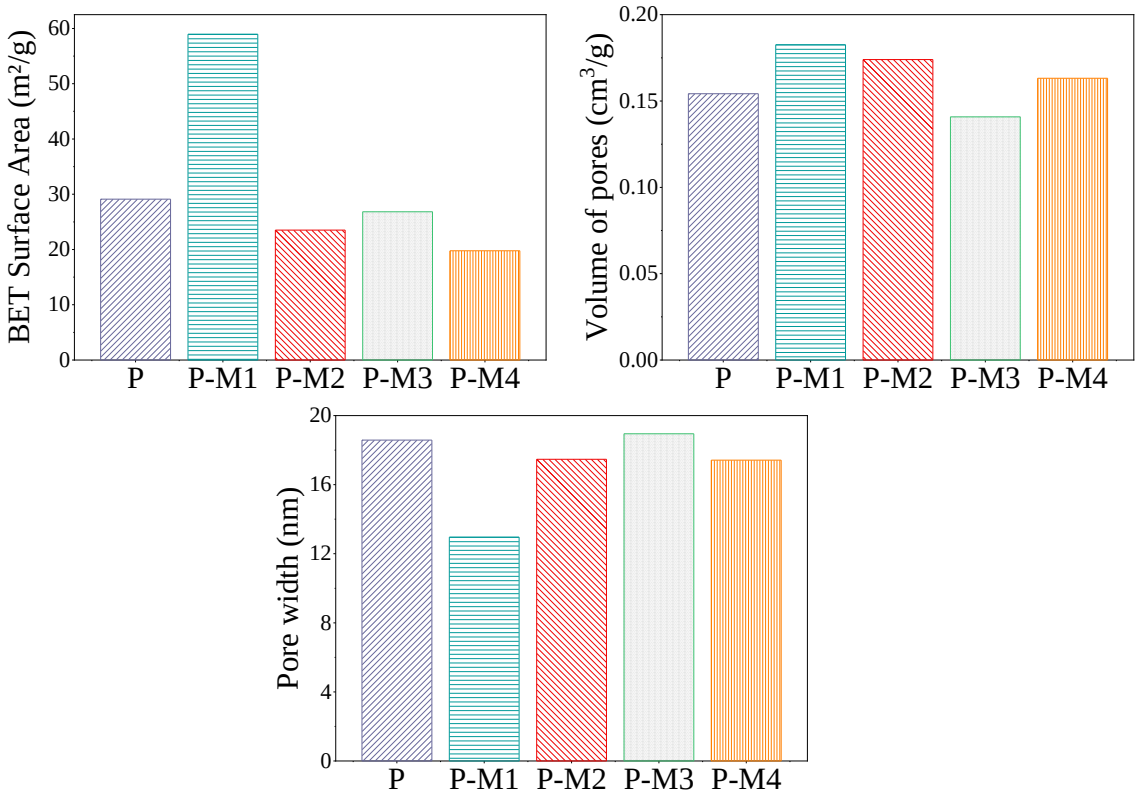

Fig. 97. Textural properties of the supports P, P-M1, P-M2, P-M3, and P-M4.

5.3.3.6 Morphology results

Morphology and microstructure of the clay supports, with and without modifications, was studied by scanning electron microscopy (SEM). Phentom Pro X desktop (SEM) with an accelerating voltage of 15 kV was used.

The raw support P (**Fig. 98**),without any modification, showed the expected minerals as quartz (**Fig. 98. c)**) and kaolinite (**Fig. 98. b)**), besides, diatomite frustules (**Fig. 98. a)**, **Fig. 98**. **d)**), can be clearly seen. Support P-M1 (**Fig. 99**), presented some surfaces attacked by the HCl, as it can be observed in the rough surfaces that appeared in minerals like kaolinite (**Fig. 99. c)**, **Fig. 99. d)**). This is due the degradation of alumina and iron oxides, confirmed previously by XRF (**Table 40**). Sample P with HCl and APTES (**Fig. 100)**, presented the same rough surfaces of the P-M1 support. Presence of APTES could not be identified visually by SEM.

Sample with DMSO, P-M3 (**Fig. 101**), showed partially delaminated kaolinite (**Fig. 101. a)**, **Fig. 101. b)**), that cannot be seen in the P support. This demonstrated that DMSO separate kaolinite platelets due to the intercalation of the molecule into the layered mineral. These results confirmed the findings of the XRD and FT-IR analyses. Finally, support with DMSO and APTES, P-M4 (**Fig. 102**), presented the same delaminated kaolinite as P-M3. As well as in the P-M2 support, the APTES presence could not be identified.

Thus, SEM analysis prove that HCl attacked the alumina and iron oxides of the samples, conferring a rough surface of some of the particles, and that DMSO was effectively intercalated into the interlayer space of the kaolinite sheets. SEM technique was not found to be useful for determined the presence of APTES and/or to identify silylated surfaces. Other techniques are more recommended for silane-grafted identification as XRD and FT-IR.

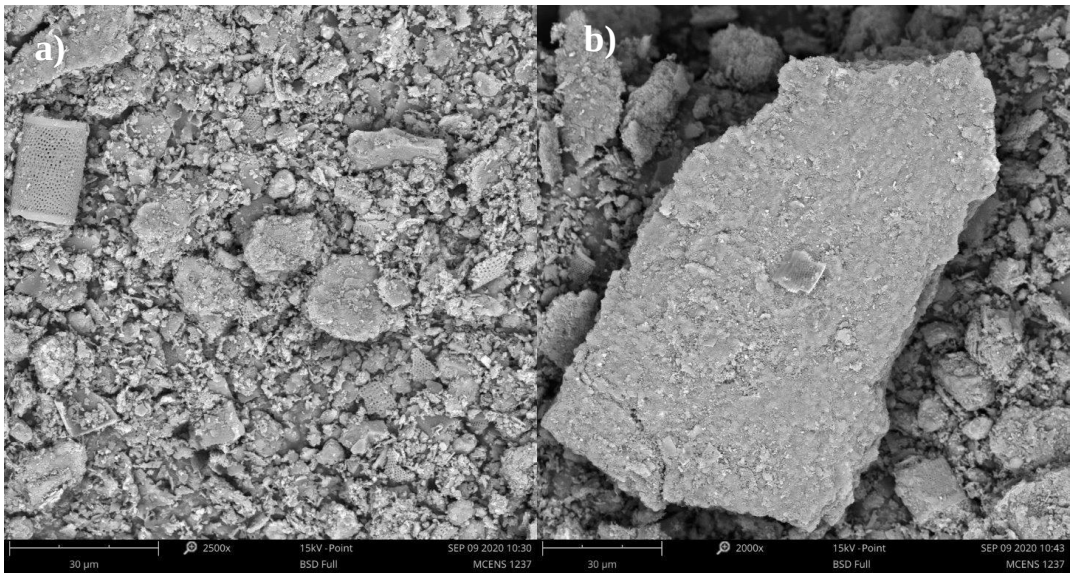

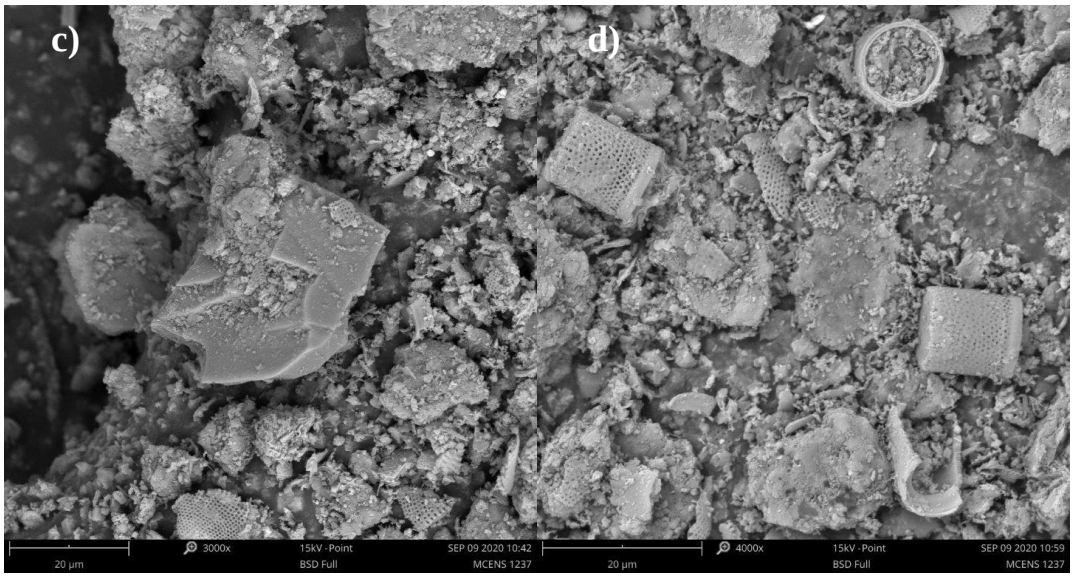

Fig. 98. SEM images of raw powder support (P).

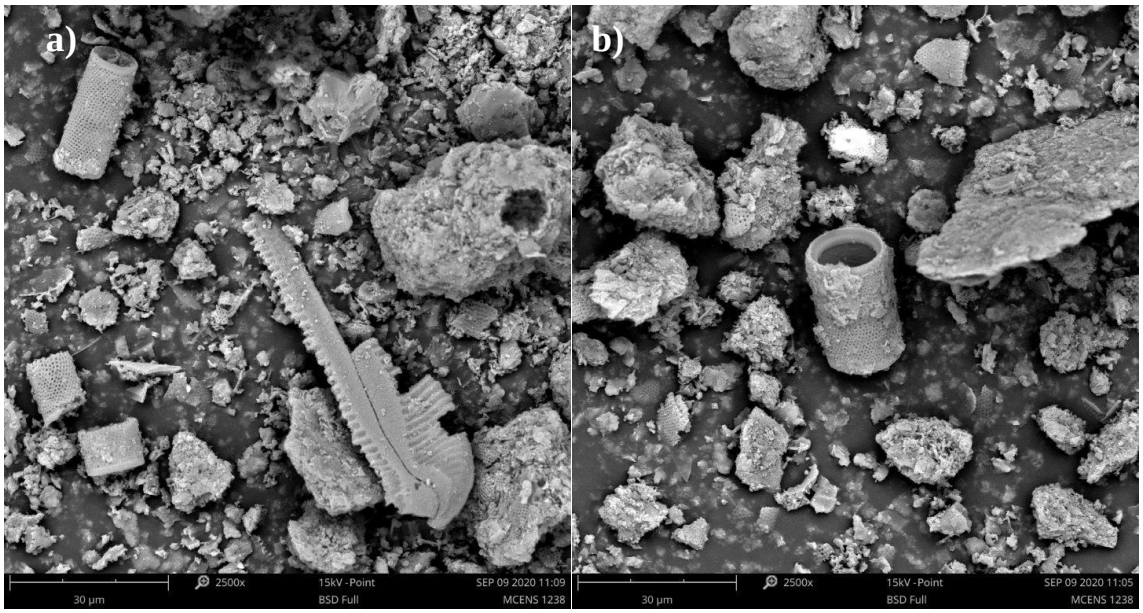

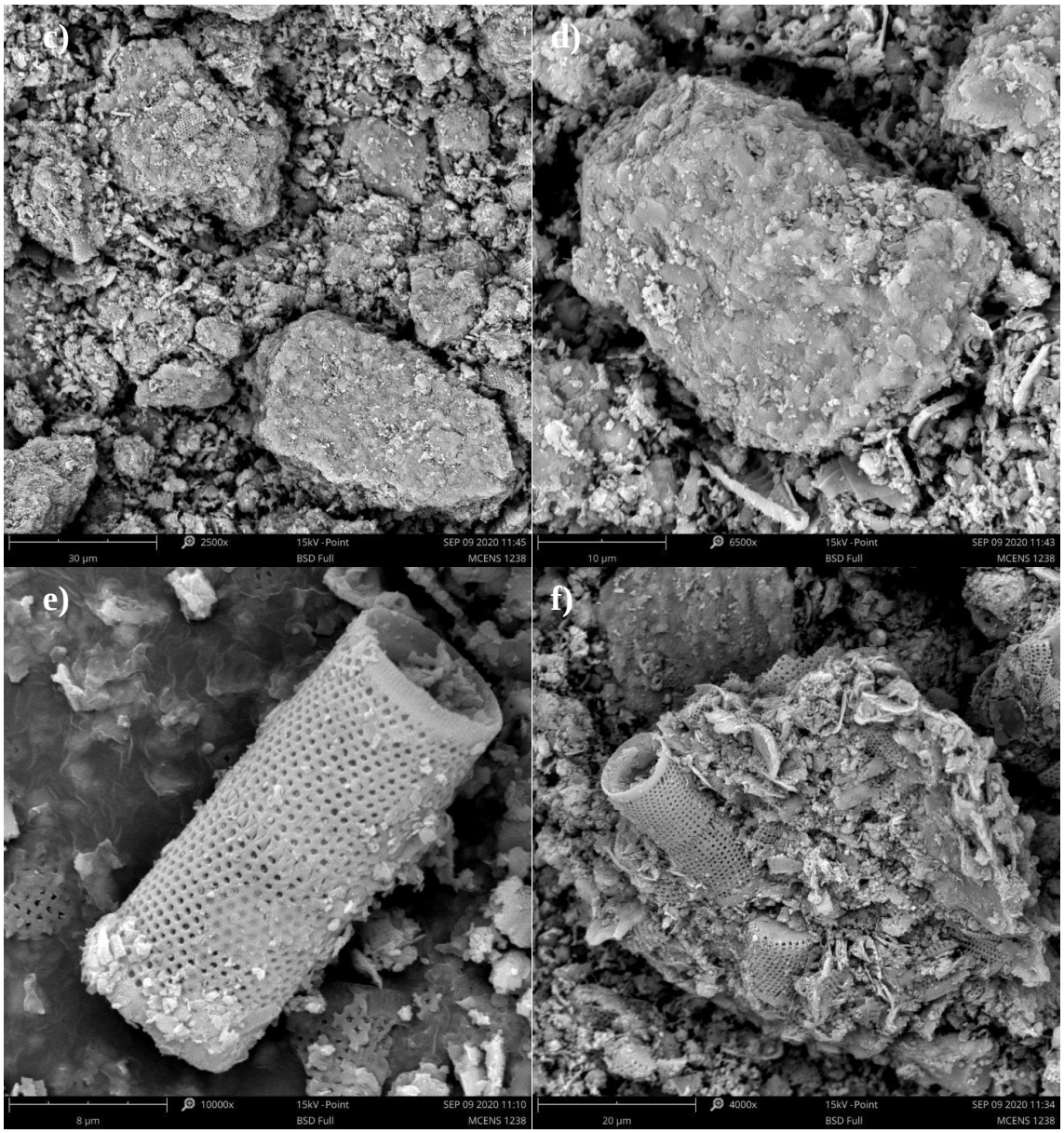

Fig. 99. SEM images of support P with HCl (P-M1).

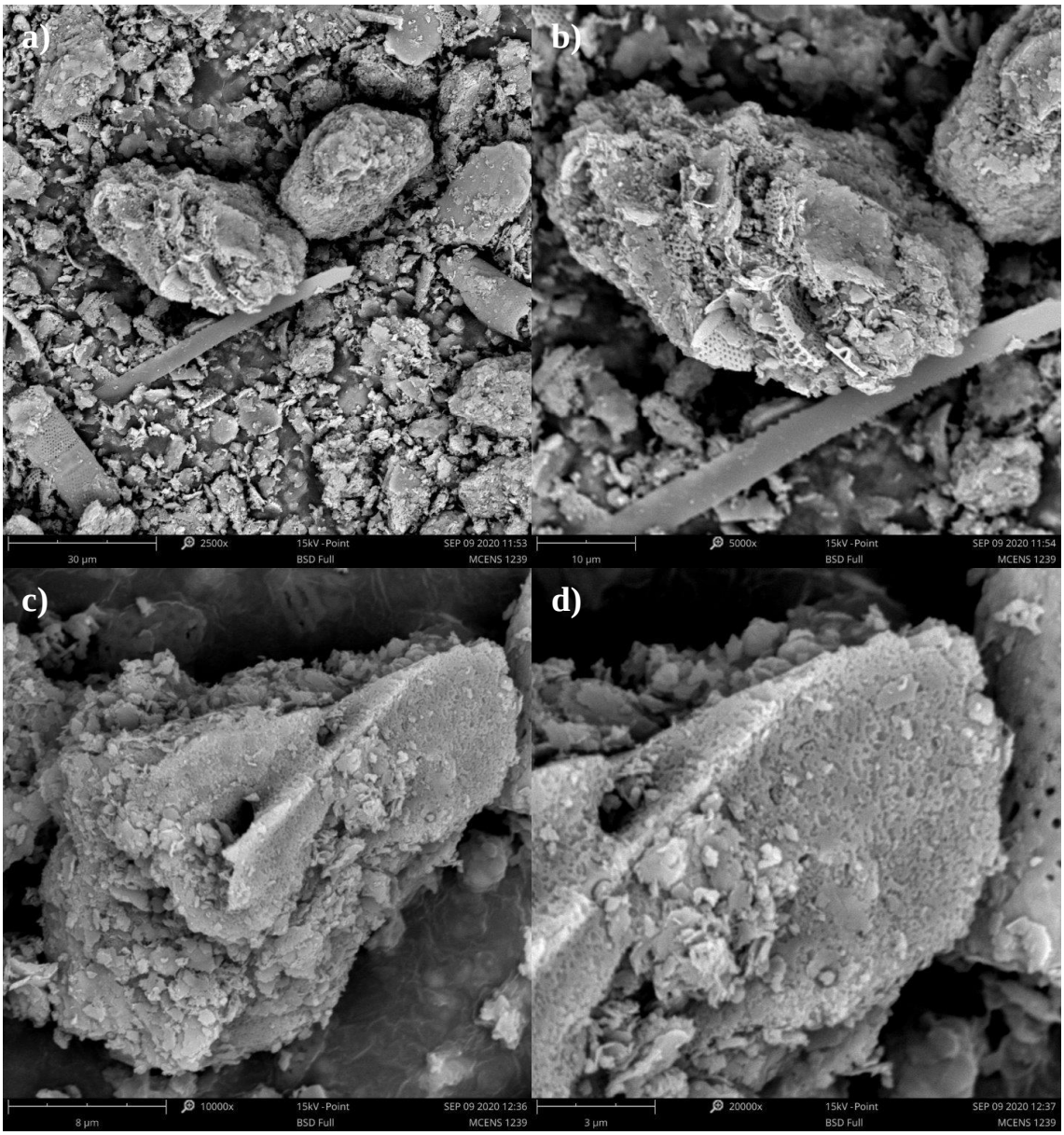

Fig. 100. SEM images of support P with HCl and APTES (P-M2).

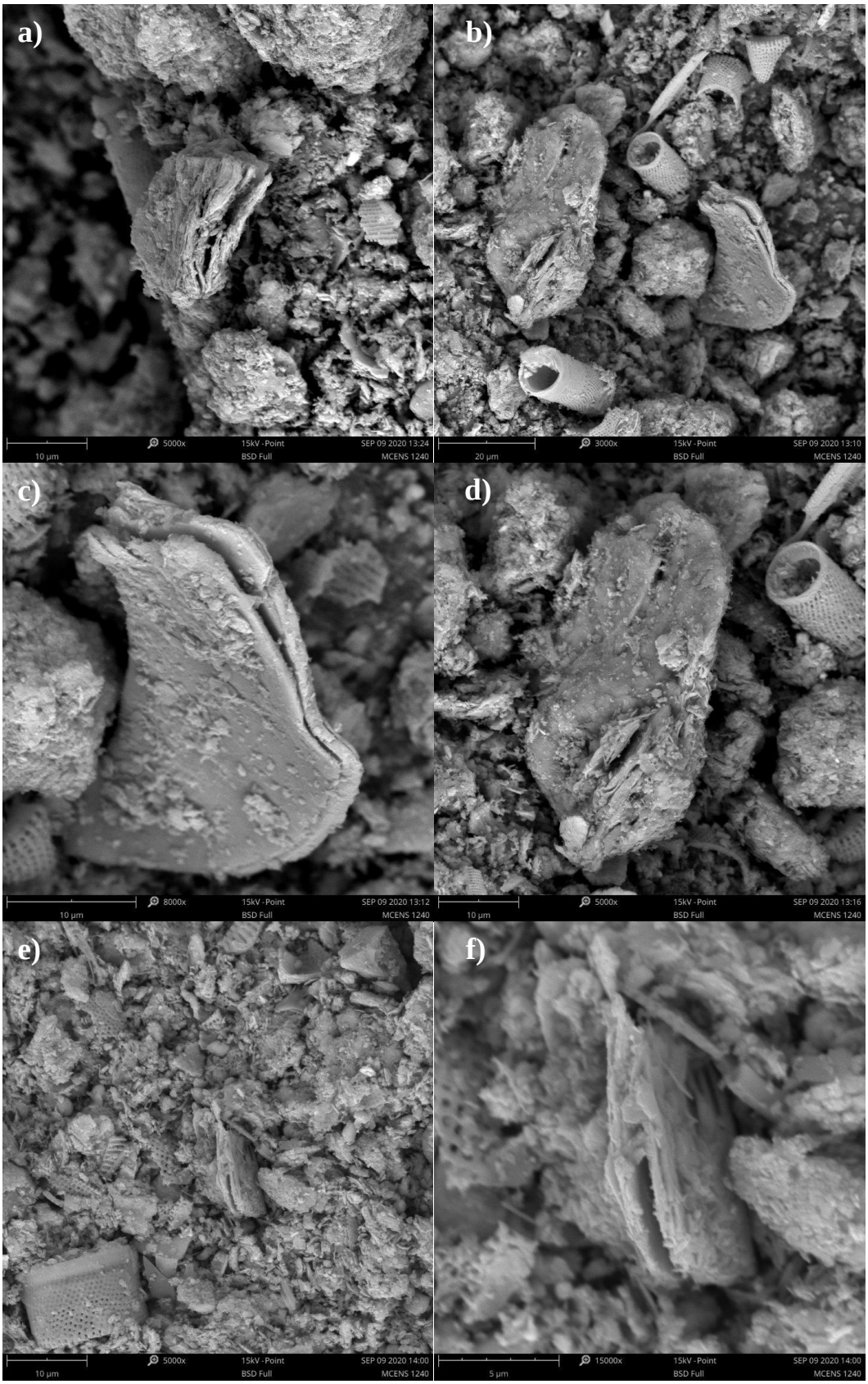

Fig. 101. SEM images of support P with DMSO (P-M3).

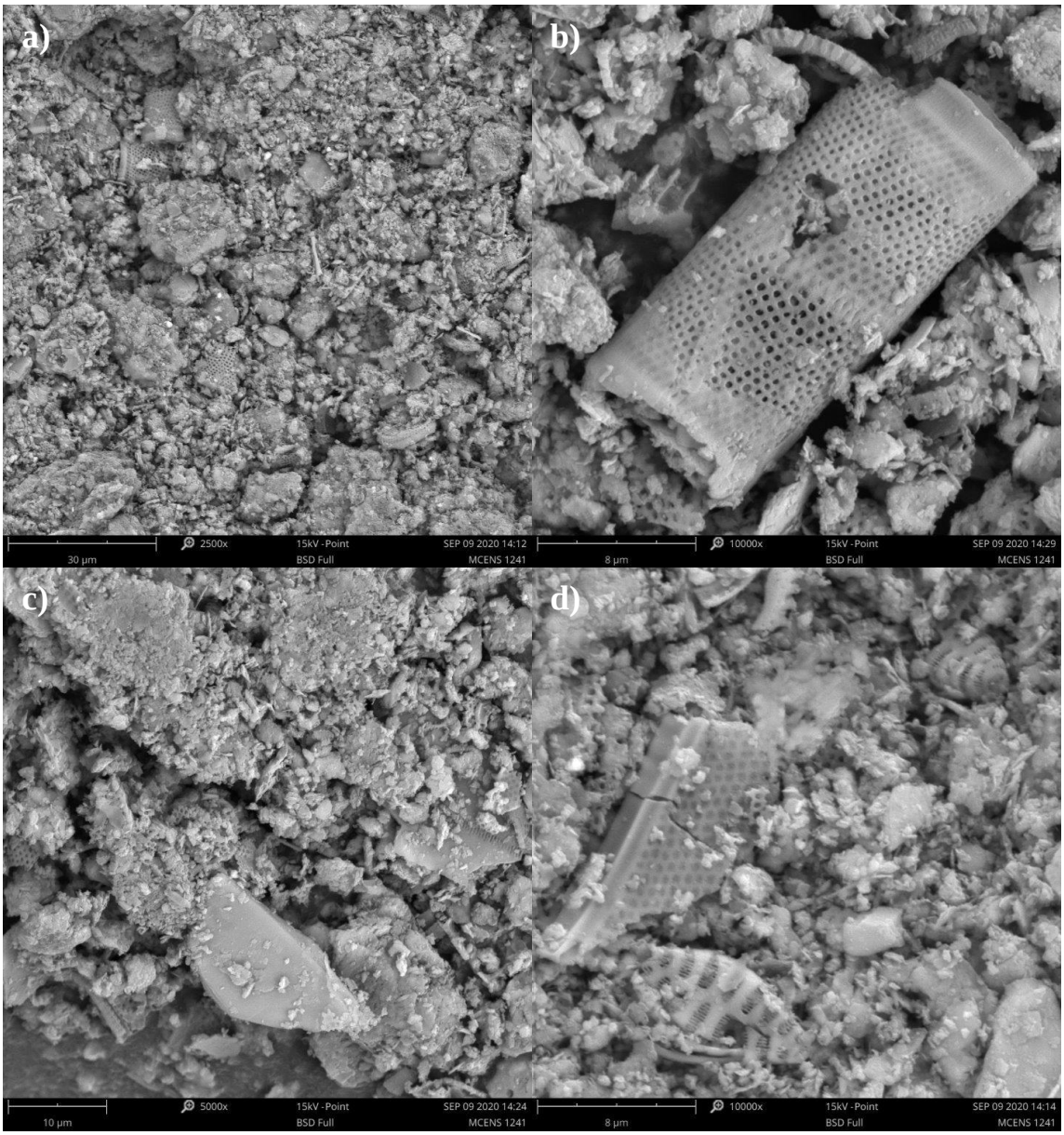

Fig. 102. SEM images of support P with DMSO and APTES (P-M4).

5.3.4. SS-PCMs based in the silylated supports

Shape-stabilized phase change materials were produced with the silylated supports P-M2 and P-M4. The PCM chosen was the eutectic mixture of capric and myristic acid, named CA/MA. The fatty acid mixture was prepared according to the procedure described in Chapter II. The eutectic compositions for CA/MA was 73.20% (w/w) of capric acid and 26.80% (w/w) of myristic acid. The peak melting phase change temperature and the latent heat of the eutectic were 25 °C and 150 kJ/kg, respectively. The SS-PCMs were produced by the vacuum assisted

impregnation method (Chapter IV), using 0.6 bar and 70 °C. The amount of CA/MA added to the P-M2 and P-M4 supports was 34.0 ± 0.6% and 39.0 ± 1.3%, thus, four composites were obtained, named PCM/M2-34, PCM/M2-39, PCM/M4-34 and PCM/M4-39. Besides, two composites based on the P support, with no superficial modification, was produced and named PCM/P-34 and PCM/P-39. Photographs of the resulting materials are shown in **Fig. 103**.

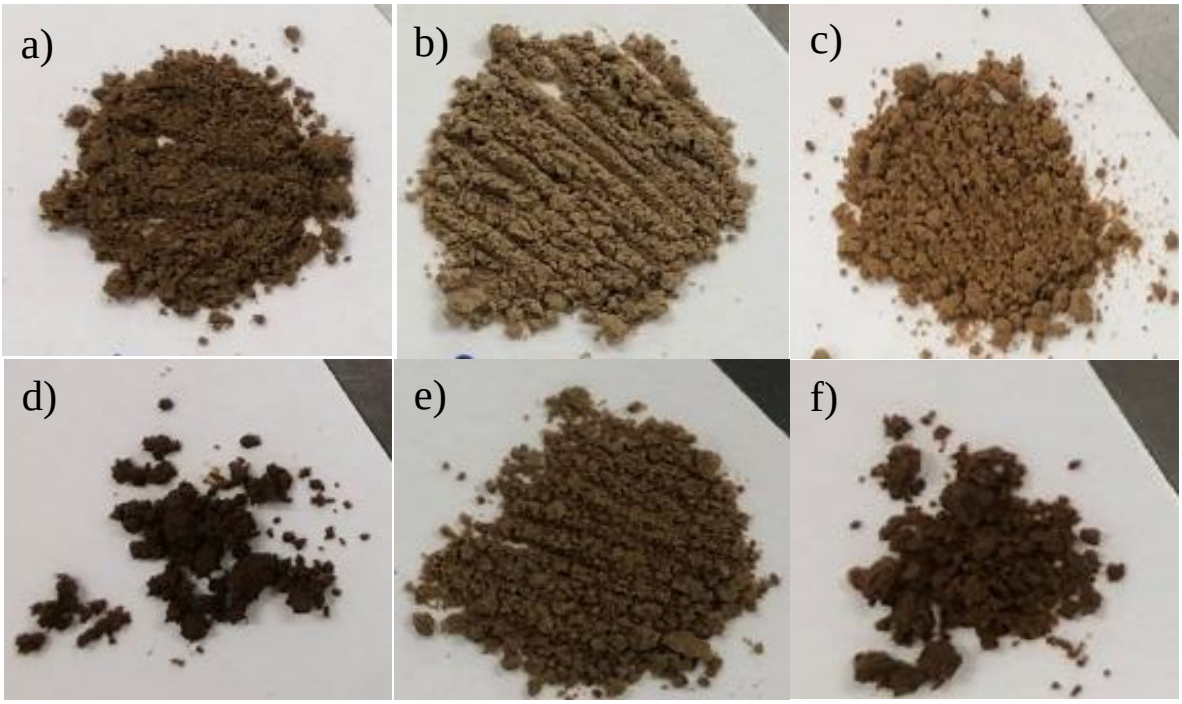

Fig. 103. Shape-stabilized phase change materials in the silylated supports a) PCM/P-34, d) PCM/P-39, b) PCM/M2-34, e) PCM/M2-39, c) PCM/M4-34, and f) PCM/M4-39.

5.3.4.1 Thermal properties and absorption of the SS-PCMs (silylated)

The leakage behavior of the six SS-PCM composites was evaluated with the filter paper method. A sample of SS-PCM was put on a template (1.4 cm x 0.2 cm) upon a filter paper, and then was heated at 60 °C. Every 2 h the sample and the filter paper were weighted after and before the next measurement, until reaching 16 h. A final measurement was taken at 34.5 h. The percentage of weight loss of the sample was taken as the leakage value. Each SS-PCM was measured three times and the errors were less than 0.5% for samples.

We have found that at the first two hours, the leakage percentage is the highest throughout the leakage cycle. Results at 2 h are shown **Fig. 104**. As expected, as the amount of

incorporated PCM increases, the leakage increases. Samples with 39% of CA/MA showed larger leakage than samples with 34% CA/MA. For the series of 34% of PCM, the leakage of the samples with supports M2 (HCl-APTES) and M4 (DMSO-APTES) were similar to the reference sample PCM/P-34, of approximately 1.60%. Composite PCM/M4-34 (1.74%) presented a leakage slightly above PCM/M2-34 (1.44%). As for the samples with 39% of CA/MA, composite PCM/M2-39 (2.22%) presented the lowest value and PCM/M4-39 (5.99%) the highest value. Support M2 improved leakage of the unmodified support in 42.5% for the highest amount of PCM added.

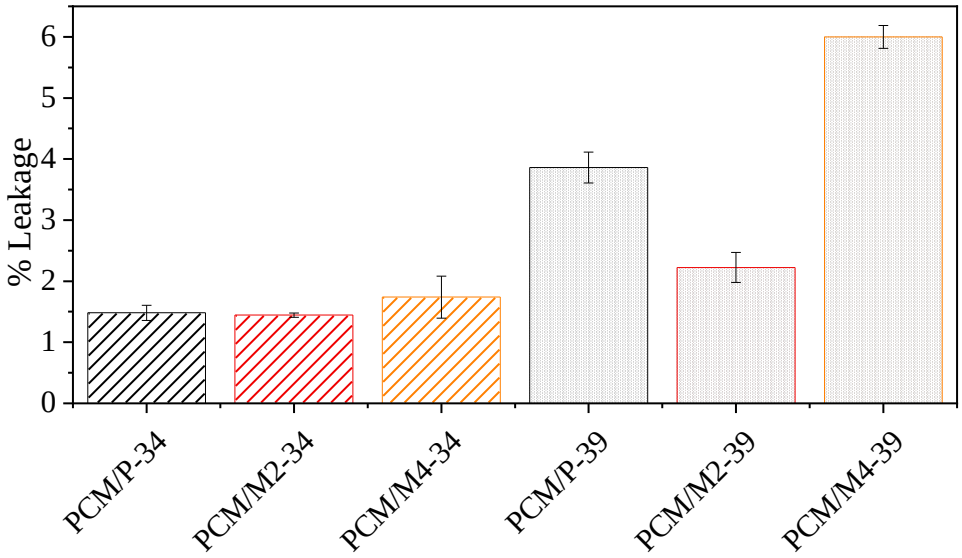

Fig. 104. Leakage of SS-PCMs (silylated supports) at 2 h.

Leakage cycle, **Fig. 105**, showed that weight losses reach stabilization from 12 to 15 hours of cycling. The final accumulated leakage, after 34 h, was 3.9%, 3.7% and 3.7% for PCM/P-34, PCM/M2-34, PCM/M4-34, and 5.1%, 4.7% and 6.9% for PCM/P-39, PCM/M2-39, PCM/M4-39, respectively. These findings indicate that CA/MA was more effectively absorbed and retained by the support modified by procedure I, M2, with acid etching pre-treatment and silane-grafting, than by the support modified by procedure II, M4. The effect achieved by the acid treatment followed by sylanization on the retention capacity of the support is better than the effect of the DMSO intercalation followed by sylanization. Probably, this is due to the more active sites of the support exposed by the HCl that allowed to generate more bond between the silane and the inorganic surface of the clay.

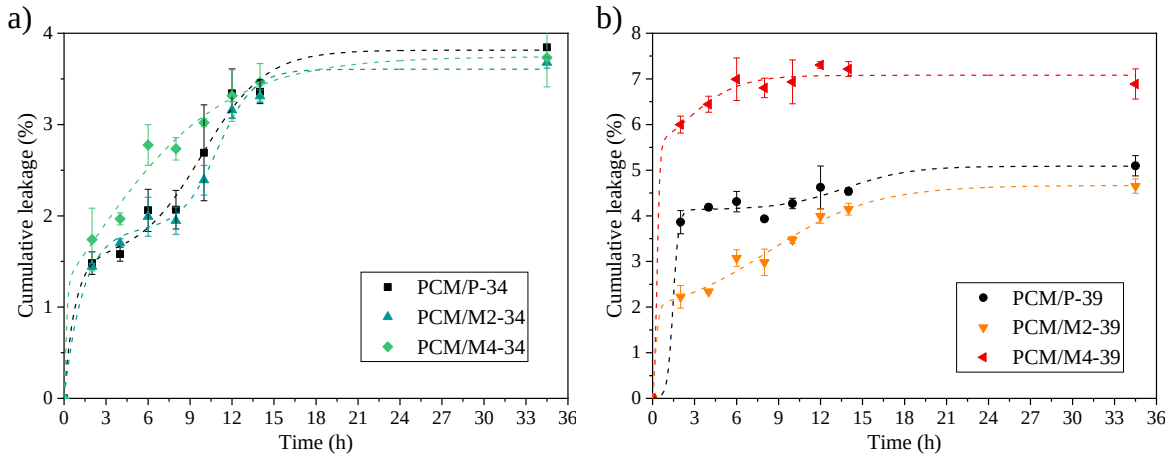

Fig. 105. Cumulative leakage until 34 h for the SS-PCM (silylated supports) with a) 34% and b) 39% of CA/MA.

Finally, enthalpy and phase change temperatures were measured for composites PCM/P-34, PCM/P-39, PCM/M2-34, PCM/M2-39, PCM/M4-34, and PCM/M4-39. These properties were measured by differential scanning calorimetry (DSC) (TA Instruments Q200 DSC) at a rate of heating and cooling of 5 °C/min, in a N_2 atmosphere, flowing at 50 mL/min. Values reported were taken after 2 heat-cooling cycles. The uncertainties of this DSC system are typically 1.16 J/g for latent heat and ± 0.29 °C for temperature. Results are shown in **Fig. 106** and **Table 42**.

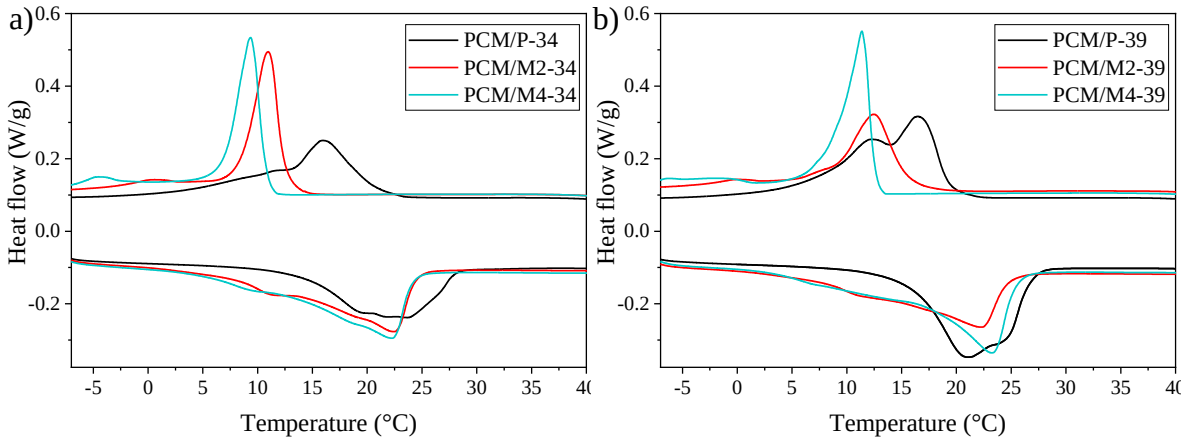

Fig. 106. DSC curves of the SS-PCM (silylated supports) with a) 34% and b) 39% of CA/MA. The curves are drawn with the exothermic peak up.

Results shown that the average melting phase change temperature (peak) for all samples was 22.06 ± 0.76 °C, this implied a decreased in about 3 °C compared to the pure eutectic

CA/MA (~25 °C). Regarding the peak solidification temperatures, and the onset melting temperatures, all samples move to lower values compared to the reference SS-PCMs without support modification, PCM/P-34 and PCM/P-39. These changes can be observed from the DSC curves (**Fig. 106**) of PCM/M2-34, PCM/M2-39, PCM/M4-34, and PCM/M4-39 as they considerably widening, lowering the temperature respect to the SS-PCM without modification.

On the other hand, enthalpy of fusion decreased, and enthalpy of solidification increased for SS-PCMs with silylated supports compared to the reference samples. This effect is probably due to the newly formed covalent bonds between the eutectic fatty acid mixture and the silylated support that required more energy to melt and less energy to solidify the PCM. Sample PCM/M2-39 did not present an increased in the melting enthalpy and showed values slightly below to the reference.

Table 42. Thermal properties of PCM/P-34, PCM/P-39, PCM/M2-34, PCM/M2-39, PCM/M4-34 and PCM/M4-39.

Sample	Melting			Freezing		
	$T_{m,onset}$ (°C)	$T_{m,peak}$ (°C)	ΔH_m (kJ/kg)	$T_{s,onset}$ (°C)	$T_{s,peak}$ (°C)	ΔH_s (kJ/kg)
PCM/P-34	13.59	21.7	18.54	20.96	16.16	14.90
PCM/M2-34	11.5	22.33	21.48	12.51	10.98	14.69
PCM/M4-34	8.89	22.19	22.45	10.77	9.38	12.75
PCM/P-39	15.66	20.89	25.26	19.43	16.53	22.75
PCM/M2-39	8.8	22.1	22.26	15.68	12.5	14.84
PCM/M4-39	14.92	23.19	26.62	12.55	11.39	14.34

The calorimetry analysis of the SS-PCMs showed that the clay support modification with APTES changes the thermal properties of the composite. Further research is recommended to optimize the achieved values as they are still low for practical applications, particularly in terms of latent heat. Even though, these results corroborate, along with the characterization performed in previous sections, that the supports were successfully silylated and that the silane interact with the PCM. These findings widen the possibilities to develop new and improved support for shape-stabilization of organic PCMs.

5.3.5. Conclusions of sylanization

Analyses like FT-IR spectroscopy, XRD, TGA, and SEM helped to study the chemical modifications made to the raw clay support. Support P-M2 (HCl+APTES) and P-M4 (DMSO+APTES) were successfully modified. Particularly, the FT-IR bands suggested that the sylanization occurred between the Al-OH and Si-O groups of the support. The XRF and SEM analyses prove that HCl attacked the alumina and iron oxides of the samples, conferring a rough surface of some of the particles, and that DMSO was effectively intercalated into the interlayer space of the kaolinite sheets. SEM technique was not found to be useful for determined the presence of APTES and/or to identify silylated surfaces. Other techniques are more recommended for silane-grafted identification as XRD and FT-IR.

After the modification, silylated supports were used for shape-stabilization of eutectic mixture CA/MA. The findings indicate that CA/MA was more effectively absorbed and retained by the support modified by procedure I, M2, than by the support modified by procedure II, M4. The effect achieved by the acid treatment followed by sylanization on the retention capacity of the support is better than the effect of the DMSO intercalation followed by sylanization. Probably, this is due to the more active sites of the support exposed by the HCl that allowed to generate more bond between the silane and the inorganic surface of the clay.

Composites SS-PCMs with 39% of CA/MA showed larger leakage than samples with 34% CA/MA. Even though, samples with 34% of PCM did not improve the leakage respect to the reference sample (SS-PCM without support modification) and was around 1.60%. On the other hand, composite PCM/M2-39 (2.22%) presented the lowest leakage percentage and PCM/M4-39 (5.99%) the highest value. Support M2 improved leakage of the unmodified support in 42.5% for the highest amount of PCM added.

Regarding thermal properties, latent heat of the modified SS-PCMs presented an increase in the fusion and a decrease in the solidification, attributable to the covalent bonds formed between the eutectic fatty acid mixture and the silylated support that demands more energy to melt and less energy to solidify the PCM. The onset temperatures were, as well, affected by the sylanization procedures. Further investigation is required to improve the obtained values and explore deeper this kind of mechanism to modified natural support that can be used for shape-stabilization of organic phase change materials.

CHAPTER VI.

Steady-state and transient thermal performance of the SS-PCMs

In this chapter, two configurations for incorporating SS-PCMs in buildings were evaluated using an equipment designed to measure thermal variables in steady-state and the dynamic response of the materials. The setup aims to simulate indoor and outdoor conditions. First, SS-CA/MA-P6-35, SS-LA/MA-P6-35, and SS-PA/SA-P6-35, in powder form, were evaluated in direct contact with the outdoor environment, to analyze its insulation capacities, heat storage and performance under diurnal cycles. Second, an acrylic-based plaster was designed with the incorporation of SS-CA/MA-P6-35 and SS-LA/MA-P6-35 mixture, which then was used as a finish of a fiber cement siding. In the last case, the SS-PCM-based acrylic plaster was evaluated as an indoor material, without direct contact to the outdoor environment. The purpose of these experiments is to analyze the viability of these samples as potential candidates to be incorporated in building envelopes.

6.1. Why using PCMs in building envelope?

Designing buildings with rational energy consumption has become among the primary issues worldwide. Everything from politics to the building envelope materials can contribute towards energy savings, balance supply and demand, increase quality of life of people, and protect the natural environment. The development of sustainable energy applications in the construction sector has received widespread attention in the last decade **[33]**, becoming a concerted effort from the different parts of the value chain. Even more, when the building sector energy consumption, just for space heating/cooling, is predicted to increase between 12% to 37% **[302]** in 2050.

Building envelope is a crucial element in providing shelter and in regulating the thermal energy of the indoor environment. In this regard, incorporation of thermal energy storage

elements, as phase change materials (PCM), is proposed as a solution to contribute to energy-efficient building performance **[302,303]**. The thermal mass of the building can be enhanced by the use of PCMs, resulting in energy savings. Material finishes that incorporate PCMs can minimize the heating and cooling loads through the building envelope due to their high energy storage capacity, achieving thermal comfort inside the building and increasing thermal inertia.

Different configurations have been proposed in literature to asset such energy savings when incorporating PCMs **[25,88,304]**. Among the most reported are the direct incorporation of the PCM, whether encapsulated or shape-stabilized, in traditional building materials from cement mortar **[305,306]**, lime mortar **[30]**, concrete **[307]**, and gypsum **[308]**, to cool roofs and membranes **[59]**. As well, fabrication of lightweight wallboards with PCMs within **[309–311]** or embedded as an intermediate layer in a multilayer building envelope **[312,313]**. Another example is the use of pipes, bags or tubes that are fulfilled with the PCM which are then embedded in the building envelope **[314,315]**. The different configuration processes imply a wide range of variables to be considered such materials compatibility, effectiveness of the thermal properties of the final building envelope, extent of PCM added, and characterization techniques. Even though, all these studies have taken us one step closer to real life applications. For instance, the company DuPont developed a panel that contains PCM called Energain® that was used in the iCon Innovation Centre (United Kingdom) as thermal mass to improve energy efficiency of the building. This kind of panels can reduce air conditioning costs by an average of 35%, decrease heating costs about 15%, help to reduce interior temperature up to 7 °C, and can therefore contribute to reducing the carbon footprint of a building **[316]**.

Hence, in this section, three binary eutectic mixtures of saturated fatty acids (CA/MA, LA/MA and PA/SA) shape-stabilized (35% wt. PCM) in the P6 support, fully studied and characterized throughout this document, were chosen as potential thermal energy storage materials for being used in building elements.

6.2. Fiber cement panels coated with an insulation paint and a PCM-based acrylic plaster

For one of the configurations, three fiber cement panels (0.5 cm thick) were measured as an attempt to simulate the effect of using SS-PCM composites with traditional building materials. The first fiber cement panel sample (FC) was evaluated without any coating as a control sample. A second panel (FC-Cool) was painted with an insulating paint called Coolguard ®, supply by Sumicol S.A.S., and a third fiber cement panel (FC-Cool-PCM) was painted with the Coolguard ® paint over one side and finished with a SS-PCM-based acrylic plaster (2 mm) in the other side. The SS-PCM-based acrylic plaster was made with a mixture of SS-CA/MA-P6-35, SS-LA/MA-P6-35 and a resin binder. Images of each fiber cement panel evaluated are shown in **Fig. 107**.

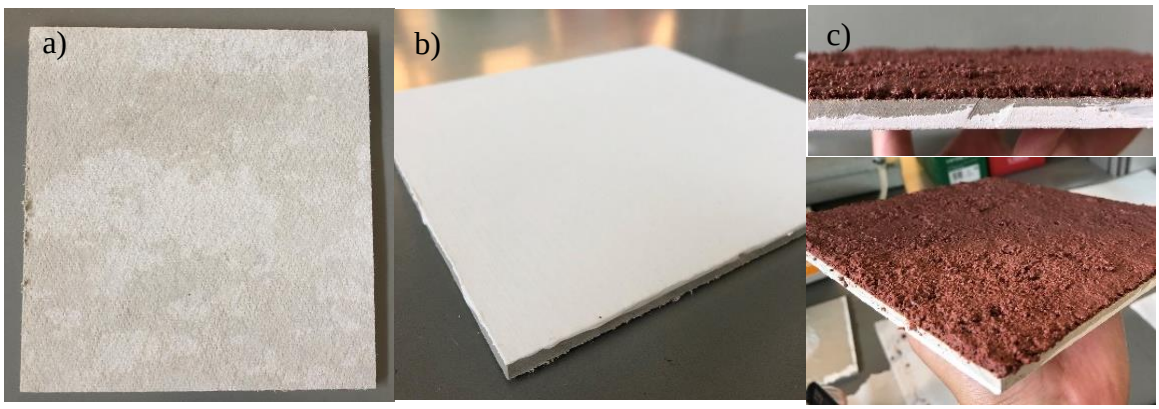

Fig. 107. Images of a) fiber cement (FC), b) fiber cement painted with Coolguard ® (FC-Cool), and c) fiber cement painted with Coolguard ® and a finishing of a SS-PCM-based acrylic plaster (FC-Cool-PCM).

6.3. Experimental setup

The equipment used in these experiments was designed by the GREiA research group from the University of Lleida **[317]**, the scheme is shown in **Fig. 108**. The setup allows the measurement of thermal transmittance, heat storage capacity and dynamical thermal response of several kinds of materials. The equipment is based on a wooden structure of 50 cm x 50 cm x 118 cm, that is insulated with 35 mm of vacuum panels (R∼0.14 m^2K/W) and 20 mm of Pyrogel (k=0.013 W/m·K). The inside of the equipment consists of two

cavities, divided by the sample that will be measured, that control the thermal conditions through two copper coils connected to programmable water baths. The SS-PCM tested samples have a dimension of ϕ 65 mm x 30 mm, while the fiber cement panels have dimensions of 190 mm x 190 mm x 60 mm. Each cavity has a thermocouple type T, with an error of ± 0.75%, and inside the SS-PCM samples, four more thermocouples were put. Each thermocouple was named after its position in the setup, as shown in the scheme in **Fig. 109**. The temperature of the fiber cement panels was measured by two surface thermocouples on each side, and the side with the insulating paint was put toward the top cavity. Besides, to measure the input and output heat flux of the samples, two heat flux sensors (hukseflux HFP01), with an accuracy of ± 5%, were fixed at the sample surfaces.

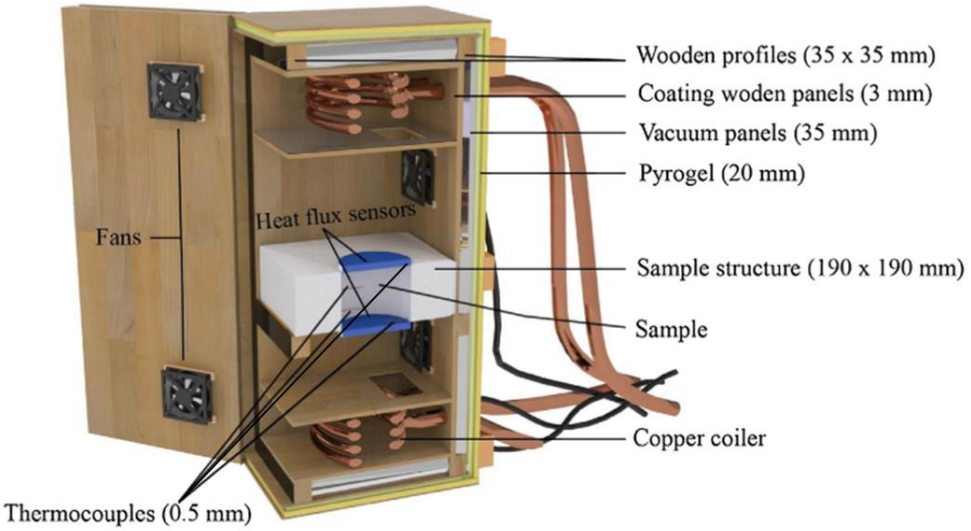

Fig. 108. Equipment used for the steady and dynamic thermal measurements. Adapted from **[318].**

6.4. Methodology of measurements

The thermal performance of the samples was evaluated through three types of experiments. The first experiment was used to calculate the thermal transmittance in steady-state (U-value). The second experiment was conducted to measure the heat storage capacity, and a third experiment was performed to evaluate the dynamic thermal response under daily temperature oscillation. The experiments are described below.

6.4.1. Thermal transmittance in steady-state (U-value)

Initially, for this experiment, both water baths of the equipment were put at a certain temperature until reaching steady-state conditions inside the cavities. Afterward, a heating ramp was programmed using the upper water bath, thus, heating the upper section. The lower water bath was used to keep the temperature in the lower section constant at the initial reached temperature. The temperatures used for each sample are shown in **Table 43**. The experiment was repeated two times for each sample to verify the reproducibility of the results.

Table 43. Temperature reached inside the equipment for calculating the U-value.

Sample	Temperature (lower cavity)	Temperature (upper cavity)
SS-CA/MA-P6-35	4.0 °C	4.0 °C to 50.0 °C
SS-LA/MA-P6-35	9.0 °C	9.0 °C to 50.0 °C
SS-PA/SA-P6-35	8.4 °C	8.4 °C to 48.0 °C
Support P6	9.0 °C	9.0 °C to 49.0 °C
FC	7.5 °C	7.5 °C to 40.0 °C
FC-Cool	5.5 °C	5.5 °C to 40.0 °C
FC-Cool-PCM	4.8 °C	4.8 °C to 38.5 °C

From this experiment the U-value of the samples can be calculated using the thermal gradient between the surfaces in steady-state conditions, according to **Eq. (14)**.

$$\text{U-value} = \frac{\dot{q}_{sample}}{A \cdot (T_{down} - T_{up})} \qquad \textbf{(14)}$$

Where $\dot{q}_{sample}$ is the heat flux across the sample, A is the area of the sample, and $(T_{down} - T_{up})$ is the difference between the bottom and top surface temperature of the sample.

6.4.2. Heat storage capacity

The heat storage capacity of the samples was calculated using this experiment. The tested sample was placed in the sample structure and both cavities were heated with the same heating ramp (**Table 44**). The sample was kept in steady-state conditions at the initial and final part of the experiment; thus, the average heat storage capacity of the sample can be calculated since there is no thermal gradient at the end of the experiment. This property was not measured for the fiber cement panels.

Table 44. Heating ramps used for calculating the heat storage capacity of the samples.

Sample	Heating ramp inside the upper and lower cavities
SS-CA/MA-P6-35	6 °C to 52 °C
SS-LA/MA-P6-35	6 °C to 52 °C
SS-PA/SA-P6-35	36 °C to 70 °C
Support P6	6 °C to 54 °C

The amount of heat stored in the sample can be known from the difference in the heat fluxes per m^2 through the top and bottom surfaces of the sample. Besides, the sample temperature will increase from T_i to T_f, and hence, the average heat capacity, $C_{p,avg}$, can be calculated according to **Eq. (15)**.

$$C_{p,avg} = \frac{q_{acc}}{m_{sample} \cdot (T_f - T_i)} \qquad \textbf{(15)}$$

Where q_{acc} is the heat accumulated in the sample during the experiment obtained from the difference between the two heat flux sensors, and m_{sample} is the mass of the sample. To confirm the repeatability of this experiment, two measurements were performed for each sample.

6.4.3. Dynamic thermal response

Finally, in this third experiment, the dynamic thermal response of the samples under a simulated diurnal temperature variation was evaluated. A programmable water bath controlled the temperature in the upper cavity simulating a diurnal cycle, that recurs every 24 h, between a high temperature and a low temperature that occurs during the same time lapse. The temperature variation is presented in **Table 45** for each evaluated sample. The temperatures for the fiber cement samples simulate the conditions generated on the roofs by the combined effect of external air and solar radiation. The lower bath was not used and was maintained in free-flowing conditions, trying to simulate the inner space of a room.

Table 45. Simulated diurnal temperature variation for the dynamic thermal response experiment.

Sample	Temperature variation for the simulated diurnal cycle (upper cavity)
SS-CA/MA-P6-35	8.0 °C to 51.5 °C
SS-LA/MA-P6-35	8.5 °C to 51.4 °C
SS-PA/SA-P6-35	12.6 °C to 72.8 °C
Support P6	12.5 °C to 50.4 °C
FC	10.0 °C to 42.8 °C
FC-Cool	8.4 °C to 41.3 °C
FC-Cool-PCM	7.5 °C to 40.7 °C

The thermal response of the samples was assessed through two parameters used to evaluate the thermal inertia of a building: the thermal lag and the decrement factor. The thermal lag, φ, also called time lag **[314]**, is the delay for the heat wave to propagate from the outer surface toward the inner surface of the material, and in this study is computed as shown in **Eq. (16)**.

$$\varphi = t_{T_{surface\ bottom,max}} - t_{T_{surface\ top,max}} \quad \textbf{(16)}$$

Where, $t_{T_{surface\ bottom,max}}$ and $t_{T_{surface\ top,max}}$ are the time in hours when inside surface and outside surface temperatures are at their maximum. The decrement factor, f, also called thermal stability coefficient (TSC) **[318]**, was evaluated by the dampening of the temperature wave when passing from outside to inside **[319,320]**, which can be calculated as the ratio between the inner (environment bottom) and outer (environment top) thermal amplitudes, as shown in **Eq. (17)**.

$$f = \frac{T_{environment\ bottom,max} - T_{environment\ bottom,min}}{T_{environment\ top,max} - T_{environment\ top,min}} \quad \textbf{(17)}$$

For dynamic thermal response analysis, it is assumed that the heat transfer through the samples is unidirectional and perpendicular to the walls of the setup and that there are no internal loads in the lower cavity. To ensure repeatability of the experiment, for each calculated parameter, two diurnal cycles were measured.

6.5. Thermal transmittance in steady-state (U-value)

The temperature profile as a function of time of the samples was obtained after the steady-state measurements. As an example of these results, the temperature profile of sample SS-

CA/MA-P6-35 is shown in **Fig. 109**, as well as the scheme of the position of the thermocouples in the equipment. The steady-state condition was accomplished after 17 h from the start of the experiment, and only the values of the surface top temperature ($T_{surface, top}$), surface bottom temperature ($T_{surface, bot}$), and the average of the heat fluxes per area ($\dot{q}/A$) from the top and bottom of the sample were used for the thermal transmittance calculation. At the beginning of the experiment steady-conditions were achieved with some heat losses, even though the samples were insulated, this heat loses were around 3 W/m^2 and were considered in the calculation of the U-value.

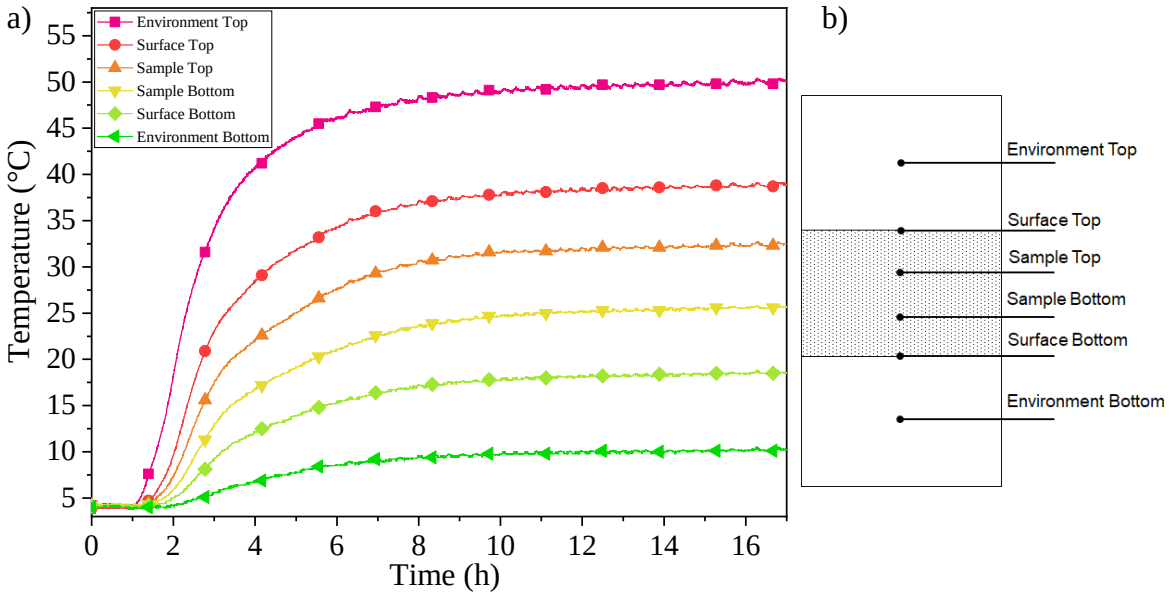

Fig. 109. Temperature profile of a) SS-CA/MA-P6-35 during thermal transmittance experiment, and b) scheme of the thermocouples in the upper and lower cavities (environment top and bottom), and inside the sample (surface top, sample top, sample bottom and surface bottom).

The parameters obtained for each sample are presented in **Table 46**. The negative sign of the heat fluxes corresponds to the polarity of the output voltage of the heat flux sensors and only indicates the direction at which the heat flows inside the equipment, from the top to the bottom cavity. The obtained U-values presented deviations less than 1%, indicating that the experiment presented good repeatability. The thermal transmittance for the P6 support showed the lowest value with 2.31 W/m^2·°C, followed by SS-LA/MA-P6-35, SS-CA/MA-P6-35, and SS-PA/SA-P6-35 composites with values of 4.92 W/m^2·°C, 5.07 W/m^2·°C, and 5.24 W/m^2·°C, respectively. Differences in the thermal transmittance values of the samples are explained as in the SS-PCM composites the PCM filled the pores of the P6 support

reducing, approximately by half, the thermal resistance of the sample. The air trapped in the pores of the P6 support makes it have a lower thermal transmittance, and thus the best insulation capacity between these samples.

Table 46. Steady state conditions used for thermal transmittance calculation of SS-PCM samples and P6 support.

	SS-CA/MA-P6-35	SS-LA/MA-P6-35	SS-PA/SA-P6-35	Support P6
$T_{env,\ top}$ (°C)	49.95 ± 0.19	49.72 ± 0.04	48.02 ± 0.70	49.12 ± 0.08
$T_{surface,\ top}$ (°C)	38.65 ± 0.38	41.02 ± 0.10	40.86 ± 0.51	44.48 ± 0.06
$T_{surface,\ bot}$ (°C)	18.50 ± 0.07	19.85 ± 0.13	21.15 ± 0.57	18.47 ± 0.20
$T_{env,\ bot}$ (°C)	10.18 ± 0.08	13.11 ± 0.09	12.86 ± 0.43	12.86 ± 0.18
$\dot{q}/A$ (top) (W/m^2)	-104.70 ± 1.33	-113.06 ± 0.96	-110.10 ± 0.56	-64.48 ± 0.74
$\dot{q}/A$ (bottom) (W/m^2)	-99.76 ± 1.37	-95.27 ± 2.69	-96.42 ± 0.21	-55.70 ± 0.27
U-value $(W/m^2 \cdot °C)$	5.07 ± 0.01	4.92 ± 0.05	5.24 ± 0.03	2.31 ± 0.003

In the same way, fiber cement samples were measured, and the steady-state conditions and parameters obtained after the experiment are shown in **Table 47**. In these samples, heat lose were also around 3 W/m^2 and were considered in the calculation of the U-value. The deviation of FC-Cool and FC-Cool-PCM samples was less than 1.5%, indicating good repeatability. As for the FC control sample, the deviation was around 32% as the heat flux variation was considerable. However, the values are in agreement with the other fiber cement samples measured in this work.

The thermal transmittance of the fiber cement (FC) and the fiber cement painted with Coolguard ® (FC-Cool), were similar, 29.17 ± 9.48 W/m^2·°C and 39.83 ± 0.58 W/m^2·°C, respectively, indicating that both panels presented similar insulation capacities. Unfortunately, the experimental setup fails to simulate the reflection capacity of the Coolguard ® paint that as a reflective coating, with micro-sphere technology, blocks heat radiation from the infrared and ultraviolet spectra. Thus, the main effect promised by the paint cannot be adequately measured in this experiment. However, fiber cement panel painted with Coolguard ® in one side and finished with the SS-PCM-based acrylic plaster in the other side (FC-Cool-PCM) showed the lowest U-value of 27.11 ± 0.32 W/m^2·°C between the fiber cement panel samples. The SS-PCM-based acrylic plaster contributed to reducing 32% of the transmitted heat per unit area per unit temperature difference under steady-state conditions compared with FC and FC-Cool.

Table 47. Steady state conditions used for thermal transmittance calculation of fiber cement samples.

	FC	FC-Cool	FC-Cool-PCM
$T_{env,\ top}$ (°C)	40.25 ± 0.28	39.24 ± 0.37	37.99 ± 0.49
$T_{surface,\ top}$ (°C)	27.38 ± 0.18	23.15 ± 0.14	23.11± 0.39
$T_{surface,\ bot}$ (°C)	23.89 ± 1.09	20.96 ± 0.14	19.74 ± 0.32
$T_{env,\ bot}$ (°C)	18.50 ± 0.64	15.16 ± 0.10	13.53 ± 0.20
$\dot{q}/A$ (top) (W/m^2)	-98.54 ± 4.97	-85.40 ± 1.73	-95.50 ± 1.15
$\dot{q}/A$ (bottom) (W/m^2)	-96.08 ± 8.01	-88.56 ± 1.19	-87.26 ± 0.64
U-value $(W/m^2 \cdot °C)$	29.17 ± 9.48	39.83 ± 0.58	27.11 ± 0.32

The thermal transmittance of the samples studied in this work were compared to some typical materials used in construction and some building PCM-based materials (**Fig. 110**). The materials comprise gypsum boards, bricks, wood, green roof soils, and glazing elements. Generally, triple glazing elements and cavity masonry walls **[321]** (brick, stone or concrete blocks) of approximately 30 cm thick, present the lowest U-values (< 1.5 W/m^2·°C), i.e., are the most insulating ones. Usually, the drawback of these traditional systems is the large volume required in the buildings. Some green roof soil substrates **[318]** present, as well, a good thermal insulation solution (U-value < 3 W/m^2·°C), but the building architecture is a pre-requisite to incorporate such bioclimatic components. The support P6 with a thermal transmittance of 2.31 W/m^2·°C can be considered in green roof soil applications. Gypsum board (1.2 cm thick) glued to a wood panel (1.8 cm thick) **[317]**, and gypsum blocks (19 x 19 x 4 cm) **[322]** present U-values of approximately 5.5 W/m^2·°C and 8.48 W/m^2·°C, respectively. The addition or impregnation with PCM (Micronal or RT21) decrease slightly those values. The thermal transmittance of the SS-PCMs characterized in this paper was close to the gypsum materials. Finally, fiber cement panels (0.5 cm thick) presented the highest thermal transmittance compared to the other systems, however, the application of the developed SS-PCM-based acrylic plaster (0.2 cm thick) increased significantly (32%) the insulation property of the system. Such construction material can be used to decrease heat transfer inside buildings in places where fast and cheap installation is required, and in cities with no seasonal changes, where no high insulation is needed, but energy savings are still demanded. The comparison made here intended to have a glimpse of construction materials used for thermal insulation in buildings, care should be taken as the thickness of the systems, the installation process and the requirements differ from each other.

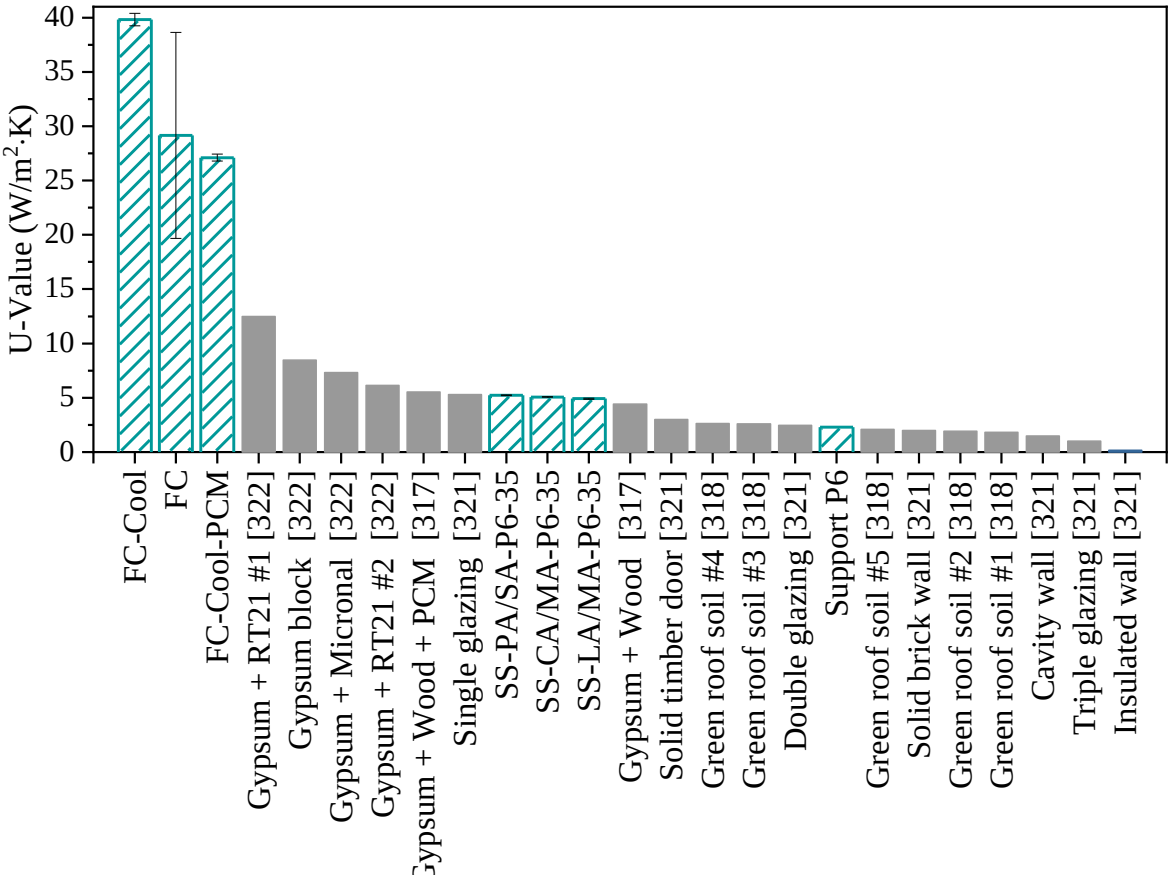

Fig. 110. Thermal transmittance values found in literature for typical construction building materials and PCM-based materials. Dashed bars correspond to the samples studied in this work.

6.6. Heat storage capacity

The thermal energy storage capacity of the SS-PCM composites and support P6 was calculated from the accumulated heat obtained during the experiment. The rate of heat accumulation is shown in **Fig. 111**. Compared to the support, all the SS-PCM samples presented a larger area under the curves, indicating that the composites accumulate more heat due to the presence of the PCM. The total heat accumulated by the support is due to the sensible heat, while the heat accumulated by the SS-PCMs corresponds to sensible heat and latent heat.

The accumulated heat by the SS-PCMs was approximately 2.3 times the accumulated heat by the support. The support accumulated 6787 J, while the energy stored by SS-CAMA-P6-35, SS-LAMA-P6-35, and SS-PASA-P6-35 was 14963 J, 16441 J, and 15649 J, respectively.

The second peak, that can be clearly seen for SS-LAMA-P6-35 and SS-PASA-P6-35 curves, corresponds to the phase change of the PCMs. The sample SS-CAMA-P6-35 presented a phase change as well but is not that evident in this curve, probably to the low phase change temperature (19.62 °C) and the amount of energy stored by the CA/MA eutectic. After approximately 10 h, when heat accumulation is almost zero, the steady-state conditions for the samples were reached. This time corresponds to the heat storage time.

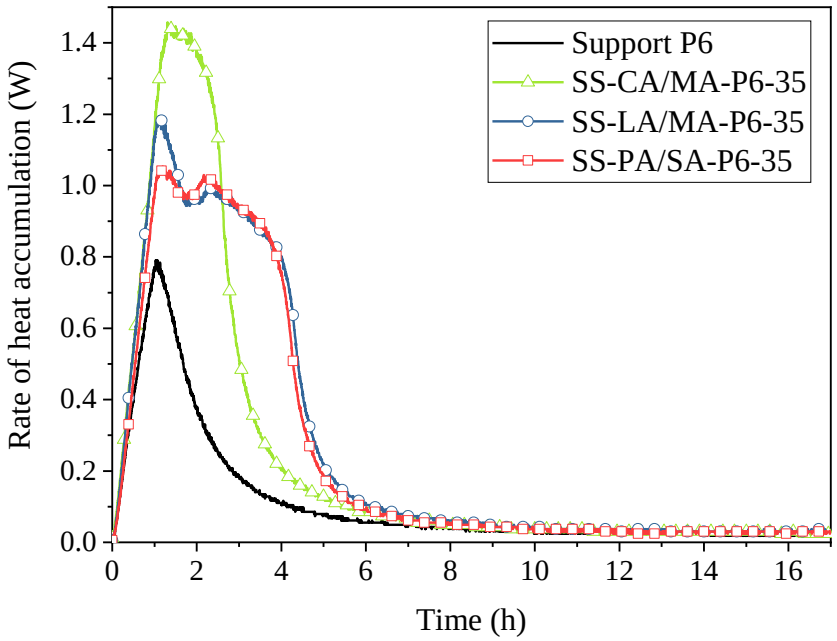

Fig. 111. Rate of heat accumulation of the samples support P6, SS-CA/MA-P6-35, SS-LA/MA-P6-35, and SS-PA/SA-P6-35.

Finally, the heat storage capacity of the samples was measured by means of **Eq. (15)**, and the results are presented in **Table 48**. In this experiment, some small heat losses, around 4 W/m^2, were found in the lateral direction of the samples and were considered for calculating the heat capacity. The good repeatability of the experiment was proved after determining the deviation of the measurements. Deviations less than 1.3% were found for all samples. The average heat storage capacity of support P6, and the composites SS-CA/MA-P6-35, SS-LA/MA-P6-35, and SS-PA/SA-P6-35 was 3161.72 J/kg·K, 4452.04 J/kg·K, 4275.03 J/kg·K, and 5669.08 J/kg·K, respectively. The composite with the highest heat capacity was SS-PA/SA-P6-35, while the other two SS-PCMs presented similar heat capacities.

Table 48. Average heat storage capacity of the support and the SS-PCM composites.

Sample	$C_{p,avg}$ (J/kg·K)
SS-CA/MA-P6-35	4452.04 ± 55.20
SS-LA/MA-P6-35	4275.03 ± 6.74
SS-PA/SA-P6-35	5669.08 ± 18.10
Support P6	3161.72 ± 29.77

These results indicate that adding 35% of PCM, in the P6 support, increases the average heat storage capacity of the system in approximately 40.8%, 35.2%, and 79.3%, when incorporating CA/MA, LA/MA, and PA/SA eutectic, respectively. These measurements highlight the ability of the SS-PCMs to store, and release, energy that could be used in several applications as building materials, domestic heat water system, or even in the food industry.

6.7. Dynamic thermal response

The dynamic thermal response corresponds to the measurement of the temperature and heat flux as a function of time of the samples when subjected to a diurnal temperature variation. The temperature response of the P6 support and the SS-PCMs are shown in **Fig. 112**. The thermocouple position scheme is shown in **Fig. 109**. As expected, every 24 h a cycle is repeated, as a probe of the repeatability of the measurement, two complete cycles (from 0 h to 48 h) are presented in the plots. Every twelve hours the temperature reaches its maximum or its minimum value, as in a regular day on equatorial countries. In the same way, all the samples followed the same trend, being the lower sections the ones with lower temperatures. As a measurement of thermal inertia of these materials the decrement factor, f, and thermal lag, φ, were calculated and are shown in **Table 49**.

Table 49. Decrement factor, f , and thermal lag, φ, of the support and the SS-PCM composites.

	Support P6	SS-CA/MA-P6-35	SS-LA/MA-P6-35	SS-PA/SA-P6-35
f	0.156 ± 0.005	0.155 ± 0.006	0.155± 0.089	0.176 ± 0.003
φ (h)	0.806 ± 0.012	0.576 ± 0.206	1.450 ± 0.291	1.192 ± 0.012

Decrement factor indicates the dampening of the temperature wave when passing from outside (upper cavity) to the inside (lower cavity) through the sample. Building materials that present a f below or equal to 0.5 are considered with good thermal inertia **[323]** as only 50%,

or less, of the external temperature fluctuation will reach the inside of the building, in this experiment simulated as the bottom cavity. As lower the f value, slower the heat transmission inside the building. For instance, the support P6 and SS-PCMs studied presented low f values (<0.2), indicating high thermal inertia.

In the experimental configuration, the samples are in direct contact with the external temperature fluctuation, thus, the P6 support and the SS-PCMs are preventing the overheating of the internal part of the configuration. It is worthy to note that this was achieved with a three-centimeter thick insulation. The SS-PCM did not show remarkable differences compared to the porous support in the decrement factor, however, the accumulated heat over the experiment is considerably different from the support P6. In **Fig. 112**, the curves for the accumulated heat, q_{acc}, in the samples are shown. The SS-PCMs presented a notable storage and release of heat when the temperature matches the phase change temperature of the eutectics, compared to the support P6 where the phenomenon is not found. It can be observed that SS-CA/MA-P6-35, SS-LA/MA-P6-35, and SS-PA/SA-P6-35 melted and solidified around 26 °C, 32 °C and 42 °C, respectively. When the SS-PCMs melted, the sample store energy, and when the samples solidify, the system release energy.

From the dynamic thermal response (**Fig. 112**) can be appreciated, as well, a reduction of the top surface temperature of the samples compared to their respective upper environment temperature (when maximum). This reduction was 4.17%, 11.87%, 10.61%, and 11.50% for support P6, SS-CA/MA-P6-35, SS-LA/MA-P6-35, and SS-PA/SA-P6-35, respectively. The same analysis was done for the reduction of the bottom surface temperature of the sample compared to the respective upper environment temperature (when maximum), and it was found a decrease of 31.01%, 30.35%, 31.83%, and 40.44%, for support P6, SS-CA/MA-P6-35, SS-LA/MA-P6-35, and SS-PA/SA-P6-35, respectively. This means that when the environmental temperature in the upper cavity reaches its maximum, the top sample surfaces are cooler than the surrounding environment, especially for the SS-PCMs that presented 2.8 times less temperature on its top surface than the support P6. The temperature of the bottom surface of the samples presented similar decreases between them, except for the SS-PA/SA-P6-35 that showed an extra 10% of reducing the superficial temperature of the bottom of the

sample. When the environment temperature reached its minimum, the phenomenon is inverted, an increase in the top and bottom surface temperature of the samples can be noticed.

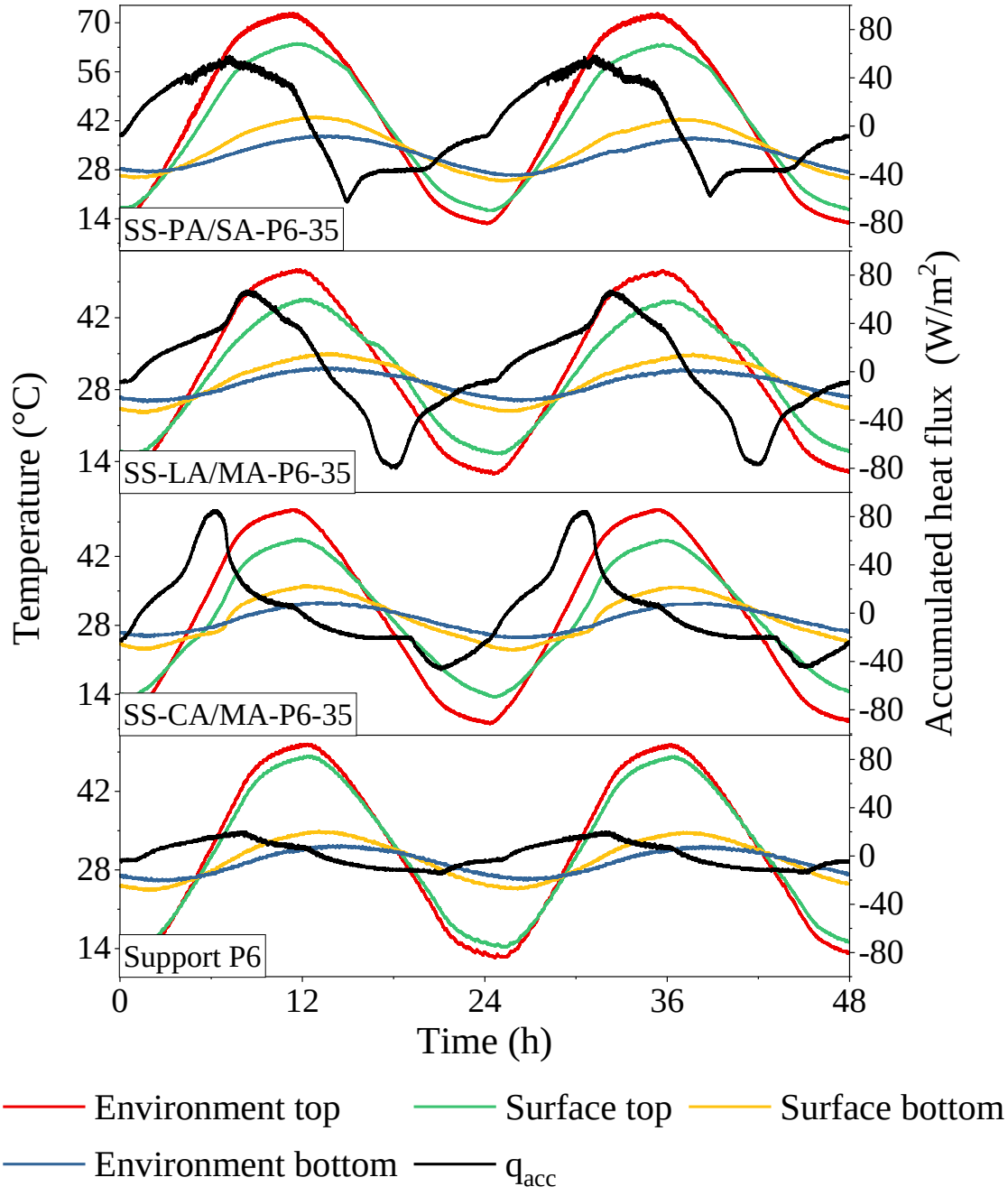

Fig. 112. Dynamic thermal response of the support P6 and the SS-PCM composites.

The increase in temperature for the top surface of support P6, SS-CA/MA-P6-35, SS-LA/MA-P6-35, and SS-PA/SA-P6-35, compared to the environment temperature (when

minimum) was 14.29%, 64.90%, 32.77%, and 28.72%, respectively. Besides, the increase in temperature for the bottom surface of support P6, SS-CA/MA-P6-35, SS-LA/MA-P6-35, and SS-PA/SA-P6-35, compared to the environment temperature (when minimum) was 95.63%, 181.88%, 102.98%, and 93.98%, respectively. These results indicate that when the environmental temperature is low, the surfaces of the samples present higher temperatures, particularly for the SS-PCMs samples. This behavior is due to the heat storage capacity of the PCM that allowed to keep the surfaces warmer when the eutectic solidifies and cooler when the eutectic melt compared to the support P6.

Another thermal inertia parameter is the thermal lag, φ, that measures the delay in the heat wave to propagate from the outer surface (surface top) to the inner surface (surface bottom) **[324]** of the material. Thermal lag is shown in **Table 49**. The best results, when the higher time lag is reached, are for the composites SS-LA/MA-P6-35 (1.45 h) and SS-PA/SA-P6-35 (1.19 h), with an increase of 180% and 148% compared to thermal lag of the support P6 (without PCM). The support P6 and the composite SS-CA/MA-P6-35 presented similar thermal lags, of 0.8 h and 0.6 h, respectively.

As for the fiber cement panels, the measurement of the dynamic thermal response and the calculation of thermal inertia parameters was performed, results are presented in **Fig. 113** and **Table 50**. The temperatures of the samples were normalized in order to perform a proper comparison between the three fiber cement panels. Here, the samples were used to simulate a construction system where the Coolguard ® paint act to reflect the radiant heat in the exterior and the SS-PCM-based acrylic plaster in the interior contributes to absorb heat in the environment and regulate the interior temperature. The higher thermal lag reached was of 0.28 h for the FC-Cool-PCM panel. As for the FC and FC-Cool panels, the thermal lags were similar, considering the measurement deviations. Thus, the SS-PCM-plaster allowed to improve the thermal lag of the system, increasing a 67.26% of the time compared to FC sample. Decrement factor for FC-Cool and FC-Cool-PCM presented a decrease of 7% and 9%, respectively, compared to the FC panel. This indicate that the insulation paint and the SS-PCM-based acrylic plaster improved the thermal stability of the fiber cement siding, decreasing the temperature fluctuations.

Table 50. Decrement factor, f , and thermal lag, φ, of the fiber cement panels.

	FC	FC-Cool	FC-Cool-PCM
f	0.416 ± 0.011	0.387 ± 0.009	0.380 ± 0.019
φ (h)	0.168 ± 0.053	0.083± 0.024	0.281 ± 0.086

In **Fig. 113**, the accumulated heat storage of each panel during the diurnal cycle can be seen. The FC and FC-Cool panels accumulate between 10 W/m^2 and 15 W/m^2, while the FC-Cool-PCM panel stored around 44 W/m^2. Furthermore, the maximum temperature reached in the lower cavity when the top environment temperature was maximum (41.3 °C) was 30.7 °C, 28.9 °C, and 28.4 °C for FC, FC-Cool, and FC-Cool-PCM, respectively. These values indicate that the Coolguard ® paint helped to decrease in 1.7 °C the temperature in the inside, while the combination of the insulation paint and the SS-PCM-based acrylic plaster decrease in 2.2 °C the interior of the simulated space, respect to the fiber cement panel of control (FC). The rate at which the heat is release, when the SS-PCM-based acrylic plaster solidifies, seems to be inferior to the heat storage rate; thus, only a small amount of heat is liberated and the temperature in the lower cavity is inferior for the FC-Cool-PCM (16.0 °C) than for the FC (17.2 °C) and FC-Cool (16.7 °C).

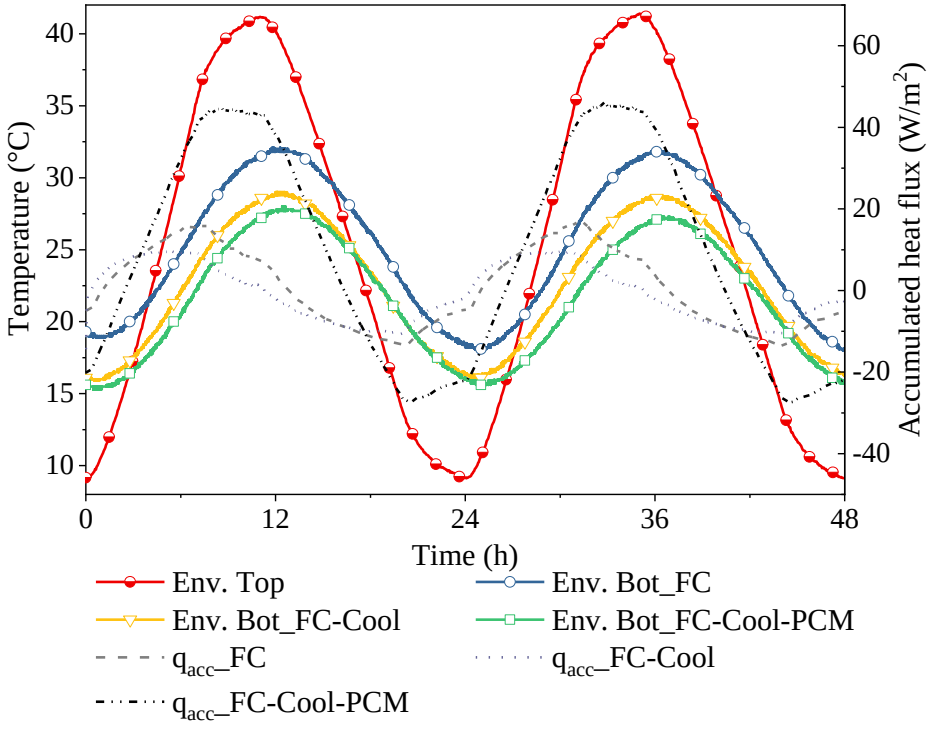

Fig. 113. Dynamic thermal response of the environment temperatures and accumulated heat of FC, FC-Cool and, FC-Cool-PCM panels.

The use of a SS-PCM-based acrylic plaster as a finish for a fiber cement siding, combine with an insulation paint as Coolguard ®, in summary, decreased in 20.8% the temperature of the interior (lower cavity), and increased 67.3% the thermal lag. The PCM-based materials can significantly contribute to control the temperature fluctuations when used along with traditional construction and building materials, as the peak temperature was considerable reduced and shifted. The SS-PCM-based acrylic plaster design in this work probe that the matrix retains the thermal characteristics of the SS-PCMs added, the resin was compatible with the composite providing structural stability and ease handling for horizontal and vertical-plane applications. However, in this study only a two SS-PCM mixed plaster was used and hence more studies need to be done to determine how much SS-PCM is required for optimize thermal response of the system in terms of storage/release heat, thermal lag and decrement factor.

6.8. Conclusions

In this section, several SS-PCM samples that can be incorporated in construction and building applications were studied regarding their thermal performance by using steady-state and dynamic experiments. Two approaches were considered, first, three powder SS-PCMs based in a porous clay support, as well as the support itself, were evaluated in terms of their thermal transmittance (U-Value), effective storage capacity and dynamic thermal response. Second, the thermal transmittance and dynamic response of three fiber cement sidings with different finishes, as an insulation paint and a SS-PCM-based acrylic plaster, design by the authors, were measured.

The powder SS-PCMs, mainly produced from CA/MA, LA/MA and PA/SA eutectics, shown thermal transmittance values close to 5 $W/m^2 \cdot °C$, while the porous clay support presented a higher insulation capacity, with a value of 2.31 $W/m^2 \cdot °C$. Meanwhile, the average heat storage capacity of the SS-PCMs was 1.5 times higher than the support. As for the dynamic thermal measurements, the inertial parameters were calculated and it was found that, in this configuration, the decrement factor of the support and the SS-PCMs was <0.2, indicating a high thermal inertia. Thermal lag of the SS-LA/MA and SS-PA/SA increase 180% and 148% compared to the thermal lag of the support. In this case, the powders were evaluated to

characterize its performance with the purpose of widen the possible applications as, for example, green roofs or insulation materials when in direct contact with the outdoor.

Regarding the fiber cement panels with various finishes, the aim was to simulate its performance as an interior wall. It was found that the incorporation of the SS-PCM-based acrylic plaster reduce 32% of the thermal transmittance under steady-state conditions compared with the other fiber cement sidings. Moreover, the SS-PCM-based acrylic plaster combine with an insulating paint decrease 20.8% the indoor temperature. Lastly, inertial parameters demonstrated that the treatment of the fiber cement siding with the SS-PCM-based acrylic plaster and the insulation paint helped to increase 67.26% of the thermal lag and to decrease 9% the decrement factor, improving the system.

In summary, it was established that these SS-PCM materials can contribute to control the temperature fluctuations, whether in relation to direct contact outdoor applications as to indoor wall uses, since the peak temperature was reduced and shifted. The combine effects of decrement factor and thermal lag can serve to reduce energy consumption in construction and building applications.

VI. GENERAL CONCLUSIONS

This investigation aimed to develop a latent heat thermal energy storage (LHTES) system using phase change materials and ore mineral resources from Colombia. The LHTES composites obtained were intended for several applications as their phase change temperature were between 23 °C and 55 °C, such as thermal comfort in buildings, use in domestic water heating tanks, or even for food industry. Particularly, the research was focus, first, in the development of potential LHTES composites useful in construction materials for thermal comfort and energy savings, and second, in widen the knowledge of shape-stabilized phase change materials based in organic PCMs and natural porous clays. Some of the drivers to work in this path was the comparatively less expensive process of shape-stabilization respect to microencapsulation, the harnessing of natural resources that can serve as supports, and the use of PCMs from renewable sources. Hence, the following main conclusions can be drawn:

1. Organic PCMs as fatty acids, particularly capric, lauric, myristic, palmitic, and stearic acid are suitable for low to moderate thermal energy storage systems. However, phase change temperatures are still higher for some applications and thus eutectic mixtures were designed as an approach to produce three PCMs with temperatures between 23 °C and 55 °C, looking for multipurpose applications. The eutectic mixtures accomplished were CA/MA (capric/myristic), LA/MA (lauric/myristic), and PA/SA (palmitic/myristic), with melting phase change temperatures of 21.88 °C, 33.81 °C and 54.24 °C, respectively. The analysis results add to a growing body of literature on thermal properties that are partially described for the above mention binary eutectic mixtures. The results included melting and solidification enthalpy, phase change temperature, thermal stability, specific heat capacity, microstructure of the eutectics, thermal conductivity and thermal reliability.

2. The ore mineral studied in this thesis presented different mineralogical phases as kaolinite (19.75%), quartz (11.88%), and illite (10.75%), besides, presented fossilized remains of diatoms (40.00%) . It was proven that the diatomite confers a porous structure to the mineral making it a feasible support for containing PCMs, moreover, the presence of laminar phases as kaolinite and illite, measured by N_2 adsorption-desorption isotherms, match or even improve the loading amount and retention of PCM into the support compared to the investigations of pure diatomite supports found in literature. Regarding

heat storage, these minerals did not contribute with latent heat but with sensible heat. Between the studied minerals kaolin presented the higher heat capacity, similar in value to the ore mineral. As well, kaolin, illite and amorphous phase (e.g. diatomite) contributed to 26.14%, 23.76%, and 31.52%, respectively, to the thermal conductivity of the ore mineral. Silica was the mineral with less contribution to thermal properties or absorption capacity of the support.

3. The production of SS-PCMs through the vacuum assisted impregnation method was successfully address for CA/MA, LA/MA and PA/SA using the raw mineral support (RP). The best composites obtained were SS-CA/MA-35, SS-LA/MA-35 and SS-PA/SA-35, using 35% of PCM impregnation, with melting temperatures of 23 °C, 36 °C and 55 °C, respectively. Leakage was less than 2% for all the SS-PCMs, indicating a good performance of the systems compared to other similar composites found in literature, and melting enthalpies were between 40 kJ/kg, and 50 kJ/kg. Likewise, empirical equations for specific heat capacity as a function of temperature were obtained for the eutectics and their SS-PCMs. These models are useful to improve the design stage of TES systems and to develop better simulations regarding solid and liquid phases. This information is not widely available in literature for binary fatty acids eutectic mixtures, nor for SS-PCMS.

4. Three types of physicochemical modifications were made to the raw mineral to subsequently use the modified supports for shape-stabilization of PCMs, with the following findings:

4.1 Modifying textural properties of the raw support (Dv.50=10.60 μm) by means of heat treatments improved the PCM impregnation and thermal properties of SS-PCMs composites. Surface area, pore volume, and pore width act as a set of required conditions and do not should be analyzed separately because can conduct to misinterpretations. In general, the increase of calcination temperature decreases the leakage of the PCM. Support calcined at 600 °C (P6) was selected as the best for shape-stabilization of 35% wt. of CA/MA, LA/MA, and PA/SA, as the leakage values were 0.99%, 1.26%, and 0.59%, respectively. The P6 support improved (decreased) the leakage in 20.2%, 27.2%, and 43.3%, for CA/MA, LA/MA, and PA/SA, respectively, compared to the raw support

(RP). These findings support the idea that materials with mesopore sizes between 16 nm and 22 nm and pore volumes around 0.14 cm^3/g plus the typical diatomite macropores (60 nm to 300 nm), shown to be appropriate to contained effectively the eutectics into the support. Moreover, the heat treatments influence the impregnation of the supports not only by controlling the pore width and volume but by exposing more silanol groups leading to a better interaction support-fatty acid, that was not seen for the RP support.

4.2 Increasing the particle size of the supports through granulation process, even with subsequent heat treatments, demonstrated to worsen the absorption capability of the material as the leakage significantly increased. Granulated supports presented larger particle size (350 µm to 1050 µm), bigger pore width and an interconnected pore network, compared to the powder supports, that probably prevent capillary forces to act and retain the PCM. Although performance was not ideal, we still believe that further complementary work needs to be carried out to establish whether is possible to improve leakage through surface modification processes as silane grafting.

4.3 Powder raw support was successfully silylated using two different pre-treatments. First route was with an acid leaching treatment and the second route with DMSO intercalation, both followed by silane grafting. The effect achieved by the acid treatment followed by sylanization on the retention capacity of the support is better than the effect of the DMSO intercalation followed by sylanization. Most likely, this is due to the active sites of the support exposed by the HCl that allowed to generate more bonds between the silane and the inorganic surface of the clay. A clear improved was achieved regarding PCM retention as the silylated support with the acid pre-treatment decreased leakage in 42.5% respect to the reference sample with 39% of CA/MA. As well, leakage decreased 35.27% respect to the composite supported in the P6 support (calcined at 600 °C). However, in average, latent heat (~23 kJ/kg) of the silylated SS-PCMs presented an increase in the fusion and a decrease in the solidification compared to the refence sample. This was attributable to the covalent bonds formed between the eutectic fatty acid mixture and the silylated support that demands more energy to melt and less energy to solidify the PCM. The latent heat values were lower than expected and there is certainly room for improvement.

5. The incorporation of composite SS-PCM-35-P6 in an acrylic plaster, which was later applied over a fiber-cement panel simulating a building envelope, reduced 32% of the thermal transmittance under steady-state conditions compared with the reference fiber cement sidings. Moreover, the SS-PCM-based acrylic plaster combine with an insulating paint decrease 20.8% the indoor temperature, increased 67.26% the thermal lag, and decrease 9% the decrement factor, thus, improving significantly the building envelope. In summary, it was established that the SS-PCM produced in this work can contribute to control the temperature fluctuations, whether in relation to direct contact outdoor applications as to indoor wall uses, since the peak temperature was reduced and shifted. The combine effects of decrement factor and thermal lag can serve to reduce energy consumption in construction and building applications.

VII. REFERENCES

[1] Pricewaterhouse Coopers, Five Megatrends and Possible Implications, 2013.

[2] World Economic Forum, Shaping the Future of Construction: Inspiring innovators redefine the industry, 2017.

[3] S.C.C.R. and A.R. Philipp Gerbert, Shaping the Future of Construction A Breakthrough in Mindset and Technology, World Econ. Forum. (2016) 1–64. https://www.bcgperspectives.com/Images/Shaping_the_Future_of_Construction_may_2016.pdf.

[4] Official Records of the UN General Assembly, The 2030 Agenda for Sustainable Development, A/RES/70/1, 16301 (2015) 13–14.

[5] C.P.O. Reyer, S. Adams, T. Albrecht, F. Baarsch, A. Boit, N. Canales Trujillo, M. Cartsburg, D. Coumou, A. Eden, E. Fernandes, F. Langerwisch, R. Marcus, M. Mengel, D. Mira-Salama, M. Perette, P. Pereznieto, A. Rammig, J. Reinhardt, A. Robinson, M. Rocha, B. Sakschewski, M. Schaeffer, C.F. Schleussner, O. Serdeczny, K. Thonicke, Climate change impacts in Latin America and the Caribbean and their implications for development, Reg. Environ. Chang. 17 (2017) 1601–1621. https://doi.org/10.1007/s10113-015-0854-6.

[6] A. Bradshaw, Regulatory change and innovation in Latin America: The case of renewable energy in Brazil, Util. Policy. 49 (2017) 156–164. https://doi.org/10.1016/j.jup.2017.01.006.

[7] J.G. Rueda, A. Guzmán, J. Cabello, R. Silva, E. Bastidas, J. Horrillo, Renewables energies in Colombia and the opportunity for the offshore wind technology, J. Clean. Prod. 220 (2019) 529–543. https://doi.org/10.1016/J.JCLEPRO.2019.02.174.

[8] M. Kottek, J. Grieser, C. Beck, B. Rudolf, F. Rubel, World Map of the Köppen-Geiger climate classification updated, Meteorol. Zeitschrift. 15 (2006) 259–263. https://doi.org/10.1127/0941-2948/2006/0130.

[9] Climate-data, Köppen-Geiger classification, (n.d.).

[10] Ministerio de Vivienda, Anexo Técnico 1: Guía de construcción sostenible para el ahorro de agua y energía en edificaciones, (2013) 89.

[11] Dinero, Aire acondicionado, un negocio de US$500 millones, (2016). https://www.dinero.com/empresas/articulo/negocio-de-aire-acondicionado-en-colombia/232018 (accessed April 26, 2018).

[12] J.M. Hernández, Industria del aire acondicionado mueve $1 billón., El Espectador. (2016). http://www.elespectador.com/noticias/economia/industria-del-aire-acondicionado-mueve-1-billon-articulo-657897 (accessed April 26, 2018).

[13] Ministerio de Minas y Energia, Caracterización energética sectores residencial, comercial y terciario, Colomb. (Bogotá D.C). (2006) 135. http://www.upme.gov.co/Upme12/2007/Upme13/Caracterizacion_energetica_sectores.pdf.

[14] A. Pinilla, Soluciones Energéticos para zonas rurales, Rev. Ing. N°44. (2016) 36–39. https://doi.org/Revista de Ingeniería.

[15] A. de Medellín, Medellín resiliente. Una estrategia para el futuro, 2016.

[16] Rockerfeller Foundation, Global Prospectus, (2018) 16.

[17] R. Foundation, Urban Resilience Prospectus: Latin America and the Caribbean, (2018).

[18] Congreso de Colombia, Ley 1715 Por medio de la cual se regula la integración de las energías renovables no convencionales al sistema energético nacional, 2014.
[19] N. Bedoya, Colombia Reports, (2014). https://colombiareports.com/colombian-government-passes-law-encourage-development-renewable-energy/ (accessed October 10, 2017).
[20] Minvivienda, Resolucion Nro 0549 de 2015, Minist. Vivienda Ciudad y Territ. (2015) 9. http://www.minvivienda.gov.co/ResolucionesVivienda/0549 - 2015.pdf.
[21] A.A. Navarro, Sustentabilidad y Energías Renovables, (2010). http://zean-renovables.blogspot.com.co/2010/03/que-es-una-vivienda-ecoeficiente-o.html (accessed June 2, 2017).
[22] H.M. Hoang, D. Leducq, A. Escardino, P. Valencia, Heat transfer study of submicro-encapsulated PCM plate for food packaging application, Int. J. Refrig. 52 (2015) 151–160. https://doi.org/10.1016/j.ijrefrig.2014.07.002.
[23] E. Alehosseini, S.M. Jafari, Micro/nano-encapsulated phase change materials (PCMs) as emerging materials for the food industry, Trends Food Sci. Technol. 91 (2019) 116–128. https://doi.org/10.1016/j.tifs.2019.07.003.
[24] Y. Lu, Y. Tian, H. Lu, L. Wu, X. Li, Study of solar heated biogas fermentation system with a phase change thermal storage device, Appl. Therm. Eng. 88 (2015) 418–424. https://doi.org/10.1016/j.applthermaleng.2014.12.065.
[25] U. Stritih, V. V. Tyagi, R. Stropnik, H. Paksoy, F. Haghighat, M.M. Joybari, Integration of passive PCM technologies for net-zero energy buildings, Sustain. Cities Soc. 41 (2018) 286–295. https://doi.org/10.1016/j.scs.2018.04.036.
[26] M.K.A. Sharif, A.A. Al-Abidi, S. Mat, K. Sopian, M.H. Ruslan, M.Y. Sulaiman, M.A.M. Rosli, Review of the application of phase change material for heating and domestic hot water systems, Renew. Sustain. Energy Rev. 42 (2015) 557–568. https://doi.org/10.1016/j.rser.2014.09.034.
[27] X. Huang, X. Chen, A. Li, D. Atinafu, H. Gao, W. Dong, G. Wang, Shape-stabilized phase change materials based on porous supports for thermal energy storage applications, Chem. Eng. J. 356 (2019) 641–661. https://doi.org/10.1016/j.cej.2018.09.013.
[28] L.F. Cabeza, A. Castell, C. Barreneche, A. De Gracia, A.I. Fernández, Materials used as PCM in thermal energy storage in buildings: A review, Renew. Sustain. Energy Rev. 15 (2011) 1675–1695. https://doi.org/10.1016/j.rser.2010.11.018.
[29] A. Marani, M.L. Nehdi, Integrating phase change materials in construction materials: Critical review, Constr. Build. Mater. 217 (2019) 36–49. https://doi.org/10.1016/j.conbuildmat.2019.05.064.
[30] V.V. Rao, R. Parameshwaran, V.V. Ram, PCM-mortar based construction materials for energy efficient buildings: A review on research trends, Energy Build. 158 (2018) 95–122. https://doi.org/10.1016/j.enbuild.2017.09.098.
[31] W. Lin, Z. Ma, H. Ren, S. Gschwander, S. Wang, Multi-objective optimisation of thermal energy storage using phase change materials for solar air systems, Renew. Energy. 130 (2019) 1116–1129.
[32] A.N. Sadeghifam, S.M. Zahraee, M.M. Meynagh, I. Kiani, Combined use of design of experiment and dynamic building simulation in assessment of energy efficiency in tropical residential buildings, Energy Build. 86 (2015) 525–533. https://doi.org/10.1016/j.enbuild.2014.10.052.
[33] K. Pielichowska, K. Pielichowski, Phase change materials for thermal energy storage,

Prog. Mater. Sci. 65 (2014) 67–123. https://doi.org/10.1016/j.pmatsci.2014.03.005.
[34] F. Mayinger, L.F. Cabeza, Heat and cold storage with PCM An up to date introduction into basics and applications, Springer, 2008.
[35] W. Su, J. Darkwa, G. Kokogiannakis, Review of solid-liquid phase change materials and their encapsulation technologies, Renew. Sustain. Energy Rev. 48 (2015) 373–391. https://doi.org/10.1016/j.rser.2015.04.044.
[36] Y.E. Milián, A. Gutiérrez, M. Grágeda, S. Ushak, A review on encapsulation techniques for inorganic phase change materials and the influence on their thermophysical properties, Renew. Sustain. Energy Rev. 73 (2017) 983–999. https://doi.org/10.1016/j.rser.2017.01.159.
[37] M. Pomianowski, P. Heiselberg, Y. Zhang, Review of thermal energy storage technologies based on PCM application in buildings, Energy Build. 67 (2013) 56–69. https://doi.org/10.1016/j.enbuild.2013.08.006.
[38] D. Zhou, C.Y. Zhao, Y. Tian, Review on thermal energy storage with phase change materials (PCMs) in building applications, Appl. Energy. 92 (2012) 593–605. https://doi.org/10.1016/j.apenergy.2011.08.025.
[39] A. Inés Fernández, A. Solé, J. Giró-Paloma, M. Martínez, Nica, M. Hadjieva, A. Boudenne, M. Constantinescu, E. Maria Anghel, M. Malikova, I. Krupa, C. Peñalosa, A. Lázaro, H.O. Paksoy, K. Cellat, J. Vecstaudza, D. Bajare, B. Sumiga, B. Boh, T. Haussmann, S. Gschwander, R. Weber, P. Furmanski, M. Jaworski, L.F. Cabeza, Unconventional experimental technologies used for phase change materials (PCM) characterization: Part 2 - Morphological and structural characterization, physico-chemical stability and mechanical properties, Renew. Sustain. Energy Rev. 43 (2015) 1415–1426. https://doi.org/10.1016/j.rser.2014.11.051.
[40] G.F. Guruprasad Alva, Yaxue Lin, An Overview of Thermal Energy Storage Systems, 144 (2018) 341–378.
[41] J. Lizana, R. Chacartegui, A. Barrios-padura, J.M. Valverde, C. Ortiz, Identification of best available thermal energy storage compounds for low-to-moderate temperature storage applications in buildings, 2018.
[42] S. Kahwaji, M.B. Johnson, A.C. Kheirabadi, D. Groulx, M. Anne, Fatty acids and related phase change materials for reliable thermal energy storage at moderate temperatures, Sol. Energy Mater. Sol. Cells. 167 (2017) 109–120. https://doi.org/10.1016/j.solmat.2017.03.038.
[43] H. Nazir, M. Batool, M. Ali, A.M. Kannan, Fatty acids based eutectic phase change system for thermal energy storage applications, Appl. Therm. Eng. 142 (2018) 466–475. https://doi.org/10.1016/j.applthermaleng.2018.07.025.
[44] W.G. Drossel, H. Kunze, A. Bucht, L. Weisheit, K. Pagel, Smart3 - Smart materials for smart applications, Procedia CIRP. 36 (2015) 211–216. https://doi.org/10.1016/j.procir.2015.01.055.
[45] A.D.B.L. Ferreira, P.R.O. Nóvoa, A.T. Marques, Multifunctional Material Systems: A state-of-the-art review, Compos. Struct. 151 (2016) 3–35. https://doi.org/10.1016/j.compstruct.2016.01.028.
[46] D.R. Askeland, P.P. Phulé, The Science and Engineering of Materials, 4th ed., Thomson, 2004.
[47] B. Zalba, J.M. Marín, L.F. Cabeza, H. Mehling, Review on thermal energy storage with phase change : materials , heat transfer analysis and applications, Appl. Therm. Eng. 23 (2003) 251–283.

[48] B. Xu, P. Li, C. Chan, Application of phase change materials for thermal energy storage in concentrated solar thermal power plants: A review to recent developments, Appl. Energy. 160 (2015) 286–307. https://doi.org/10.1016/j.apenergy.2015.09.016.
[49] F. Pacheco-Torgal, Eco-efficient construction and building materials research under the EU Framework Programme Horizon 2020, Constr. Build. Mater. 51 (2014) 151–162. https://doi.org/10.1016/j.conbuildmat.2013.10.058.
[50] L. Navarro, A. de Gracia, S. Colclough, M. Browne, S.J. McCormack, P. Griffiths, L.F. Cabeza, Thermal energy storage in building integrated thermal systems: A review. Part 1. active storage systems, Renew. Energy. 88 (2016) 526–547. https://doi.org/10.1016/j.renene.2015.11.040.
[51] L. Navarro, A. de Gracia, D. Niall, A. Castell, M. Browne, S.J. McCormack, P. Griffiths, L.F. Cabeza, Thermal energy storage in building integrated thermal systems: A review. Part 2. Integration as passive system, Renew. Energy. 85 (2016) 1334–1356. https://doi.org/10.1016/j.renene.2015.06.064.
[52] T. Kousksou, P. Bruel, A. Jamil, T. El Rhafiki, Y. Zeraouli, Energy storage: Applications and challenges, Sol. Energy Mater. Sol. Cells. 120 (2014) 59–80. https://doi.org/10.1016/j.solmat.2013.08.015.
[53] Y. Zhao, X. Zhang, X. Xu, S. Zhang, Research progress of phase change cold storage materials used in cold chain transportation and their different cold storage packaging structures, J. Mol. Liq. 319 (2020) 114360. https://doi.org/10.1016/j.molliq.2020.114360.
[54] L.F. Cabeza, Advances in Thermal Energy Storage Systems. Methods and applications, 2015. https://doi.org/10.1016/c2013-0-16453-7.
[55] K. Vignarooban, X. Xu, A. Arvay, K. Hsu, A.M. Kannan, Heat transfer fluids for concentrating solar power systems - A review, Appl. Energy. 146 (2015) 383–396. https://doi.org/10.1016/j.apenergy.2015.01.125.
[56] I. Dincer, M. Rosen, Thermal Energy Storage: Systems and Applications, Second Edi, 2011.
[57] A. Abhat, Low temperature latent heat thermal energy storage: Heat storage materials, Sol. Energy. 30 (1983) 313–332. https://doi.org/10.1016/0038-092X(83)90186-X.
[58] F. Kuznik, J. Virgone, K. Johannes, In-situ study of thermal comfort enhancement in a renovated building equipped with phase change material wallboard, Renew. Energy. 36 (2011) 1458–1462. https://doi.org/10.1016/j.renene.2010.11.008.
[59] A.L. Pisello, E. Fortunati, S. Mattioli, L.F. Cabeza, C. Barreneche, J.M. Kenny, F. Cotana, Innovative cool roofing membrane with integrated phase change materials: Experimental characterization of morphological, thermal and optic-energy behavior, Energy Build. 112 (2016) 40–48. https://doi.org/10.1016/j.enbuild.2015.11.061.
[60] H.J. Alqallaf, E.M. Alawadhi, Concrete roof with cylindrical holes containing PCM to reduce the heat gain, Energy Build. 61 (2013) 73–80. https://doi.org/10.1016/j.enbuild.2013.01.041.
[61] L. Royon, L. Karim, A. Bontemps, Thermal energy storage and release of a new component with PCM for integration in floors for thermal management of buildings, Energy Build. 63 (2013) 29–35. https://doi.org/10.1016/j.enbuild.2013.03.042.
[62] R.L. Plante, Solar Domestic Hot Water--A Practical Guide to Solar Heat Storage : Latent Heat Materials--Vol . I : Background and Scientific Principles , George A . Structure and Bonding : Solar Energy Materials , Vol . 49 , (1982) 476.
[63] M. Song, F. Niu, N. Mao, Y. Hu, S. Deng, Review on building energy performance

improvement using phase change materials, Energy Build. 158 (2018) 776–793. https://doi.org/10.1016/j.enbuild.2017.10.066.

[64] W. Hu, M. Song, Y. Jiang, Y. Yao, Y. Gao, A modeling study on the heat storage and release characteristics of a phase change material based double-spiral coiled heat exchanger in an air source heat pump for defrosting, Appl. Energy. 236 (2019) 877–892. https://doi.org/10.1016/j.apenergy.2018.12.057.

[65] W.D.J. Callister, Materials science and engineering. An introduction, 2007. https://doi.org/10.1007/BF01184995.

[66] T.L. Bergman, A.S. Lavine, Fundamentals of Heat and Mass Transfer, Eighth Ed., Wiley, 2017.

[67] S. Wu, T. Yan, Z. Kuai, W. Pan, Thermal conductivity enhancement on phase change materials for thermal energy storage: a review, Energy Storage Mater. 25 (2020) 251–295. https://doi.org/10.13374/j.issn2095-9389.2019.07.19.001.

[68] S. Drissi, T.C. Ling, K.H. Mo, Thermal efficiency and durability performances of paraffinic phase change materials with enhanced thermal conductivity – A review, Thermochim. Acta. 673 (2019) 198–210. https://doi.org/10.1016/j.tca.2019.01.020.

[69] Z.A. Qureshi, H.M. Ali, S. Khushnood, Recent advances on thermal conductivity enhancement of phase change materials for energy storage system : A review, Int. J. Heat Mass Transf. 127 (2018) 838–856. https://doi.org/10.1016/j.ijheatmasstransfer.2018.08.049.

[70] Y. Lin, Y. Jia, G. Alva, G. Fang, Review on thermal conductivity enhancement, thermal properties and applications of phase change materials in thermal energy storage, Renew. Sustain. Energy Rev. 82 (2017) 2730–2742. https://doi.org/10.1016/j.rser.2017.10.002.

[71] W. Zhao, Y. Yang, Z. Bao, D. Yan, Z. Zhu, Methods for measuring the effective thermal conductivity of metal hydride beds: A review, Int. J. Hydrogen Energy. 45 (2020) 6680–6700. https://doi.org/10.1016/j.ijhydene.2019.12.185.

[72] A. Palacios, L. Cong, M.E. Navarro, Y. Ding, C. Barreneche, Thermal conductivity measurement techniques for characterizing thermal energy storage materials – A review, Renew. Sustain. Energy Rev. 108 (2019) 32–52. https://doi.org/10.1016/j.rser.2019.03.020.

[73] ASTM, ASTM E1952-17 Standard Test Method for Thermal Conductivity and Thermal Diffusivity by Modulated Temperature Differential Scanning Calorimetry, (2017) 1–7. https://doi.org/10.1520/E1952-17.2.

[74] C-Therm, How to Measure Thermal Conductivity: Method selection guide, 2018. https://doi.org/10.1007/978-94-017-8969-1_8.

[75] E. Jebasingh B., V. Arasu A., Characterisation and stability analysis of eutectic fatty acid as a low cost cold energy storage phase change material, J. Energy Storage. 31 (2020). https://doi.org/10.1016/j.est.2020.101708.

[76] X. Zhang, Z. Yin, D. Meng, Z. Huang, R. Wen, Shape-stabilized composite phase change materials with high thermal conductivity based on stearic acid and modified expanded vermiculite, Renew. Energy. 112 (2017) 113–123. https://doi.org/10.1016/j.renene.2017.05.026.

[77] D. Xiao, Y. Qu, S. Hu, H. Han, Y. Li, J. Zhai, Y. Jiang, H. Yang, Study on the phase change thermal storage performance of palmitic acid/carbon nanotubes composites, Compos. Part A Appl. Sci. Manuf. 77 (2015) 50–55. https://doi.org/10.1016/j.compositesa.2015.06.020.

[78] A. Sarı, A. Bicer, F.A. Al-sulaiman, A. Karaipekli, V. V Tyagi, Diatomite/CNTs/PEG composite PCMs with shape-stabilized and improved thermal conductivity : Preparation and thermal energy storage properties, Energy Build. 164 (2018) 166–175. https://doi.org/10.1016/j.enbuild.2018.01.009.

[79] G. Wang, J. Fan, X. Wang, F. Song, Q. Wang, L. Zhang, Experimental investigations on the liquid thermal conductivity of five saturated fatty acid methyl esters components of biodiesel, Fluid Phase Equilib. 473 (2018) 106–111. https://doi.org/10.1016/j.jct.2018.05.019.

[80] N. Zhang, Y. Yuan, Y. Yuan, T. Li, X. Cao, Lauric – palmitic – stearic acid / expanded perlite composite as form-stable phase change material : Preparation and thermal properties, Energy Build. 82 (2014) 505–511. https://doi.org/10.1016/j.enbuild.2014.07.049.

[81] A. Jamekhorshid, S.M. Sadrameli, M. Farid, A review of microencapsulation methods of phase change materials (PCMs) as a thermal energy storage (TES) medium, Renew. Sustain. Energy Rev. 31 (2014) 531–542. https://doi.org/10.1016/j.rser.2013.12.033.

[82] Y.E. Milián, A. Gutiérrez, M. Grágeda, S. Ushak, A review on encapsulation techniques for inorganic phase change materials and the influence on their thermophysical properties, Renew. Sustain. Energy Rev. 73 (2017) 983–999. https://doi.org/10.1016/j.rser.2017.01.159.

[83] A. Yataganbaba, B. Ozkahraman, I. Kurtbas, Worldwide trends on encapsulation of phase change materials: A bibliometric analysis (1990–2015), Appl. Energy. 185 (2017) 720–731. https://doi.org/10.1016/j.apenergy.2016.10.107.

[84] A. Calderón, C. Barreneche, K. Hernández-Valle, E. Galindo, M. Segarra, A.I. Fernández, Where is Thermal Energy Storage (TES) research going? – A bibliometric analysis, Sol. Energy. (2019). https://doi.org/10.1016/j.solener.2019.01.050.

[85] L. Waltman, N.J. van Eck, P. Wouters, Counting publications and citations: Is more always better?, Proc. ISSI 2013 - 14th Int. Soc. Sci. Inf. Conf. 1 (2013) 455–467.

[86] L. Waltman, N.J. van Eck, E.C.M. Noyons, A unified approach to mapping and clustering of bibliometric networks, J. Informetr. 4 (2010) 629–635. https://doi.org/10.1016/j.joi.2010.07.002.

[87] A. Perianes-Rodriguez, L. Waltman, N.J. van Eck, Constructing bibliometric networks: A comparison between full and fractional counting, J. Informetr. 10 (2016) 1178–1195. https://doi.org/10.1016/j.joi.2016.10.006.

[88] N. Soares, J.J. Costa, A.R. Gaspar, P. Santos, Review of passive PCM latent heat thermal energy storage systems towards buildings' energy efficiency, Energy Build. 59 (2013) 82–103. https://doi.org/10.1016/j.enbuild.2012.12.042.

[89] R. Jacob, F. Bruno, Review on shell materials used in the encapsulation of phase change materials for high temperature thermal energy storage, Renew. Sustain. Energy Rev. 48 (2015) 79–87. https://doi.org/10.1016/j.rser.2015.03.038.

[90] J. Giro-Paloma, M. Martínez, L.F. Cabeza, A.I. Fernández, Types, methods, techniques, and applications for microencapsulated phase change materials (MPCM): A review, Renew. Sustain. Energy Rev. 53 (2016) 1059–1075. https://doi.org/10.1016/j.rser.2015.09.040.

[91] Y. Konuklu, H. Paksoy, Polystyrene-based caprylic acid microencapsulation for thermal energy storage, Sol. Energy Mater. Sol. Cells. 159 (2017) 235–242. https://doi.org/10.1016/j.solmat.2016.09.016.

[92] S. Lu, T. Shen, J. Xing, Q. Song, J. Shao, J. Zhang, C. Xin, Preparation and

characterization of cross-linked polyurethane shell microencapsulated phase change materials by interfacial polymerization, Mater. Lett. 211 (2018) 36–39. https://doi.org/10.1016/j.matlet.2017.09.074.

[93] S. Lashgari, H. Arabi, A.R. Mahdavian, V. Ambrogi, Thermal and morphological studies on novel PCM microcapsules containing n-hexadecane as the core in a flexible shell, Appl. Energy. 190 (2017) 612–622. https://doi.org/10.1016/j.apenergy.2016.12.158.

[94] G. Fang, Z. Chen, H. Li, Synthesis and properties of microencapsulated paraffin composites with SiO2 shell as thermal energy storage materials, Chem. Eng. J. 163 (2010) 154–159. https://doi.org/10.1016/j.cej.2010.07.054.

[95] S. Yu, X. Wang, D. Wu, Microencapsulation of n-octadecane phase change material with calcium carbonate shell for enhancement of thermal conductivity and serving durability: Synthesis, microstructure, and performance evaluation, Appl. Energy. 114 (2014) 632–643. https://doi.org/10.1016/j.apenergy.2013.10.029.

[96] G.B. Gao, C.X. Qian, M.J. Gao, Preparation and characterization of hexadecane microcapsule with polyurea-melamine formaldehyde resin shell materials, Chinese Chem. Lett. 21 (2010) 533–537. https://doi.org/10.1016/j.cclet.2009.11.021.

[97] Y. Konuklu, H.O. Paksoy, M. Unal, S. Konuklu, Microencapsulation of a fatty acid with Poly(melamine-urea-formaldehyde), Energy Convers. Manag. 80 (2014) 382–390. https://doi.org/10.1016/j.enconman.2014.01.042.

[98] W. Li, X.X. Zhang, X.C. Wang, J.J. Niu, Preparation and characterization of microencapsulated phase change material with low remnant formaldehyde content, Mater. Chem. Phys. 106 (2007) 437–442. https://doi.org/10.1016/j.matchemphys.2007.06.030.

[99] F. Tang, L. Liu, G. Alva, Y. Jia, G. Fang, Synthesis and properties of microencapsulated octadecane with silica shell as shape-stabilized thermal energy storage materials, Sol. Energy Mater. Sol. Cells. 160 (2017) 1–6. https://doi.org/10.1016/j.solmat.2016.10.014.

[100] F. He, X. Wang, D. Wu, New approach for sol–gel synthesis of microencapsulated n-octadecane phase change material with silica wall using sodium silicate precursor, Energy. 67 (2014) 223–233. https://doi.org/10.1016/j.energy.2013.11.088.

[101] D. Platte, U. Helbig, R. Houbertz, G. Sextl, Microencapsulation of alkaline salt hydrate melts for phase change applications by surface thiol-michael addition polymerization, Macromol. Mater. Eng. 298 (2013) 67–77. https://doi.org/10.1002/mame.201100338.

[102] Y. Ma, J. Zong, W. Li, L. Chen, X. Tang, N. Han, J. Wang, X. Zhang, Synthesis and characterization of thermal energy storage microencapsulated n-dodecanol with acrylic polymer shell, Energy. 87 (2015) 86–94. https://doi.org/10.1016/j.energy.2015.04.096.

[103] F. Chen, M.P. Wolcott, Miscibility studies of paraffin/polyethylene blends as form-stable phase change materials, Eur. Polym. J. 52 (2014) 44–52. https://doi.org/10.1016/j.eurpolymj.2013.09.027.

[104] F. Chen, M. Wolcott, Polyethylene/paraffin binary composites for phase change material energy storage in building: A morphology, thermal properties, and paraffin leakage study, Sol. Energy Mater. Sol. Cells. 137 (2015) 79–85. https://doi.org/10.1016/j.solmat.2015.01.010.

[105] C. Alkan, A. Sari, Fatty acid/poly(methyl methacrylate) (PMMA) blends as form-

stable phase change materials for latent heat thermal energy storage, Sol. Energy. 82 (2008) 118–124. https://doi.org/10.1016/j.solener.2007.07.001.

[106] C. Yang, L. Fischer, S. Maranda, J. Worlitschek, Rigid polyurethane foams incorporated with phase change materials: A state-of-the-art review and future research pathways, Energy Build. 87 (2015) 25–36. https://doi.org/10.1016/j.enbuild.2014.10.075.

[107] C. Li, H. Yu, Y. Song, M. Wang, Z. Liu, A n-octadecane/hierarchically porous TiO2 form-stable PCM for thermal energy storage, Renew. Energy. 145 (2020) 1465–1473. https://doi.org/10.1016/j.renene.2019.06.070.

[108] M.E. Darzi, S.I. Golestaneh, M. Kamali, G. Karimi, Thermal and electrical performance analysis of co-electrospun-electrosprayed PCM nanofiber composites in the presence of graphene and carbon fiber powder, Renew. Energy. 135 (2019) 719–728. https://doi.org/10.1016/j.renene.2018.12.028.

[109] C. Chen, L. Wang, Y. Huang, A novel shape-stabilized PCM: Electrospun ultrafine fibers based on lauric acid/polyethylene terephthalate composite, Mater. Lett. 62 (2008) 3515–3517. https://doi.org/10.1016/j.matlet.2008.03.034.

[110] S.I. Golestaneh, A. Mosallanejad, G. Karimi, M. Khorram, M. Khashi, Fabrication and characterization of phase change material composite fibers with wide phase-transition temperature range by co-electrospinning method, Appl. Energy. 182 (2016) 409–417. https://doi.org/10.1016/j.apenergy.2016.08.136.

[111] G. Chen, T. Shi, X. Zhang, F. Cheng, X. Wu, G. Leng, Y. Liu, M. Fang, X. Min, Z. Huang, Polyacrylonitrile / polyethylene glycol phase-change material fibres prepared with hybrid polymer blends and nano-SiC fillers via centrifugal spinning, Polymer (Guildf). (2019) 122012. https://doi.org/10.1016/j.polymer.2019.122012.

[112] Y. Zhang, S. Zheng, S. Zhu, J. Ma, Z. Sun, M. Farid, Evaluation of paraffin infiltrated in various porous silica matrices as shape-stabilized phase change materials for thermal energy storage, Energy Convers. Manag. 171 (2018) 361–370. https://doi.org/10.1016/j.enconman.2018.06.002.

[113] Z.R. Peizhao Lv, Chenzhen Liu, Review on clay mineral-based form-stable phase change materials: Preparation, characterization and applications, Renew. Sustain. Energy Rev. 67 (2017) 1139–1152. https://doi.org/10.1016/j.rser.2015.06.026.

[114] E.S. Dana, DANA´S Manual of Mineralogy, 1950.

[115] Y. Konuklu, O. Ersoy, Preparation and characterization of sepiolite-based phase change material nanocomposites for thermal energy storage, Appl. Therm. Eng. 107 (2016) 575–582. https://doi.org/10.1117/12.2230039.

[116] R. Wen, X. Zhang, Y. Huang, Z. Yin, Z. Huang, M. Fang, Y. Liu, X. Wu, Preparation and properties of fatty acid eutectics/expanded perlite and expanded vermiculite shape-stabilized materials for thermal energy storage in buildings, Energy Build. 139 (2017) 197–204. https://doi.org/10.1016/j.enbuild.2017.01.025.

[117] Z. Liu, D. Hu, H. Lv, Y. Zhang, F. Wu, D. Shen, P. Fu, Mixed mill-heating fabrication and thermal energy storage of Diatomite/Paraffin phase change composite incorporated gypsum-based materials, Appl. Therm. Eng. (2017). https://doi.org/10.1016/j.applthermaleng.2017.02.057.

[118] O. Chung, S.G. Jeong, S. Kim, Preparation of energy efficient paraffinic PCMs/expanded vermiculite and perlite composites for energy saving in buildings, Sol. Energy Mater. Sol. Cells. 137 (2015) 107–112. https://doi.org/10.1016/j.solmat.2014.11.001.

[119] C.H. Zhou, G.L. Li, X.Y. Zhuang, P.P. Wang, D.S. Tong, H.M. Yang, C.X. Lin, L. Li, H. Zhang, S.F. Ji, W.H. Yu, Roles of texture and acidity of acid-activated sepiolite catalysts in gas-phase catalytic dehydration of glycerol to acrolein, Mol. Catal. 434 (2017) 219–231. https://doi.org/10.1016/j.mcat.2016.12.022.

[120] S. Ramakrishnan, X. Wang, J. Sanjayan, J. Wilson, Assessing the feasibility of integrating form-stable phase change material composites with cementitious composites and prevention of PCM leakage, Mater. Lett. 192 (2017) 88–91. https://doi.org/10.1016/j.matlet.2016.12.052.

[121] T. Qian, J. Li, X. Min, Y. Deng, W. Guan, L. Ning, Diatomite: A promising natural candidate as carrier material for low, middle and high temperature phase change material, Energy Convers. Manag. 98 (2015) 34–45. https://doi.org/10.1016/j.enconman.2015.03.071.

[122] E. De Tommasi, J. Gielis, A. Rogato, Diatom Frustule Morphogenesis and Function: a Multidisciplinary Survey, Mar. Genomics. 35 (2017) 1–18. https://doi.org/10.1016/j.margen.2017.07.001.

[123] M. Li, Z. Wu, H. Kao, Study on preparation and thermal properties of binary fatty acid/diatomite shape-stabilized phase change materials, Sol. Energy Mater. Sol. Cells. 95 (2011) 2412–2416. https://doi.org/10.1016/j.solmat.2011.04.017.

[124] M. Li, H. Kao, Z. Wu, J. Tan, Study on preparation and thermal property of binary fatty acid and the binary fatty acids/diatomite composite phase change materials, Appl. Energy. 88 (2011) 1606–1612. https://doi.org/10.1016/j.apenergy.2010.11.001.

[125] X. Li, J.G. Sanjayan, J.L. Wilson, Fabrication and stability of form-stable diatomite/paraffin phase change material composites, Energy Build. 76 (2014) 284–294. https://doi.org/10.1016/j.enbuild.2014.02.082.

[126] C. Cárdenas-Ramírez, M.A. Gómez, F. Jaramillo, Characterization of a porous mineral as a promising support for shape- stabilized phase change materials, J. Energy Storage. 26 (2019) 101041. https://doi.org/10.1016/j.est.2019.101041.

[127] A.S. Avramenko, M. V. Cherepanova, V.S. Pushkar', S.B. Yarusova, Diatom characteristics of the Far East siliceous organogenic deposits, Russ. Geol. Geophys. 56 (2015) 947–958. https://doi.org/10.1016/j.rgg.2015.05.010.

[128] F. Tang, D. Su, Y. Tang, G. Fang, Synthesis and thermal properties of fatty acid eutectics and diatomite composites as shape-stabilized phase change materials with enhanced thermal conductivity, Sol. Energy Mater. 141 (2015) 218–224. https://doi.org/10.1016/j.solmat.2015.05.045.

[129] E. Haeckel, Kunstformen der Natur, Leipzig and Wien, 1899.

[130] A. Sari, Thermal energy storage characteristics of bentonite-based composite PCMs with enhanced thermal conductivity as novel thermal storage building materials, Energy Convers. Manag. 117 (2016) 132–141. https://doi.org/10.1016/j.enconman.2016.02.078.

[131] A. Karaipekli, A. Sari, Development and thermal performance of pumice/organic PCM/gypsum composite plasters for thermal energy storage in buildings, Sol. Energy Mater. Sol. Cells. 149 (2016) 19–28. https://doi.org/10.1016/j.solmat.2015.12.034.

[132] S. Song, L. Dong, Y. Zhang, S. Chen, Q. Li, Y. Guo, S. Deng, Lauric acid/intercalated kaolinite as form-stable phase change material for thermal energy storage, Energy. 76 (2014) 385–389. https://doi.org/10.1016/j.energy.2014.08.042.

[133] A. Sari, C. Alkan, A.N. Özcan, Synthesis and characterization of micro/nano capsules of PMMA/capric-stearic acid eutectic mixture for low temperature-thermal energy

storage in buildings, Energy Build. (2015). https://doi.org/10.1016/j.enbuild.2015.01.013.
[134] A. Sarı, Fabrication and thermal characterization of kaolin-based composite phase change materials for latent heat storage in buildings, Energy Build. 96 (2015) 193–200. https://doi.org/10.1016/j.enbuild.2015.03.022.
[135] R. Wang, M. Ren, X. Gao, L. Qin, Preparation and properties of fatty acids based thermal energy storage aggregate concrete, Constr. Build. Mater. 165 (2018) 1–10. https://doi.org/10.1016/j.conbuildmat.2018.01.034.
[136] S. Song, F. Qiu, W. Zhu, Y. Guo, Y. Zhang, Y. Ju, R. Feng, Y. Liu, Z. Chen, J. Zhou, C. Xiong, L. Dong, Polyethylene glycol/halloysite@Ag nanocomposite PCM for thermal energy storage: Simultaneously high latent heat and enhanced thermal conductivity, Sol. Energy Mater. Sol. Cells. 193 (2019) 237–245. https://doi.org/10.1016/j.solmat.2019.01.023.
[137] R. Ye, W. Lin, K. Yuan, X. Fang, Z. Zhang, Experimental and numerical investigations on the thermal performance of building plane containing CaCl 2 ·6H 2 O/expanded graphite composite phase change material, Appl. Energy. 193 (2017) 325–335. https://doi.org/10.1016/j.apenergy.2017.02.049.
[138] M. Gaeini, A.L. Rouws, J.W.O. Salari, H.A. Zondag, C.C.M. Rindt, Characterization of microencapsulated and impregnated porous host materials based on calcium chloride for thermochemical energy storage, Appl. Energy. 212 (2018) 1165–1177. https://doi.org/10.1016/j.apenergy.2017.12.131.
[139] A.M. Goitandia, G. Beobide, E. Aranzabe, A. Aranzabe, Development of content-stable phase change composites by infiltration into inorganic porous supports, Sol. Energy Mater. Sol. Cells. 134 (2015) 318–328. https://doi.org/10.1016/j.solmat.2014.12.010.
[140] S.J. Chang, S. Wi, J. Lee, S. Kim, Development of vacuum impregnation equipment and preparation of mass/uniform shape-stabilized phase change materials, Int. J. Heat Mass Transf. 132 (2019) 817–824. https://doi.org/10.1016/j.ijheatmasstransfer.2018.11.161.
[141] M. Li, Z. Wu, A review of intercalation composite phase change material: Preparation, structure and properties, Renew. Sustain. Energy Rev. 16 (2012) 2094–2101. https://doi.org/10.1016/j.rser.2012.01.016.
[142] Y. Cai, Y. Hu, L. Song, Q. Kong, R. Yang, Y. Zhang, Z. Chen, W. Fan, Preparation and flammability of high density polyethylene/paraffin/organophilic montmorillonite hybrids as a form stable phase change material, Energy Convers. Manag. 48 (2007) 462–469. https://doi.org/10.1016/j.enconman.2006.06.021.
[143] A. Babapoor, G. Karimi, S.I. Golestaneh, M.A. Mezjin, Coaxial electro-spun PEG/PA6 composite fibers: Fabrication and characterization, Appl. Therm. Eng. 118 (2017) 398–407. https://doi.org/10.1016/j.applthermaleng.2017.02.119.
[144] B. Zhao, Hierarchical Templates and Their Application to Multimodal Porous Materials Fabrication, Virginia Commonwealth University, 2012.
[145] L.L. Hench, J.O.N.K. West, The Sol-Gel Process, Chem. Rev. 90 (1990) 33–72.
[146] T. Feczkó, L. Trif, D. Horák, Latent heat storage by silica-coated polymer beads containing organic phase change materials, Sol. Energy. 132 (2016) 405–414. https://doi.org/10.1016/j.solener.2016.03.036.
[147] B. Németh, Á.S. Németh, A. Ujhidy, J. Tóth, L. Trif, J. Gyenis, T. Feczkó, Fully bio-originated latent heat storing calcium alginate microcapsules with high coconut oil

loading, Sol. Energy. 170 (2018) 314–322. https://doi.org/10.1016/j.solener.2018.05.066.
[148] Y. Lin, C. Zhu, G. Alva, G. Fang, Microencapsulation and thermal properties of myristic acid with ethyl cellulose shell for thermal energy storage, Appl. Energy. 231 (2018) 494–501. https://doi.org/10.1016/j.apenergy.2018.09.154.
[149] F. Li, X. Wang, D. Wu, Fabrication of multifunctional microcapsules containing n-eicosane core and zinc oxide shell for low-temperature energy storage, photocatalysis, and antibiosis, Energy Convers. Manag. 106 (2015) 873–885. https://doi.org/10.1016/j.enconman.2015.10.026.
[150] K. Sun, H. Liu, X. Wang, D. Wu, Innovative design of superhydrophobic thermal energy-storage materials by microencapsulation of n-docosane with nanostructured ZnO/SiO2 shell, Appl. Energy. 237 (2019) 549–565. https://doi.org/10.1016/j.apenergy.2019.01.043.
[151] X. Huo, W. Li, Y. Wang, N. Han, J. Wang, N. Wang, X. Zhang, Chitosan composite microencapsulated comb-like polymeric phase change material via coacervation microencapsulation, Carbohydr. Polym. 200 (2018) 602–610. https://doi.org/10.1016/j.carbpol.2018.08.003.
[152] T. Wang, S. Wang, R. Luo, C. Zhu, T. Akiyama, Z. Zhang, Microencapsulation of phase change materials with binary cores and calcium carbonate shell for thermal energy storage, Appl. Energy. 171 (2016) 113–119. https://doi.org/10.1016/j.apenergy.2016.03.037.
[153] N. Şahan, H. Paksoy, Determining influences of SiO2 encapsulation on thermal energy storage properties of different phase change materials, Sol. Energy Mater. Sol. Cells. 159 (2017) 1–7. https://doi.org/10.1016/j.solmat.2016.08.030.
[154] J. Shi, X. Wu, R. Sun, B. Ban, J. Li, J. Chen, Nano-encapsulated phase change materials prepared by one-step interfacial polymerization for thermal energy storage, Mater. Chem. Phys. 231 (2019) 244–251. https://doi.org/10.1016/j.matchemphys.2019.04.032.
[155] J. hua Huo, Z. gang Peng, K. Xu, Q. Feng, D. yang Xu, Novel micro-encapsulated phase change materials with low melting point slurry: Characterization and cementing application, Energy. 186 (2019). https://doi.org/10.1016/j.energy.2019.115920.
[156] V. De Matteis, A. Cannavale, F. Martellotta, R. Rinaldi, P. Calcagnile, F. Ferrari, U. Ayr, F. Fiorito, Nano-encapsulation of phase change materials: From design to thermal performance, simulations and toxicological assessment, Energy Build. 188–189 (2019) 1–11. https://doi.org/10.1016/j.enbuild.2019.02.004.
[157] C. Li, G. He, H. Yan, H. Yu, Y. Song, Synthesis of microencapsulated stearic acid with amorphous TiO2 as shape-stabilized PCMs for thermal energy storage, Energy Procedia. 152 (2018) 390–394. https://doi.org/10.1016/j.egypro.2018.09.162.
[158] N. Şahan, D. Nigon, S.C. Mantell, J.H. Davidson, H. Paksoy, Encapsulation of stearic acid with different PMMA-hybrid shell materials for thermotropic materials, Sol. Energy. 184 (2019) 466–476. https://doi.org/10.1016/j.solener.2019.04.026.
[159] D.G. Atinafu, W. Dong, X. Huang, H. Gao, G. Wang, Introduction of organic-organic eutectic PCM in mesoporous N-doped carbons for enhanced thermal conductivity and energy storage capacity, Appl. Energy. 211 (2018) 1203–1215. https://doi.org/10.1016/j.apenergy.2017.12.025.
[160] P. Lv, M. Ding, C. Liu, Z. Rao, Experimental investigation on thermal properties and thermal performance enhancement of octadecanol/expanded perlite form stable phase

change materials for efficient thermal energy storage, Renew. Energy. 131 (2019) 911–922. https://doi.org/10.1016/j.renene.2018.07.102.

[161] P. Lv, C. Liu, Z. Rao, Experiment study on the thermal properties of paraffin/kaolin thermal energy storage form-stable phase change materials, Appl. Energy. 182 (2016) 475–487. https://doi.org/10.1016/j.apenergy.2016.08.147.

[162] D. Yang, F. Peng, H. Zhang, H. Guo, L. Xiong, C. Wang, S. Shi, X. Chen, Preparation of palygorskite paraffin nanocomposite suitable for thermal energy storage, Appl. Clay Sci. 126 (2016) 190–196. https://doi.org/10.1016/j.clay.2016.03.014.

[163] Y. Deng, J. Li, H. Nian, Y. Li, X. Yin, Design and preparation of shape-stabilized composite phase change material with high thermal reliability via encapsulating polyethylene glycol into flower-like TiO2 nanostructure for thermal energy storage, Appl. Therm. Eng. 114 (2017) 328–336. https://doi.org/10.1016/j.applthermaleng.2016.11.082.

[164] R.S. Andriamitantsoa, W. Dong, H. Gao, G. Wang, PEG encapsulated by porous triamide-linked polymers as support for solid-liquid phase change materials for energy storage, Chem. Phys. Lett. 671 (2017) 165–173. https://doi.org/10.1016/j.cplett.2017.01.028.

[165] X. Zong, Y. Cai, G. Sun, Y. Zhao, F. Huang, L. Song, Y. Hu, H. Fong, Q. Wei, Fabrication and characterization of electrospun SiO2 nanofibers absorbed with fatty acid eutectics for thermal energy storage/retrieval, Sol. Energy Mater. Sol. Cells. 132 (2015) 183–190. https://doi.org/10.1016/j.solmat.2014.08.030.

[166] Y. Cai, G. Sun, M. Liu, J. Zhang, Q. Wang, Q. Wei, Fabrication and characterization of capric-lauric-palmitic acid/electrospun SiO2 nanofibers composite as form-stable phase change material for thermal energy storage/retrieval, Sol. Energy. 118 (2015) 87–95. https://doi.org/10.1016/j.solener.2015.04.042.

[167] L. Cao, Y.J. Tang, G.Y. Fang, Preparation and properties of shape-stabilized phase change materials based on fatty acid eutectics and cellulose composites for thermal energy storage, Energy. 80 (2015) 98–103. https://doi.org/10.1016/j.energy.2014.11.046.

[168] A.B. Rezaie, M. Montazer, One-step fabrication of fatty acids/nano copper/polyester shape-stable composite phase change material for thermal energy management and storage, Appl. Energy. 228 (2018) 1911–1920. https://doi.org/10.1016/j.apenergy.2018.07.041.

[169] J.F. Hoffmann, J.F. Henry, G. Vaitilingom, R. Olives, M. Chirtoc, D. Caron, X. Py, Temperature dependence of thermal conductivity of vegetable oils for use in concentrated solar power plants, measured by 3omega hot wire method, Int. J. Therm. Sci. 107 (2016) 105–110. https://doi.org/10.1016/j.ijthermalsci.2016.04.002.

[170] J. Franklin White, Flammability characterization of fat and oil derived phase change materials, University of Missouri-Columbia, 2005.

[171] J. Pullen, K. Saeed, An overview of biodiesel oxidation stability, Renew. Sustain. Energy Rev. 16 (2012) 5924–5950. https://doi.org/10.1016/j.solmat.2015.06.039.

[172] N.M. Riaño H., M.J. Chica M., L.F. Echeverri G., J.L. Aguirre M., A. Ortiz, R.P. Pineda S.R., H.H. Olarte N., Total fat, profile of fatty acids and triglycerides from fine cocoa aroma: Colombia, ecuador, perú, Venezuela, Vitae. 23 (2016) S226–S230.

[173] L.F. Campuzano-Duque, F. Cardeño-López, Fatty acids composition of genotypes of Jatropha curcas L., in Colombia, Agron. Mesoamerican. 31 (2020) 95–104. https://doi.org/10.15517/AM.V31I1.37574.

[174] S.M. Walas, Phase Equilibria in Chemical Engineering., Butterworth-Heinemann, 1985. https://doi.org/https://doi.org/10.1016/C2013-0-04304-6.
[175] P. Kauranen, K. Peippo, P.D. Lund, An organic PCM storage system with adjustable melting temperature, Sol. Energy. 46 (1991) 275–278.
[176] Y. Yuan, N. Zhang, W. Tao, X. Cao, Y. He, Fatty acids as phase change materials : A review, Renew. Sustain. Energy Rev. 29 (2014) 482–498. https://doi.org/10.1016/j.rser.2013.08.107.
[177] A. Sharma, A. Shukla, C.R. Chen, S. Dwivedi, Development of phase change materials for building applications, Energy Build. 64 (2013) 403–407. https://doi.org/10.1016/j.enbuild.2013.05.029.
[178] S. Kahwaji, M. Anne, Data supporting the prediction of the properties of eutectic organic phase change materials, 17 (2018) 724–730.
[179] S. Kahwaji, M.B. Johnson, A.C. Kheirabadi, D. Groulx, M.A. White, Stable, low-cost phase change material for building applications: The eutectic mixture of decanoic acid and tetradecanoic acid, Appl. Energy. 168 (2016) 457–464. https://doi.org/10.1016/j.apenergy.2016.01.115.
[180] Y. He, X. Zhang, Y. Zhang, Q. Song, X. Liao, Utilization of lauric acid-myristic acid/expanded graphite phase change materials to improve thermal properties of cement mortar, Energy Build. 133 (2016) 547–558. https://doi.org/10.1016/j.enbuild.2016.10.016.
[181] P. Zhao, Q. Yue, H. He, B. Gao, Y. Wang, Q. Li, Study on phase diagram of fatty acids mixtures to determine eutectic temperatures and the corresponding mixing proportions, Appl. Energy. 115 (2014) 483–490. https://doi.org/10.1016/j.apenergy.2013.10.048.
[182] A. Sari, Eutectic mixtures of some fatty acids for latent heat storage: Thermal properties and thermal reliability with respect to thermal cycling, Energy Convers. Manag. 47 (2006) 1207–1221. https://doi.org/10.1016/j.enconman.2005.07.005.
[183] A. Sari, H. Sari, A. Önal, Thermal properties and thermal reliability of eutectic mixtures of some fatty acids as latent heat storage materials, Energy Convers. Manag. 45 (2004) 365–376. https://doi.org/10.1016/S0196-8904(03)00154-7.
[184] C. Cárdenas-Ramírez, F. Jaramillo, M.A. Gómez, Systematic review of encapsulation and shape-stabilization of phase change materials, J. Energy Storage. 30 (2020) 101495. https://doi.org/10.1016/j.est.2020.101495.
[185] G. Ferrer, C. Barreneche, A. Palacios, A. Solé, A.I. Fernández, L.F. Cabeza, Empirical equations for viscosity and specific heat capacity determination of fatty acids, J. Energy Storage. (2017) 20–27. https://doi.org/10.1088/1757-899X/251/1/012114.
[186] S.W. Benson, J.H. Buss, Additivity rules for the estimation of molecular properties. Thermodynamic properties, J. Chem. Phys. 29 (1958) 546–572. https://doi.org/10.1063/1.1744539.
[187] J.A. Noël, M.A. White, Heat capacities of potential organic phase change materials, J. Chem. Thermodyn. 128 (2019) 127–133. https://doi.org/10.1016/j.jct.2018.08.014.
[188] R. Ceriani, R. Gani, A.J.A. Meirelles, Prediction of heat capacities and heats of vaporization of organic liquids by group contribution methods, Fluid Phase Equilib. 283 (2009) 49–55. https://doi.org/10.1016/j.fluid.2009.05.016.
[189] M. Zábranský, V. Růžička, Estimation of the heat capacities of organic liquids as a function of temperature using group additivity: An amendment, J. Phys. Chem. Ref. Data. 33 (2004) 1071–1081. https://doi.org/10.1063/1.1797811.

[190] ASTM, E1269-Standard Test Method for Determining Specific Heat Capacity by Differential Scanning, in: 2012: pp. 1–6. https://doi.org/10.1520/E1269-11R18.Copyright.
[191] S. Kahwaji, M.A. White, Prediction of the properties of eutectic organic phase change materials, Thermochim. Acta. (2018) 94–100. https://doi.org/10.1016/j.dib.2018.01.102.
[192] G. Ferrer, C. Barreneche, A. Solé, I. Martorell, L.F. Cabeza, New proposed methodology for specific heat capacity determination of materials for thermal energy storage (TES) by DSC, J. Energy Storage. 11 (2017) 1–6. https://doi.org/10.1016/j.est.2017.02.002.
[193] S. Gschwander, T. Haussmann, G. Hagelstein, A. Sole, L.. Cabeza, Standardization of PCM Characterization via DSC, in: 13th Int. Conf. Energy Storage, 2015: pp. 1–8.
[194] ASTM, E2716-09 Standard Test Method for Determining Specific Heat Capacity by Sinusoidal Modulated Temperature Differential Scanning Calorimetry, Annu. B. ASTM Stand. i (2015) 1–4. https://doi.org/10.1520/E2716-09R14.2.
[195] S.L. Simon, Temperature-modulated differential scanning calorimetry: Theory and application, Thermochim. Acta. 374 (2001) 55–71. https://doi.org/10.1016/S0040-6031(01)00493-2.
[196] E. De Robertis, E.H.H. Cosme, R.S. Neves, A.Y. Kuznetsov, A.P.C. Campos, S.M. Landi, C.A. Achete, Application of the modulated temperature differential scanning calorimetry technique for the determination of the specific heat of copper nanofluids, Appl. Therm. Eng. 41 (2012) 10–17. https://doi.org/10.1016/j.applthermaleng.2012.01.003.
[197] S. Solarski, M. Ferreira, E. Devaux, Characterization of the thermal properties of PLA fibers by modulated differential scanning calorimetry, Polymer (Guildf). 46 (2005) 11187–11192. https://doi.org/10.1016/j.polymer.2005.10.027.
[198] H. Chen, Z. Yue, D. Ren, H. Zeng, T. Wei, K. Zhao, R. Yang, P. Qiu, L. Chen, X. Shi, Thermal Conductivity during Phase Transitions, Adv. Mater. 31 (2019) 1–7. https://doi.org/10.1002/adma.201806518.
[199] F.O. Koenig, Chemical Thermodynamics, 1955. https://doi.org/10.1021/ja01629a137.
[200] R.J. Thorn, On the origin of the lambda-type transition in heat capacity, J. Chem. Thermodyn. 34 (2002) 973–985. https://doi.org/10.1006/jcht.2001.0947.
[201] P. Lv, C. Liu, Z. Rao, Review on clay mineral-based form-stable phase change materials: Preparation, characterization and applications, Renew. Sustain. Energy Rev. 68 (2017) 707–726. https://doi.org/10.1016/j.rser.2016.10.014.
[202] Amir C. Akhavan, Overview of Silica Polymorphs, (2013). http://www.quartzpage.de/gen_mod.html (accessed November 27, 2020).
[203] Y.M. Mos, A.C. Vermeulen, C.J.N. Buisman, J. Weijma, X-Ray Diffraction of Iron Containing Samples: The Importance of a Suitable Configuration, Geomicrobiol. J. 35 (2018) 511–517. https://doi.org/10.1080/01490451.2017.1401183.
[204] MIT, X-Ray Diffraction Shared Experimental Facility, (2018). http://prism.mit.edu/xray/education/downloads.html (accessed March 5, 2018).
[205] G. Wang, H. Wang, N. Zhang, In situ high temperature X-ray diffraction study of illite, Appl. Clay Sci. 146 (2017) 254–263. https://doi.org/10.1016/j.clay.2017.06.006.
[206] P. Romero-Gómez, J.C. González, A. Bustamante, A. Ruiz-Conde, P.J. Sánchez-Soto, Estudio in-situ de la transformación térmica de limonita utilizada como pigmento procedente de Perú, Bol. La Soc. Esp. Ceram. y Vidr. 52 (2013) 127–131.

https://doi.org/10.3989/cyv.162013.
[207] D.K. Smith, Opal, cristobalite, and tridymite: Noncrystallinity versus crystallinity, nomenclature of the silica minerals and bibliography, Powder Diffr. 13 (1998) 2–19. https://doi.org/10.1017/S0885715600009696.
[208] E. Besoain, Mineralogía de Arcillas de Suelos, (1985) 1053.
[209] J.M. Elzea, I.E. Odom, W.J. Miles, Distinguishing well ordered opal-CT and opal-C from high temperature cristobalite by x-ray diffraction, Anal. Chim. Acta. 286 (1994) 107–116. https://doi.org/10.1016/0003-2670(94)80182-7.
[210] R. Zheng, Z. Ren, H. Gao, A. Zhang, Z. Bian, Effects of calcination on silica phase transition in diatomite, J. Alloys Compd. 757 (2018) 364–371. https://doi.org/10.1016/j.jallcom.2018.05.010.
[211] P. Yuan, D.Q. Wu, H.P. He, Z.Y. Lin, The hydroxyl species and acid sites on diatomite surface: A combined IR and Raman study, Appl. Surf. Sci. 227 (2004) 30–39. https://doi.org/10.1016/j.apsusc.2003.10.031.
[212] A. Bogdan, M. Kulmala, B. Gorbunov, A. Kruppa, NMR study of phase transitions in pure water and binary H2O/HNO3films adsorbed on surface of pyrogenic silica, J. Colloid Interface Sci. 177 (1996) 79–87. https://doi.org/10.1006/jcis.1996.0008.
[213] D. Barthelmy, Mineralogy database, (2012). http://www.webmineral.com/ (accessed October 20, 2018).
[214] M. Thommes, K. Kaneko, A. V. Neimark, J.P. Olivier, F. Rodriguez-Reinoso, J. Rouquerol, K.S.W. Sing, Physisorption of gases, with special reference to the evaluation of surface area and pore size distribution (IUPAC Technical Report), Pure Appl. Chem. 87 (2015) 1051–1069. https://doi.org/10.1515/pac-2014-1117.
[215] Y. Zhang, S. Zheng, S. Zhu, J. Ma, Z. Sun, M. Farid, Evaluation of paraffin infiltrated in various porous silica matrices as shape-stabilized phase change materials for thermal energy storage, Energy Convers. Manag. 171 (2018) 361–370. https://doi.org/10.1016/j.enconman.2018.06.002.
[216] J.P. Angle, Z. Wang, C. Dames, M.L. Mecartney, Comparison of two-phase thermal conductivity models with experiments on dilute ceramic composites, J. Am. Ceram. Soc. 96 (2013) 2935–2942. https://doi.org/10.1111/jace.12488.
[217] T. Nomura, N. Okinaka, T. Akiyama, Impregnation of porous material with phase change material for thermal energy storage, Mater. Chem. Phys. 115 (2009) 846–850. https://doi.org/10.1016/j.matchemphys.2009.02.045.
[218] L. Fu, Q. Wang, R. Ye, X. Fang, Z. Zhang, A calcium chloride hexahydrate/expanded perlite composite with good heat storage and insulation properties for building energy conservation, Renew. Energy. 114 (2017) 733–743. https://doi.org/10.1016/j.renene.2017.07.091.
[219] N. Zhang, Y. Yuan, X. Wang, X. Cao, X. Yang, S. Hu, Preparation and characterization of lauric – myristic – palmitic acid ternary eutectic mixtures / expanded graphite composite phase change material for thermal energy storage, Chem. Eng. J. 231 (2013) 214–219. https://doi.org/10.1016/j.cej.2013.07.008.
[220] X. Yang, Y. Yuan, N. Zhang, X. Cao, C. Liu, Preparation and properties of myristic – palmitic – stearic acid / expanded graphite composites as phase change materials for energy storage, Sol. Energy. 99 (2014) 259–266. https://doi.org/10.1016/j.solener.2013.11.021.
[221] X. Guo, Y. Huang, J. Cao, Performance of a thermal energy storage composite by incorporating diatomite stabilized paraffin as phase change material, Energy Build.

158 (2018) 1257–1265. https://doi.org/10.1016/j.enbuild.2017.11.032.
[222] Y. Konuklu, O. Ersoy, O. Gokce, Easy and industrially applicable impregnation process for preparation of diatomite-based phase change material nanocomposites for thermal energy storage, Appl. Therm. Eng. 91 (2015) 759–766. https://doi.org/10.1016/j.applthermaleng.2015.08.040.
[223] A. Karaipekli, A. Biçer, A. Sarı, V.V. Tyagi, Thermal characteristics of expanded perlite/paraffin composite phase change material with enhanced thermal conductivity using carbon nanotubes, Energy Convers. Manag. 134 (2017) 373–381. https://doi.org/10.1016/j.enconman.2016.12.053.
[224] H. Ke, Phase diagrams, eutectic mass ratios and thermal energy storage properties of multiple fatty acid eutectics as novel solid-liquid phase change materials for storage and retrieval of thermal energy, Appl. Therm. Eng. 113 (2017) 1319–1331. https://doi.org/10.1016/j.applthermaleng.2016.11.158.
[225] W. Chalco-Sandoval, M.J. Fabra, A. López-Rubio, J.M. Lagaron, Development of polystyrene-based films with temperature buffering capacity for smart food packaging, J. Food Eng. 164 (2015) 55–62. https://doi.org/10.1016/j.jfoodeng.2015.04.032.
[226] American Society for Testing and Materials (ASTM), ASTM E11-20: Standard Specification for Woven Wire Test Sieve Cloth and Test Sieves, (2020) 1–9. https://doi.org/10.1520/E0011-20.
[227] F. Bergaya, B.K.G. Theng, G. Lagaly, Handbook of Clay Science, 2006. https://doi.org/10.1016/S1572-4352(05)01039-1.
[228] H. Aguedal, H. Hentit, D.R. Merouani, A. Iddou, A. Shishkin, J.C. Jumas, Improvement of the sorption characteristics of diatomite by heat treatment, Key Eng. Mater. 721 (2016) 111–116. https://doi.org/10.4028/www.scientific.net/KEM.721.111.
[229] T. Li, C. Wu, Continual refined isothermal adsorption of pure illite in shale with gravimetric method, J. Pet. Sci. Eng. 172 (2019) 190–198. https://doi.org/10.1016/j.petrol.2018.09.059.
[230] B. Zsirka, E. Horváth, Z. Járvás, A. Dallos, É. Makó, J. Kristóf, Structural and energetical characterization of exfoliated kaolinite surfaces, Appl. Clay Sci. 124–125 (2016) 54–61. https://doi.org/10.1016/j.clay.2016.01.035.
[231] M.B. Pinson, T. Zhou, H.M. Jennings, M.Z. Bazant, Inferring pore connectivity from sorption hysteresis in multiscale porous media, J. Colloid Interface Sci. 532 (2018) 118–127. https://doi.org/10.1016/j.jcis.2018.07.095.
[232] L. Randazzo, G. Montana, A. Hein, A. Castiglia, G. Rodonò, D.I. Donato, Moisture absorption, thermal conductivity and noise mitigation of clay based plasters: The influence of mineralogical and textural characteristics, Appl. Clay Sci. 132–133 (2016) 498–507. https://doi.org/10.1016/j.clay.2016.07.021.
[233] Y. Xu, D. Sun, Z. Zeng, H. Lv, Effect of temperature on thermal conductivity of lateritic clays over a wide temperature range, Int. J. Heat Mass Transf. 138 (2019) 562–570. https://doi.org/10.1016/j.ijheatmasstransfer.2019.04.077.
[234] F.P. Soorbaghi, M. Kokabi, A.R. Bahramian, Predicting the effective thermal conductivity of silica/clay mineral nanocomposite aerogels, Int. J. Heat Mass Transf. 136 (2019) 899–910. https://doi.org/10.1016/j.ijheatmasstransfer.2019.03.059.
[235] Y. Wu, P. Tahmasebi, C. Lin, M.J. Munawar, V. Cnudde, Effects of micropores on geometric, topological and transport properties of pore systems for low-permeability

porous media, J. Hydrol. 575 (2019) 327–342. https://doi.org/10.1016/j.jhydrol.2019.05.014.
[236] Z. Jiang, K. Wu, G.D. Couples, J. Ma, The impact of pore size and pore connectivity on single-phase fluid flow in porous media, Adv. Eng. Mater. 13 (2011) 208–215. https://doi.org/10.1002/adem.201000255.
[237] P. Yuan, D. Yang, Z. Lin, H. He, X. Wen, L. Wang, F. Deng, Influences of pretreatment temperature on the surface silylation of diatomaceous amorphous silica with trimethylchlorosilane, J. Non. Cryst. Solids. 352 (2006) 3762–3771. https://doi.org/10.1016/j.jnoncrysol.2006.05.035.
[238] X. Li, H. Chen, L. Liu, Z. Lu, J.G. Sanjayan, W.H. Duan, Development of granular expanded perlite/paraffin phase change material composites and prevention of leakage, Sol. Energy. 137 (2016) 179–188. https://doi.org/10.1016/j.solener.2016.08.012.
[239] R. Liu, F. Zhang, W. Su, H. Zhao, C.A. Wang, Impregnation of porous mullite with Na2SO4 phase change material for thermal energy storage, Sol. Energy Mater. Sol. Cells. 134 (2015) 268–274. https://doi.org/10.1016/j.solmat.2014.12.012.
[240] L. Han, G. Ma, S. Xie, J. Sun, Y. Jia, Y. Jing, Thermal properties and stabilities of the eutectic mixture: 1,6-hexanediol/lauric acid as a phase change material for thermal energy storage, Appl. Therm. Eng. 116 (2017) 153–159. https://doi.org/10.1016/j.applthermaleng.2017.01.082.
[241] Y. Qu, S. Wang, Y. Tian, D. Zhou, Comprehensive evaluation of Paraffin-HDPE shape stabilized PCM with hybrid carbon nano-additives, Appl. Therm. Eng. 163 (2019) 114404. https://doi.org/10.1016/j.applthermaleng.2019.114404.
[242] C. Cárdenas-Ramírez, M.A. Gómez, F. Jaramillo, Comprehensive analysis of the thermal properties of capric-myristic, lauric-myristic and palmitic-stearic acids and their shape-stabilization in an inorganic support, J. Energy Storage. 34 (2021) 102015. https://doi.org/10.1016/j.est.2020.102015.
[243] C. Cárdenas-Ramírez, F. Jaramillo, A.G. Fernández, L.F. Cabeza, M.A. Gómez, Influence of thermal treatments on the absorption and thermal properties of a clay mineral support used for shape-stabilization of fatty acids, J. Energy Storage. 36 (2021) 102427. https://doi.org/10.1016/j.est.2021.102427.
[244] J.B. Clark, J.. Hastie, L.H.. Kihlborg, R. Metselaar, M. Thackeray, Definitions of terms relating to phase transitions of the solid state (IUPAC Recommendations 1994), 1994.
[245] Y. Mnyukh, On the Phase Transitions That Cannot Materialize, 4 (2013) 1–12. https://doi.org/10.5923/j.ajcmp.20140401.01.
[246] F. Körmann, A.A.H. Breidi, S.L. Dudarev, N. Dupin, G. Ghosh, T. Hickel, P. Korzhavyi, J.A. Muñoz, I. Ohnuma, Lambda transitions in materials science: Recent advances in CALPHAD and first-principles modelling, Phys. Status Solidi Basic Res. 251 (2014) 53–80. https://doi.org/10.1002/pssb.201350136.
[247] N. Song, C.S. Hong, Y. Mao, P. Lin, Q. Zhang, L. Zhang, Realization of the lambda transition temperature of liquid 4He, Cryogenics (Guildf). 31 (1991) 87–93. https://doi.org/10.1016/0011-2275(91)90251-Q.
[248] G. Raam Dheep, A. Sreekumar, Thermal reliability and corrosion characteristics of an organic phase change materials for solar space heating applications, J. Energy Storage. 23 (2019) 98–105. https://doi.org/10.1016/j.est.2019.03.009.
[249] L. Yang, X. Cao, N. Zhang, B. Xiang, Z. Zhang, B. Qian, Thermal reliability of typical

fatty acids as phase change materials based on 10,000 accelerated thermal cycles, Sustain. Cities Soc. 46 (2019) 101380. https://doi.org/10.1016/j.scs.2018.12.008.
[250] L. Miró, C. Barreneche, G. Ferrer, A. Solé, I. Martorell, L.F. Cabeza, Health hazard, cycling and thermal stability as key parameters when selecting a suitable phase change material (PCM), Thermochim. Acta. 627–629 (2016) 39–47. https://doi.org/10.1016/j.tca.2016.01.014.
[251] I. Martorell, C. Barreneche, L.F. Cabeza, A. Solé, G. Ferrer, Review on the methodology used in thermal stability characterization of phase change materials, Renew. Sustain. Energy Rev. 50 (2015) 665–685. https://doi.org/10.1016/j.rser.2015.04.187.
[252] V. V. Tyagi, D. Buddhi, Thermal cycle testing of calcium chloride hexahydrate as a possible PCM for latent heat storage, Sol. Energy Mater. Sol. Cells. 92 (2008) 891–899. https://doi.org/10.1016/j.solmat.2008.02.021.
[253] A. Sari, A. Biçer, Thermal energy storage properties and thermal reliability of some fatty acid esters/building material composites as novel form-stable PCMs, Sol. Energy Mater. Sol. Cells. 101 (2012) 114–122. https://doi.org/10.1016/j.solmat.2012.02.026.
[254] L. Navarro, A. Solé, M. Martín, C. Barreneche, L. Olivieri, J.A. Tenorio, L.F. Cabeza, Benchmarking of useful phase change materials for a building application, Energy Build. 182 (2019) 45–50. https://doi.org/10.1016/j.enbuild.2018.10.005.
[255] Y. KONUKLU, F. ERZİN, H.B. AKAR, A.M. TURAN, Cellulose-based myristic acid composites for thermal energy storage applications, Sol. Energy Mater. Sol. Cells. 193 (2019) 85–91. https://doi.org/10.1016/j.solmat.2019.01.006.
[256] M.N.R. Dimaano, A.D. Escoto, Preliminary assessment of a mixture of capric and lauric acids for low-temperature thermal energy storage, Energy. 23 (1998) 421–427. https://doi.org/10.1016/S0360-5442(97)00108-4.
[257] G. Raam Dheep, A. Sreekumar, Thermal reliability and corrosion characteristics of an organic phase change materials for solar space heating applications, J. Energy Storage. 23 (2019) 98–105. https://doi.org/10.1016/j.est.2019.03.009.
[258] A. Sari, Thermal reliability test of some fatty acids as PCMs used for solar thermal latent heat storage applications, Energy Convers. Manag. 44 (2003) 2277–2287. https://doi.org/10.1016/S0196-8904(02)00251-0.
[259] S. Mengjie, W.M. Pun, D. Swapnil, P. Dongmei, M. Ning, Thermal stability of organic binary PCMs for energy storage, Energy Procedia. 142 (2017) 3287–3294. https://doi.org/10.1016/j.egypro.2017.12.459.
[260] M. George, A.K. Pandey, N. Abd Rahim, V. V. Tyagi, S. Shahabuddin, R. Saidur, A novel polyaniline (PANI)/ paraffin wax nano composite phase change material: Superior transition heat storage capacity, thermal conductivity and thermal reliability, Sol. Energy. 204 (2020) 448–458. https://doi.org/10.1016/j.solener.2020.04.087.
[261] A.A. El-Sebaii, S. Al-Heniti, F. Al-Agel, A.A. Al-Ghamdi, F. Al-Marzouki, One thousand thermal cycles of magnesium chloride hexahydrate as a promising PCM for indoor solar cooking, Energy Convers. Manag. 52 (2011) 1771–1777. https://doi.org/10.1016/j.enconman.2010.10.043.
[262] A. Vasu, F.Y. Hagos, R. Mamat, J. Kaur, M.M. Noor, The effect of thermal cyclic variation on the thermophysical property degradation of paraffin as a phase changing energy storage material, Appl. Therm. Eng. 149 (2019) 22–33.
[263] M.K. Rathod, J. Banerjee, Thermal stability of phase change materials used in latent heat energy storage systems: A review, Renew. Sustain. Energy Rev. 18 (2013) 246–

258. https://doi.org/10.1016/j.rser.2012.10.022.
[264] V. V. Tyagi, D. Buddhi, Thermal cycle testing of calcium chloride hexahydrate as a possible PCM for latent heat storage, Sol. Energy Mater. Sol. Cells. 92 (2008) 891–899. https://doi.org/10.1016/j.solmat.2008.02.021.
[265] A. Sari, Thermal reliability test of some fatty acids as PCMs used for solar thermal latent heat storage applications, Energy Convers. Manag. 44 (2003) 2277–2287. https://doi.org/10.1016/S0196-8904(02)00251-0.
[266] A. Sari, Eutectic mixtures of some fatty acids for latent heat storage: Thermal properties and thermal reliability with respect to thermal cycling, Energy Convers. Manag. 47 (2006) 1207–1221. https://doi.org/10.1016/j.enconman.2005.07.005.
[267] J. Shen, Z. Cai, C. Wang, X. Liu, R. Zheng, Preparation and thermal performances of 1, 10-decanediol-stearic acid eutectic as phase change material, Thermochim. Acta. 690 (2020) 8–13. https://doi.org/10.1016/j.tca.2020.178648.
[268] H. Wei, X. Xie, X. Li, X. Lin, Preparation and characterization of capric-myristic-stearic acid eutectic mixture/modified expanded vermiculite composite as a form-stable phase change material, Appl. Energy. 178 (2016) 616–623. https://doi.org/10.1021/acs.energyfuels.7b03933.
[269] A. Karaipekli, A. Sari, Capric-myristic acid/expanded perlite composite as form-stable phase change material for latent heat thermal energy storage, Renew. Energy. 33 (2008) 2599–2605. https://doi.org/10.1016/j.renene.2008.02.024.
[270] A. Sarı, A. Bicer, C. Alkan, A.N. Özcan, Thermal energy storage characteristics of myristic acid-palmitic eutectic mixtures encapsulated in PMMA shell, Sol. Energy Mater. Sol. Cells. 193 (2019) 1–6. https://doi.org/10.1016/j.solmat.2019.01.003.
[271] Z. Sun, Y. Zhang, S. Zheng, Y. Park, R.L. Frost, Preparation and thermal energy storage properties of paraffin/calcined diatomite composites as form-stable phase change materials, Thermochim. Acta. 558 (2013) 16–21. https://doi.org/10.1016/j.tca.2013.02.005.
[272] W. min Guan, J. hong Li, T. ting Qian, X. Wang, Y. Deng, Preparation of paraffin/expanded vermiculite with enhanced thermal conductivity by implanting network carbon in vermiculite layers, Chem. Eng. J. 277 (2015) 56–63. https://doi.org/10.1016/j.cej.2015.04.077.
[273] M.A. Izquierdo-Barrientos, C. Sobrino, J.A. Almendros-Ibáñez, Experimental heat transfer coefficients between a surface and fixed and fluidized beds with PCM, Appl. Therm. Eng. 78 (2015) 373–379.
[274] M.A. Izquierdo-Barrientos, C. Sobrino, J.A. Almendros-Ibáñez, C. Barreneche, N. Ellis, L.F. Cabeza, Characterization of granular phase change materials for thermal energy storage applications in fluidized beds, Appl. Energy. 181 (2016) 310–321. https://doi.org/10.1016/j.apenergy.2016.08.081.
[275] J. Coates, Interpretation of Infrared Spectra, A Practical Approach, Encycl. Anal. Chem. (2004) 1–23. http://www3.uma.pt/jrodrigues/disciplinas/QINO-II/Teorica/IR.pdf.
[276] C.A.R. Reyes, C. Williams, O.M.C. Alarcón, Nucleation and growth process of sodalite and cancrinite from kaolinite-rich clay under low-temperature hydrothermal conditions, Mater. Res. 16 (2013) 424–438. https://doi.org/10.1590/S1516-14392013005000010.
[277] M.F. Zawrah, R.A. Gado, R.M. Khattab, Optimization of slag content and properties improvement of metakaolin-slag geopolymer mixes, Open Mater. Sci. J. 12 (2018)

40–57. https://doi.org/10.2174/1874088X01812010040.
[278] C. Li, L. Fu, J. Ouyang, H. Yang, Enhanced performance and interfacial investigation of mineral-based composite phase change materials for thermal energy storage, Sci. Rep. 3 (2013) 1–8. https://doi.org/10.1038/srep01908.
[279] J. Mazo, M. Delgado, C. Peñalosa, P. Dolado, I. Miranda, A. Lázaro, J.M. Marín, B. Zalba, Evaluation of the suitability of different calorimetric methods to determine the enthalpy-temperature curve of granular PCM composites, Appl. Therm. Eng. 125 (2017) 306–316. https://doi.org/10.1016/j.applthermaleng.2017.07.035.
[280] Y. Quanying, H. Ran, L. Lisha, Thermal energy storage properties of paraffin and fatty acid binary systems, Int. J. Sustain. Energy. 31 (2012) 269–275. https://doi.org/10.1080/1478646X.2011.563307.
[281] J. Lizana, R. Chacartegui, A. Barrios-Padura, J.M. Valverde, Advances in thermal energy storage materials and their applications towards zero energy buildings: A critical review, Appl. Energy. 203 (2017) 219–239. https://doi.org/10.1016/j.apenergy.2017.06.008.
[282] S. Bee, M.A.A. Abdullah, S. Bee, L. Tin, A.R. Rahmat, Polymer nanocomposites based on silylated-montmorillonite : A review, Prog. Polym. Sci. 85 (2018) 57–82.
[283] H. He, J. Duchet, J. Galy, J.F. Gerard, Grafting of swelling clay materials with 3-aminopropyltriethoxysilane, J. Colloid Interface Sci. 288 (2005) 171–176. https://doi.org/10.1016/j.jcis.2005.02.092.
[284] L.R. Avila, E.H. de Faria, K.J. Ciuffi, E.J. Nassar, P.S. Calefi, M.A. Vicente, R. Trujillano, New synthesis strategies for effective functionalization of kaolinite and saponite with silylating agents, J. Colloid Interface Sci. 341 (2010) 186–193. https://doi.org/10.1016/j.jcis.2009.08.041.
[285] S. qin Yang, P. Yuan, H. ping He, Z. hua Qin, Q. Zhou, J. xi Zhu, D. Liu, Effect of reaction temperature on grafting of γ-aminopropyl triethoxysilane (APTES) onto kaolinite, Appl. Clay Sci. 62–63 (2012) 8–14. https://doi.org/10.1016/j.clay.2012.04.006.
[286] Q. Liu, H. Cheng, Y. Zhou, Effect of alkylamine chain length on high-temperature phase transformation and thermal decomposition process of kaolinite intercalation compounds, J. Phys. Chem. Solids. 136 (2020). https://doi.org/10.1016/j.jpcs.2019.109170.
[287] T. Kristóf, Z. Sarkadi, Z. Ható, G. Rutkai, Simulation study of intercalation complexes of kaolinite with simple amides as primary intercalation reagents, Comput. Mater. Sci. 143 (2018) 118–125. https://doi.org/10.1016/j.commatsci.2017.11.010.
[288] S. Zhang, Q. Liu, H. Cheng, Y. Zhang, X. Li, R.L. Frost, Intercalation of γ-aminopropyl triethoxysilane (APTES) into kaolinite interlayer with methanol-grafted kaolinite as intermediate, Appl. Clay Sci. 114 (2015) 484–490. https://doi.org/10.1016/j.clay.2015.06.035.
[289] W. Xiao, M. Zhan, Z. Li, Organically modifying and modeling analysis of montmorillonites, Mater. Des. 24 (2003) 455–462. https://doi.org/10.1016/S0261-3069(03)00064-5.
[290] M.R. Guilherme, L.H.C. Mattoso, N. Gontard, S. Guilbert, E. Gastaldi, Synthesis of nanocomposite films from wheat gluten matrix and MMT intercalated with different quaternary ammonium salts by way of hydroalcoholic solvent casting, Compos. Part A. 41 (2010) 375–382. https://doi.org/10.1016/j.compositesa.2009.11.004.
[291] V. Mittal, Polymer layered silicate nanocomposites: A review, Materials (Basel). 2

(2009) 992–1057. https://doi.org/10.3390/ma2030992.
[292] Z. Yang, J. Li, X. Luan, S. Song, Effects of acid leaching and organic intercalation on the thermophysical properties of paraffin/expanded vermiculite composite phase change materials, Appl. Clay Sci. 196 (2020). https://doi.org/10.1016/j.clay.2020.105754.
[293] P. Yuan, D. Liu, D.Y. Tan, K.K. Liu, H.G. Yu, Y.H. Zhong, A.H. Yuan, W. Bin Yu, H.P. He, Surface silylation of mesoporous/macroporous diatomite (diatomaceous earth) and its function in Cu(II) adsorption: The effects of heating pretreatment, Microporous Mesoporous Mater. 170 (2013) 9–19. https://doi.org/10.1016/j.micromeso.2012.11.030.
[294] W. Yu, L. Deng, P. Yuan, D. Liu, W. Yuan, P. Liu, Surface silylation of natural mesoporous / macroporous diatomite for adsorption of benzene, J. Colloid Interface Sci. 448 (2015) 545–552.
[295] M. Raji, M.E.M. Mekhzoum, D. Rodrigue, A. el kacem Qaiss, R. Bouhfid, Effect of silane functionalization on properties of polypropylene/clay nanocomposites, Compos. Part B Eng. 146 (2018) 106–115. https://doi.org/10.1016/j.compositesb.2018.04.013.
[296] K.S. Abou-El-Sherbini, E.A.M. Elzahany, M.A. Wahba, S.A. Drweesh, N.S. Youssef, Evaluation of some intercalation methods of dimethylsulphoxide onto HCl-treated and untreated Egyptian kaolinite, Appl. Clay Sci. 137 (2017) 33–42. https://doi.org/10.1016/j.clay.2016.12.005.
[297] D. Carroll, H.C. Starkey, Reactivity of clay minerals with acids and alkalies, Clays Clay Miner. 19 (1971) 321–333. https://doi.org/10.1346/CCMN.1971.0190508.
[298] S. Bhattacharyya, P.S. Behera, Synthesis and characterization of nano-sized α-alumina powder from kaolin by acid leaching process, Appl. Clay Sci. 146 (2017) 286–290. https://doi.org/10.1016/j.clay.2017.06.017.
[299] S.A. Drweesh, N.A. Fathy, M.A. Wahba, A.A. Hanna, A.I.M. Akarish, E.A.M. Elzahany, I.Y. El-Sherif, K.S. Abou-El-Sherbini, Equilibrium, kinetic and thermodynamic studies of Pb(II) adsorption from aqueous solutions on HCl-treated Egyptian kaolin, J. Environ. Chem. Eng. 4 (2016) 1674–1684. https://doi.org/10.1016/j.jece.2016.02.005.
[300] J.A. Mbey, J.M. Siéwé, C.J.N. Sabouang, A. Razafitianamaharavo, S. Kong, F. Thomas, Dmso intercalation in selected kaolinites: Influence of the crystallinity, ChemEngineering. 4 (2020) 1–10. https://doi.org/10.3390/chemengineering4040066.
[301] H. Cheng, Q. Liu, J. Yang, S. Ma, R.L. Frost, The thermal behavior of kaolinite intercalation complexes - A review, Thermochim. Acta. 545 (2012) 1–13. https://doi.org/10.1016/j.tca.2012.04.005.
[302] Q. Al-Yasiri, M. Szabó, Incorporation of phase change materials into building envelope for thermal comfort and energy saving: A comprehensive analysis, J. Build. Eng. 36 (2021). https://doi.org/10.1016/j.jobe.2020.102122.
[303] J.M. Sala-Lizarraga, A. Picallo-Perez, Exergy Analysis and Thermoeconomics of Buildings, Elsevier, 2020. https://doi.org/10.1016/c2018-0-01196-2.
[304] M. Pomianowski, P. Heiselberg, Y. Zhang, Review of thermal energy storage technologies based on PCM application in buildings, Energy Build. 67 (2013) 56–69. https://doi.org/10.1016/j.enbuild.2013.08.006.
[305] H. Yu, C. Li, K. Zhang, Y. Tang, Y. Song, M. Wang, Preparation and thermophysical performance of diatomite-based composite PCM wallboard for thermal energy storage

in buildings, J. Build. Eng. 32 (2020). https://doi.org/10.1016/j.jobe.2020.101753.
[306] L. Navarro, L.F. Cabeza, J.A. Tenorio, L. Olivieri, D. Revuelta, Developing a PCM-enhanced mortar for thermally active precast walls, Constr. Build. Mater. 181 (2018) 638–649. https://doi.org/10.1016/j.conbuildmat.2018.06.013.
[307] A. D'Alessandro, A.L. Pisello, C. Fabiani, F. Ubertini, L.F. Cabeza, F. Cotana, Multifunctional smart concretes with novel phase change materials: Mechanical and thermo-energy investigation, Appl. Energy. 212 (2018) 1448–1461. https://doi.org/10.1016/j.apenergy.2018.01.014.
[308] A. Fernandez, S. Serrano, L. Haurie, A. Navarro, L. Cabeza, C. Barreneche, Study of Fresh and Hardening Process Properties of Gypsum with Three Different PCM Inclusion Methods, Materials (Basel). 8 (2015) 6589–6596. https://doi.org/10.3390/ma8105324.
[309] C. Li, H. Yu, Y. Song, Y. Tang, P. Chen, H. Hu, M. Wang, Z. Liu, Experimental thermal performance of wallboard with hybrid microencapsulated phase change materials for building application, J. Build. Eng. 28 (2020). https://doi.org/10.1016/j.jobe.2019.101051.
[310] F. Kuznik, J. Virgone, J. Noel, Optimization of a phase change material wallboard for building use, Appl. Therm. Eng. 28 (2008) 1291–1298. https://doi.org/10.1016/j.applthermaleng.2007.10.012.
[311] D. Zhou, P. Eames, Phase Change Material Wallboard (PCMW) melting temperature optimisation for passive indoor temperature control, Renew. Energy. 139 (2019) 507–514. https://doi.org/10.1016/j.renene.2019.02.109.
[312] H. Abbasi Hattan, M. Madhkhan, A. Marani, Thermal and mechanical properties of building external walls plastered with cement mortar incorporating shape-stabilized phase change materials (SSPCMs), Constr. Build. Mater. 270 (2021). https://doi.org/10.1016/j.conbuildmat.2020.121385.
[313] Y.A. Lakhdari, S. Chikh, A. Campo, Analysis of the thermal response of a dual phase change material embedded in a multi-layered building envelope, Appl. Therm. Eng. 179 (2020). https://doi.org/10.1016/j.applthermaleng.2020.115502.
[314] P.K.S. Rathore, S.K. Shukla, N.K. Gupta, Yearly analysis of peak temperature, thermal amplitude, time lag and decrement factor of a building envelope in tropical climate, J. Build. Eng. 31 (2020). https://doi.org/10.1016/j.jobe.2020.101459.
[315] S. Lu, Y. Chen, S. Liu, X. Kong, Experimental research on a novel energy efficiency roof coupled with PCM and cool materials, Energy Build. 127 (2016) 159–169. https://doi.org/10.1016/j.enbuild.2016.05.080.
[316] Isabelle Lomholt, DuPont Energain : iCon Innovation Centre in Daventry, E-Architect. (2011). https://www.e-architect.com/products/dupont-energain (accessed May 29, 2021).
[317] A. De Gracia, C. Barreneche, M.M. Farid, L.F. Cabeza, New equipment for testing steady and transient thermal performance of multilayered building envelopes with PCM, Energy Build. 43 (2011) 3704–3709. https://doi.org/10.1016/j.enbuild.2011.10.010.
[318] J. Coma, A. de Gracia, M. Chàfer, G. Pérez, L.F. Cabeza, Thermal characterization of different substrates under dried conditions for extensive green roofs, Energy Build. 144 (2017) 175–180. https://doi.org/10.1016/j.enbuild.2017.03.031.
[319] L. Bellahcene, A. Cheknane, S.M.A. Bekkouche, D. Sahel, The effect of the thermal inertia on the thermal transfer in building wall, E3S Web Conf. 22 (2017).

https://doi.org/10.1051/e3sconf/20172200013.
[320] A. De Gracia, A. Castell, M. Medrano, L.F. Cabeza, Dynamic thermal performance of alveolar brick construction system, Energy Convers. Manag. 52 (2011) 2495–2500. https://doi.org/10.1016/j.enconman.2011.01.022.
[321] Designing Buildings Wiki, U-values, (2021). https://www.designingbuildings.co.uk/wiki/U-values (accessed January 14, 2021).
[322] C. Barreneche, A. De Gracia, S. Serrano, M. Elena Navarro, A.M. Borreguero, A. Inés Fernández, M. Carmona, J.F. Rodriguez, L.F. Cabeza, Comparison of three different devices available in Spain to test thermal properties of building materials including phase change materials, Appl. Energy. 109 (2013) 544–552. https://doi.org/10.1016/j.apenergy.2013.02.061.
[323] F.J. Neila-González, C. Bedoya, El comportamiento térmico y la enercia térmica de las fábricas con bloques Termoarcilla, Conarquitectura. (1997) 63–76.
[324] H. Asan, Investigation of wall's optimum insulation position from maximum time lag and minimum decrement factor point of view, Energy Build. 32 (2000) 197–203. https://doi.org/10.1016/S0378-7788(00)00044-X.